Using Model Spectral Energy Distributions to Study Galaxy Masses: Now and in the Future

by

Robert Sorba

A Thesis Submitted to Saint Mary's University, Halifax, Nova Scotia,
in Partial Fulfillment of the Requirements for the Degree of PhD in Astronomy

Approved: Dr. Marcin Sawicki
Supervisor

Approved: Dr. C. Ian Short
Reader

Approved: Dr. Rob Thacker
Reader

Approved: Dr. Adam Muzzin
External Examiner

Date: March 16, 2017

Acknowledgments

This is for me. So I can look my son in the eye, and say "Dad's no quitter."

Completing this thesis would not have been possible without the help of my friends, family, and various members of the scientific community. I am indebted to everyone who helped create all of the public data and all of the open source software I used. I could never have done it from scratch. I want to thank Anneya for all her help; Liz for waking up with me for early morning work sessions and all the invaluable moral support; Shona and Cameron for giving me a place to sleep; My parents for loving me and supporting me no matter the outcome; My sister, Christina, for reminding me how awesome she is. Don't ever let me forget. I miss you; My supervisor, Marcin, for supporting me and encouraging me and for dragging me through this kicking and screaming; and finally my wonderful wife Catherine, for somehow managing to keep our family functioning when this project swallowed me whole.

Contents

List of Figures

List of Tables

Abstract

Using Model Spectral Energy Distributions to Study Galaxy Masses: Now and in the Future

by Robert Sorba

The determination of galaxy masses is an essential tool for our understanding of galaxy evolution. Looking at 67 local galaxies, we find that galaxy stellar masses are underestimated using traditional methods that assume homogeneous stellar populations as compared to spatially resolved methods. The underestimate is correlated with specific star-formation rate (sSFR), and is as high as 25% in high-SFR nearby galaxies. At higher redshifts we find a similar effect, except the linear trend with sSFR becomes much more dramatic: unresolved mass measurements may be too low by factors of two to five for the highest sSFR galaxies. The increasing mass correction with sSFR resolves a long-standing discrepancy between the directly observed star-formation rate density and that implied by the stellar mass density. A definitive confirmation of this trend will require observations with JWST. We use the spatially resolved data of our high redshift galaxies to create simulations of the JWST's NIRISS instrument, and find that analysis tools need to ensure they can account for spatially inhomogeneous spectra within a galaxy in order to obtain the most accurate line emission measurements. Additionally, we examine how photometric redshifts can be improved for future space-based weak lensing missions such as Euclid. Weak lensing tomography depends critically upon accurate redshift estimation in order to map the three dimensional mass distribution of the universe. We demonstrate the poor quality of photometric redshifts these missions would expect without optical bandpasses and show how the addition of a U and/or G filter could remove their reliance on ground-based surveys.

March 16, 2017

Chapter 1

Introduction

1.1 Galaxies

Our universe contains billions of galaxies, each of which is composed of dark matter, gas, dust, black holes, and billions upon billions of stars. But, in describing a galaxy, we want to know more than just a list of its components; we also want to know how all the various parts interact with one-another to govern the galaxy's evolution and eventual fate. In a simplistic sense, a galaxy can be thought of as a stellar factory, its gravitational well slowly accreting hydrogen and helium gas and converting it into stars. However, star formation does not continue indefinitely throughout a galaxy's lifetime, and many galaxies observed have little to no star formation.

Early classification schemes of galaxies exhibited a stark dichotomy in morphological type (Hubble, 1926) which was later shown to also be related to a galaxy's environment (Oemler, 1974; Davis & Geller, 1976; Dressler, 1980). Recent large scale surveys (Strateva et al., 2001; Baldry et al., 2004; Balogh et al., 2004; Bell et al., 2004; Weiner et al., 2005; Willmer et al., 2006; Kriek et al., 2008; Brammer et al., 2009; Taylor et al., 2009) also give a bimodal view of galaxy classification, dividing galaxies into two categories by color, a proxy for star formation. Star-forming galaxies are typically blue in color due to the presence of hot O and B stars and tend to have a spiral morphology at low redshift (Kauffmann et al.,

2003). Quiescent galaxies (often referred to as "red and dead") are typically more massive, have an elliptical morphology, and a much redder color since cooler stars are long-lived. It should be noted that these two categories are not clear-cut. In addition to outliers such as Ultra Luminous Infrared Galaxies (Chapman et al., 2003; Conselice et al., 2003), recent large scale projects such as Galaxy Zoo have found red spirals, blue ellipticals, and "green valley" galaxies (thought to be in transition between star-forming and quiescent; Martin et al., 2007; Schawinski et al., 2014). In broad strokes, however, the classification of galaxies into either star-forming or quiescent is a useful paradigm. It leads us to naturally question what caused the cessation of star-formation, and what factors influence a galaxy's life and death.

One clear characteristic governing a galaxy's evolution is its environment. Galaxy mergers and interactions can act to funnel gas into a galaxy, leading to an intense burst of star-formation (Sanders et al., 1988), but interactions can also lead to near complete quenching through accretion shocks (Balogh, Navarro & Morris, 2000; Dekel & Birnboim, 2006), strangulation (Larson, Tinsley & Caldwell, 1980), and/or ram-pressure stripping (Gunn & Gott, 1972; Abadi, Moore & Bower, 1999). Feedback from both supernovae (Springel, Di Matteo & Hernquist, 2005) and active galactic nuclei (Di Matteo, Springel & Hernquist, 2005; Hopkins & Hernquist, 2006) also plays a key role in restricting star-formation, but the exact details of these quenching processes are not yet fully understood. Unfortunately, the long timescale on which galaxy evolution takes place inhibits us from observing the often stochastic changes in star-formation in real time. However, the finite speed of light and extreme size of our universe allow us to look back in time and develop a statistical overview of how galaxies have evolved. A large body of research has made it clear that one of the best factors for describing a galaxy's life cycle that we can observe and measure is the stellar mass (SM).

The SM of a galaxy is correlated with the mass of the dark matter halo in which the galaxy resides (Behroozi, Conroy & Wechsler, 2010; Moster et al., 2010; Yang et al., 2012), and thus with the total gravitational potential well. It has been shown to correlate well

with a wide range of properties including brightness and size (Trujillo et al., 2006; Williams et al., 2010), rotational velocity or velocity dispersion (Faber & Jackson, 1976; Tully & Fisher, 1977), star-formation rate (the "main sequence" Daddi et al., 2007; Sawicki, 2012b), metallicity (Savaglio et al., 2005; Mannucci et al., 2010), and mean stellar age (Gallazzi et al., 2005). An examination of stellar mass functions has shown that the most massive galaxies formed first in the early universe (Pérez-González et al., 2008; Ilbert et al., 2013; Muzzin et al., 2013), but these massive galaxies also had the greatest chance of being quenched the soonest, resulting in a "downsizing" phenomenon (Cowie et al., 1996; Heavens et al., 2004) where star-formation now continues most effectively in smaller galaxies. Additionally, the stellar mass in the universe is inextricably linked to the entire star formation history of the universe (e.g. Wilkins, Trentham & Hopkins, 2008). Galaxy masses play a fundamental role in our understanding of structure formation and galaxy evolution, and the following sections will review how masses are determined, with a special emphasis on the role of model spectral energy distributions (SEDs).

1.2 Stellar Population Synthesis Modeling

For some galaxies, it is possible to determine the dynamical masses through either rotation curve or velocity dispersion measurements, sometimes with satellite galaxies. However, performing these measurements for large scale surveys or at high redshift is simply too costly/technically infeasible. The vast majority of galaxy mass measurements depend on modeling the mass-to-light (M_*/L) ratio of the stars in the galaxies. It is important to note that this is the stellar mass-to-light ratio, as denoted by the subscript asterisk. It includes light and mass only from stars still converting mass to energy through nuclear fusion. Notably, it does not include the mass contribution from dark matter, stellar remnants, or gas and dust in the interstellar medium (ISM). Throughout this work, care has been taken to clarify when referring to stellar mass, and when referring to the mass of a galaxy as a whole. Nevertheless, as discussed above, the stellar mass provides a wealth of information

and accurately modelling the M_*/L is of the utmost importance.

To model the stellar M_*/L ratio of a galaxy appears deceptively simple. We have detailed knowledge of stellar evolution (e.g. Paxton et al., 2011) and can accurately model how a star's spectrum changes with time given an initial zero-age main sequence mass (although, there are a few caveats–see below). Naively then, one might think it trivial to then add up several different stars' spectra to yield a composite spectral energy distribution (SED) for a galaxy. One would then know all the light produced by the stars in the galaxy, the total mass contained in those stars, and thus the stellar M_*/L ratio of the galaxy at any given wavelength. While this is the basic approach of stellar population synthesis (SPS) modelling (see Conroy (2013) and Section 2 of Courteau et al. (2014) for reviews), there are several difficulties that arise in practice.

Firstly, there are certain phases of stellar evolution that are not currently well modeled. Several authors have commented on differing treatments of the thermally pulsating asymptotic giant branch (TP-AGB) stars (Maraston et al., 2006; Conroy, Gunn & White, 2009; Kriek et al., 2010; Zibetti et al., 2013, among others) and how it can affect the M_*/L ratio by a factor of approximately two at near-infrared (NIR) wavelengths. The presence of blue stragglers in globular clusters (stars that remain on the main sequence after their predicted turn off age) is not well understood and must be accounted for empirically (Conroy, Gunn & White, 2009). Stellar rotation is often completely ignored, even though it can have drastic effects on stellar mass loss and bolometric luminosity (Maeder & Meynet, 2012; Lovekin, 2012). As well, an increasing number of stars in our galaxy are found to be in binary systems, but the effects of binarity on stellar evolution (e.g. rejuvenation through mass transfer) are not included in most current SPS models (although Eldridge & Stanway, 2009, is an exception). All stars are assumed to evolve in isolation.

Our general lack of knowledge of exactly what distribution of stars comprise a galaxy imposes several assumptions when creating a model galaxy spectra. Unlike a globular cluster, where all stars are a coeval simple stellar population (SSP) of the same composition, galaxies are composed of several different SSPs. These (possibly differing) SSPs must be

added together to form a composite stellar population (CSP) (see stellar population synthesis codes such as Bruzual & Charlot, 2003; Maraston, 2005; Conroy, Gunn & White, 2009). Each SSP can, in principle, have its own chemical composition, usually parameterized as the metallicity Z. A truly accurate representation of chemical enrichment in a galaxy would indeed have almost zero metallicity in the first stars, and higher and higher chemical abundances as future SSPs are formed. However, a single (usually solar) metallicity is typically assumed for all SSPs (Conroy, 2013). Metal rich stars are cooler and fainter because of increased opacity expanding the outer envelope, and increase absorption features leading to redder colors in the spectra. The M_*/L ratio is less affected at NIR wavelengths by metallicity (Lee et al., 2007).

When creating an SSP of a particular metallicity, an initial mass function (IMF) must be assumed. The IMF describes the distribution of masses of the stars born in a burst of star formation. The form of the IMF is typically a broken power law distribution, with the slopes of the high-mass and low-mass ends given by either Salpeter (1955), Kroupa (2001), or Chabrier (2003). Because it determines the relative weights of bright, massive stars to fainter stars, the choice of IMF has a direct systematic effect of the M_*/L ratio, albeit one that can easily be converted from one IMF to another. For example, a Chabrier IMF leads to mass estimates that are about double those made with a Salpeter IMF. There is a great deal of uncertainty in the IMF, particularly at the massive end where stars are short-lived. IMF observations also predominantly come from the local group, and we have very little evidence of how, if at all, the IMF changes as a function of time. Models of extremely metal-poor Population III stars have predicted that the IMF would be very different for the first generations of stars (Stacy, Bromm & Lee, 2016; Bromm, Coppi & Larson, 2002). Lack of observational constraints though, lead to the assumption that each SSP is created with the same IMF.

How SSPs are added together as a function of time is known as the star-formation history (SFH). An analytic form is normally assumed, with an exponentially declining τ-model ($SFR \propto \exp -t/\tau$) being the most common. Other forms such as an inverted-τ

(exponentially increasing; Maraston et al., 2010) or delayed τ (linearly increasing before exponential decay; Lee et al., 2010) have also been proposed. Further complexities such as adding sporadic bursts of star-formation (with each burst population having it's own composition and SFH) on top of an underlying population have also been advocated (Pérez-González et al., 2008; Noll et al., 2009). Similarly to the IMF, a galaxy's SFH also controls the ratio of bright, young stars to older, fainter stars, and hence the M_*/L ratio. However, it is much more difficult, if not impossible, to directly convert mass estimates from one assumed SFH to another. Because the flux of younger stellar populations dominates so thoroughly at optical wavelengths, any two model CSPs with roughly similar young stellar components will have very similar observed spectra, even if their M_*/L ratios differ greatly. This phenomenon is referred to as outshining (Maraston et al., 2010; Pforr, Maraston & Tonini, 2012), or sometimes frosting (Courteau et al., 2014). Outshining can be regarded as the loss of constraints on the SFH (and thus M_*/L ratio) because details are hidden behind bright, young stars.

The presence of dust in a galaxy further changes the M_*/L ratio by absorbing energy at bluer wavelengths and re-emitting it in the infrared portion of the spectrum. In general, dust extinction is a result of the size and shape distribution of the dust grains (Witt & Gordon, 2000). A galaxy's SED is strongly affected by the geometric distribution of the dust with respect to the stars. The complex dependence of the dust attenuation on geometry and grain size is usually simplified by fixing the shape of the attenuation curve and parameterizing its normalization (Conroy, 2013). Common dust attenuation laws include Calzetti et al. (2000), MW, LMC, SMC, and the stellar age dependent Charlot & Fall (2000) model.

1.3 SED Fitting

The most commonly used method of applying model SPS M_*/L ratios to real galaxies is by comparing their broadband flux in several different bandpasses. There exist relations between certain rest-frame colors (e.g. $B-R$, $g-i$, $I-K$) and stellar mass, although

there are systematic differences of 0.1-0.2 dex for color M_*/L ratios and up to 0.4 dex for NIR colors where the treatment of TP-AGB stars is most impactful (Conroy, 2013, and references therein). Color M_*/L ratios are often used to derive stellar masses without devoting too much time or effort, but with the caveat that they are highly dependent on systematics of the models used to derive the relations (Bell et al., 2003; Zibetti, Charlot & Rix, 2009). Additionally, these relations are typically given only for a certain metallicity, and suffer at optical wavelengths from the age-metallicity degeneracy. That is, an older stellar population leads to redder optical colors, and so does a metal-rich population, so it is difficult to disentangle the two effects. Since metallicity has less of an effect at NIR wavelengths, a good approach to measuring color M_*/L ratios is to fit the SED simultaneously in at least three band passes, with at least one in the NIR (Courteau et al., 2014, and references therein).

Indeed, when observations of multiple bandpasses are available it is possible to use information from all of them simultaneously to determine the best fitting SED model. This approach began with Sawicki & Yee (1997) and continues into the modern era. One can use a χ^2 statistic to determine the best fitting model (e.g. Sawicki, 2012a; Brammer, van Dokkum & Coppi, 2008), although Bayesian approaches (Benitez, 2000), and neural network approaches (Collister & Lahav, 2004) have also been attempted. Throughout this work, we compare observed fluxes (f_{obs}) with model fluxes (f_{mod}) using the χ^2 statistic given by

$$\chi^2 = \sum_i \frac{(f_{obs,i} - s f_{mod,i})^2}{\sigma_i^2} \tag{1.1}$$

where σ is the uncertainty in the observed flux and the sum is over each of the i bandpasses. The factor s represents the scaling between the observed and model fluxes, and can be determined analytically by minimizing the χ^2 statistic with respect to s yielding

$$s = \frac{\sum_i f_{obs,i} f_{mod,i} \sigma_i^{-2}}{\sum_i f_{mod,i}^2 \sigma_i^{-2}}. \tag{1.2}$$

Multiplying the mass of the best fitting model template by the scale factor determines the mass of the observed galaxy. The model spectrum that minimizes the χ^2 statistic is the one that best fits the observations.

In order to determine error bars, several Monte Carlo instances are created, where the observed photometry is perturbed by randomly drawing a new observed flux for each bandpass from a normal distribution with mean $f_{obs,i}$ and standard deviation σ_i. The mass estimate least likely to be biased by catastrophic failures in the fitting procedure due to model degeneracies is the median mass of the Monte Carlo instances (Taylor et al., 2011), and the 1-σ upper and lower bounds the 84th and 16th percentiles respectively. The stellar mass estimate is the most robust measurement derived from SPS fitting. The uncertainties on stellar mass estimates can still be large, however, up to a factor of 0.3 dex when all uncertainties in model assumptions are taken into account (Conroy, Gunn & White, 2009).

Systematic biases can arise from one's choice of model parameter space, which constitutes a prior assumption of M_*/L ratios. For example, Gallazzi & Bell (2009) found that including a large fraction of bursty models could underestimate the M_*/L ratio of older smooth-SFH galaxies. Additionally, they found that the fraction of bursty versus smooth SFH models can bias fits of noisy observations, which, all other things being equal, would have an equal chance of being fit to either the bursty or smooth models.

One other aspect that must be taken into account is that in most cases the redshift of a galaxy is not known *a priori*. Due to the presence of spectral breaks, it is possible to include the redshift as a parameter in the SED models, and indeed finding the photometric redshift was one of the first implementations of broadband SPS fitting (Sawicki & Yee, 1997). Photometric redshifts are less precise than spectroscopic redshifts, but have been shown to be reasonably accurate, with a $|z_{spec} - z_{phot}|/(1+z)$ typically much less than 0.1 (Rafelski et al., 2015; Ilbert et al., 2009; Brammer, van Dokkum & Coppi, 2008). Although less accurate and prone to catastrophic errors, photometric redshifts can be performed efficiently for a large number of galaxies and can probe fainter galaxies than spectroscopic redshifts. The fitted redshift also affects the M_*/L ratio of the model spectra, since the

expansion of the universe introduces an additional scale factor of $1 + z$.

1.4 Weak Lensing

SPS modeling traces the mass contained in visible matter, but the majority of mass remains hidden in the invisible dark matter halo. While there is a correlation between stellar mass and halo mass, in many ways it would be beneficial to have a more direct probe of the full matter distribution of the universe. Cosmological simulations of galaxy formation primarily follow the collapse of dark matter, and assume the baryonic matter traces the dark matter. However, it is non-trivial to compare the simulated dark matter distribution to the observable stellar mass distribution. It would be much simpler to test the numerical simulations if we could examine the dark matter distribution directly.

Weak lensing is one manner in which we can probe the entire matter distribution of the universe. The dark matter halos around galaxies curve the path of incoming photons, acting as a lens to distort and magnify the image of background galaxies. Unlike strong lensing, where giant arcs or multiple images of the same galaxy can be observed, the effects of weak lensing are much more subtle, and only through a statistical analysis of the shapes of an ensemble of galaxies can the signal be measured (Munshi et al., 2008, and references therein). To observe this cosmic shear requires immense surveys that are both wide in coverage and relatively deep (Refregier, 2003). The advent of several new instruments in the coming decade, including the Large Synoptic Survey Telescope (LSST), WFIRST, and Euclid, will usher in a new era of weak lensing measurements.

Perhaps surprisingly, weak lensing surveys also rely heavily on model SED fitting to derive the mass distribution of the universe. While the M_*/L ratio of the model spectra is of no concern, weak lensing relies on knowing the redshift distribution of galaxies to form a three dimensional map, and the quality of the redshifts directly affects the quality of the weak lensing analysis (Huterer et al., 2006; Sun et al., 2009; Bernstein & Huterer, 2010). The vast amount of area that must be covered (20,000 deg^2 for LSST), negates the use of

traditional spectroscopic redshifts, and hence a dependence on model spectral templates.

1.4.1 This work

In this work, we used model SEDs in various ways to help study the masses of galaxies in the universe. In Chapter 1, we fit model SEDs to each pixel in nearby galaxies from the Sloan Digital Sky Survey (SDSS), using the two-dimensional spatial information to uncover and understand any differences in mass measurement between the resolved and integrated photometry. There was a bias due to outshining, which depended upon the galaxy's sSFR. In Chapter 2, we extended this analysis to galaxies at higher redshifts in the the Hubble Extreme Deep Field (XDF). We again observed a bias in mass measurements due to outshining, which, when corrected for, could account for the difference between the directly observed star-formation rate density (SFRD) and that inferred from the stellar mass density (SMD). In Chapter 3, we used the pixel-by-pixel SED fits of the XDF to create mock wide field slitless spectroscopy (WFSS) observations, in order to test analysis software for WFSS instruments aboard future space telescopes such as JWST and WFIRST. Although WFSS is not typically used to directly measure galaxy masses, the resolved line emission maps it yields tell us a great deal of information regarding how and where the stellar mass formed. In Chapter 4, we used model SEDs to examine what wavelength coverage provides the best constraints on photometric redshifts (and hence the mass distribution of the universe) for weak lensing surveys. This was done in the context of Euclid, which has subsequently been finalized and approved, but the results apply just as well to any future weak lensing mission. Throughout this work, we use the AB magnitude system (Oke, 1974) and assume a WMAP7 cosmology (Komatsu et al., 2011) unless otherwise specified.

Chapter 2

Missing Stellar Mass in SED Fitting: Spatially Unresolved Photometry can Underestimate Galaxy Masses

---

This chapter was originally published in 2015 in the Monthly Notices of the Royal Astronomical Society, Volume 452, pp 235-245.

DOI: 10.1093/mnras/stv1235

We fit model spectral energy distributions to each pixel in 67 nearby ($<z>= 0.0057$) galaxies using broadband photometry from the Sloan Digital Sky Survey and GALEX. For each galaxy, we compare the stellar mass derived by summing the mass of each pixel to that found from fitting the entire galaxy treated as an unresolved point source. We find that, while the pixel-by-pixel and unresolved masses of galaxies with low specific star formation rates (such as ellipticals and lenticulars) are in rough agreement, the unresolved

mass estimate for star-forming galaxies is systematically lower then the measurement from spatially-resolved photometry. The discrepancy is strongly correlated with sSFR, with the highest sSFRs in our sample having masses underestimated by 25% (0.12 dex) when treated as point sources. We found a simple relation to statistically correct mass estimates derived from unresolved broad-band SED fitting to the resolved mass estimates: $m_{resolved} = m_{unresolved}/(-0.057 \log(sSFR) + 0.34)$ where sSFR is in units of yr^{-1}. We study the effect of varying spatial resolution by degrading the image resolution of the largest images and find a sharp decrease in the pixel-by-pixel mass estimate at a physical scale of approximately 3 kpc, which is comparable to spiral arm widths. The effects we observe are consistent with the "outshining" idea which posits that the youngest stellar populations mask more massive, older – and thus fainter – stellar populations. Although the presence of strong dust lanes can also lead to a drastic difference between resolved and unresolved mass estimates (up to 45% or 0.3 dex) for any individual galaxy, we found that resolving dust does not affect mass estimates on average. The strong correlation between mass discrepancy and sSFR is thus most likely due to the outshining systematic bias.

2.1 Introduction

Exactly how a galaxy's stellar content evolves over time is unknown to us. In general, the build-up of stars—thought to be a steady stream of star-formation complemented by stochastic bursts triggered by interactions with neighboring galaxies—is halted at certain times by various quenching mechanisms, such as tidal stripping or feedback from e.g. active galactic nuclei. While the overall picture is clear, the precise star-formation history (SFH) of any individual galaxy is hidden from us. Over the past decade it has become apparent that a galaxy's evolution is in large part described by its stellar mass. Several tight correlations have been found linking the stellar mass of a galaxy to a wide range of properties. A galaxy's brightness and size (Trujillo et al., 2006; Williams et al., 2010), rotational velocity or velocity dispersion (Faber & Jackson, 1976; Tully & Fisher, 1977), star formation rate

(SFR; Reddy et al., 2006) if on the "main sequence" (Daddi et al., 2007; Sawicki, 2012b), metallicity (Savaglio et al., 2005; Mannucci et al., 2010), and mean stellar age (Gallazzi et al., 2005), are all well correlated with the mass of a galaxy's stellar content.

Because a galaxy's stellar mass plays such a vital role in our understanding of galaxy evolution, it behooves us to understand the estimating methods available as well as their limitations. Stellar population synthesis (SPS) modeling (Bruzual A. & Charlot, 1993; Bruzual & Charlot, 2003; Maraston, 2005; Conroy, Gunn & White, 2009; Conroy, 2013, for a review) is a tool used nearly universally to estimate stellar masses in large surveys and at high redshift (e.g. Sawicki & Yee, 1998; Kauffmann et al., 2003; PérezGonzález et al., 2008; Marchesini et al., 2009; Ilbert et al., 2010; Sorba & Sawicki, 2010; Maraston et al., 2013). At its most basic, an SPS model can be created by combining all the light from stellar models in a simple stellar population (SSP)—defined as a group of stars all born at the same time, with the same metallicity, and with a mass distribution described by a chosen initial mass function (IMF)—and tracking how the combined light changes as the stars evolve with time. Composite stellar population (CSP) models can then be created by adding different SSPs together as a function of time determined by some fiducial SFH. The stellar mass is determined by fitting a SPS model grid to observed broad-band photometry and scaling the stellar mass of the best-fitting model.

The uncertainties in the stellar mass estimate derived from broad-band SPS fitting can be large, up to a factor of 0.3 in dex when all uncertainties in model assumptions are taken into account (Conroy, Gunn & White, 2009). This large variance does not, of course, account for any assumptions that we are not aware of. For example, Maraston et al. (2006) found that differing treatment of the thermally pulsating asymptotic giant branch (TP-AGB) stage of stellar evolution systematically decreased the predicted stellar mass of galaxies by a factor of two. Note, however, that there is still some controversy over how to correctly treat these stars (Kriek et al., 2010). Another model assumption that systematically affects the derived stellar mass estimates is one's choice of IMF, since the IMF directly affects the mass-to-light (M_*/L) ratio of the models. A third systematic bias was first noted by Sawicki

& Yee (1998) and then emphasized by Papovich, Dickinson & Ferguson (2001) who stated that star-forming galaxies had the potential to hide underlying older stellar populations by outshining them. The fitting procedures preferentially favor matching the large amount of flux coming from the younger stellar population, and could potentially under-estimate the M_*/L ratio by missing the relatively low amount of flux emanating from the older stars (where a majority of the stellar mass could rest). Unlike the two previously mentioned biases, the outshining bias is inherent to the broad-band SPS fitting procedure, rather than emerging explicitly from one's choice of models. It is thus perhaps particularly insidious because it cannot be easily corrected for from one study to another. Moreover, because the bias would affect star-forming galaxies more strongly than quiescent galaxies, its differential nature could act to either produce spurious relations or mask true ones.

The outshining bias essentially arises from our lack of knowledge of the SFH of any particular galaxy, and the SFH's influence on the M_*/L ratio. If it were possible to know the precise SFH to use when creating a model SED, then we would know the exact ratio of old to young stars and, hence, would not miss any of their mass when fitting preferentially to the flux emanating from the younger stellar population. However, since the SFH is unknown, its form must be assumed and often parameterized in the model grid to account for many possible differing histories. Maraston et al. (2010) and Pforr, Maraston & Tonini (2012) used mock galaxies to test the effects of mismatched SFHs on derived parameters, and found that the stellar masses of star-forming galaxies are typically underestimated, in part due to outshining, by 0.3 dex for $z \sim 2$ galaxies and up to 0.6 dex for lower redshift galaxies. They found that the mass measurement could be better reproduced by using an inverted-τ SFH (i.e. exponentially increasing), which is presumably closer to the true SFH of their galaxies. However, even if the true SFH is present in the model SED grid, unless it is the only SFH present, an outshining bias can still occur. Because the flux of younger stellar populations dominates so thoroughly at optical wavelengths, any two models with roughly similar young stellar components would have roughly an equal chance of being selected as the best-fit model, even if one model had the true SFH and the other a vastly different one.

Outshining can thus be regarded as the loss of constraints on the SFH (and thus M_*/L ratio) because the details are hidden behind bright, young stars. Gallazzi & Bell (2009) explicitly examined the uncertainties in M_*/L in the case where the true SFH is present in the model library, with the assumption that the redshift is known and neglecting dust corrections. They were able to quantify biases from mismatched SFHs and in the prior distribution of SFHs compared to the true distribution, which they found could be as high as 0.1 dex.

The extent of any bias from outshining in our observations of low redshift galaxies has been hinted at, but not rigorously determined. Drory, Bender & Hopp (2004) compared masses derived from spectra to photometric masses and found that for objects with strong $H\alpha$ equivalent widths (i.e. star-forming), the photometric mass was systematically lower than the spectroscopic mass by up to 0.15 dex. Zibetti, Charlot & Rix (2009) fit SPS models to individual pixels in nine SINGS galaxies, and compared the resolved and unresolved mass estimates. They also found that the unresolved mass estimate (i.e. fitting all the light from the galaxy at once as if it were a point source) could be underestimated compared to the resolved mass by up to 40% (0.15 dex). However, they attribute this effect to unresolved dust lanes, rather than star-forming regions. Taylor et al. (2010), on the other hand, compared stellar masses with dynamical masses and placed an upper limit on any differential bias in stellar mass estimates at less than 0.12 dex. It is clear that a systematic bias is present, although the large scatter in any individual mass measurement make it difficult to put an exact value on the offset due to outshining. In order to have the best understanding of stellar mass estimates, it is crucial to better constrain this bias. The large statistical variance is stellar mass estimates necessitate the use of a large number of objects to penetrate through the noise.

With this in mind, we follow the approach of Zibetti, Charlot & Rix (2009) and compare spatially resolved versus unresolved mass estimates, as this method only requires broad-band photometry which is readily available from a myriad of different surveys. We set out to constrain the average systematic offset from fitting broad band photometry of star-

forming galaxies to SPS models. We stress that in this work we are in no way trying to determine the actual amount of stellar material in galaxies, but are instead focused on a comparative study between the pixel-by-pixel and unresolved broad-band SED fitting mass estimates. We are solely interested in the effects of outshining as an inherent procedural bias. In Section 2.2 we describe our data and pixel-by-pixel (PXP) SPS fitting procedure, and in Section 2.3 we discuss the resulting comparisons between resolved and unresolved stellar mass estimates. Throughout this work we assume a WMAP7 (Komatsu et al., 2011) flat ΛCDM cosmology ($H_0 = 70.4$ km s^{-1} Mpc^{-1}, $\Omega_M = 0.272$) and use the AB magnitude system.

2.2 Method

2.2.1 Data

We used publicly available u, g, r, i, z data from the Sloan Digital Sky Survey (SDSS) Data Release 10 (Eisenstein et al., 2011) supplemented with publicly available NUV data from the GALEX Ultraviolet Atlas (GUA; Gil de Paz et al., 2007), which also provides measurements of the spectroscopic redshift, major and minor diameter, and morphological classification for each galaxy. Although FUV data were also available from GALEX, we found that their signal-to-noise (S/N) ratio was typically too low to get accurate photometry in a single pixel. These six bandpasses should provide more than adequate wavelength coverage to derive stellar masses from SPS fitting, which could be done using only the five SDSS filters[1] (e.g. Maraston et al., 2013). The NUV bandpass adds a second measurement below the 4000Å break and provides additional information about the young stellar population and extinction. It acts to break some of the degeneracies inherent in the models (see Figure

[1]We compared stellar mass estimates derived using only the five SDSS filters with those made with the additional NUV bandpass. We found that the inclusion of the NUV had a slight effect on mass estimates, increasing them by approximately 7% on average, although with large scatter. However, this average difference was present in both the resolved and unresolved mass estimates, and so does not qualitatively affect our conclusions. We postulate that the observed mass difference arises from the NUV limiting the amount of unrealistic extinction available to the fit. That is to say, we found the pixels (and galaxies) were nearly universally fit with higher extinction models when the NUV data was not included. The greater amount of extinction for the same amount of flux led to greater mass estimates when the NUV data was not included.

2.1).

Starting with the approximately 1000 objects in the GUA which contains all galaxies larger than one arcminute in diameter observed with GALEX, we cross-correlated with the SDSS frames using the bulk image search functionality of the Sloan website. We then visually inspected each matching frame and removed any galaxies that lay too close to the border of the SDSS frame. This step ensures that any edge effects, whether from the raw photometry or due to convolution (see below), will not affect a pixel's final colors. Additionally, we removed any galaxies that spanned the entire SDSS frame since there would be no way to get an accurate background measurement for that frame. The remaining galaxies were processed following the procedure in Section 2.2.2 and color images were made from the resulting aligned and psf-matched images. The color images were again visually inspected and any galaxies with obvious artifacts (e.g. excessive bleeding from foreground stars) were discarded. In total these criteria left us with 67 galaxies including eight elliptical, one lenticular, and four irregular galaxies, with the remainder being some form of spiral galaxy.

2.2.2 Processing

For each galaxy, we downloaded the appropriate SDSS frame, mask, and point spread function (PSF) which was read at the center of the galaxy using the read_PSF software package provided on the SDSS website.[2] The GALEX raw count, high resolution relative response, and flag images were downloaded. We use the GALEX PSF available on the Galex website.[3] We created a square cut-out of the GALEX images centered on the galaxy with sides equal to 1.5 times the galaxy's major diameter. Although background subtracted intensity images are provided, we found through visual inspection of the sky background images that the provided background maps tended to overestimate the background of extended galaxies, likely due to diffuse radiation from the galaxy (see also Zou et al., 2011). We thus derived

[2]https://www.sdss3.org/dr10/algorithms/read_psf.php
[3]http://www.galex.caltech.edu/researcher/techdoc-ch5.html

our own background estimates in the raw count cut-out by first masking the galaxy and then performing a sigma-clipping function in 50 pixel by 50 pixel square regions and fitting a plane to the background estimates in each region. Since counts from NUV photons are few, the estimated background value in each step of the sigma-clipping algorithm was set to be equal to the variance (rather than the mean) of the values in each square region. This was done to account for the lack of symmetry in the Poisson distribution when number counts are low; using the mean would overestimate the background value slightly. A background subtracted intensity map with units of counts per second per pixel was created using the formula

$$I = (C - B)/R, \tag{2.1}$$

where C represents the raw count map, B the background map, and R the relative response. We then created a root-mean-square (rms) noise map for the intensity image by

$$\sigma_I = \sqrt{\sigma_C^2 + \sigma_B^2}/R, \tag{2.2}$$

where σ_C is the square root of the count image (i.e. Poissonian uncertainty) and σ_B is the standard deviation of the background determined using our sigma-clipping method above.

The SDSS images are already background subtracted as part of the SDSS pipeline, but this process over-estimates the background of extended objects (Blanton et al., 2005; Bernardi et al., 2007). We therefore reinstated the background subtracted by the SDSS pipeline and performed our own background estimation, similar to what is described above, but using the mean in each square region as the best background estimate as allowed by the much larger count numbers. Each SDSS frame had to be converted to data numbers using the provided calibration layer of the fits file. The rms images were then made for the SDSS images using the formula

$$\sigma_I = \sqrt{x\sigma_C^2 + x\sigma_B^2} \tag{2.3}$$

where I is now in units of nanomaggies, B is again the background map, x is the calibration layer value, and σ_C, the uncertainty in the data number image, is now given by

$$\sigma_C = \sqrt{C/g + \sigma_{dark}^2} \tag{2.4}$$

where C/g is the data number divided by the gain to yield the Poissonian variance of the counts, and σ_{dark} is the Poissonian noise from the dark current.

Having created background subtracted images with corresponding noise maps in each of the desired bandpasses, we next aligned the SDSS images with the GALEX cut-out and resampled the SDSS pixel scale to the GALEX pixel scale (1.5 arcsec per pixel) using the SWARP software package (Bertin et al., 2002). Although losing spatial resolution seems contrary to our purpose, the reasons for degrading the SDSS pixel scale are threefold: 1) Artificially chopping up a NUV pixel into smaller pixels may not result in realistic spatial distribution of the NUV photons (even if interpolation is used), which would lead to erroneous colors in each individual pixel. 2) Combining the SDSS pixels together leads to a higher S/N ratio which is crucial when striving for accurate photometry on a pixel-by-pixel basis. 3) Having fewer pixels speeds up computation time of all future steps immensely.

We also performed a re-alignment and resampling of the SDSS PSF by placing the PSF at the same location in the frame as the center of the galaxy and using the same parameters for SWARP. It is important to have an estimate of the PSF prior to resampling, otherwise one is likely to have an undersampled PSF and encounter problems when trying to estimate it from the resampled image.

The GALEX PSF was the broadest, so to ensure that each pixel contains light from the same physical location it was necessary to find a convolution kernel that would translate each image from its current PSF to the broadest PSF. We found the transformation kernel by taking the ratio of the two PSFs in Fourier space and then inverse-transforming the result. We masked any saturated pixels and foreground stars (found using the 2MASS catalog; Skrutskie et al., 2006) and then convolved each SDSS image with the appropriate

transformation kernel using scipy's ndimage convolve routine with pixel values set to have zero value outside the image. The uncertainty was propagated by convolving the variance map with the square of the transformation kernel to yield the variance map of the convolved SDSS image.

With the resulting set of background subtracted, aligned, resampled, PSF-matched images we then made photometry catalogs of each pixel with a S/N of at least 5 in every SDSS filter. To make a fair comparison between pixel-by-pixel SED-fitting result and those using spatially unresolved fluxes, we calculated the unresolved magnitudes not from aperture photometry, but by summing the flux from each pixel included in the pixel-by-pixel catalog and then converting to AB magnitude. Doing this is key as it ensures that the same amount of light is being compared in each case.

2.2.3 Models

We fit the broadband photometry from the six SDSS and GALEX bandpasses to model spectral energy distributions (SEDs) created using the FSPS population synthesis code (Conroy, Gunn & White, 2009; Conroy & Gunn, 2010). Our model set is comprised of two component burst models similar to those used in Noll et al. (2009) where there is an underlying older stellar population combined with a more recent burst of star formation. In principle, each of the two components (young and old) can have its own SFH, age (i.e. the time since the burst was initiated), IMF, and metallicity history, as well as various parameters controlling how dust absorbs and re-emits light. Here, we describe our chosen model parameters, which we found to adequately represent our photometric observations (listed in Table 2.1).

We parameterized the SFH of the older stellar component as a delayed (sometimes referred to as extended) exponential decay (i.e. of the form $\psi(t) \sim te^{-t/\tau}$ so that SF at first increases linearly with time) with e-folding time τ_{old} spaced roughly logarithmically between 0.1 and 10. The delayed-τ models (Lee et al., 2010) are a good compromise between the commonly used τ models and the inverted-τ models of Maraston et al. (2010), particularly

Table 2.1: Parameters used in two-component model SEDs

Symbol	Value(s)
Z_{old}	0.0016 ($\sim$0.084 $Z_\odot$)
Z_{young}	0.019 ($Z_\odot$)
τ_{old}	[0.1, 0.25, 0.625, 1.25, 2.5, 5, 10]
τ_{young}	0.1
t_{old}	10
t_{young}	[6, 6.5, 7, 7.5, 7.75, 8, 8.25, 8.5, 8.75, 9, 9.25, 9.5]
f_{young}	[0, 10^{-4}, 10^{-3}, 0.01, 0.1, 0.25, 0.5, 0.75, 0.9, 0.99]
$E(B-V)$	[0, 0.05, 0.1, 0.15, 0.2, 0.25, 0.3, 0.35, 0.4, 0.5]

The ages are in units of log years.

for low redshift galaxies which have seen a decline in SFR density since $z \sim 2$ (Madau et al., 1996; Sawicki & Yee, 1997). Simha et al. (2014) found that delayed-τ models were much more successful at reproducing the SFH of simulated galaxies than plain τ models. The SFH of the younger burst is a standard exponential decay with τ_{young} held constant at 0.1. Each of the young and old components also has an age (t). For the older component, this was held constant with star formation starting 10 billion years ago, while the younger burst had onset ages ranging from 10^9 to 10^6 years ago. We combined the older and younger components so that the mass fraction of the younger component has a value f_{young} which we allowed to vary between zero and one. The two component models used here provide a wide variety of SFHs and are similar in construction to those of Noll et al. (2009) which were found to adequately represent galaxies in the SINGS survey similar to those being studied here.

We used a Chabrier (2003) IMF for all models and set the metallicity of the younger component equal to solar metallicity and that of the older component equal to 0.0016 (i.e. $\sim$8% $Z_\odot$). The choice of significantly sub-solar metallicity for the older stellar component was motivated by the simplistic assumption that the overall metallicity of the universe should be lower at earlier times, as well as the results of Zou et al. (2011), which showed evidence for a double peaked metallicity distribution in NGC 628 with the metal poor component peaking at [Fe/H] = -1.15 . Additionally we found that the inclusion of a sub-solar metallicity component yielded a model space that better matched the observed

pixel-by-pixel colors (see Figure 2.1). Particularly, the $g - z$ color was too red if solar metallicity was used in both stellar components.

For extinction due to dust, we assumed a Calzetti et al. (2000) dust law with $E(B-V)$ values ranging between 0 and 0.5. To save computation time and limit the parameter space we arbitrarily enforced models comprised mainly of older stars to only have $E(B-V)$ values less than 0.3.

In total our parameter space is defined by four free parameters: $\tau_{old}, t_{young}, f_{young}$, and $E(B-V)$. In Figure 2.1 we show a comparison between our models at $z = 0.0057$ (the average redshift of our galaxy set) and the pixel-by-pixel photometry for the brightest i-band quartile of pixels histogrammed from all galaxies. Although there is a larger spread in the observations than the models due to photometric noise and differing redshifts, our models appear to generally lie on the locus of the observations and adequately span the color-space. It is important to note, however, that since we are doing a comparative study of resolved versus unresolved fitting, it is not imperative that our choice of models actually represent reality to the fullest extent as long as the same set of models is used throughout the study.

In order to determine the best-fitting model to a given galaxy's pixel's broadband photometry we redshifted the model spectrum to the spectroscopic redshift of the galaxy and corrected for dust in the Milky Way (Schlegel, Finkbeiner & Davis, 1998; Schlafly & Finkbeiner, 2011). The spectrum was then convolved with the broadband filter transmission curves to give model magnitudes in each of the six bandpasses of interest. We used the SEDfit software package (Sawicki, 2012a) to generate the model magnitudes and then to find the best-fitting model employing a χ^2 minimization routine. In order to determine uncertainties, SEDfit performs a number of iterations for each pixel with the photometry randomly perturbed by selecting a random variable from a Gaussian distribution with standard deviation equal to the uncertainty in the photometry. We performed 300 iterations and used the median mass of these iterations as our final mass estimate. This avoids biases in the χ^2 best-fit estimate (see, for example, Taylor et al. (2011)).

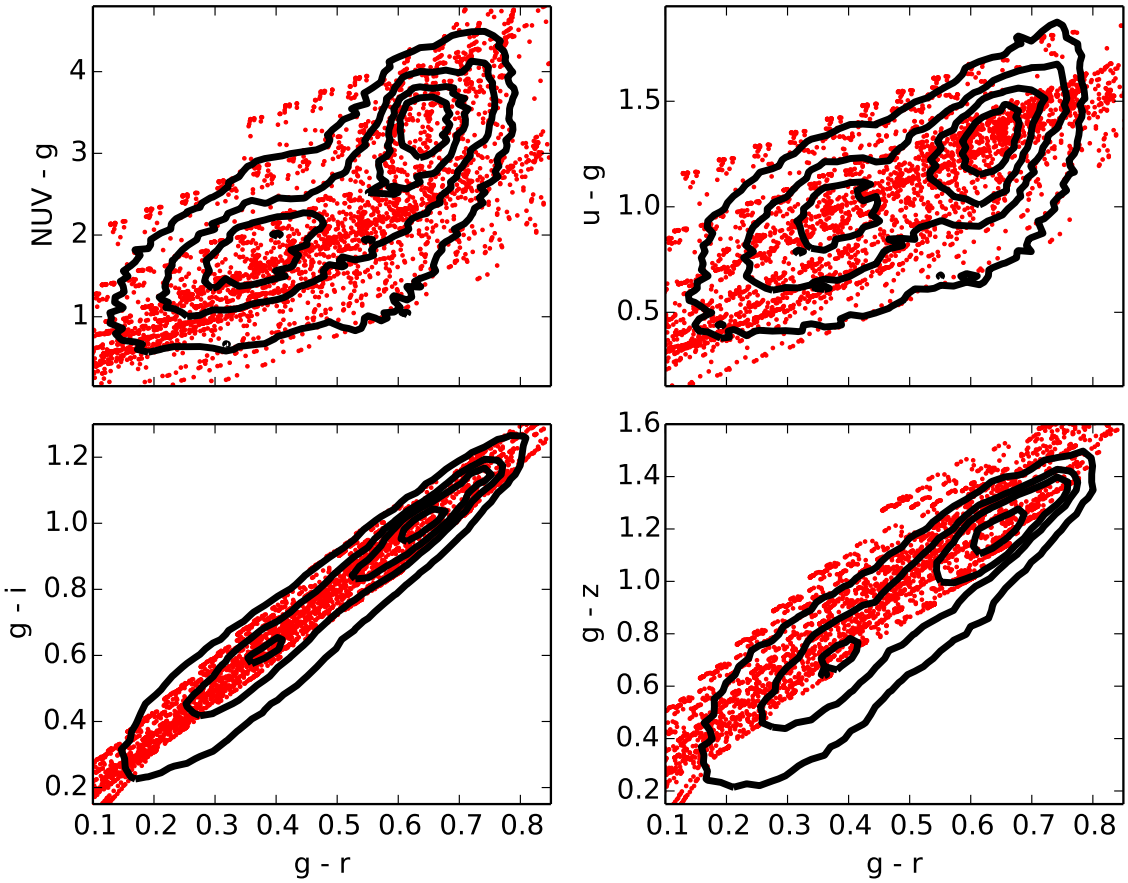

Figure 2.1: Color-color diagrams showing how our model colors compare with the observed photometry. The black lines represent the 10, 33, 66, and 90% contour levels of the histogram of the brightest (i-band) quartile of pixels for all galaxies. The total number of pixels binned is 187445. The red points are where our models lie in color-color space for a galaxy at $z = 0.0057$ which is the average redshift of our galaxy sample. The models generally show good agreement with the observations, tending to lie on the locus in each sub-plot.

2.3 Results

In Figure 2.2 we show false color images and best-fit model property maps for a subset of our galaxies (the full set is available as an online supplement). The false color images are made using u, g, and i-band images as the blue, green, and red colors respectively. The property maps show the strength of the D4000 break as a proxy for stellar age (since two component models don't have a well defined age; see e.g. Noll et al., 2009), the stellar mass, the star formation rate (SFR), and the extinction spatial distributions in each galaxy. As expected, regions in the spiral arms that are very bright in u-band (i.e. flux generated from younger stars) are fit to models with weaker D4000 breaks and SFRs that are higher than the surrounding population. The mass distribution, however, is relatively smooth, emphasizing that the mass-to-light ratio in each pixel is a function of the stellar population, and that older stars comprise the bulk of a galaxy's total stellar mass while not contributing as significantly to the galaxy's total brightness.

2.3.1 Unresolved fitting can underestimate stellar mass

In order to determine how well unresolved broadband SED fitting can recover the true stellar mass content of a galaxy, we calculated the ratio of the unresolved stellar mass divided by the "true" stellar mass (here assumed to be the sum of the stellar mass of the best-fitting model in each pixel). We plot this ratio as a function of unresolved specific star formation rate (sSFR, SFR per unit stellar mass) in Figure 2.3. We calculated the average unresolved-resolved mass ratio for different morphologies in each of the 300 Monte Carlo iterations and show the median and 1-σ spread as horizontal lines in blue for spiral galaxies and red for elliptical and lenticular galaxies. Doing so reveals that the stellar mass estimates of elliptical/lenticular galaxies (red squares) tend to have stellar mass estimates that are roughly the same whether resolved or unresolved. On the other hand, spiral galaxies (blue circles) are typically under-estimated by 13% (0.06 dex) on average when structure is unresolved. Moreover, there is a clear decline in the unresolved-resolved mass ratio for the

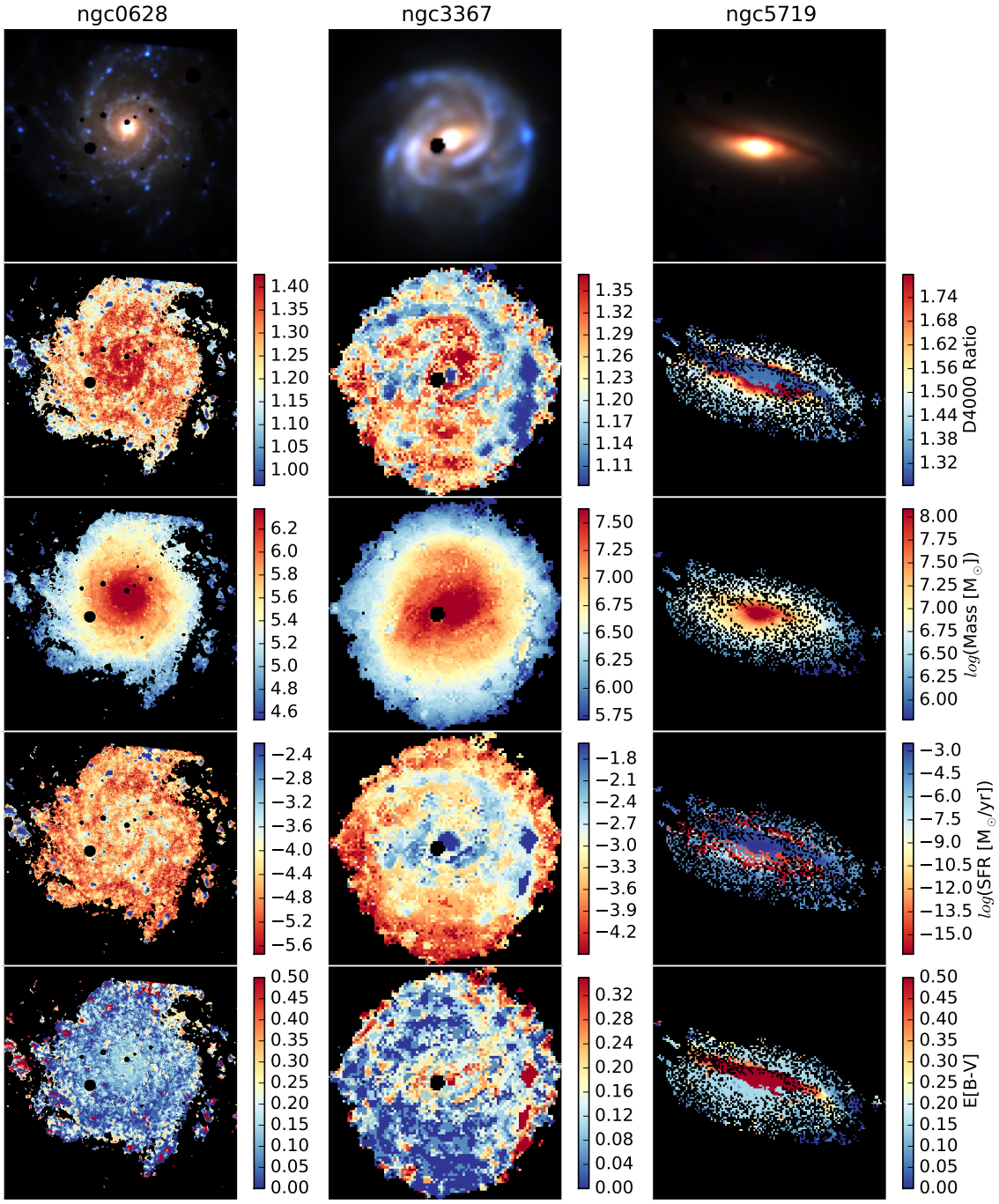

Figure 2.2: Maps showing (from top to bottom) false color *ugi*, 4000Åbreak strength, stellar mass, SFR, and extinction in each pixel for three illustrative galaxies from our sample of 67. Areas of low S/N as well as those containing foreground Galactic stars are masked out in black. Maps for the remaining galaxies can be found in an online supplement.

spiral galaxies as sSFR increases. To parametrize this dual nature, we fit the broken linear relation

$$f(x) = \begin{cases} b_1 & : x \leq p \\ b_2 + (b_1 - b_2)x/p & : x > p, \end{cases} \tag{2.5}$$

(which is a horizontal line with intercept b_1 up to some point $x = p$ and has some other slope thereafter) to the galaxies in each of the 300 Monte Carlo iterations. The median and 1-σ confidence intervals of these fits are shown as the purple solid line and shaded region in Figure 2.3. In all Monte Carlo instances, there is a clear trend of increasing average mass discrepancy with increasing sSFR, with unresolved stellar mass estimates underestimated by 25% (0.12 dex) at the highest specific star formation rates in our set of galaxies. Put another way, to correct the unresolved stellar mass estimate to the pxp stellar mass estimate for these high sSFR, one would have to add 33% to the unresolved mass, which is much more significant than adding the statistical average correction of 15% (0.06 dex).

Since the break point of the piecewise functions all exist at the lowest extremes of our measured sSFRs, separating the data into two regimes may be an unnecessary complication. For simplicity, we fit a simple linear relation to our median Monte Carlo mass ratios (shown as the purple dashed line in Figure 2.3). This line lies within the shaded 1-σ confidence region, and provides a close approximation to the more complex median of the piecewise fit distribution. It also allows for a simple formula to convert an unresolved stellar mass estimate to pixel-by-pixel one based on the unresolved sSFR. The conversion relation is

$$m_{resolved} = \frac{m_{unresolved}}{-0.057 \log(sSFR) + 0.34}, \tag{2.6}$$

where sSFR is in units of yr^{-1}.

2.3.2 Origin of the discrepancy

In Figure 2.4 we superimpose false-color images of each of the galaxies onto their location in Figure 2.3. It is apparent that the most egregious outliers from the one-to-one relation (NGC

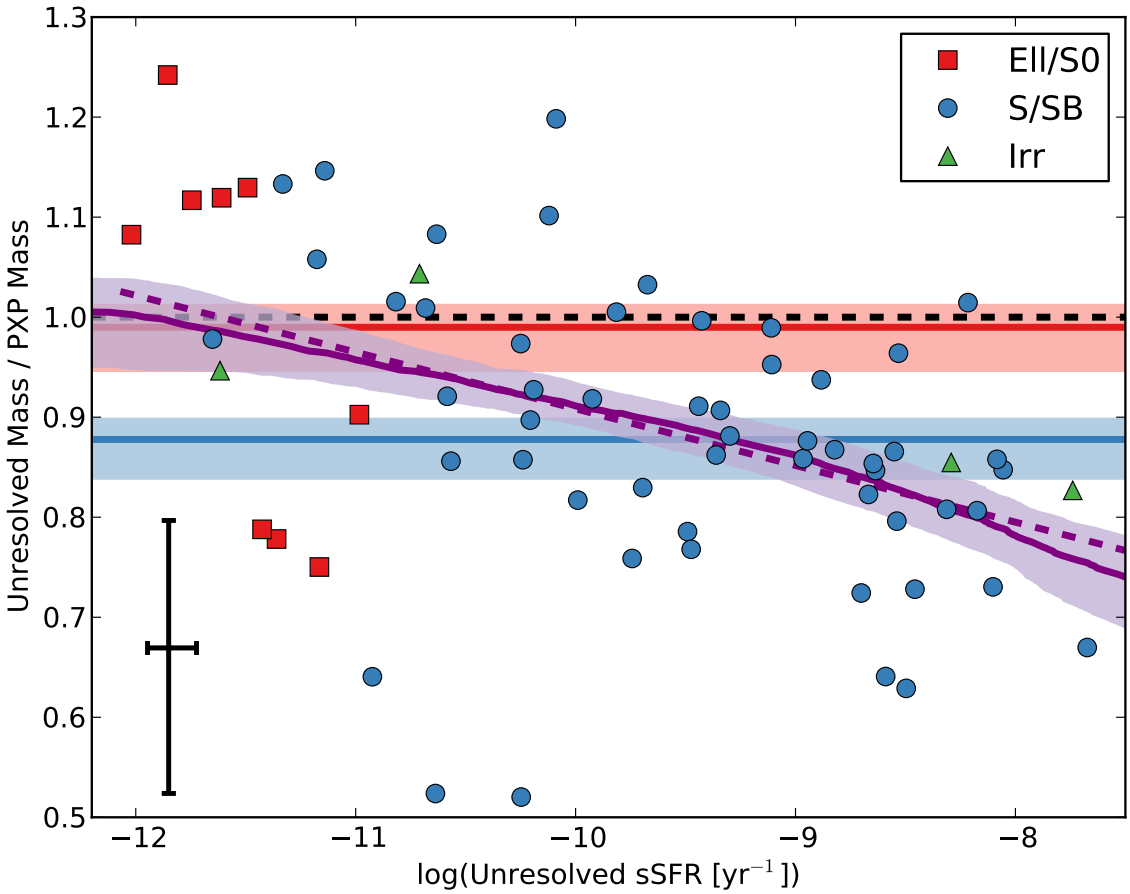

Figure 2.3: Ratio of unresolved stellar mass estimate and the PXP stellar mass estimate as a function of sSFR. The dashed horizontal black line represents a one-to-one correspondence. Spiral galaxies (blue points) tend to lie below the one-to-one line, while elliptical galaxies (red points) tend to lie on it (on average). The blue line shows the average ratio of the spiral galaxies indicating ≈ 13 percent of the stellar mass is missed by fitting all the light as if the galaxy were an unresolved point source. The red line shows the average ratio for elliptical galaxies, which lies nearly on the one-to-one ratio. The shaded blue and red regions show the 1-σ confidence regions for these average ratios as determined from Monte Carlo iterations. The purple solid line and shaded region show the median and 1-σ confidence region of fitting a broken linear relationship to all the galaxies in each of the 300 Monte Carlo iterations. The purple dashed line shows a linear fit to the data. A clear trend with sSFR is present. Typical error bars are shown in the lower left corner.

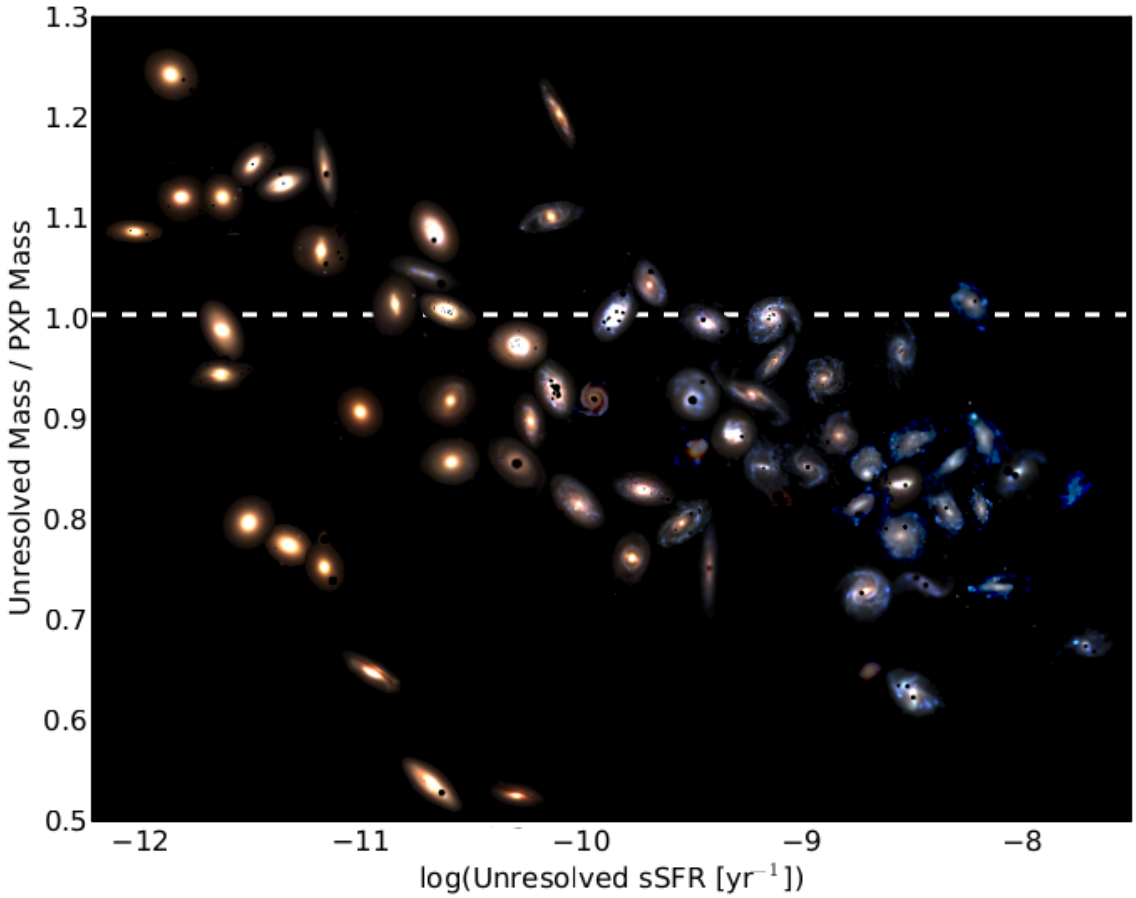

Figure 2.4: Same as Figure 2.3, except showing a false color *ugi* image for each galaxy. All galaxies have been scaled to be roughly the same size, and some of their positions have been slightly altered for clarity.

3190, NGC 4419 and NGC 5719 located in the lower left corner with unresolved-resolved mass ratios less than 0.65, but also edge-on M98 near the top center) all have strong dust lanes with heavy amounts of extinction running through them. To try to determine whether resolving dust or SFR is the dominant driver of the unresolved-resolved mass discrepancy, we refit the pixel-by-pixel photometry but constrained the extinction to be the same as determined from the best fit to the unresolved photometry. The results are shown in Figure 2.5 where we plot the ratio between the fixed extinction PXP mass and the free extinction PXP mass versus sSFR. In this figure, the closer the points lie to the same mass ratio as Figure 2.3, the more important role dust plays in the unresolved-resolved mass discrepancy, whereas points near the one-to-one line are little affected by resolving dust. In the cases of NGC3190, NGC4419 and NGC5719, the effects of resolving the strong dust lanes accounts for the majority of the difference between unresolved and resolved stellar mass estimates, as they again lie well below the one-to-one relation. We also find that the large majority of the spread in elliptical galaxies and those with low sSFR is due to allowing extinction to be a free parameter from pixel to pixel. Removing this freedom essentially eliminates any difference between resolved and unresolved stellar mass estimates for the low-sSFR galaxies.

What is not present in Figure 2.5 is any trend with sSFR. Even though the mass difference due to resolving dust can be drastic for any one galaxy, the deviation appears centered on the one-to-one line so that, on average, not resolving dust does not systematically bias mass estimates of large numbers of galaxies. The strong linear trend seen in Figure 2.3 must then be due to distinguishing the strongly and weakly star-forming regions and, thus, accounting for the outshining bias in broad-band SED fitting.

2.3.3 The effect of varying spatial resolution

In an effort to understand how resolution affects the PXP parameter estimations, we artificially degraded the images of the ten largest face-on spiral galaxies by progressively doubling the pixel scale. This process was done for those ten (of our 67) galaxies with large enough areas that after eight degradation steps they were completely unresolved and

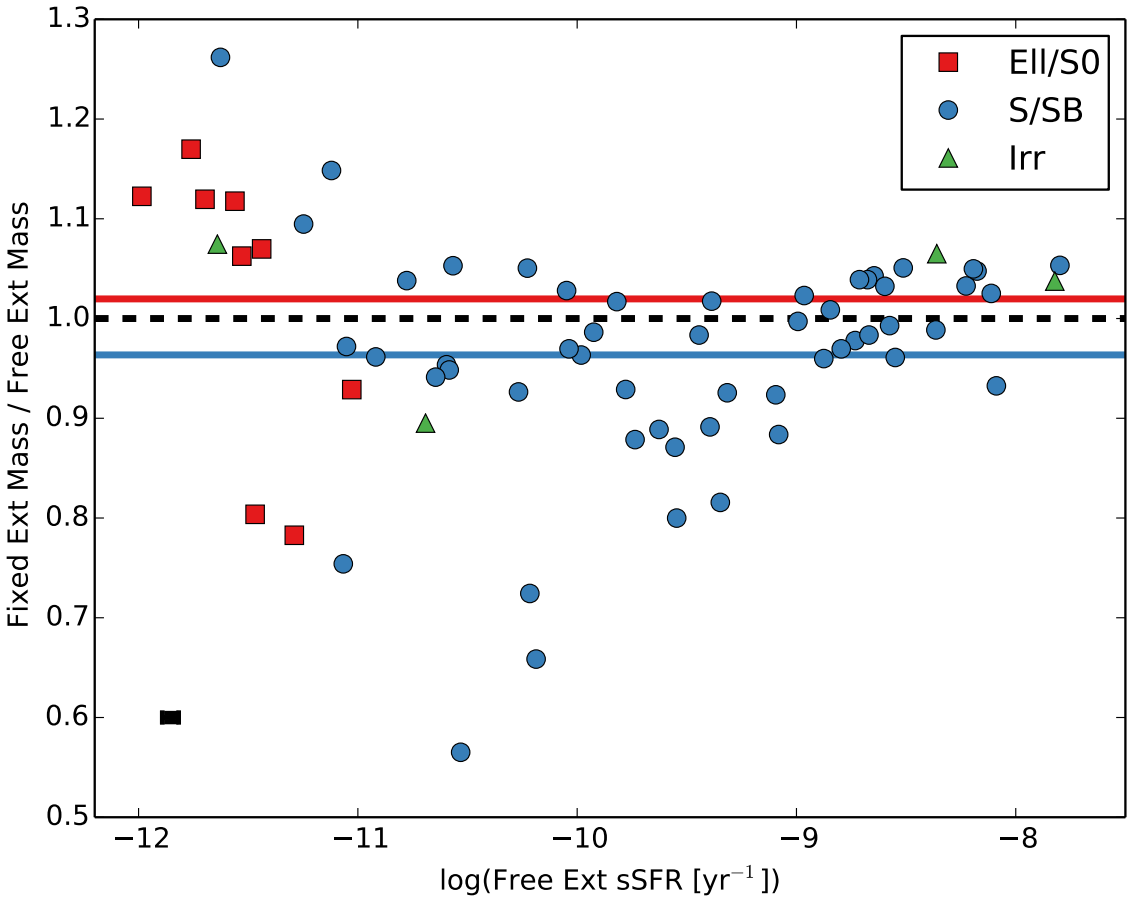

Figure 2.5: As in Figure 2.3, a mass ratio is plotted versus the sSFR. Blue circles are morphologically classified as spirals, red squares ellipticals, and green triangle irregular galaxies. Here, the vertical axis shows the ratio of the PXP mass found when holding the extinction value fixed to the amount determined by the best-fitting unresolved estimate, to the PXP mass found when extinction is a free parameter.

contained within one or two pixels. Figure 2.6 shows quartile ranges for the ratio of the degraded resolution PXP stellar mass estimate over the full resolution PXP stellar mass estimate as a function of physical scale. At the highest resolutions, the mass ratio slowly decreases to about 0.97, but drops sharply when the pixel scale becomes greater than 2-3 kpc/pixel. The mass ratio then stabilizes near the 13% under-estimate mark, although with much higher variance in the quartile ranges. It should be made clear that any one galaxy does not display a mass ratio that monotonically decreases with increasing resolution; the variance of mass estimates from SED is too large to show this. It is only by looking at an ensemble of galaxies that we can see on average how the mass estimate behaves as the spatial resolution gets poorer and poorer.

The physical scale of of 3 kpc/resolution element (here being pixel because the artificial degradation makes each pixel larger than the PSF) corresponding with the comparatively steep drop in mass ratio is much larger than the size of typical star forming regions in these galaxies (a few hundred parsecs; Efremov, 1995; Gusev, Egorov & Sakhibov, 2013). The scale may be more commensurate with the width of spiral arms (Kennicutt & Hodge, 1982; Seigar & James, 1998). To adequately separate young and old stellar populations and thus minimize the effect of outshining bias, it seems necessary to at least be able to resolve any spiral structure in the galaxy. This result may just be an artifact of our resolution study sample however, as these galaxies all have star forming populations concentrated in spiral arms. Note also that several irregular galaxies shown in Figure 2.4 follow the linear trend due to outshining despite the lack of any clear spiral structure. Nevertheless, as spiral structure has been observed to have formed much earlier in the history of the universe than previously thought possible (Law et al., 2012), it is still relevant to know that resolving spiral arms goes a long way toward mitigating any bias due to outshining. Perhaps more generally, one can say that pixel-by-pixel SED fitting can greatly reduce the effects of outshining only when any structure that distinguishes older and younger stellar populations is able to be resolved. In the case of our low redshift sample, this structure is spiral arms with a physical scale of approximately 3 kpc. If this level of resolution is

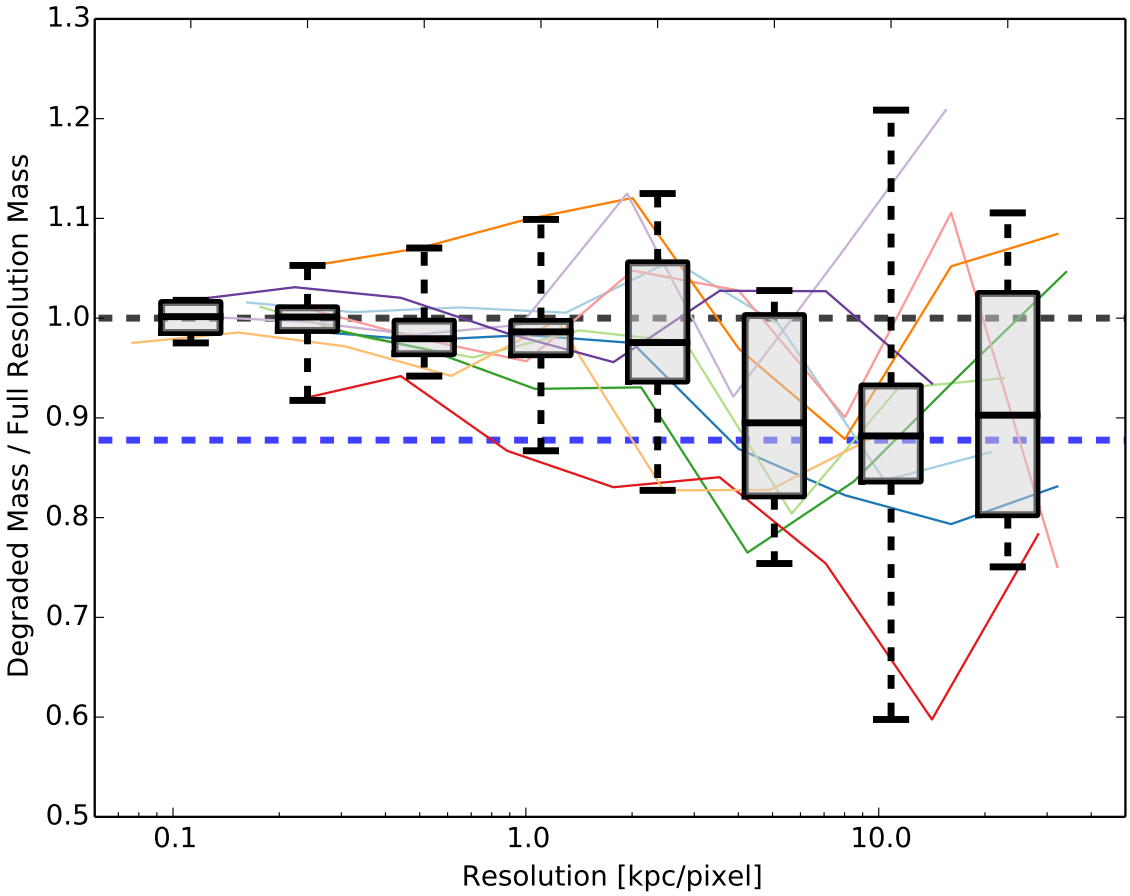

Figure 2.6: Ratio of degraded resolution PXP stellar mass estimate and the highest resolution PXP stellar mass at various pixel scales for 10 spiral galaxies with the largest area. The boxes and whiskers represent quartiles of the data grouped in bins of width ~ 0.33 dex in resolution. As in Figure 2.3, the dashed black line shows the one-to-one correspondence and the dashed blue line the average mass ratio for spiral galaxies. There is a sharp transition in the mass ratio near 3 kpc/pixel. The thin solid colored lines show the individual tracks for each of the 10 galaxies.

impossible, one can use the conversion relation given in Section 2.3.1.

2.4 Discussion

2.4.1 Testing Model Space Dependence

As discussed in Gallazzi & Bell (2009), the model template grid used constitutes a prior assumption which can bias the mass-to-light ratios determined from broad band colors. In order to test the extent to which our results depend on our model space we performed two tests. Firstly, Gallazzi & Bell (2009) found that including a large fraction of bursty models could underestimate the mass-to-light ratio of older, smooth-SFH galaxies. Although we found the unresolved and PXP masses of ellipticals do not differ on average, we nevertheless tested the robustness of our results using a smooth SFH. While it is impossible to exhaustively test every SFH, we repeated our procedure using τ SFH models and arrived at qualitatively similar results (namely the unresolved mass estimates of galaxies with low sSFRs were no different than the resolved mass estimates on average, whereas star-forming galaxies were underestimated by approximately 0.07 dex on average, although without as strong a dependence on sSFR). From this we conclude that, while our results are not entirely independent of our choice of SFH (one could always construct unrealistic SFHs that would produce vastly different results, say if all star forming models had no underlying older stellar population at all), for any reasonable or commonly adopted SFH our results should be qualitatively similar, with unresolved stellar mass estimates of star-forming galaxies underestimated by somewhere between 0.05 and 0.08 dex on average.

Secondly, as examined in Gallazzi & Bell (2009), the signal-to-noise ratio of the observations combined with the model template prior distribution can lead to biased results. In brief, they found that when the model template set is a mixture of bursty and smooth SFHs with differing M_*/L ratios, good data will constrain the fits to only those models with the proper M_*/L ratio. But, as the amount of noise in the data increases, the fit will be more free to explore the model space, and hence the determined M_*/L ratio will depend on the

ratio of bursty to smooth SFHs in the model template set. Since our stated criteria for a pixel to be included in our mass estimation was S/N greater than five in all SDSS bandpasses, this effect could play a prominent role in our results. However, in practice the S/N in g, r, i is much better than that in either u or z, and our criteria is essentially equivalent to $S_u/N_u > 5$ (although, in a very small percentage of pixels, the z band is the limiting one). The large S/N in g, r, i give the fits much less freedom than initially implied by our selection criteria. To test this, we took the unresolved photometry (which has extremely good signal to noise) and artificially increased the uncertainty in each bandpass, refitting the median Monte Carlo mass at each step. To realistically approximate the uncertainty growth in each bandpass for our data, for each galaxy we created histograms of the S/N in each bandpass and found the i^{th} percentile where i is a multiple of ten. We converted this to an uncertainty in magnitude for the Monte Carlo fits. Figure 2.7 shows the ratio of the increasingly noisy mass estimate and the unresolved mass estimate as a function of u-band S/N. The typical r-band S/N at this stage is also shown for reference, and is typically 8-10 times that of the u-band. The binned average (red squares) shows little deviation from a one-to-one correspondence. There may be a slight downward trend at $S/N_u < 10$, but it is at the 2% level. Since the low S/N pixels are also the least massive, any bias of this level in their mass determination has a net effect of much less than 1% on the total PXP mass of the galaxy. Additionally, since the noisy mass would underestimate the true mass, this bias would only work to increase the unresolved-resolved mass discrepancy found above, if only very slightly.

2.4.2 Impact on previously derived relations

The average offset of 13% for star-forming galaxies is equivalent to approximately 0.06 dex. This is not an outstandingly large discrepancy, and any current relationship with stellar mass would not change dramatically if corrected for this offset. However, the differential nature of the offset (affecting higher sSFR galaxies more than those with lower sSFR) can compound the effect given the right circumstances. For instance, plotted in Figure 2.8 in

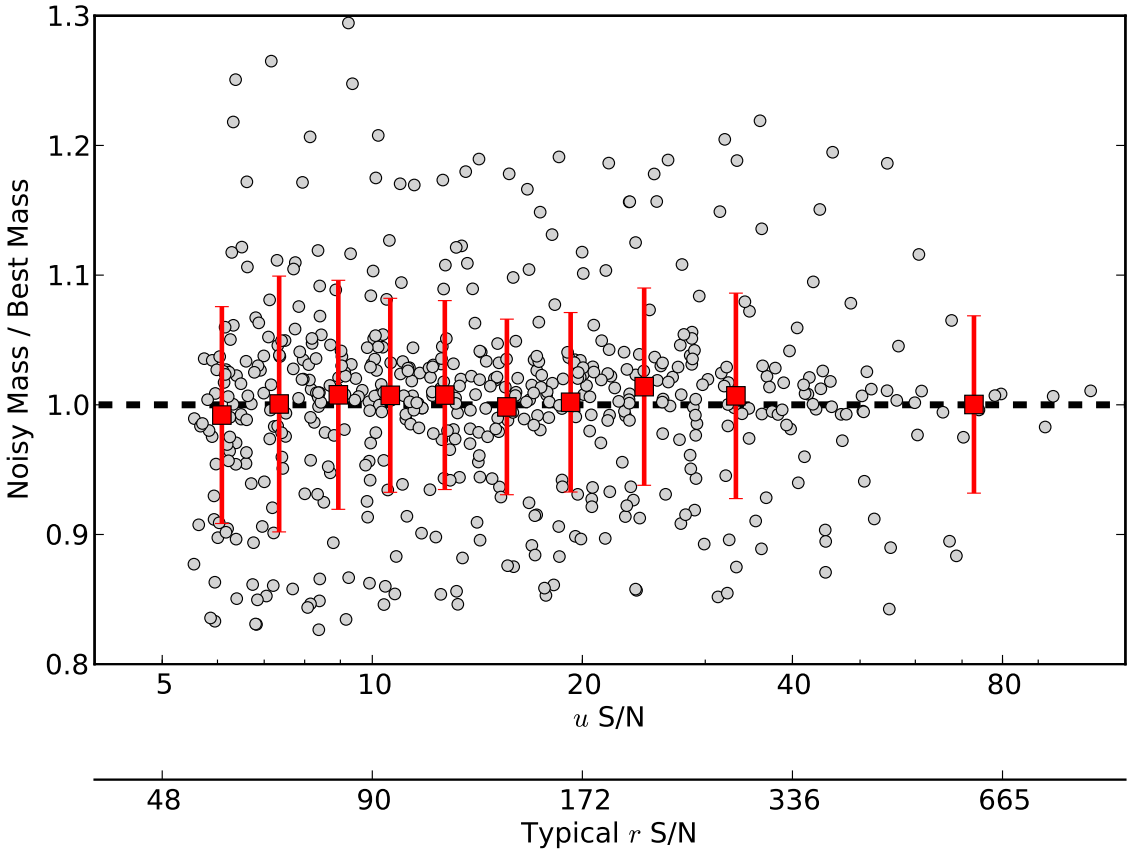

Figure 2.7: Ratio of mass estimates from unresolved photometry with artificially increased uncertainties and those with lowest uncertainties as a function of u-band S/N. The artificially increased uncertainty in each bandpass is determined by taking the i^{th} percentile of the S/N histogram where i is a multiple of 10. The typical r-band S/N determined from these percentiles is also shown for reference. The grey points show the mass ratio for each galaxy at each noise percentile. The red squares show the average of the grey points in bins of $1/10^{th}$ of the data. The black dashed line shows the one-to-one correspondence. The mass estimates show no bias with increasing S/N within our cut-off limit of 5.

green is the star forming main sequence (SFR-M_* relation) from Whitaker et al. (2012) and isometallicities of the $M_* - Z - SFR$ surface from Mannucci et al. (2010) in blue. Dashed red lines show corrections to these relations based on interpolating the purple line in Figure 2.3 of this work. The shallow slope of the Whitaker et al. (2012) relation in the SFR-M_* log-log plane leads to little difference when corrected for outshining. At best one can say the slope is a little steeper, requiring slightly faster evolution from the flatter relation at higher redshift (assuming no effect of outshing at higher redshift). However, the effects of outshining become more apparent when metallicity dependence is included in the relationship. The $M_* - Z - SFR$ relationship exists throughout the SFR-M_* log-log plane, allowing one to see the larger offsets in high sSFR regions (upper left of Figure 2.8) compared to lower sSFR regions. The steeper slope of the isometallicities also lead to outshining corrections being larger in the full $M_* - Z - SFR$ (though still not extremely large).

The sSFR dependence of the unresolved-resolved mass difference can manifest itself in other, possibly less obvious ways. For instance, Patton et al. (2013) compare star formation rates in interacting galaxy pairs with a control sample selected to have similar masses as the paired galaxies. Since the SFR is enhanced in the paired galaxies, however, so too is the sSFR. Thus, a larger correction must be applied to the paired galaxy's unresolved mass estimate than must be applied to the control sample, possibly making the control sample not representative. It turns out not to be an issue in this particular case, because the maximum SFR enhancement is approximately a factor of 2, meaning the difference between the enhanced corrected mass and control corrected mass is only 5%, well within their stated control bounds of 0.1 dex in stellar mass. However, awareness that mass selected samples may not be as homogeneous in mass due to differing sSFRs is still important to acknowledge.

Even within a single galaxy the sSFR-dependent mass correction may be important to note. Several works (e.g. Allen et al., 2006; Simard et al., 2011; Mendel et al., 2014) decompose a galaxy into an inner and outer components (i.e. bulge and disc) with SF occurring primarily in the outer regions. The sSFR of the outer region is thus enhanced

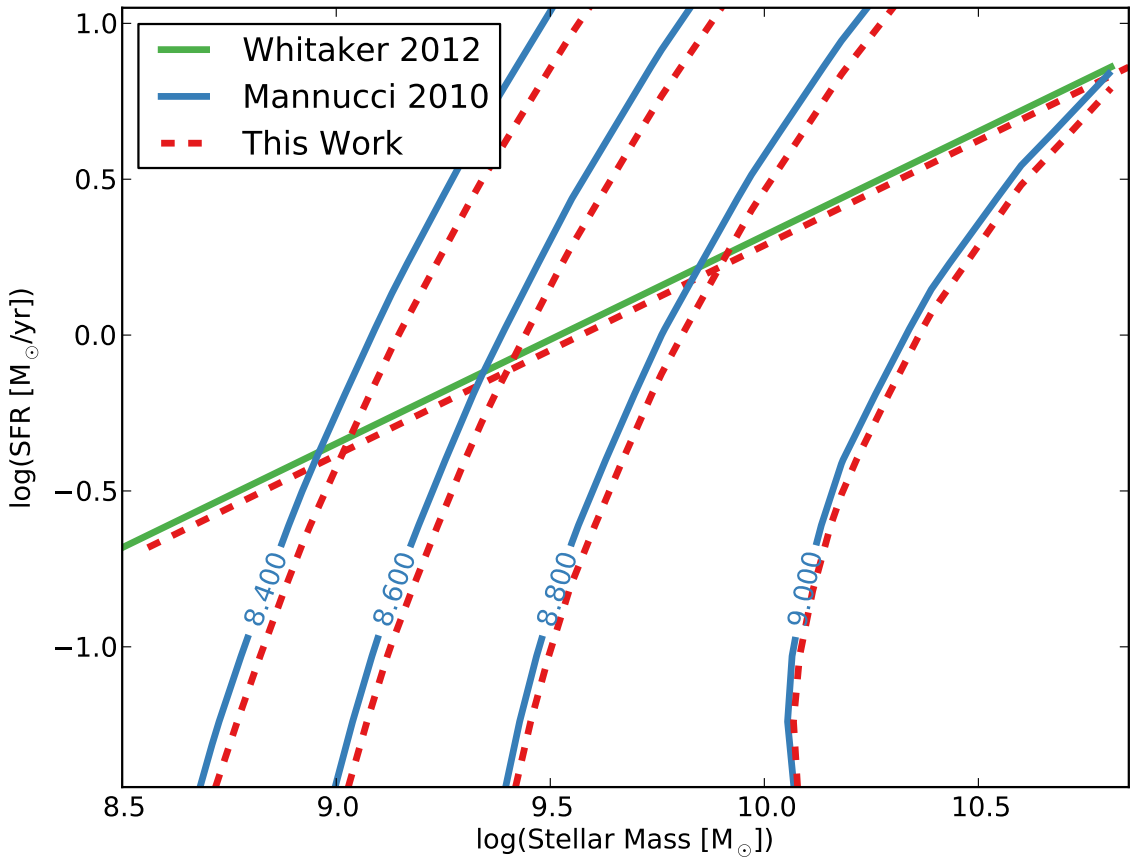

Figure 2.8: SFR-M_* relation from Whitaker et al. (2012) in green and isometallicity contours of the $M_* - Z - SFR$ relation from Mannucci et al. (2010) in blue. The numbers on the contours are in units of $12 + log(O/H)$. The red dashed lines show corrections to these relations based on this work.

compared to the inner region, and so a differential correction (perhaps up to 0.1 dex) must be applied when comparing the masses of the inner and outer components. In general, the outshining mass correction should be considered for broad-band SED fitting in any cases with high sSFRs, or when comparing two sets of data with differing sSFRs.

2.4.3 Outshining at higher redshifts

How the systematic bias described above might change with redshift is an open question. The sSFR of star-forming galaxies increases with redshift (Feulner et al., 2005), and so we might expect the outshining effect to become more drastic at earlier times in the universe. For example, taken at face value, the relation given by the purple line in Figure 2.3 implies that galaxies with sSFRs between -8 and -7 yr^{-1} (rates much more common during the era of peak SFR density) would have to be corrected by between 0.1 and 0.2 dex respectively. However, as outshining is a product of incorrect SFHs, galaxies at higher redshift should be less affected because there has been less time for differences in the assumed versus true SFH to accumulate. Put another way, there would be fewer older stars (and hence less mass) hiding behind the bright younger stars simply because there has not been enough time to form a significant older stellar population. See, for example, Pforr, Maraston & Tonini (2012) on the effects of assumed SFH as a function of redshift. It is clear that, at some value of redshift, outshining would cease to be an issue as there would not be a significant older population of stars to obscure. In the limiting case, the first burst of stars formed in a galaxy would essentially be a SSP, and thus have no outshining.

Pixel-by-pixel SED fitting has been performed for high-redshift galaxies at $z \sim 1$ and $z \sim 2$ by Wuyts et al. (2012) using data taken with Wide Field Camera 3 (WFC3) on board the Hubble Space Telescope (HST) as part of the Cosmic Assembly Near-infrared Deep Extragalactic Legacy Survey (CANDELS; Grogin et al., 2011; Koekemoer et al., 2011). They found that the unresolved mass estimate from these galaxies was robust, and that there was no discrepancy between the resolved and unresolved mass estimates. Their PSF matched images had a resolution of 0.18 arcseconds FWHM, which corresponds to a physical

scale of 1.46 and 1.54 kpc at redshifts 1 and 2 respectively. From our results in Section 2.3.3 (Figure 2.6), this resolution should be adequate to detect any discrepancy if it existed at high redshift. However, Wuyts et al. (2012) also further bin pixels to increase signal-to-noise, making their effective resolving power much worse the the PSF FWHM. Indeed, they state that they do find a mass discrepancy of 0.2 dex for $z \sim 2$ star-forming galaxies when no pixel binning is performed, although they attribute this to low signal-to-noise pixels having spurious mass-to-light ratios. How outshining effects mass estimates at high redshift thus remains an open question, one that may not be able to be answered until the advent of the next generation of telescopes such as the James Webb Space Telescope (JWST) or Thirty Meter Telescope (TMT), which will provide roughly 2.5 and 10 times greater resolution than Hubble respectively.

2.5 Conclusions

We fit SPS models to broad-band fluxes in each pixel for 67 nearby galaxies and compared the stellar mass estimates found from summing each pixel's median Monte Carlo mass with the median Monte Carlo mass found when the models were fit to all the light from the galaxy at once, as if it were an unresolved point source.

The unresolved mass estimate systematically underestimated the resolved mass estimate, displaying a clear trend of increasing discrepancy with increasing sSFR. Galaxies with low sSFR ($log(sSFR[yr^{-1}]) \sim -12$) were consistent with no mass discrepancy between resolved and unresolved mass estimates, whereas unresolved mass estimates of the highest sSFR galaxies ($log(sSFR[yr^{-1}]) \sim -8$) typically underestimate the mass by 25% (0.12 dex). We provide a conversion formula (Equation 2.6) to correct unresolved mass estimates at low redshift based on a galaxy's sSFR.

We found the mass discrepancy's correlation with sSFR to be due to outshining, i.e. young stellar populations obscuring older stellar populations behind their bright flux. However, several egregious outliers from this relation were caused by the presence of strong

dust lanes. The presence of dust can cause differences between the resolved and unresolved mass estimates of up to 45% (0.35 dex). Although very significant for individual galaxies, resolving the 2D distribution of dust did not have any affect on average stellar mass estimates.

By artificially degrading the resolution of the largest spiral galaxies, we found that a resolution of at least 3 kpc is needed to significantly reduce the systematic under-estimation in stellar mass due to outshining. This scale is commensurate with the width of spiral arms in these galaxies.

Although it is unclear how the relation between resolved and unresolved stellar mass estimates changes at higher redshifts, we recommend that caution be taken when considering mass estimates of galaxies with high sSFRs that have been derived from broad band SED fitting. Be aware that these masses are likely systematically underestimated by 13-25% (0.06-0.12 dex) on average due to outshining. The differential nature of this effect should be taken into account when comparing masses of populations with different sSFRs (e.g. disc versus bulge, "mass-matched" galaxies with a range of SFRs). In the case of any individual galaxy, note that the presence of dust lanes can greatly impact the mass estimate (by a factor of $\sim$2 or 0.3 dex), but that the effects from dust should average out when considering an ensemble.

Chapter 3

Pixel-by-Pixel SED Fitting in the Hubble Extreme Deep Field

We performed pixel-by-pixel SED fitting on galaxies in the Hubble Extreme Deep Field (XDF). Through a comparison of the resolved and unresolved mass estimates, we found that unresolved mass estimates for galaxies up to $z = 2.5$ can be underestimated by factors of 2-5. The ratio of the unresolved to pixel-by-pixel mass measurement depends on the galaxy's specific star formation rate (sSFR). At low sSFRs, the ratio changes roughly linearly with sSFR, going down from approximately 1 at sSFR= 10^{-12} yr^{-1} to roughly 0.9 at sSFR= $10^{-9.5}$ yr^{-1}. At sSFRs above this level, however, the underestimate increases rapidly such that galaxies with sSFRs equal to 10^{-8} yr^{-1} have unresolved mass estimates of only one half to one fifth the resolved estimate. Correcting galaxy stellar mass functions based on these results brings the inferred star formation rate density more in line with the directly measured one, eliminating the "missing mass" problem.

3.1 Introduction

Spatially resolved (i.e. pixel-by-pixel) broadband SED fitting provides an exciting tool to study the spatial distribution of stellar matter in a galaxy, particularly for high redshift

galaxies where obtaining 2-D spectra is cost prohibitive. Resolving features in a galaxy's spatial distribution allows us to uncover details that are obscured and blotted out by integrated photometry. The technique of pixel-by-pixel SED fitting was first developed by Abraham et al. (1999), who matched spectral synthesis models to resolved multicolor data of $z \sim 1$ galaxies in the Hubble Deep Field in order to study ages and evolutionary histories of stellar populations in those galaxies. An analysis of how pixel-by-pixel fitting affected mass estimates was performed by Zibetti, Charlot & Rix (2009) for 75 nearby ($D < 30$ Mpc) SINGS galaxies. They fit SPS models to individual pixels and found that the unresolved mass estimate (i.e. fitting all the light from the galaxy at once as if it were a point source) could be underestimated compared to the resolved mass by up to 40% (0.22 dex). They postulated that the presence of large dust lanes contributed to the mass discrepancy. Sorba & Sawicki (2015) corroborated this by using pixel-by-pixel analysis on a similar set of 67 nearby galaxies in the Sloan Digital Sky Survey (SDSS; Eisenstein et al., 2011). They found that the presence of strong dust lanes could cause unresolved mass estimates to be underestimated by 45% (0.25 dex) for an individual galaxy, but only in extreme cases, and that dust did not affect mass estimates on average. However, by being able to disentangle older stellar populations from younger ones, Sorba & Sawicki (2015) were able to find an increasing bias in a galaxy's mass estimation with specific star-formation rate (sSFR). They found the effect was small (unresolved masses were underestimated by 13% or 0.06 dex on average), but strongly correlated with sSFR leading to a maximum bias of 25% (0.12 dex) at sSFRs of around $10^{-8} yr^{-1}$, and they concluded this bias was due to outshining. Essentially, young massive stars have a much smaller stellar mass-to-light (M_*/L) ratio than older stars. They are orders of magnitude brighter than solar type stars. But they are also short-lived, meaning they are only present in currently star-forming regions. When all the light from a galaxy is integrated together, however, the light from young stars dominates a galaxy's SED at optical wavelengths. Thus model SED fits to broadband photometry preferentially fit the M_*/L of the younger stellar population, often missing mass from older components (for further discussion on outshining and its effects, see Sawicki & Yee, 1998;

Papovich, Dickinson & Ferguson, 2001; Maraston et al., 2010; Pforr, Maraston & Tonini, 2012).

Spatially resolved stellar property maps have also been created for high redshift ($0.5 < z < 2.5$) star-forming galaxies in the Cosmic Assembly Near-infrared Deep Extragalactic Legacy Survey (CANDELS; Grogin et al., 2011; Koekemoer et al., 2011) by Wuyts et al. (2012). They used the maps to examine star-forming clumps and variations in rest-frame color, stellar surface mass density, age, and extinction as a function of radius, finding results consistent with inside-out disk-growth. They also compared unresolved to pixel-by-pixel mass estimates, but found no discrepancy. However, their binning of low signal-to-noise (S/N) pixels may have impacted their effective spatial resolution, leaving an open question as to how outshining may change at higher redshifts. In this work we set out to examine the influence of outshining as a function of cosmic time. We do so following the pixel-by-pixel method laid out in Sorba & Sawicki (2015). Throughout this work we assume a WMAP7 (Komatsu et al., 2011) flat ΛCDM cosmology ($H_0 = 70.4$ km s^{-1} Mpc^{-1}, $\Omega_M = 0.272$) and use the AB magnitude system.

3.2 Method

3.2.1 Data

To examine pixel-by-pixel SED fitting at higher redshifts we used the Hubble eXtreme Deep Field (XDF; Illingworth et al., 2013) publicly available dataset, which combines data from a decade of observations made with the Hubble Space Telescope (HST) creating optical/NIR images unsurpassed in depth. The extreme depth of this dataset is particularly important for a pixel-by-pixel analysis, increasing the number of pixels with acceptable signal-to-noise (S/N) and enabling us to probe fainter regions of galaxies. The XDF dataset contains mosaic images covering approximately four square arcminutes in nine passbands (ACS/WFC $F435W, F606W, F775W, F814W$, and $F850LP$; WFC3/IR $F105W, F125W, F140W$, and $F160W$) that have all had their background flux removed, been astrometrically aligned,

and drizzled onto the same 60 mas pixel scale.

It is important when doing pixel-by-pixel photometry that all images have the same point spread function (PSF). To measure the PSF of each bandpass, we started by visually inspecting stars from the catalog of stars in the Hubble Ultra-Deep Field (Pirzkal et al., 2005) and selecting those that weren't contaminated by noise or nearby galaxies. These stars were recentered to their intensity-weighted sub-pixel centers, normalized, and median-stacked to form the PSF. The WFC3 PSFs were augmented at larger radii using model PSFs created using the TinyTim software package (Krist, 1995; Krist, Hook & Stoehr, 2011) to account for the relatively large amount of flux contained in the broad wings of the NIR PSFs (van der Wel et al., 2012; Rafelski et al., 2015). The broadest PSF belonged to the $F160W$ image, which had a PSF full-width-at-half-maximum (FWHM) of approximately 0.20 arcseconds. For each bandpass other than $F160W$, we convolved the images to match the broadest PSF by creating an 11×11 convolution kernel using the method described in Alard & Lupton (1998), employing a delta function at each pixel in the kernel as the set of basis functions (Becker et al., 2012). The small size of the kernel provided a good compromise, limiting the tendency of our choice of basis function to over-fit and match the noise in the wings of the PSF, but was still large enough to capture all the features of the transformation kernel.

After convolving the images to the same PSF, we created a multi-band detection image by summing each image weighted by the inverse variance on a pixel-by-pixel basis. This process created an image where galaxies that are bright at the bluest wavelengths but faint in the NIR (such as low redshift starbursts) are present, but so are galaxies with very faint observer-frame optical fluxes but stronger observer-frame NIR flux (such as faint quiescent galaxies or galaxies at higher redshifts). The multiwavelength detection image maximized the number of galaxies present in the image, and limited any bias in choosing which wavelength to select pixels from. We included in our pixel-by-pixel catalog any pixels that had a S/N ratio greater than five in the detection image.

We labeled galaxies and assigned redshifts using the spectroscopic and photometric

redshift catalogs provided by Rafelski et al. (2015). The photometric redshifts were derived using 11 bandpasses covering the near ultraviolet (NUV) to NIR from WFC3 observations in the UDF. Rafelski et al. (2015) provide photometric redshifts found using two different codes–BPZ (Benitez, 2000; Benitez et al., 2004; Coe et al., 2006) and EAZY (Brammer, van Dokkum & Coppi, 2008). We chose to use the BPZ redshifts, which had a slightly smaller scatter when compared to spectroscopic redshifts as measured by the normalized median absolute deviation ($\sigma_{NMAD} = 0.028$ for BPZ versus 0.030 for EAZY), and a slightly lower outlier fraction (2.4% versus 5.9% for EAZY). Although averaging the two redshift measurements is possible, it runs the risk of increasing the catastrophic outlier fraction, and thus we chose to only use a single set of measurements for the photometric redshifts. The spectroscopic redshifts were compiled from nine different sources and contain robust measurements for 169 galaxies.

We assigned pixels to separate galaxies by converting the RA and DEC given in the Rafelski et al. (2015) catalog to pixel coordinates, and used these as initial seeds for basin markers for a watershed segmentation (Soille & Ansoult, 1990). Whereas traditional segmentation through deblending with, e.g., SExtractor (Bertin & Arnouts, 1996), requires multiple run-throughs with different parameters in order to accurately segment both nearby galaxies blended together and large galaxies split into separate objects (see Barden et al., 2012; Rafelski et al., 2015), the watershed algorithm for segmentation is useful when one already knows roughly where objects are located. Briefly, one can imagine the light profile from our detection image flipped upside down to create "basins" which are labeled by the initial markers and bounded by our S/N acceptance criteria. The basins are flooded with water starting from the initial seeds, and where one basin overflows into another marks the delineation between the two objects. The use of initial markers is important for the success of this algorithm; simply using local minima leads to over-segmentation due to noise.

From this segmentation map we created a pixel-by-pixel flux catalog and an unresolved total flux catalog. The fluxes were corrected for extinction due to foreground dust according to Schlafly & Finkbeiner (2011). Similarly to Sorba & Sawicki (2015), in order to compare

the same light with the same light, the unresolved flux catalog was made by summing all of the flux from each pixel for each galaxy. We removed any objects flagged as stars in Pirzkal et al. (2005) and removed by eye any objects too close to the borders of the image, or with obvious artifacts. In total, the analysis in the following sections included 162 galaxies with spectroscopic redshifts and 1060 with photometric redshifts. The minimum, median, and maximum number of pixels in the spectroscopic sample were 72, 921, and 17499 pixels respectively. For the photometric sample, we restricted the minimum number of pixels required in order to be included in the analysis to 64. Below this threshhold, we found that uncertainties in mass estimates (and specifically the ratio of the unresolved to resolved masses) became inordinantly large. The median and maximum number of pixels for the photometric redshift galaxies were 182 and 12228 pixels respectively.

3.2.2 Models

We created model SED templates using the Flexible Stellar Population Synthesis (FSPS; Conroy, Gunn & White, 2009; Conroy & Gunn, 2010) code. The model set assumed solar metallicity, a Chabrier (2003) IMF, and a Calzetti et al. (2000) dust law, and were corrected for extinction due to intergalactic hydrogen following the Madau (1995) prescription. Nebular line emission was also included in these model templates (Byler et al., 2016), which is a relatively new feature available to FSPS.

While the assumption of solar metallicity becomes less accurate at higher redshifts, both Bolzonella et al. (2010) and Pforr, Maraston & Tonini (2012) found that the differences in mass estimation between different metallicity setups is small. Since in this work we are most interested in recovering stellar masses, fitting with solar metallicity should be sufficient, and helps to reduce the parameter space.

For each galaxy's pixel, we shifted the model spectrum to the redshift given by Rafelski et al. (2015), defaulting to the spectroscopic redshift when available. Model broadband fluxes were created from each spectrum by convolving with broadband filter transmission curves, and the best-fitting model was found using the SEDfit software package (Sawicki,

2012b), which finds the minimum χ^2 in our model parameter space. SEDfit determines uncertainties through an iterative Monte Carlo procedure. For each Monte Carlo realization, the observed flux in each bandpass is changed by adding a normally distributed perturbation (with standard deviation equal to the uncertainty to the observed bandpass and centered on the original measurement). We performed 300 of these realizations for each pixel and used the the median mass estimate to avoid biases arising from minimal χ^2 best-fits (Taylor et al., 2011).

Departing from Sorba & Sawicki (2015), we chose to parameterize the SFH of our model SEDs as an exponential decay (i.e. τ-models), in part for easy comparison with other pixel-by-pixel works that used an exponentially declining SFH (Wuyts et al., 2012; Welikala et al., 2011). Whereas our previous work found that photometry of nearby galaxies in the Sloan Digital Sky Survey was well matched by two-component burst SFH models, we found the burst SFH models were poor representations for higher redshift galaxies. This is shown in Figure 3.1 where we can see the two-dimensional stellar mass and SFR distributions are not at all smooth. The stellar mass maps contain wispy filaments of pixels much less massive than the surrounding stellar material, and the SFR maps show no discernible structure when we would expect them to roughly trace the blue stars in the spiral arms. Why two-component burst models would work well for the SDSS galaxies, but fail for XDF galaxies is an open question. It could be that the SDSS observations probe smaller physical scales, but it may also be related to the results of Gallazzi & Bell (2009), who found that including a large fraction of bursty models could under-estimate the mass-to-light ratio of galaxies with smoother SFHs. As we observe galaxies at greater redshifts, it becomes more likely that they will have had smoother SFHs, as any recent bursts will have stellar populations not too dissimilar from the underlying older stellar populations.

It could also be that the two-component burst models are too degenerate at higher redshifts. Specifically, the mass fraction of the young stellar component can not be constrained by the observations, and not only could the models fail to capture a true underlying older population of stars, they could erroneously add a large fraction of mass to a strictly

younger population of stars by over-estimating the older stellar component. This would not be the case for low redshift galaxies in the SDSS, since it is very unlikely to observe a pixel actively forming stars that did not have an underlying older stellar component. The models may over-fit the older component somewhat at low redshift, but not nearly as drastically as is possible at higher redshifts, where there has not been as much time to assemble mass in the older population. The over-estimation of the older stellar component would also affect SFR measurements since each component's SFH is modelled as an exponential decay. This would explain the poor reproduction of the star-forming regions seen in the bottom row of Figure 3.1. To ensure realistic spatially resolved stellar property maps, we use one-component τ-models, which were shown to give qualitatively similar mass estimates as two-component burst models for galaxies in the SDSS (Sorba & Sawicki, 2015). Note that with one-component models, outshining will always act to hide the mass of older stars.

We found that it is imperative to have a parameter space that is well sampled with regards to SFH when doing pixel-by-pixel SED fitting. Figures 3.2 and 3.3 show stellar mass and SFR maps when using coarse and fine model grids respectively. The coarse grid contains six different values for τ, ranging from 0.3 to 10 Gyr and the spacing between each step roughly doubling each time, and ten different ages between $10^{7.75}$ and 10^{10} years, with the exponent increasing in steps of 0.25. Our minimum τ was chosen based on the recommendation from Wuyts et al. (2011), who found that forcing the e-folding timescale to be greater than several 100 Myr was most effective at reproducing UV+IR measured SFRs. As can be seen in Figure 3.2, although the stellar population property maps are smoother than those of the burst models, the SFR map in particular still shows sharp discontinuities that seem unrelated to any features visible in the false-color images. These discontinuities disappear when using finer spacings for the SFH parameters, as shown in Figure 3.3. Here the model grid consists of 20 different τ values spaced roughly evenly logarithmically between 0.3 and 10, and log(ages/yr) ranging from 7.7 to 10.1 in steps of 0.05. The finer model grid displays much smoother property maps with no unphysical discontinuities. It is this set of models that we chose to use as our ultimate template grid.

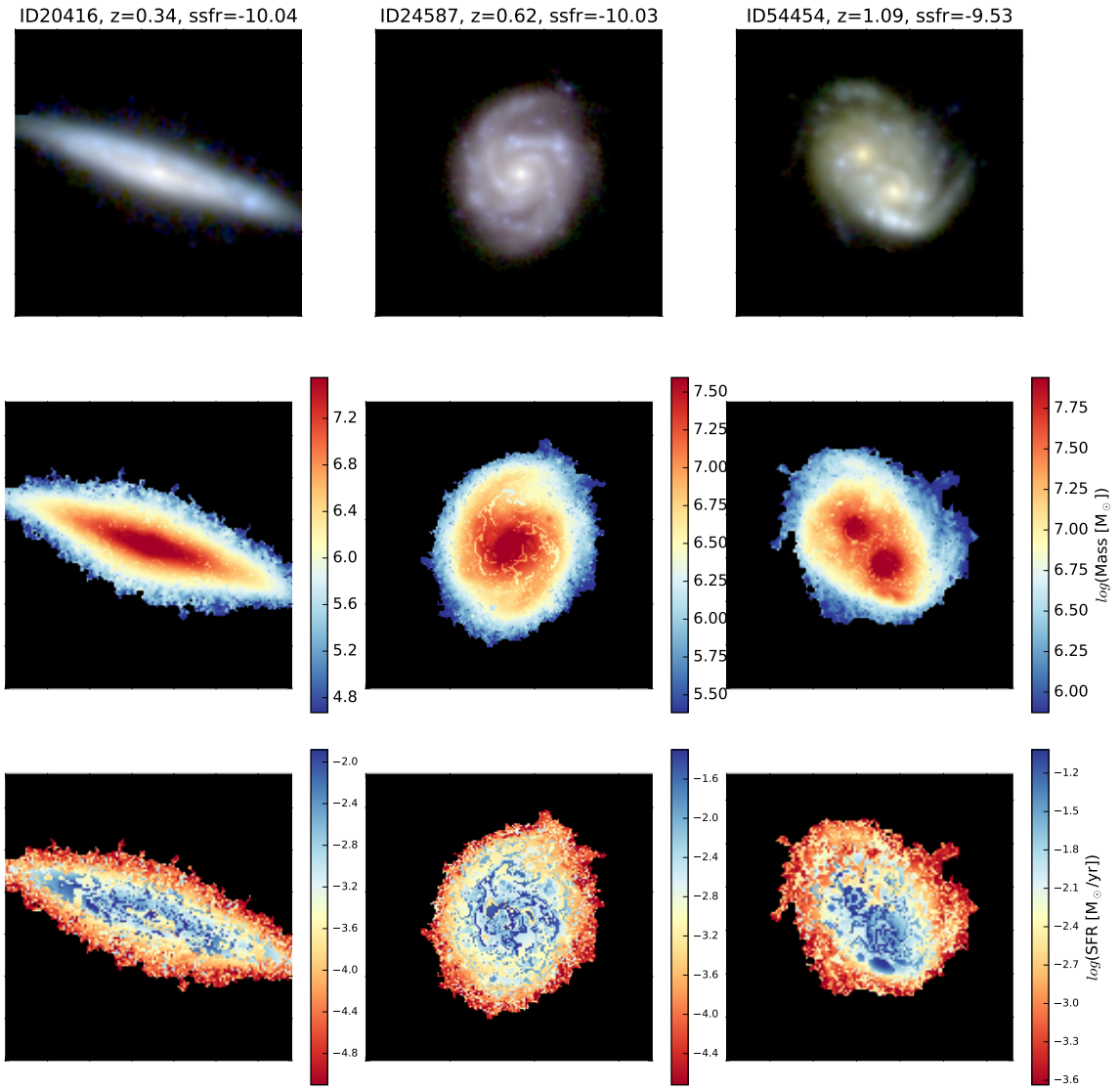

Figure 3.1: Two-dimensional maps of three representative XDF galaxies created using the same model SED set as Sorba & Sawicki (2015). From top to bottom we show false-color images in approximately rest-frame *ugr*, stellar mass, and SFR. This model set did not provide adequate pixel-by-pixel SED fitting. The galaxies have, from left to right, $RA = \{53.1712061°, 53.1699419°, 53.14785833°\}, Dec = \{-27.81471020°, -27.7710194°, -27.77403611°\}, z_{spec} = \{0.337, 0.622, 1.088\}$, and $\log(M_*/\mathrm{M}_\odot) = \{10.3, 10.7, 10.9\}$ where the mass measurement is the median pixel-by-pixel mass from our final catalog.

Note that the need for a finely spaced model grid may also have played a role in the poor performance of the two-component models above. However, because two-component models have many more free parameters, the total number of models grows quickly as the resolution of each parameter is increased, and can become cumbersome to work with.

Studying the right-most mass map of Figure 3.3 we can see an example of outshining happening on a small scale as evidenced by the two "dimples" of less massive pixels to the left and right of the upper bulge. It is unlikely that there are massive holes in the galaxy when the rest of the mass map shows a very smooth gradient. These two areas correspond to the bright blue star-forming regions visible in the false-color image, indicating that the youngest stars are obscuring an older stellar population, leading to an erroneous M_*/L ratio. Similar dimples can also be seen for the brightest blue spots in the spiral arms of the left-most galaxy. This effect seems unavoidable with τ models, and even in SED fitting general since the light from very different SFHs can be dominated by the younger stellar populations. With no easy way to distinguish between SFHs with different M_*/L ratios, noisy observations can easily be fit to models that underestimate the stellar mass, even if the correct SFH was present in the model grid. We do not correct our pixel-by-pixel masses for this dimpling effect, but estimating the missing mass by interpolating the surrounding pixels shows that any correction would be of order less than 1% of the total mass of the galaxy.

3.3 Results

3.3.1 Outshining at high redshift

To see if the results of Sorba & Sawicki (2015) extend to galaxies at higher redshift, we plot in Figure 3.4 the ratio of stellar mass estimates derived from unresolved photometry to those determined from pixel-by-pixel SED fitting as a function of specific star formation rate (sSFR) for galaxies with spectroscopic redshifts. The color of each data point is related to the galaxy's redshift (bluer colors for lower redshifts, redder for higher redshifts). If the

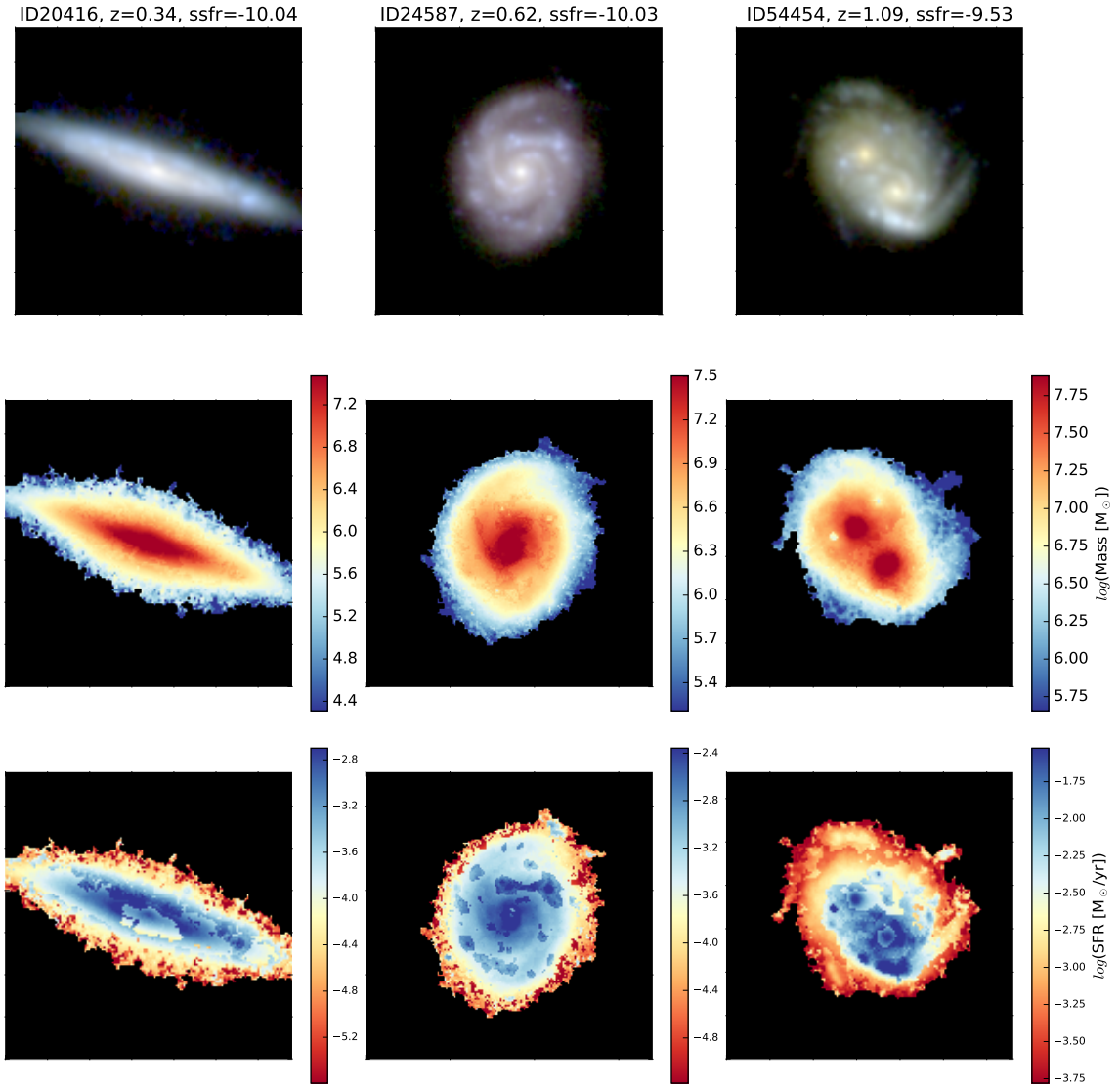

Figure 3.2: Same as Figure 3.1, except created using a coarse grid of τ-models. These show a slight improvement over the burst models.

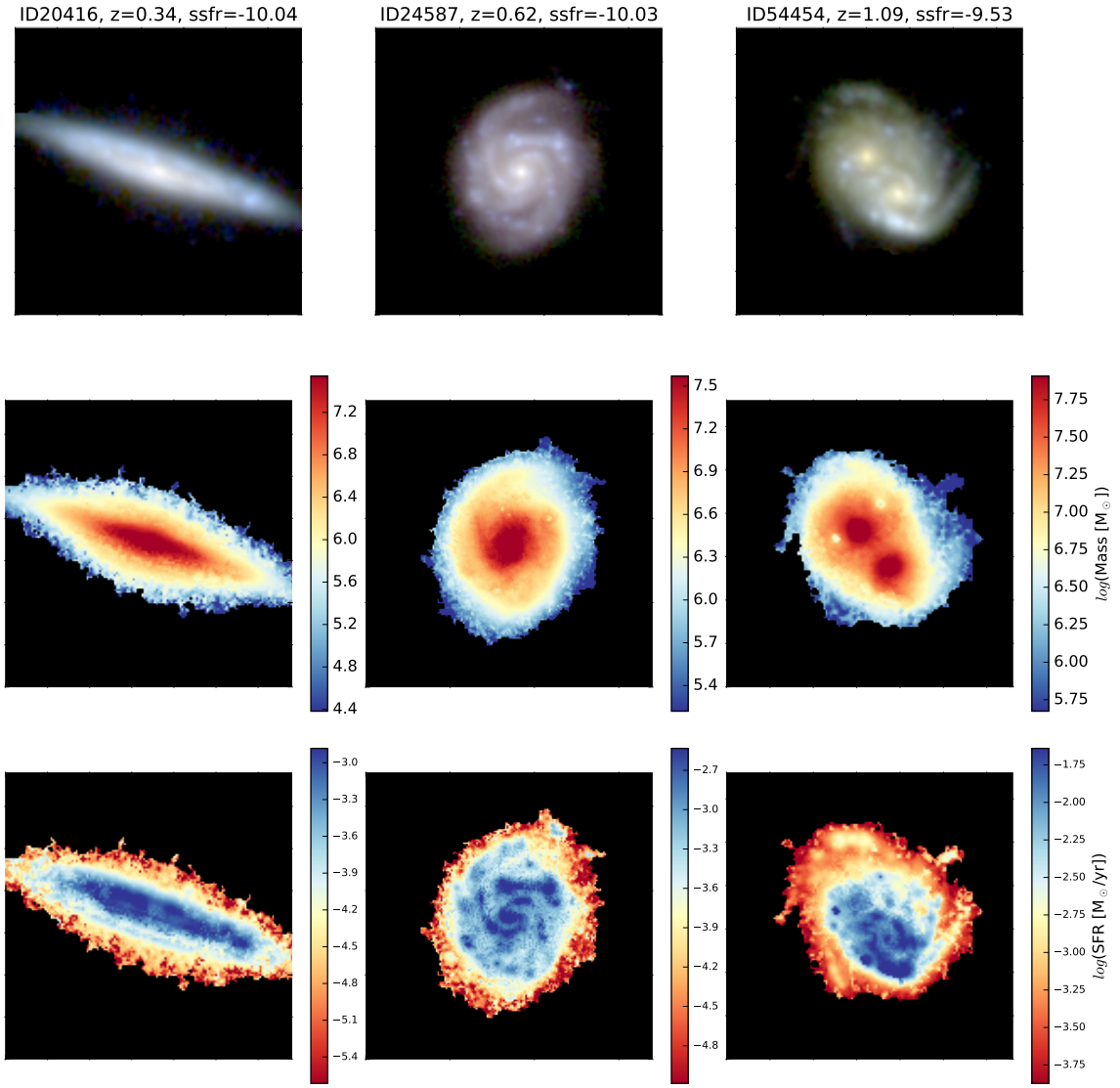

Figure 3.3: Same as Figure 3.1, except created using a fine grid of τ-models. These show a vast improvement over the burst models.

pixel-by-pixel and unresolved stellar mass estimates were the same, all points would lie along the one-to-one correspondence horizontal dashed black line. For the large majority of galaxies, the mass ratio is below one, meaning that unresolved photometry SED fitting tends to underestimate the true mass, if we assume the pixel-by-pixel mass is closer to the true mass. Looking at the colors of the points, there is no discernible difference in where a galaxy's mass ratio falls as a function of redshift, other than the fact that higher redshift galaxies tend to have higher sSFRs (Feulner et al., 2005). Note that this does not necessarily exclude differing behavior as a function of redshift, only that the large uncertainty in stellar masses (typical 1-σ and 2-σ confidence regions are shown by the dark and light green ellipses) obscures any relation if it were present. There is a slight correlation introduced by having the unresolved mass present in both axes, but the skew is small compared to the range of data covered, and this correlation could in now way completely explain the observable trends in the figure.

Significantly, there appear to be two regimes in Figure 3.4: a roughly linear decrease in the mass ratio at sSFRs less than -8.75, followed by a much sharper decrease beyond. A broken power law fit is shown by the magenta dashed line to demonstrate this dual nature. A false-color visual representation of these galaxies is shown in Figure 3.5. Sorba & Sawicki (2015) and Zibetti, Charlot & Rix (2009) found that the presence of dust lanes can drastically affect the mass estimates of galaxies compared to their pixel-by-pixel mass estimates, but no obvious dust lanes or other artifacts are present in the galaxies with the higher sSFRs where the mass discrepancy is the most egregious.

Figure 3.6 shows the same plot as Figure 3.4, but this time using the photometric redshift for galaxies with $z_{phot} < 2.5$ (a limit chosen for ease of comparison with other works; see Section 3.4.2). The same broken power law trend is visible with these galaxies as with the spectroscopic redshift galaxies. Again, no discernible difference in behavior with redshift is distinguishable, but this does not necessarily preclude an offset that steepens with redshift. We chose to focus our analysis on a redshift invariant offset that changes behaviour at a certain sSFR, but it is possible that future surveys with greater galaxy numbers could

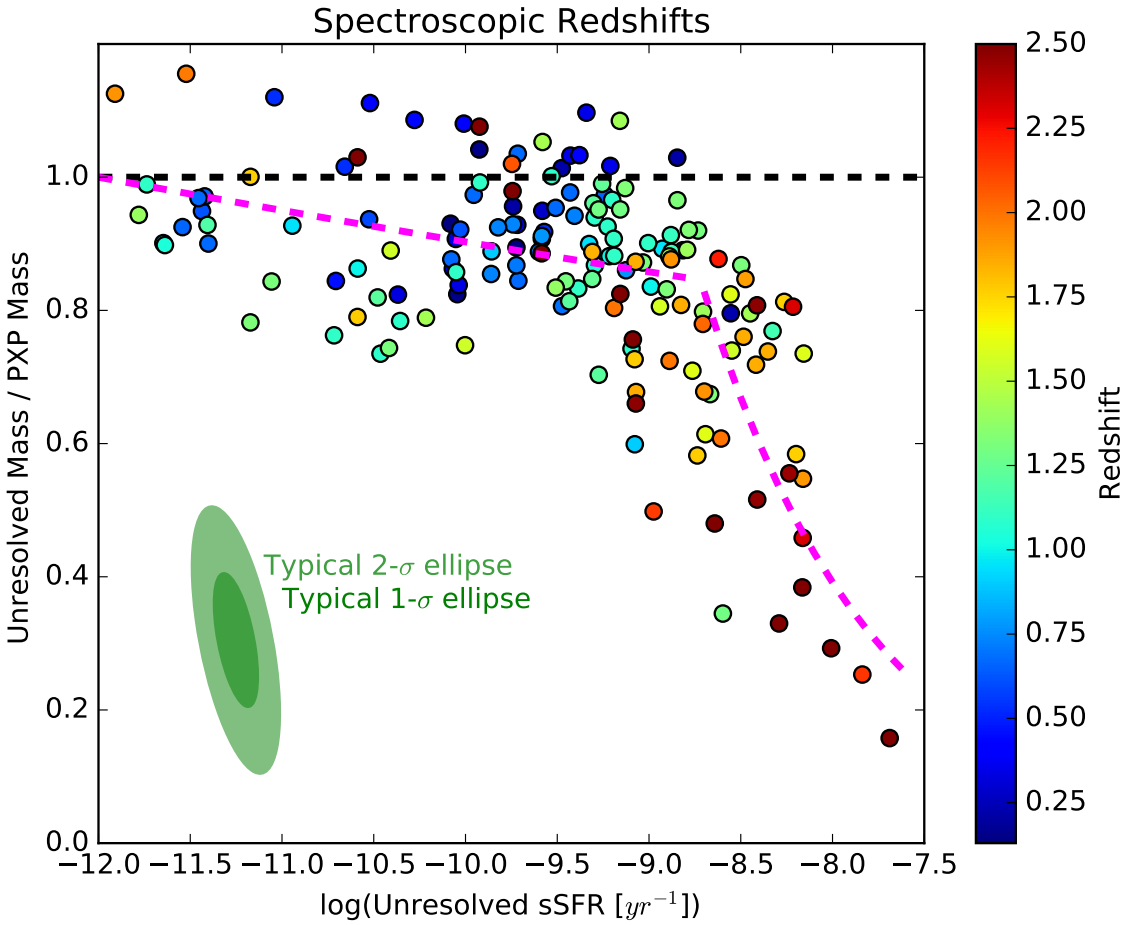

Figure 3.4: Ratio of the median unresolved mass estimate and the median pixel-by-pixel mass estimate as a function of specific star formation rate for galaxies in the XDF with spectroscopic redshifts. Points are colored based on their redshift. The horizontal black dashed line shows where the two mass estimates are equal. The magenta dashed line shows a broken power law fit to the data to demonstrate the two regime behavior.

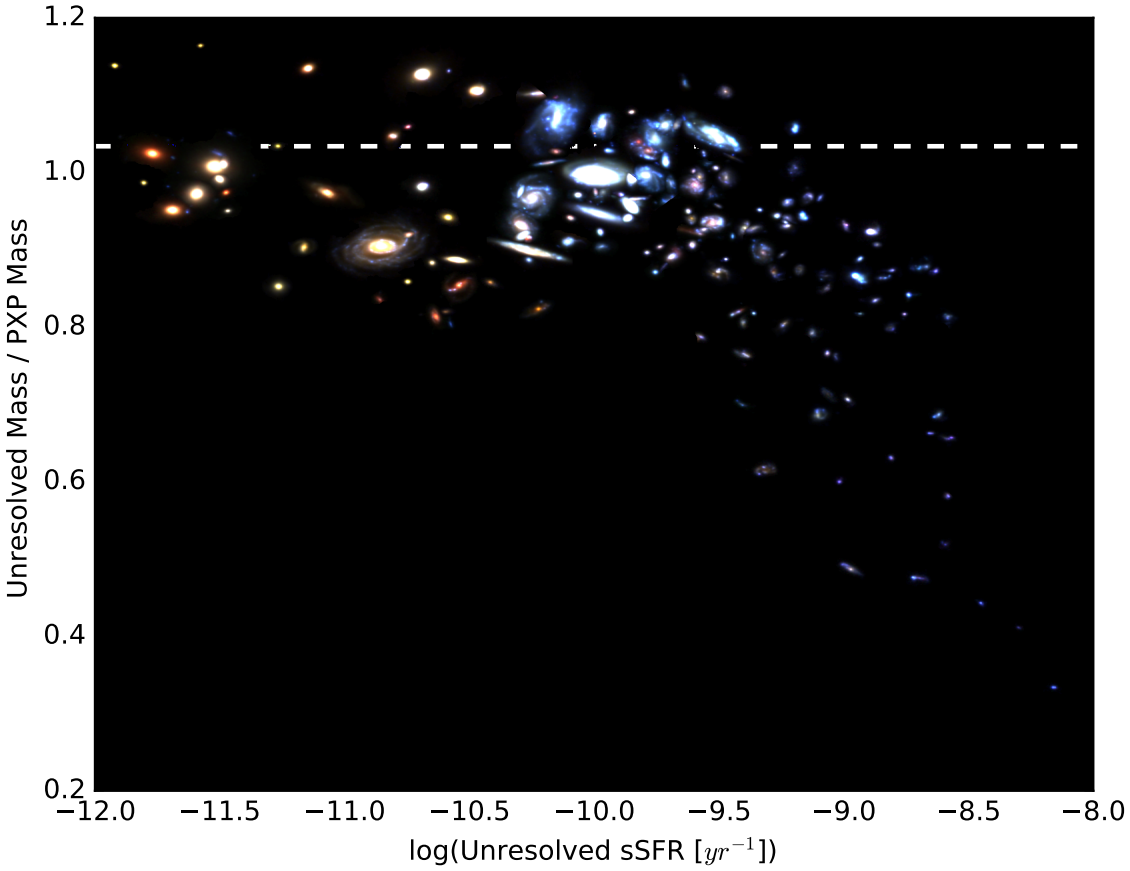

Figure 3.5: Ratio of the median unresolved mass estimate and the median pixel-by-pixel mass estimate as a function of specific star formation rate for galaxies in the XDF with spectroscopic redshifts. The false-color cutouts are made such that blue, green, and red correspond to roughly rest-frame u, g and r respectively. No dust lanes or other artifacts seem to be responsible for the large discrepancy at high sSFRs.

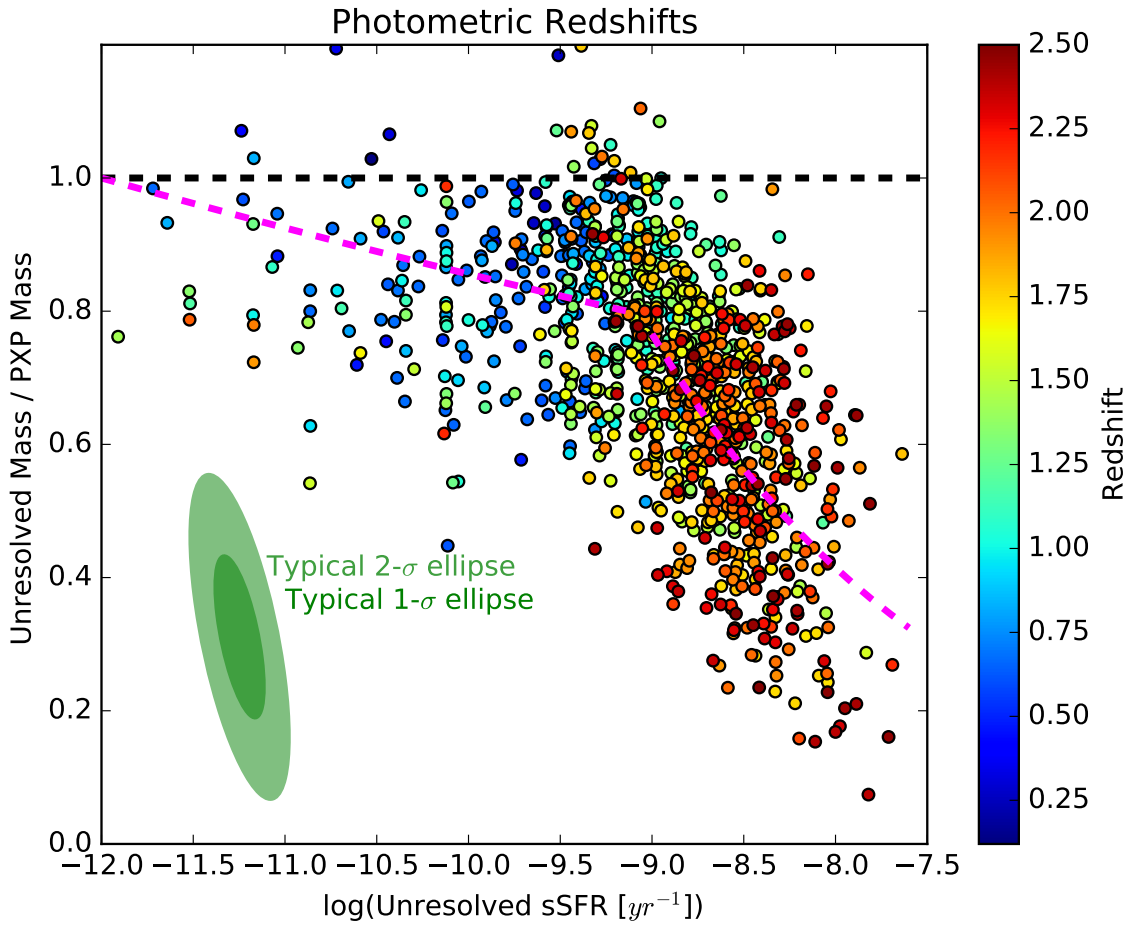

Figure 3.6: Same as Figure 3.4, except for galaxies with only photometric redshift measurements.

extract a redshift dependence.

Although the shallow linear decrease at low sSFRs is consistent with Sorba & Sawicki (2015), the sharper exponential decay at higher sSFRs is surprising, and perhaps alarming. Taken at face value, this would mean that a large number of stellar mass measurements would be underestimated by a factor of 2-3 or some as high as 5 (0.3-0.5 dex or 0.7 dex respectively). The abrupt change in the nature of the mass ratio/sSFR relation hints that there may be other factors involved.

3.3.2 Is the effect due to systematic error?

It is possible that the poorer signal-to-noise ratios for these galaxies is biasing the SED fits, an effect described by Gallazzi & Bell (2009). Indeed if we restrict our examination to only galaxies that have an unresolved median stellar mass estimate greater than 10^{10} $M_{\odot}$ then the second steeper power law is not visible, but only because these galaxies all have sSFRs lower than the best fitting break sSFR of approximately -9 dex. To see how our mass estimates could be biased by the relatively low signal-to-noise ratios of pixels, we first found how the noise in each bandpass grows, finding the i^{th} percentiles of the photometric magnitude error of every pixel in galaxies split into 8 redshift bins. This yielded the typical magnitude uncertainty (denoted as $\Delta m(B, i, z)$), which is inversely proportional to the signal-to-noise and is a function of bandpass(B), redshift, and "noisiness" (i), where i ranges from 10 to 99 in steps of 10 with the 99^{th} percentile being the noisiest pixels. We next took the unresolved photometric catalogs and refit them to our model SED grid ten different times, each time replacing the photometric uncertainties with successively noisier and noisier Δm. Figure 3.7 compares the masses of these noisy fits compared to the mass of the most accurate unresolved mass.

The increase in mass estimate with increasing noise shows that our model SED set does introduce a prior bias, increasing mass by a maximum of approximately 2.5% for the 70^{th} noisiest percentile pixels at the higher redshifts. Interestingly, the mass bias begins to decrease as the pixels become even noisier than that. There is a dichotomy between pixels with redshifts above approximately 1.5; although the curves all have a similar qualitative rise and fall, the higher redshift bias increases more steeply. Now, this is a fractional bias, and the noisiest pixels will also in general be the least massive, and thus contribute less to the total mass bias of the galaxy. For each galaxy, we calculate a predicted fractional mass bias (F) by

$$F = \frac{\sum_x M_x^* B_{p(x),z} - \sum_x M_x^*}{\sum_x M_x^*} \tag{3.1}$$

where M_x^* is the median stellar mass in the x^{th} pixel and $B_{p(x),z}$ is the bias interpolated

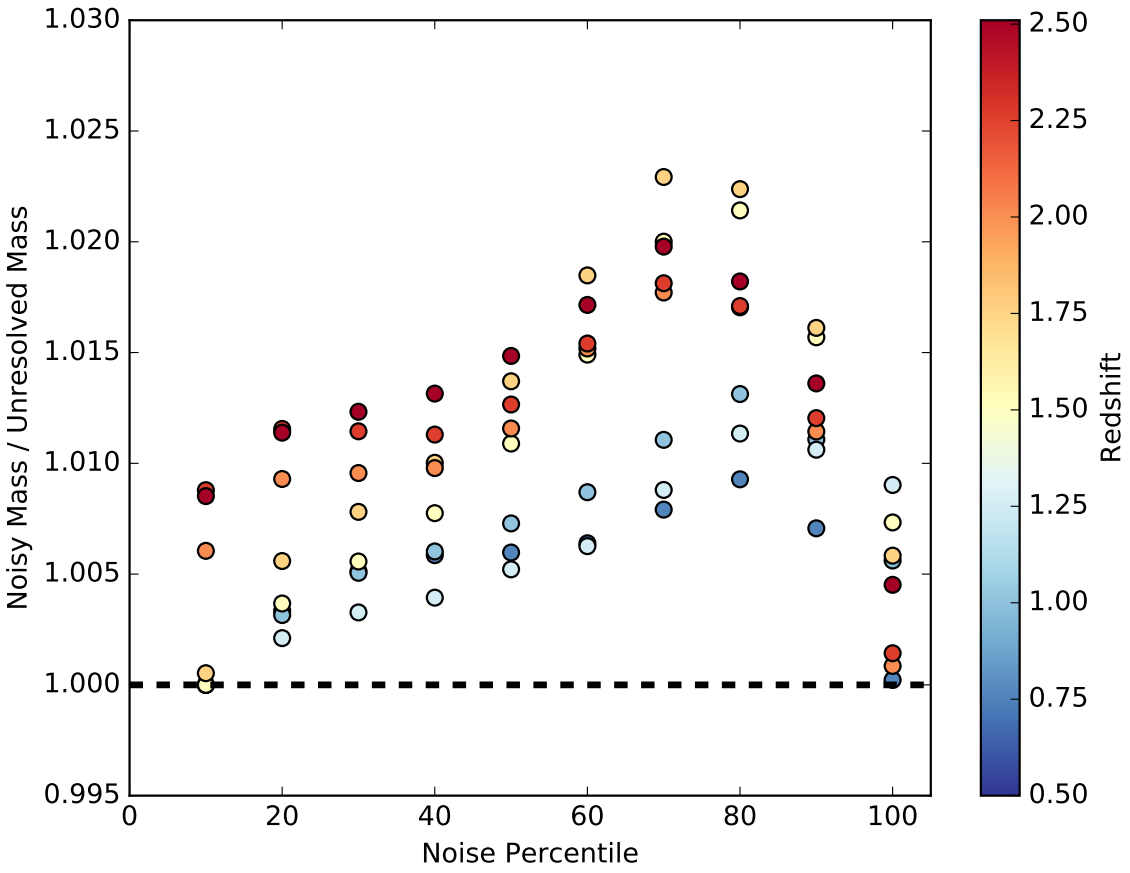

Figure 3.7: Ratio of mass estimates from unresolved photometry with artificially increased photometric uncertainties to those with the lowest possible uncertainties. The noise is increased by taking the i^{th} percentile of the photometric uncertainties of every pixel in every galaxies in eight redshift bins from 0.5 to 2.5.

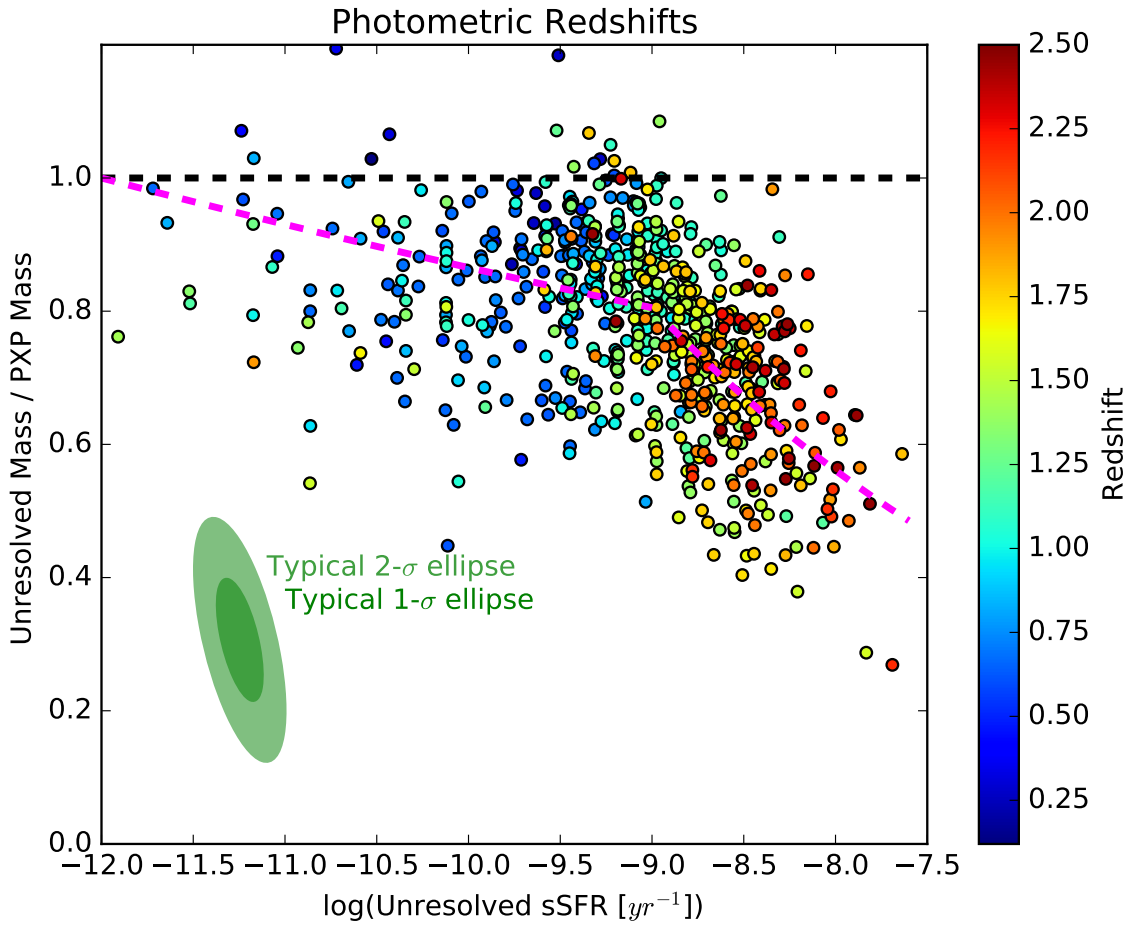

Figure 3.8: Same as Figure 3.6, except removing galaxies whose masses could be unduly biased by noisy pixels. The overall kink at high specific star formation rates in unchanged, which is unsurprising since our maximum estimated bias was only 2.2%, much lower than could account for large relative mass differences at high sSFRs.

from Figure 3.7 where $p(x)$ is the average photometric error percentile in that pixel and z is the galaxy's redshift. The maximum mass bias from low S/N pixels was 2.2% of the mass of the galaxy, which is not significant compared to the factor of two (or more) discrepancy. For demonstration purposes, we removed from our sample any galaxies with predicted fractional mass biases greater than 1%. Doing so left us with 684 galaxies shown in Figure 3.8, and shifted the median number of pixels in these galaxies to 242 pixels. The double power law is still present, and the feature remains even with more stringent cuts of F ¡ 0.005.

The sharp downturn happens almost exclusively for high redshift ($z > 1.5$) galaxies,

where our reddest bandpass ($F160W$) is only probing rest-frame visual regions of the galaxies' spectra. A large number of works (Maraston et al., 2006; Kannappan & Gawiser, 2007; Bolzonella et al., 2010; Lee et al., 2009; Ilbert et al., 2010; Pforr, Maraston & Tonini, 2012) found that coverage in the rest-frame NIR was crucial to stellar mass estimates from SED fitting, with Pforr, Maraston & Tonini (2012) stating that excluding NIR bandpasses can lead to masses that are underestimated by up to 2 dex. However, Shapley et al. (2005), van der Wel et al. (2006), and Muzzin et al. (2009) did not find as strong a need for NIR coverage. Moreover, our pixel-by-pixel versus unresolved comparison should have both the pixel-by-pixel and unresolved masses affected in a similar manner by the lack of NIR data. It should be emphasized that our method examines relative mass differences, and is unconcerned with evaluating the true total stellar mass in each galaxy.

To see if our lack of redder bandpasses for high redshift galaxies could be affecting our mass estimates, we make use of the photometric catalogs provided by Lundgren et al. (2014), who included Spitzer/IRAC photometry. We cross-correlated that catalog with that of Rafelski et al. (2015) based on a search in RA and DEC utilizing a maximum matching distance of 3 arcseconds (approximately five pixels in the XDF images), matching only galaxies that had IRAC 3.6 and 4.5 measurements and with a photometric redshift between 1.5 and 2.5. To ensure that the objects in each catalog were in fact representing the same galaxy, we compared the $F606W$ flux in each catalog and removed any objects where this did not match to within the 1-sigma uncertainties, leaving 71 galaxies. We performed (unresolved) SED fitting on these galaxies once using only photometry from the Rafelski et al. (2015) catalog in the nine XDF bandpasses, and a second time also including the two IRAC bandpasses from Lundgren et al. (2014). As shown in Figure 3.9, we found no consistent bias in the median Monte Carlo mass estimates of these $z \sim 2$ galaxies when either including or excluding the two IRAC bandpasses. The median mass ratio ($M^*_{noIRAC}/M^*_{withIRAC}$) of the 71 galaxies was 0.89 with upper and lower inner quartile bounds at 1.24 and 0.68 respectively. Examining solely galaxies with $1.9 < z < 2.2$, the median mass ratio does drop to 0.68, leading one to think the effect may become more

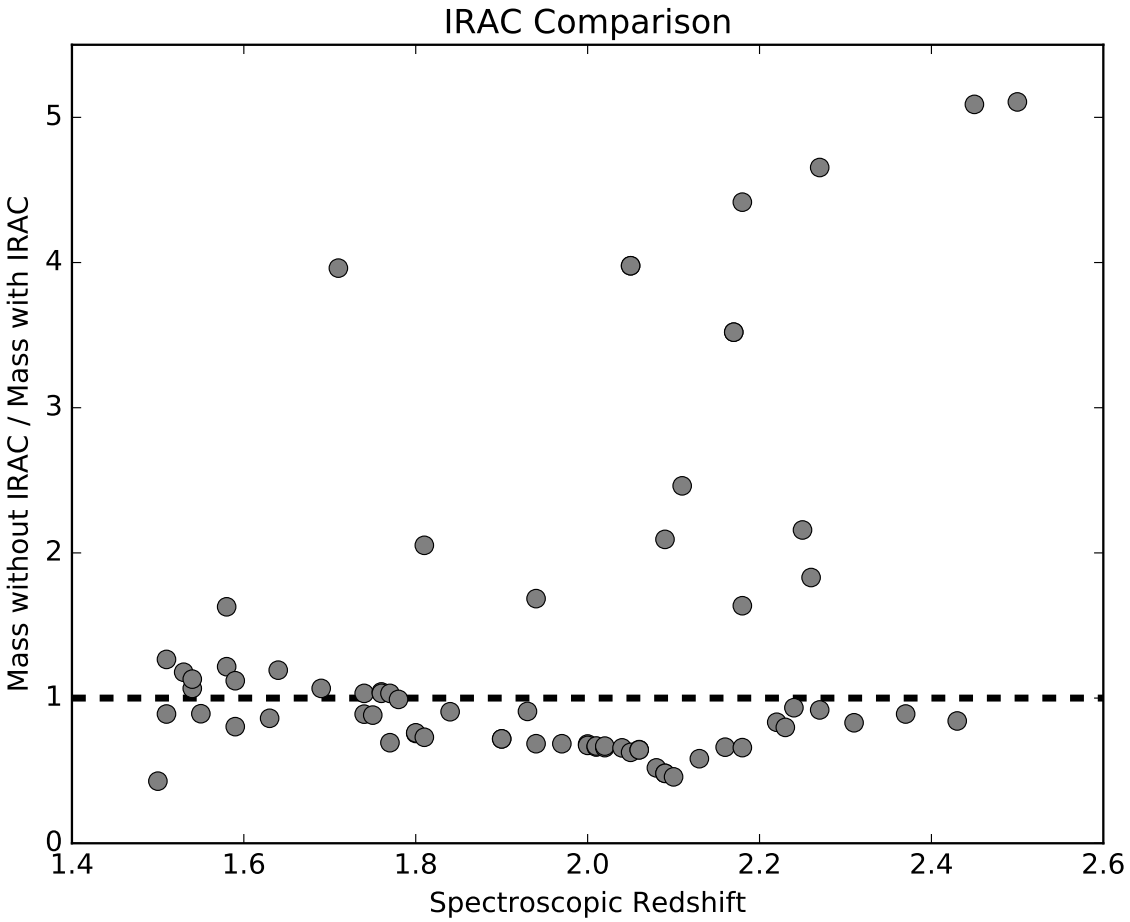

Figure 3.9: Comparison of mass estimates using photometry from Rafelski et al. (2015) and either including or excluding IRAC photometry from Lundgren et al. (2014).

dramatic as redshift increases, but then the median mass ratio rises up to 0.93 again for galaxies with $z > 2.2$, suggesting that the previous dip was likely noise. Although the masses were, in general, slightly smaller without IRAC photometry, the discrepancy was nowhere near as drastic as that found in the pixel-by-pixel analysis. There were also no discernible trends with either sSFR or redshift. It is further questionable whether any differences in the mass estimates are due to the presence of IRAC photometry, or due simply to systematic differences between the two catalogs used here.

To more deeply probe the effects of including rest-frame NIR photometry on our mass estimates, we refit galaxies with spectroscopic redshifts less than 1.2, only this time ex-

cluding the four WFC3 bandpasses. This removes their rest-frame NIR bands, allowing us to test whether NIR data is important. The results are shown in Figure 3.10. Similarly to the mass estimates with and without IRAC photometry, the mass estimates of these lower redshift galaxies show no obvious systematic bias when the WFC3 photometry is included/excluded. Again no obvious trend with redshift is present. The median mass ratio when comparing the mass estimates without the four WFC3 bandpasses versus those with is 1.11, with a lower-quartile value of 0.89 and an upper-quartile value of 1.35. Interestingly, this slight offset is in the opposite direction of that found with the IRAC bandpasses. Here, mass estimates including rest-frame NIR photometry are typically lighter than when NIR photometry is excluded. In either case, even if rest-frame NIR photometry does have an effect on the absolute mass estimate, the relative mass ratio from comparing pixel-by-pixel to integrated mass estimates for any one galaxy should not be altered, since both mass estimates are made using the same set of bandpasses. Despite the apparent lack of influence from including rest-frame NIR observations, the large body of work stating their significance puts into question our mass estimates for higher redshift galaxies. We therefore divide our analysis into two parts. In the next section (3.3.3), we restrict our analysis to galaxies with redshifts less than 1.2, meaning all galaxies have photometric observations up to at least rest-frame I band, and compare to previous results from Sorba & Sawicki (2015). In Section 3.3.4, we examine the increasing discrepancy for galaxies up to $z = 2.5$, and discuss the implications if the effect is real.

3.3.3 Outshining up to redshift 1.2

Figure 3.11 shows the XDF $z_{spec} \leq 1.2$ and $z_{phot} \leq 1.2$ samples as yellow and blue circles respectively, and the SDSS galaxies from Sorba & Sawicki (2015) as gray squares. We have removed any galaxies that could have their mass estimates biased by more than 1% due to low signal-to-noise pixels. The lines show linear fits to the different samples using the method of ordinary least-squares. The best-fit parameters can be found in Table 3.1, and uncertainties were found by refitting lines for each of our Monte Carlo instances and taking

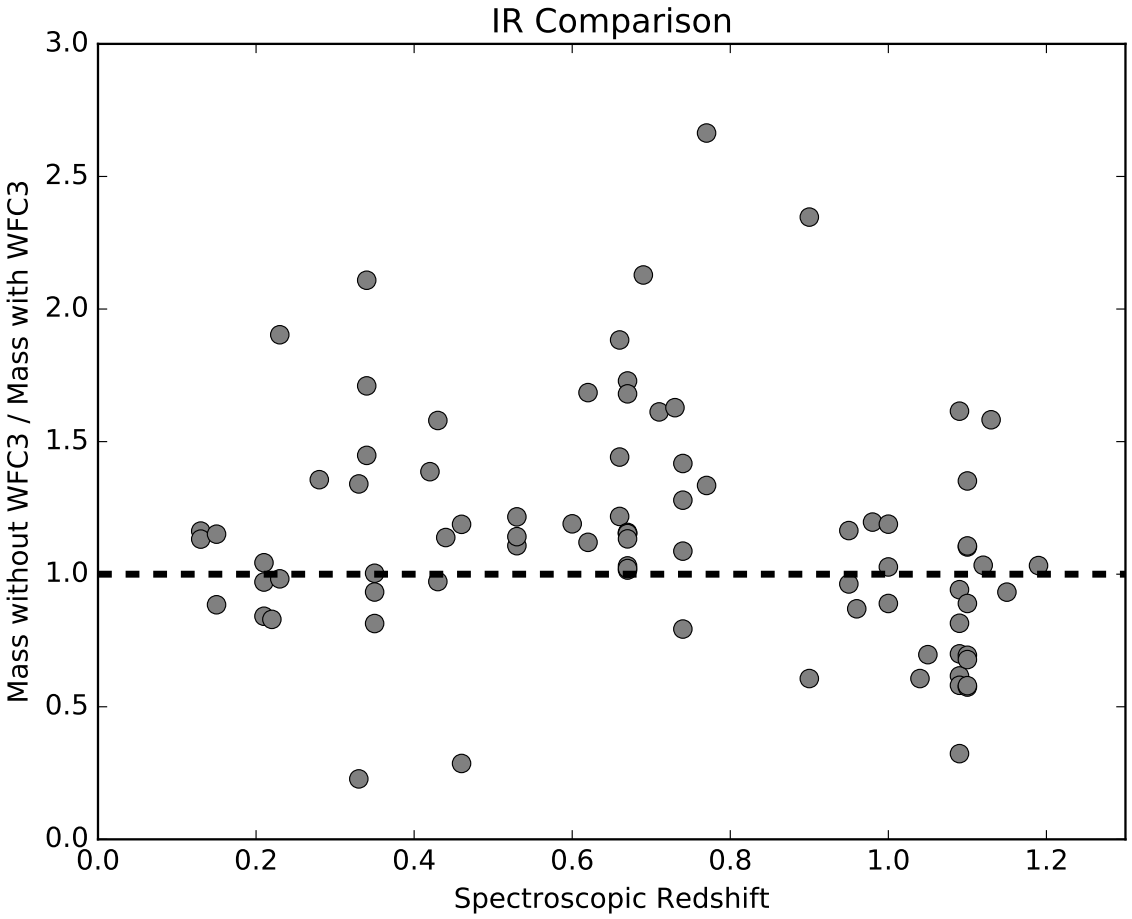

Figure 3.10: Comparison of mass estimates for $z_{spec} < 1.2$ galaxies made both including WFC3 photometry and excluding it.

the 16th and 84th percentile values. The slopes and intercepts of all three datasets agree to within uncertainty. The fact that the $z \sim 0$ sample falls so well along the same relation as the XDF samples despite differences in photometry and modeling strongly implies that any effects of outshining do not change significantly up to $z \sim 1$. However, there may be a slight steepening of the slope as redshift decreases from approximately one to the present day, accompanied by a subsequent rise in the intercept. The best-fit slope of the XDF spec-z and photo-z samples together gives a slope of -0.029 which is shallower than the best-fit SDSS slope of -0.057, and the slope fit to just the spectroscopic XDF sample is shallower still at -0.017. There is a great deal of scatter in the data about the linear trend. Partly, this is due to the effect of dust lanes on pixel-by-pixel fitting (Zibetti, Charlot & Rix, 2009; Sorba & Sawicki, 2015), and partly due to the inherent noise in stellar mass estimates. Additionally, the linear fits to the XDF data may be affected by the artificial cut-off at $z = 1.2$, as well as the relative lack of low sSFR galaxies at higher redshifts. Combining the XDF and Sorba & Sawicki (2015) galaxies, we fit an updated linear trend shown as the solid red line in Figure 3.11. This represents our new best estimate at a correction factor for outshining:

$$M^*_{resolved} = \frac{M^*_{unresolved}}{-0.040 \log(sSFR) + 0.50} \tag{3.2}$$

where the M^* are given in $M_\odot$ and sSFR is in units of yr^{-1}.

We also show the same plot in Figure 3.12, but this time including those galaxies which may be slightly biased by low S/N pixels. This results in a best fit line with essentially the same slope as that in Figure 3.11, but with a slightly lower y-intercept.

3.3.4 Outshining up to redshift 2.5

For galaxies at higher redshifts (and thus generally higher sSFRs), the unresolved versus pixel-by-pixel mass ratio decreases sharply at sSFRs greater than roughly 10^{-9} yr^{-1}. In Figure 3.13, we show a piecewise fit to this behavior for galaxies at both low and high

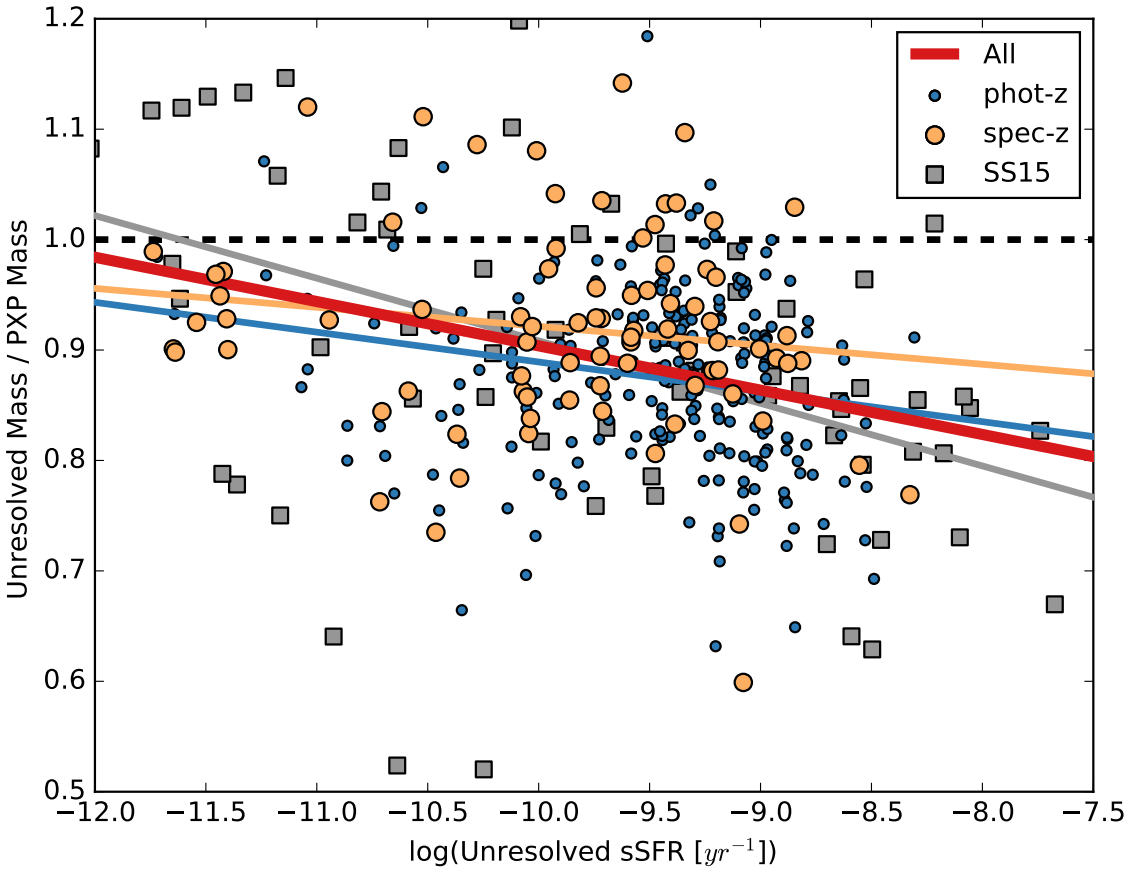

Figure 3.11: Linear fits to the resolved pixel-by-pixel mass ratio as a function of sSFR. Yellow (blue) points represent XDF galaxies with spectroscopic (photometric) redshifts less than 1.2. The grey squares are $z \sim 0$ SDSS galaxies from Sorba & Sawicki (2015). The colored dashed lines show linear fits to their corresponding dataset. The thick red line shows a linear fit to the combined yellow points and grey squares. It represents our new best relation for correcting outshining for galaxies in the range $0 < z < 1.2$.

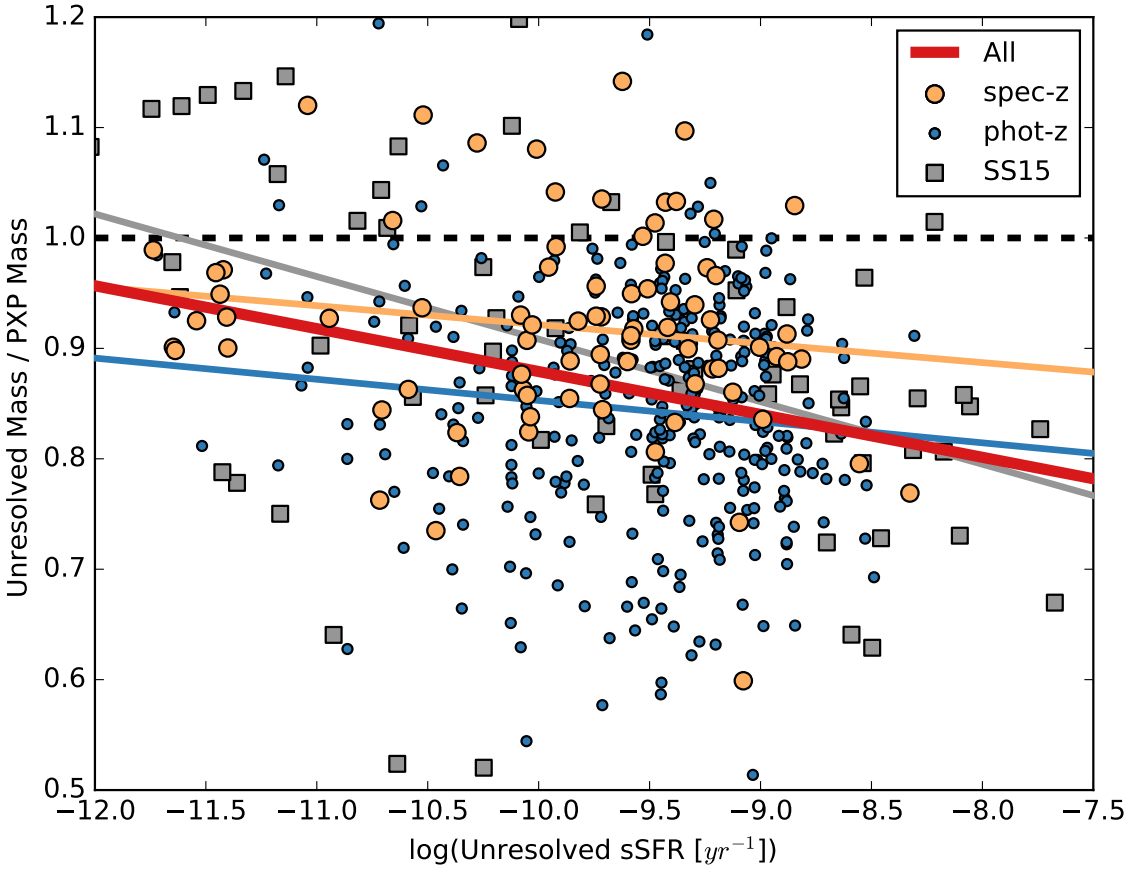

Figure 3.12: Same as Figure 3.11, but including galaxies with pixel-by-pixel masses that may be slightly biased from low S/N pixels.

Table 3.1: Best fit parameters of linear fits $y = mx + b$. All galaxies have $0 < z \leq 1.2$. Here, z_s and z_p respectively refer to spectroscopic and photometric redshift samples.

Data Set	m	b
SS15	$-0.057^{+0.022}_{-0.019}$	$0.34^{+0.20}_{-0.18}$
XDF z_s	$-0.017^{+0.008}_{-0.021}$	$0.75^{+0.07}_{-0.22}$
excluding galaxies with low S/N pix		
XDF z_p	$-0.027^{+0.006}_{-0.014}$	$0.62^{+0.06}_{-0.13}$
XDF $(z_s + z_p)$	$-0.029^{+0.009}_{-0.007}$	$0.61^{+0.08}_{-0.06}$
XDF $(z_s + z_p)$ + SS15	$-0.040^{+0.011}_{-0.008}$	$0.50^{+0.10}_{-0.08}$
including galaxies with low S/N pix		
XDF z_p	$-0.019^{+0.005}_{-0.012}$	$0.66^{+0.05}_{-0.11}$
XDF $(z_s + z_p)$	$-0.027^{+0.007}_{-0.007}$	$0.60^{+0.07}_{-0.06}$
XDF $(z_s + z_p)$ + SS15	$-0.039^{+0.010}_{-0.008}$	$0.48^{+0.10}_{-0.07}$

redshifts in our sample, removing any galaxies that might have their pixel-by-pixel masses biased by low S/N pixels (as discussed in the previous section). The piecewise function is described in log-log space as

$$f(x) = \begin{cases} m(x+12)+b & : x \leq p \\ k_2x^2 + k_1x + k_0 & : x > p, \end{cases} \tag{3.3}$$

which is a linear relation to the left of the break point p, and a parabola to the right. The free parameters are p, m, b, and k_2. To ensure continuity and differentiability at p, k_0 and k_1 are constrained to be

$$k_1 = -2k_2p + m \tag{3.4}$$

$$k_0 = b + 12m + (m - k_1)p - k_2p^2. \tag{3.5}$$

Because of the nature of a piecewise function that can have a shallow slope abruptly changing to a extremely steep slope, we use orthogonal distance regression (ODR) to find the best fitting parameters, listed in Table 3.2. ODR minimizes the orthogonal distance from the fitted line to each point (i.e. the line going through the point that intersects the fitted line at a right angle), rather than minimizing the vertical distance from each point to the fitted line as is done in ordinary least squares minimization. In this manner, galaxies which are close to the break point p are matched to the part of the piecewise function they are nearest to, rather than whichever part they happen to be above or below. Uncertainties were again found by performing the same fitting procedure on each of the Monte Carlo instances and taking the 16th and 84th percentiles for each parameter.

We also show a similar plot in Figure 3.14, but this time including the galaxies with low S/N pixels. The inclusion of the noisier galaxies shifts the break point, p, to the left (from -8.62 to -9.05) and yields a shallower linear slope, m, that is more in line with that found when examining solely the spectroscopic redshift galaxies and with Sorba & Sawicki (2015). However, all parameters agree to within uncertainty. Because of this, and taking

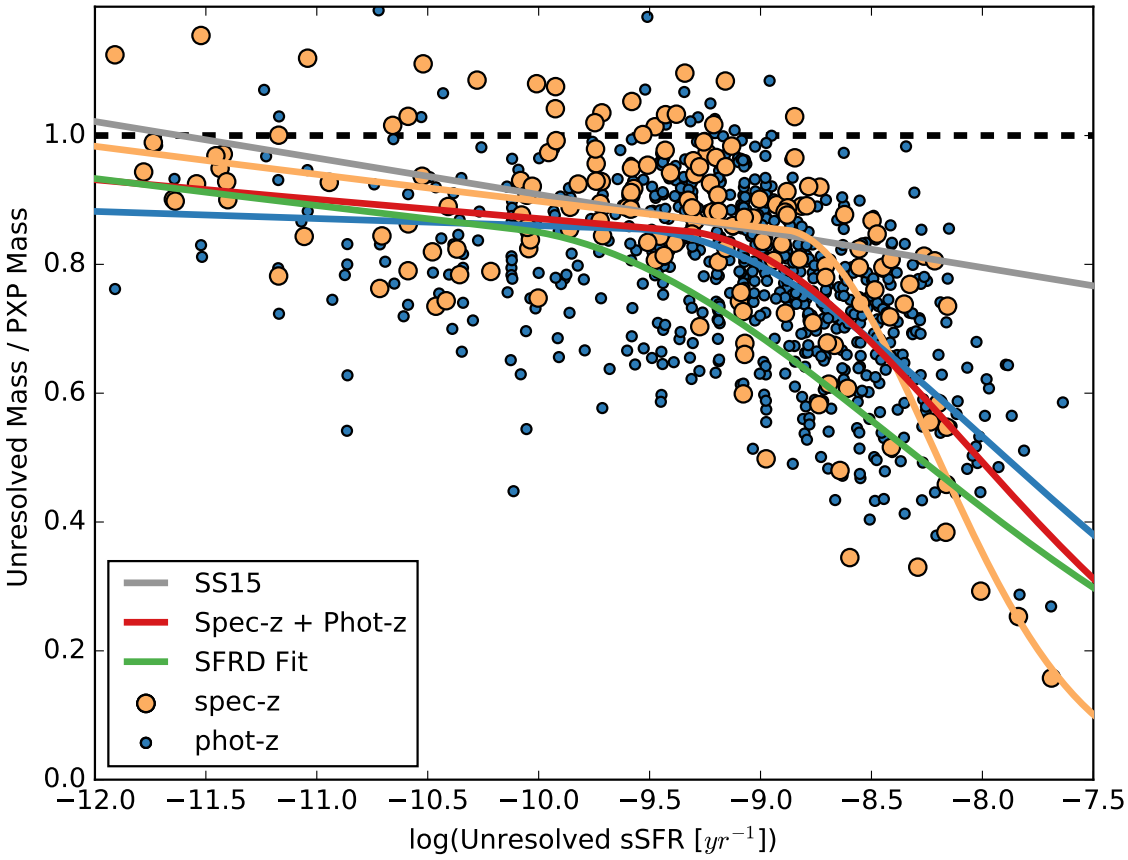

Figure 3.13: Same as Figure 3.11, but including galaxies up to redshift 2.5. Piecewise linear-parabolic fits in log-log space are shown in yellow (fit to the spectroscopic redshift sample) and red (fit to both the spectroscopic and photometric redshift samples). The linear relation from Sorba & Sawicki (2015) is shown for comparison, and is not included in any of the piecewise fits. The green line shows the correction that best matches the observed SFRD history from Madau & Dickinson (2014) (see Section 3.4.1). Galaxies with low S/N pixels that could affect the pixel-by-pixel mass estimate above the 1% level are not shown.

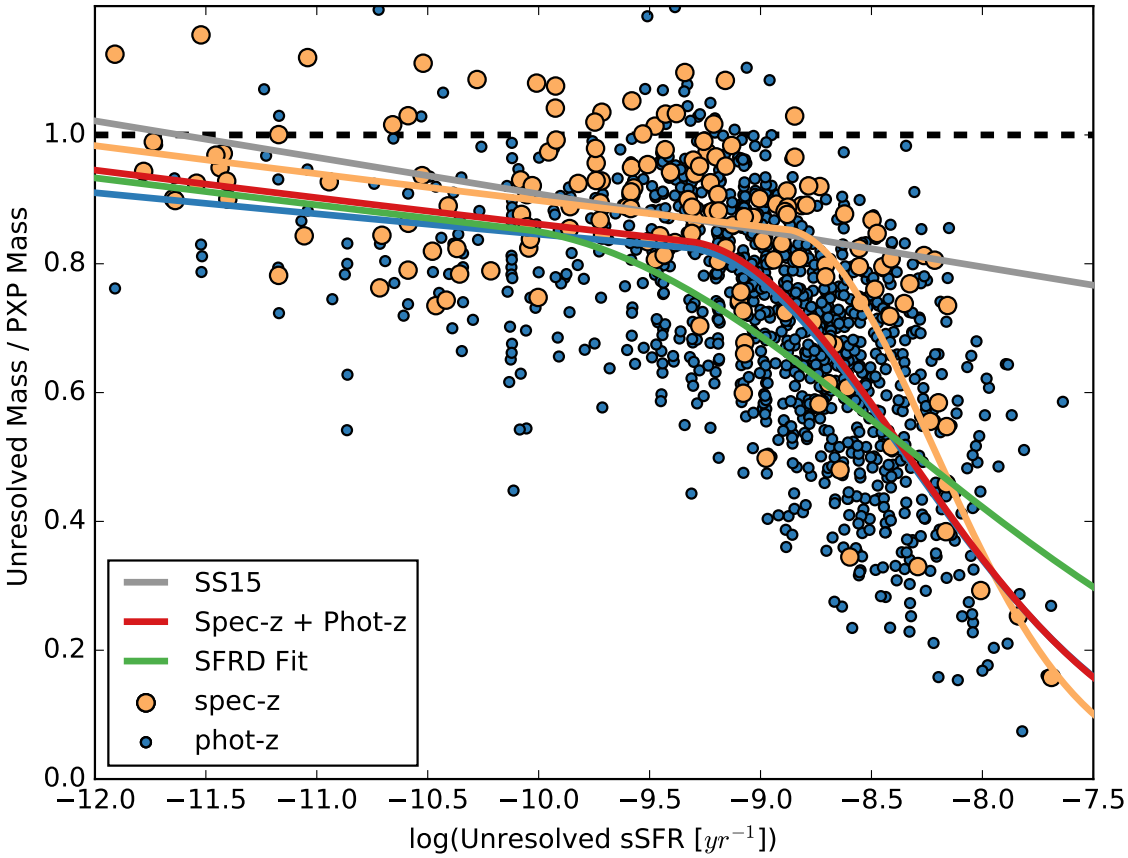

Figure 3.14: Same as Figure 3.13, but including all galaxies.

into account the low maximum bias from noisy pixels (2.2%) as well as the fact that the photometric redshift galaxies do not deviate from the spectroscopic redshift sample (which did not have any significant bias due to noisy pixels), we chose to use this best-fit relation for all further analysis in this section.

3.3.5 Resolved versus Unresolved SFRs

In Figure 3.15, we also compare unresolved versus pixel-by-pixel SFR estimates with the caveat that SFR estimates from SED fitting are highly dependent on the choice of SFH, and that there are more degeneracies between the SFR estimate and other model parameters

Table 3.2: Best fit parameters of piecewise fits. Here, z_s and z_p respectively represent the spectroscopic and photometric XDF samples.

Data Set	p	m	b	k_2
XDF z_s	$-8.88^{+0.04}_{-0.18}$	$-0.020^{+0.010}_{-0.004}$	$-0.007^{+0.010}_{-0.018}$	$-0.47^{+0.14}_{-0.05}$
excluding galaxies w. low S/N pix				
XDF z_p	$-9.59^{+0.74}_{-0.53}$	$-0.006^{+0.004}_{-0.018}$	$-0.054^{+0.057}_{-0.029}$	$-0.08^{+0.05}_{-0.44}$
XDF $(z_s + z_p)$	$-9.35^{+0.51}_{-0.29}$	$-0.015^{+0.005}_{-0.009}$	$-0.031^{+0.033}_{-0.006}$	$-0.12^{+0.05}_{-0.40}$
including galaxies w. low S/N pix				
XDF z_p	$-9.34^{+0.49}_{-0.28}$	$-0.016^{+0.006}_{-0.008}$	$-0.041^{+0.043}_{-0.016}$	$-0.20^{+0.12}_{-0.31}$
XDF $(z_s + z_p)$	$-9.32^{+0.47}_{-0.26}$	$-0.020^{+0.011}_{-0.004}$	$-0.024^{+0.027}_{-0.001}$	$-0.21^{+0.12}_{-0.31}$

than there are with mass estimates (which are generally more robust). As such, one should not use the following analysis to correct SFRs to be inline with what one would get from a pixel-by-pixel analysis. We wish only to demonstrate in general how SFR estimates change when going from unresolved to resolved SED fits. The first thing to notice when looking at Figure 3.15 is the opposite nature from the mass comparison. Here, unresolved SED fits under-estimate the SFR at low sSFRs compared to the pixel-by-pixel estimates, and the ratio curves upward toward unity (and beyond) as sSFR increases. Above sSFRs of $10^{-9.5}$ yr, the two different SFR estimates are within a factor of two of each other, a difference which could be accounted for given the effects of resolved dust and the vastly more complicated SFH of pixel-by-pixel photometry compared to a simple τ-model (see Section 3.4.3).The great deal of scatter in this regime makes extrapolations to higher sSFRs suspect (for example, when looking at the spectroscopic redshift sample above sSFRs of $10^{-9.5}$ yr, the points could easily be a scatter around unity rather than an increasing trend). However, it is interesting to examine why pixel-by-pixel SED fitting would consistently measure SFRs for quiescent galaxies (here defined arbitrarily as galaxies with sSFR $< 10^{10.5}$ yr) that are 2-4 times larger than unresolved fits. In Figure 3.16 we show false-color images and mass and SFR maps of three example galaxies with low sSFRs. One can easily see small pockets of star-formation, possibly from satellite galaxies. These pockets of star-formation have negligible mass (and total flux), but easily account for as much star-formation as the rest of the galaxy. Clearly what is happening is almost an inverse-outshining, where the extremely

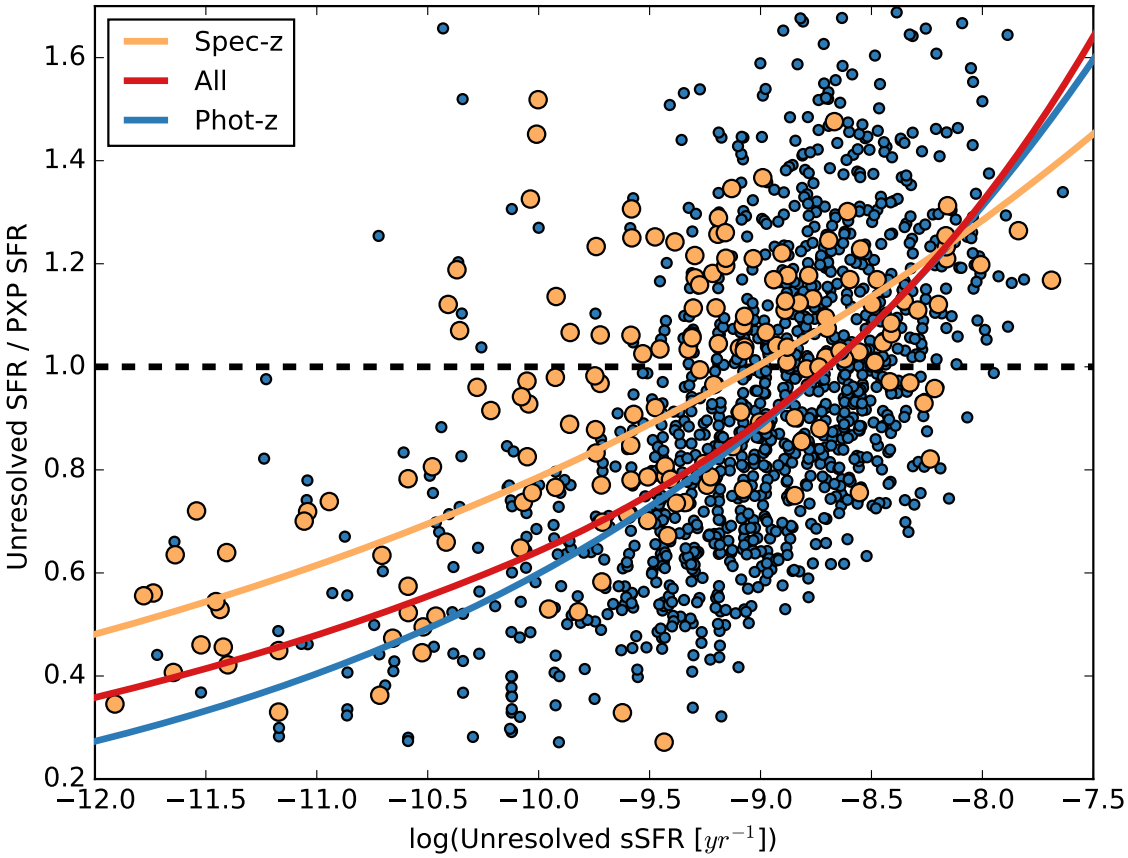

Figure 3.15: Ratio of unresolved to pixel-by-pixel SFR estimates. Colors are as in Figure 3.13.

massive quiescent core dominates the small satellite galaxies masking the star-formation. Unresolved SED fitting misses the small pockets of star-formation, but a pixel-by-pixel analysis uncovers them.

3.4 Discussion

3.4.1 Implications

The increasing disparity between unresolved and pixel-by-pixel mass estimates, if real, has implications for several previously published results derived using masses from SED template fitting. Perhaps most obviously, the relationship between a galaxy's mass and SFR

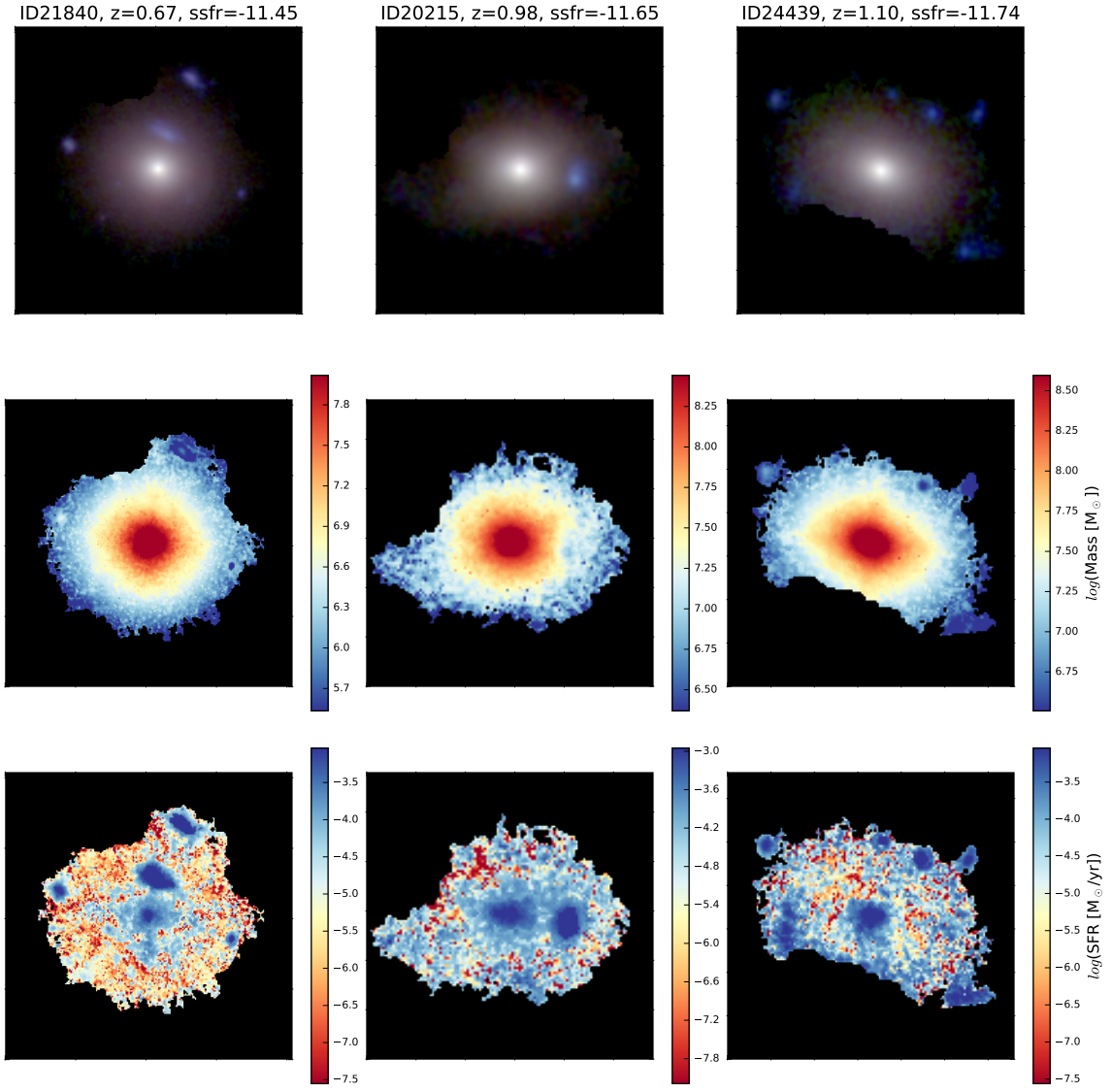

Figure 3.16: Two-dimensional maps of three XDF galaxies with low sSFRs. From top to bottom we show false-color images in approximately rest-frame *ugr* scaled on a log scale, followed by stellar mass and SFR maps.

(when it is actively star-forming), known as the star-forming main sequence, is directly affected. In Figure 3.17 we show how correcting the galaxies' masses for outshining would change two recent parameterizations of the star-forming main sequence from Whitaker et al. (2014) and Johnston et al. (2015) at three different redshifts. The sharp decline at higher sSFRs leads to certain areas of the mass-SFR plane changing more drastically than others. For the Johnston et al. (2015) parameterization, the lowest redshift main sequence is barely affected at all, but there is a much larger correction for the higher redshift galaxies because of their increased SFR. The larger correction at higher sSFRs leads to a main sequence which is no longer linear. Non-linear main sequences were also proposed by Whitaker et al. (2014), who fit broken power laws to star-forming galaxies in different redshift ranges. The corrections due to outshining are less dramatic for this parameterization because the kink in the main sequence brings it down out of the highest sSFR region of the mass-SFR plane. Once again, the lowest redshift relation is barely affected, but the $z = 2.25$ has a higher offset.

Additionally, the intrinsic scatter of the star-forming main sequence is linked to smoothness (or, conversely, burstiness) of the SFH of the universe (Kurczynski et al., 2016; Abramson et al., 2014). The small observed scatter around the SFR-M_* correlation implies a steady, gradual assembly of stellar material rather than a history dominated by bursts. Because the bias in mass estimation found here is linked to a galaxy's sSFR, it causes a shear in the intrinsic scatter. Galaxies located in higher sSFR regions of the SFR-M_* plane are affected more so than others. In Figure 3.18, we demonstrate this effect, and show that the shearing leads to a smaller intrinsic scatter. The blue points in the top row of Figure 3.18 are randomly generated using the intrinsic scatter and star-forming main-sequence parameters of Kurczynski et al. (2016) at various redshift ranges corrected for a Chabrier IMF rather than a Salpeter. The red points in the top row show where these galaxies would lie once their mass has been corrected for the effects of outshining based on this work. The shearing and subsequent tightening of the correlation can be seen. The bottom row displays what happens to the intrinsic scatter after the mass correction. In all cases the intrinsic

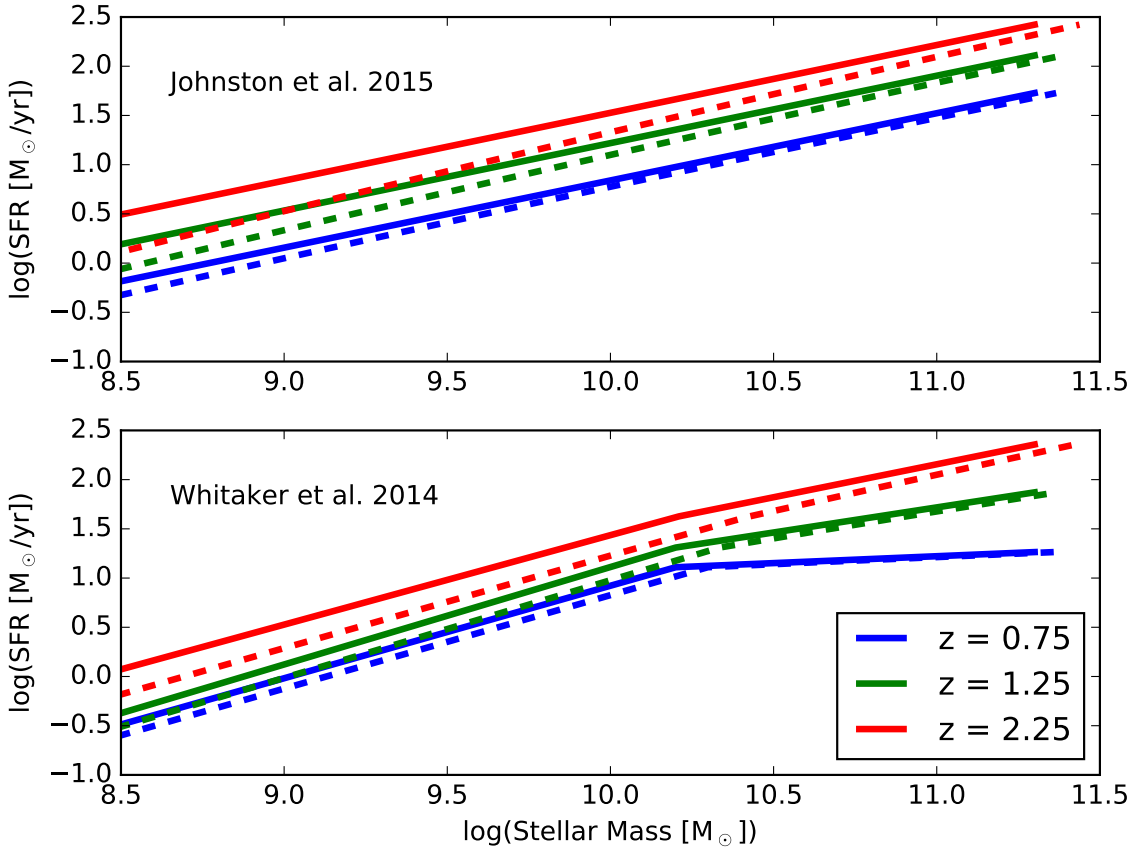

Figure 3.17: Corrections to previously published star-forming main sequence relations at various redshifts made using our piecewise fit to the XDF ($z_s + z_p$) galaxies. The top panel shows relations from Johnston et al. (2015) and the bottom panel those of Whitaker et al. (2014). The solid lines show the original relationships, and the dashed lines the corrections based on this work. The blue, green, and red colors show redshift 0.75, 1.25, and 2.25 respectively.

scatter decreases (from 0.43, 0.27, 0.26, 0.28 to 0.34, 0.21, 0.17, 0.21 for each of the redshift bins respectively), implying that the formation of stars in galaxies is even smoother than previously thought.

Finally, the effects of outshining may shed some light on a long-standing tension between observations of the stellar mass density (SMD) of the universe and the star-formation rate density (SFRD). The SMD at any time should be the integral of the SFRD corrected for mass lost and returned to the interstellar medium. A large body of work has reported a discrepancy between the inferred SFRD and the directly measured one, particularly at higher redshifts. Wilkins, Trentham & Hopkins (2008) found instantaneous indicators of the SFRD were 0.6 dex higher than those fit to the stellar mass history at $z > 2$. Ilbert et al. (2013) compared their inferred star formation history to data compiled by Behroozi, Wechsler & Conroy (2013) and found a difference of 0.2 dex at $z > 1.5$ (although the discrepancy was still within the expected uncertainties). Huertas-Company et al. (2016) recently inferred a star formation history extremely similar to Ilbert et al. (2013) despite a completely different dataset, but, when they compared their results to a recent compilation of direct SFRD measurements by Madau & Dickinson (2014), they found the direct measurements were ~ 1.25 times larger than their inferred SFRD at $z > 2$ (solid versus broken black lines in Figure 3.19). Reddy & Steidel (2009) and Sawicki (2012b) attributed this difference to poor constraints on the low mass tail of the stellar mass functions, but the issue has persisted even with more recent and deeper surveys, and an alternate explanation may be required.

To test how outshining would affect SMD measurements, we first took the best-fit Schecter function parameters for all galaxy morphologies listed in Table 2 of Huertas-Company et al. (2016), which were divided at different redshifts into star-forming and passive mass functions. We estimated the star-formation rate of the star-forming galaxies using the main sequence relation of Johnston et al. (2015), whose parameterization allowed us to calculate SFRs easily at any redshift. Then, now knowing the sSFRs of the star-forming population of galaxies, we corrected the star-forming mass function at each redshift to account for the mass bias found in this work. Following Huertas-Company et al.

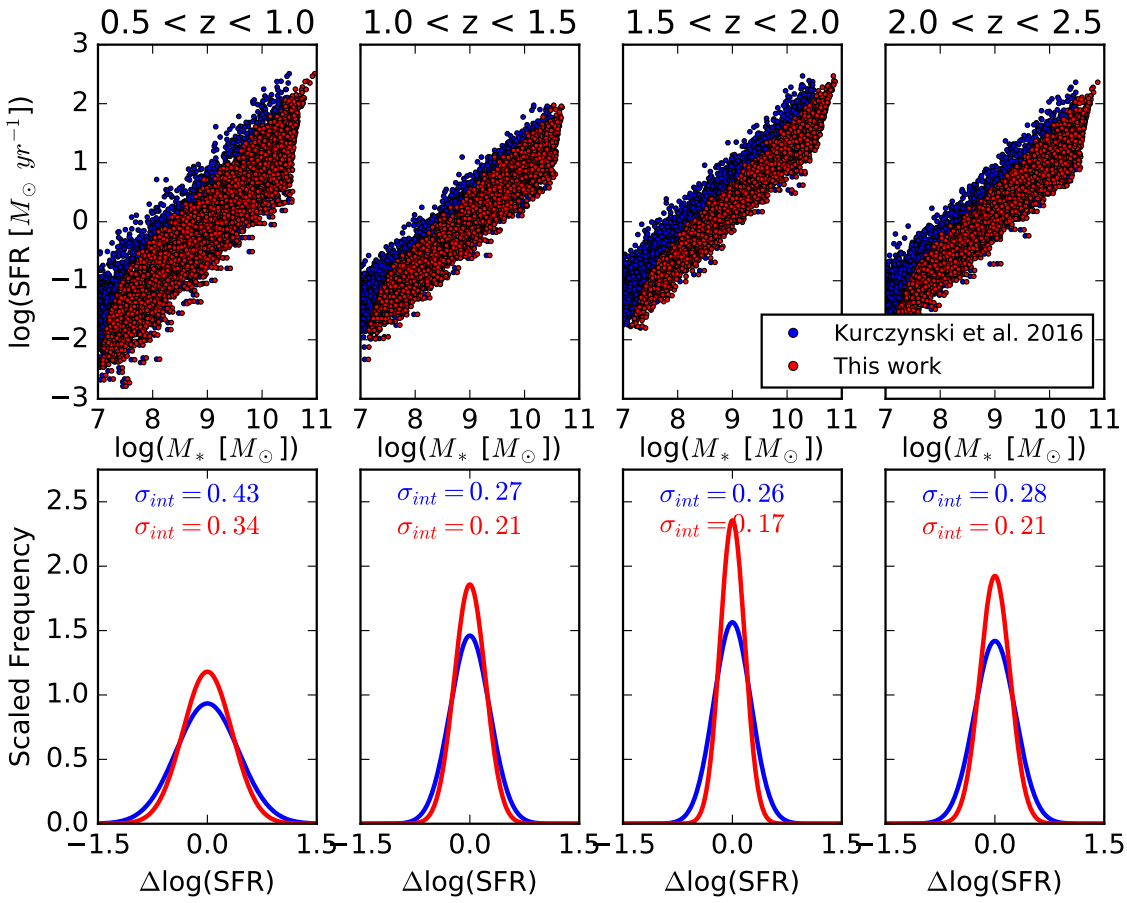

Figure 3.18: Effects of outshining on the intrinsic scatter about the star-forming main-sequence. Columns show different redshift ranges. Blue points in top row are randomly generated from Kurczynski et al. (2016) relations and converted to Chabrier IMF. Red points in top row show correction to stellar mass based on this work. Bottom row shows intrinsic scatter about linear fits to the data sets. In all cases, the shearing caused by the sSFR dependent correction leads to a lower intrinsic scatter.

(2016), we integrated below the new curve at each redshift from masses between 10^8 and 10^{12} $M_\odot$, and added the integral of the passive mass function to find the SMD as a function of redshift. Following the procedure laid out by Wilkins, Trentham & Hopkins (2008), we related the SMD to the SFRD using

$$SMD = \int_0^t SFRD(t')(1 - 0.05\ln(1 + \frac{t - t'}{0.3\text{Myr}}))dt' \tag{3.6}$$

where the parameterization for the return fraction is assumed to be that given by Conroy & Wechsler (2008) for a Chabrier IMF.

The functional form of the SFRD is taken to be that given by Behroozi, Wechsler & Conroy (2013), namely

$$SFRD(z) = \frac{C}{10^{A(z-z_0)} + 10^{B(z-z_0)}}. \tag{3.7}$$

The SFRD is then fit holding A fixed at -1 as done in the previous works. Our best fit parameters were $B = 0.15$, $C = 0.12$, and $z_0 = 0.99$. Because it is not our intent to actually measure the star formation history of the universe, only show how a pixel-by-pixel mass correction would affect previous results, we have refrained from performing any uncertainty analysis on these parameters.

The results of the best-fitting parameters are shown in Figure 3.19. The solid black curve shows the original best-fit star formation history of Huertas-Company et al. (2016), and the most recent compilation of direct SFRD measurements from Madau & Dickinson (2014) is shown as the dashed black curve. The discrepancy between these two different measurements is evident, particularly above $z \sim 1.5$. Our correction to the inferred star formation rate history is shown as the yellow and red curves for fits to the z_s and $(z_s + z_p)$ XDF samples respectively. They follow the original curve of Huertas-Company et al. (2016) closely at low redshift, but begin to diverge significantly around $z > 1.5$, and become more inline with the direct SFRD measurements. There is still a maximum offset of 0.03 dex at $z \sim 2$ between our $z_s + z_p$ correction and the direct measurements, and the slope at the highest redshifts may be too shallow compared to that found by Madau & Dickinson

(2014), but these differences may be explained by the different functional parameterization used by Madau & Dickinson (2014), or due to our assumed conversion between a galaxy's mass and SFR given by Johnston et al. (2015), which had a higher sSFR for lower mass galaxies than the relation from Whitaker et al. (2014). In general, it is clear that the mass correction presented in this work acts to increase the SMD at higher redshifts, and thus greatly reduce the tension between inferred (from stellar mass functions) star formation histories and directly measured ones. To see how close a mass correction of the same piecewise form studied here could come to the direct observations, we worked backward by converting the Madau & Dickinson (2014) SFRD into a SMD and then found the best piecewise parameters that would make the Huertas-Company et al. (2016) mass functions match this stellar mass density as a function of redshift. The resulting best correction is shown in Figures 3.13, 3.14, and 3.19 as the solid green curve, and it is generated using the parameters $p, m, b, k_2 = -10.1, -0.02, -0.03, -0.06$. The best-fit correction to match the directly measured SFRD has a linear component that is within uncertainty of the XDF fits, but a break-point (p) that lies just to the left the 1-σ confidence region, and a parabolic component that is shallower than would be expected from the XDF data. The general similarity between the form of the best-fitting correction and the XDF corrections (if not the exact details) lends more credence to the observed kink in the mass discrepancy at high sSFRs. Overall, we find that correcting the observed stellar mass functions for mass missed by unresolved SED fitting eliminates the "missing mass" problem that is otherwise seen when comparing direct measurements of the SFRD with those inferred from the SMD.

A caveat regarding these results: the Hubble XDF is a small slice of the sky compared to the scale that most stellar mass functions are measured from (4 $arcmin^2$ compared to 880 $arcmin^2$ for Huertas-Company et al. (2016), or 1.62 deg^2 for Muzzin et al. (2013)). The (relatively) small number of galaxies limit how sweeping our conclusions can be. For example, there are only a small number of galaxies (55) with masses between $10^{10.4}$ and $10^{11.4}\mathrm{M}_{\odot}$, which corresponds roughly to plus or minus three times M^*. While the M^* galaxies in our sample all follow the trend shown in Figure 3.14, they all have sSFRs that

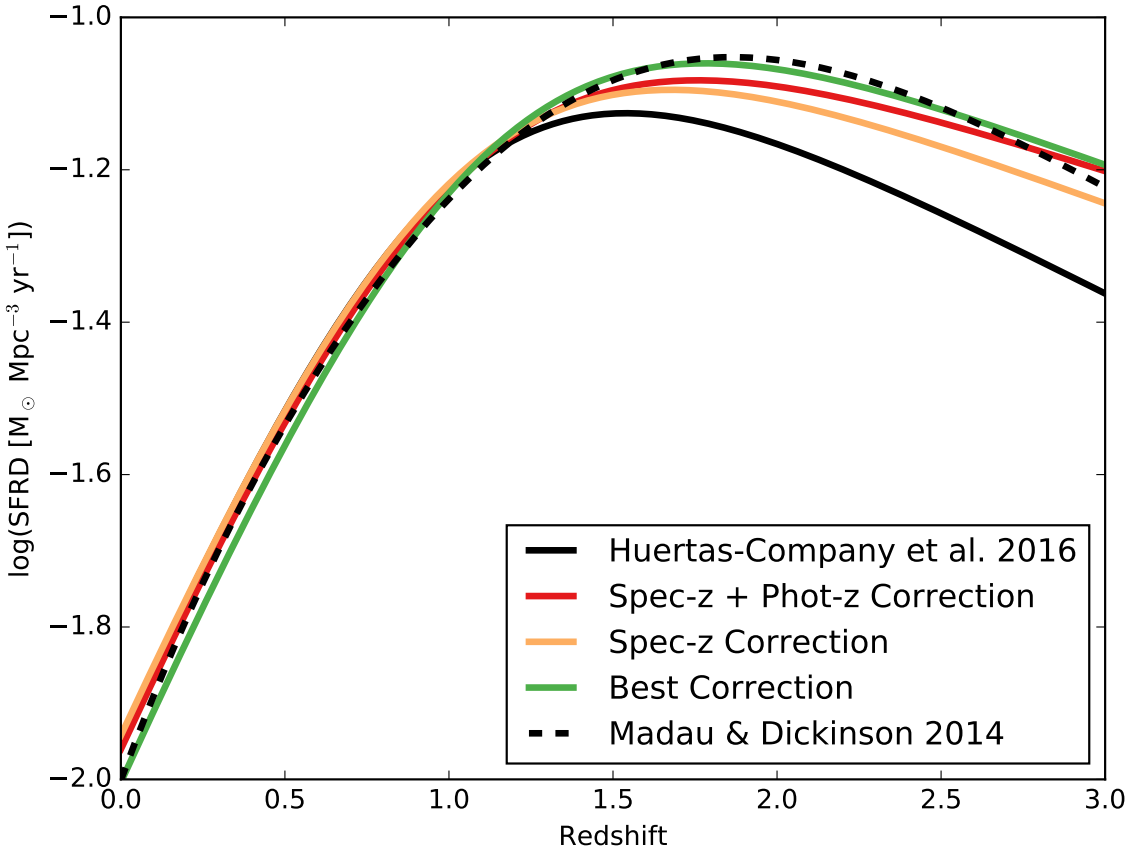

Figure 3.19: Corrections to previously published star-formation history from Huertas-Company et al. (2016). The solid black line shows the original curve inferred from galaxy stellar mass functions, and the solid colored lines the correction based on this work. The correction brings the star formation history closer in line to directly measured observations of the SFRD compiled by Madau & Dickinson (2014), shown as the dashed curve.

lie to the left of the break point, meaning it is unclear if the population of M^* galaxies would also turn sharply downward. Fortunately, the XDF does include a large number of sub-M^* galaxies, which is where the bulk of stellar mass lies (approximately 80% as shown in Figure 1 of Sawicki & Thompson (2006) for a faint end slope α of -1.4, consistent with deep SMF estimates from Tomczak et al. (2014)). In order to study how pixel-by-pixel mass estimates perform with varying galaxy populations, greater numbers are needed, and must wait for the onset of next generation astronomical instruments, such as WFIRST.

3.4.2 Why was this bias not seen before?

As discussed above, Sorba & Sawicki (2015) observed a bias in stellar mass measurement due to outshining for nearby galaxies at low redshift. This work shows a similar trend for galaxies up to $z = 1.2$, and a more egregious offset in mass for galaxies from $1.2 < z < 2.5$. However, previous pixel-by-pixel analysis at high redshift by Wuyts et al. (2012) found zero mass discrepancy when comparing the pixel-by-pixel and unresolved mass estimates for star-forming galaxies galaxies at $0.5 < z < 1.5$ and $1.5 < z < 2.5$. Although their selection criteria differed from ours (they only performed pixel-by-pixel SED fitting on galaxies with masses greater than 10^{10} $M_\odot$ and sSFRs greater than -9.76 yr^{-1} and -9.51 yr^{-1} for their low-z and high-z samples respectively), our results indicate that they should have seen an unresolved versus resolved mass bias regardless. It is necessary to understand what led to our disparate results. Perhaps the most obvious factor that could have contributed to the outshining bias not being measured is that it is a small effect, at least for galaxies with lower sSFRs. When averaged over all sSFRs, our XDF low redshift ($z \leq 1.2$) spectroscopic sample displays a mean bias of only 0.04 dex. It is only the increasing difference with sSFR that makes the bias particularly notable. Nevertheless, here we examine the differences in our methodologies to see what other factors would influence the unresolved to pixel-by-pixel mass ratios.

The first difference is Wuyts et al. (2012) constructed their model SED templates with Bruzual & Charlot (2003) models, whereas we used FSPS models. Although the manner in

which various codes treat certain phases of stellar evolution such as the Thermally Pulsating Asymptotic Giant Branch (TP-AGB) can have strong effects on M_*/L ratios, this should not affect the mass ratios in each work, as both the pixels and integrated light are fit consistently within that work.

Second, Wuyts et al. (2012) used a modified χ^2 statistic which incorporated additional integrated fluxes (U, K_s, and the four IRAC bandpasses) in order to find the best fitting model. The statistic they minimized was

$$\chi^2_{res+int} = \chi^2_{res} + \sum_{j=1}^{N_{int}} \frac{(F_j - \sum_{i=1}^{N_{bin}} M_{i,j})^2}{E_j^2} \tag{3.8}$$

where χ^2_{res} is the sum of all the χ^2 values as normally found in SED fitting for each spatial bin (essentially each pixel) using only bandpasses that are fully spatially resolved, N_{int} is the number of spatially-integrated-only bandpasses, N_{bin} is the number of spatial bins, F_j and E_j are the observed flux and error in the j^{th} integrated only bandpass, and $M_{i,j}$ the model flux in the j^{th} integrated only bandpass and i^{th} spatial bin. Because the parameter space of this statistic is very large, they started with an initial guess using the best-fit model of each spatial bin found using only the resolved bandpasses and then iteratively adjusted one spatial bin's model at a time to improve the $\chi^2_{res+int}$. This iteration was continued until no improvement was found or a maximum of 500 iterations. In contrast, our pixels were treated essentially as their own, independent, objects. This would seem to be a major difference in our approaches, but Wuyts et al. (2012) clearly state that the good correspondence between pixel-by-pixel and unresolved mass estimates remains even if constraints from integrated fluxes were ignored.

Perhaps their choice to use the model with the minimum χ^2 as their best-fit mass estimate versus our use of the median mass from several hundred Monte Carlo iterations makes a difference. Taylor et al. (2011) have shown how using the best-fitting model to define the stellar mass can induce strong systematic effects. A simple check of finding the mass ratios of our best-fit model masses (rather than median masses) for the spectroscopic

sample gives an average mass ratio of 0.94 ± 0.10 which is higher than the average of the median mass ratios of 0.91 ± 0.06, but not significantly. More telling, the best-fit mass ratios show a lack of a linear trend with sSFR, with a slope of -0.014 ± 0.11, which emphasizes the importance of using the median mass of many perturbed SED fits. It also helps explain why Wuyts et al. (2012) did not see a discrepancy, despite selecting only galaxies with relatively high sSFRs.

Finally, in order to increase signal-to-noise in their spatial bins, Wuyts et al. (2012) combine pixels together using the Voronoi two dimensional binning technique of Cappellari & Copin (2003). The pixel binning degrades their spatial resolution, which is a key factor in allowing pixel-by-pixel analysis to uncover any bias due to outshining. The pixel-by-pixel SED fitting allows one to separately fit spatially segregated stellar populations, thus better constraining the M_*/L ratio of the galaxy built up over its entire star-forming history. As the spatial resolution gets poorer and poorer, the ability to see fainter stars behind the bright stars necessarily goes away (Sorba & Sawicki, 2015). It is likely then, that the spatial binning performed by Wuyts et al. (2012) pushed the pixel-by-pixel mass estimates into a regime where outshining could not be measured. In fact, when they compared resolved to unresolved mass estimates without binning, they found the pixel-by-pixel masses were systematically heavier by 0.2 dex (about 27%). They state that the binning to a minimum signal-to-noise is necessary to avoid biases in SED fits that lead to erroneously large M_*/L ratios. This is a true concern as discussed above, exacerbated by their use of minimum χ^2 best-fits which places undue significance on the measured colors in the photometric catalog without properly accounting for how the colors can vary with uncertainty. The systematic offset they found of 0.2 dex is likely not real. Their use of binning was entirely justified, especially considering the focus of their analysis on star-forming clumps and overall surface profiles as a function of half-mass/half-light radii. The binning did, however, along with the use of minimum χ^2 masses, act to obscure evidence of the outshining bias found in our work.

3.4.3 Pixel-by-pixel Star Formation Histories

One feature of pixel-by-pixel stellar population fitting is the ability to construct empirical star formation histories by examining the age and mass estimates in each pixel. Although the SFH in each pixel has an assumed, simple, parameterization, the SFH found from linear combination of the stellar populations in each pixel can be much more complex. Wuyts et al. (2012) found their spatially integrated SFHs fell below a line of constant star-formation implying that star formation was slow early on in a galaxy's life and sped up at later times. This would be consistent with an exponentially increasing "inverted-τ" SFH. On the other hand, Conroy & van Dokkum (2016) created non-parametric SFHs from color-magnitude diagrams for pixels in HST observations of the disk and bulge of M31 and found that they were consistent with a smooth exponentially declining SFH of τ equal to 4 and 2 respectively, albeit this was at a much smaller spatial scale and for a galaxy at $z \sim 0$.

In the left panel of Figure 3.20 we show the cumulative mass history (i.e. the integrated SFH) of galaxies in the spectroscopic XDF sample, averaged in initial mass bins of one dex and in redshift bins of 0.4. In general, it seems that at each redshift the most massive galaxies obtained their mass quickly and then formed relatively fewer stars afterwards. This is in agreement with expectations since the most massive galaxies in our sample have very red colors and a more elliptical morphology, meaning that we would expect there to be very little recent star-formation. It is also consistent with the down-sizing scenario, wherein the most galaxies formed their stars first, and star-formation shifted to lower mass galaxies at later times. It also appears that within a mass bin the onset of more intense star formation happens at later times for lower redshift galaxies, but this is likely a selection effect: we do not see the high-z galaxies with flat mass histories because they are too faint to see.

In the right panel of Figure 3.20, we show examples of different popular SFH parameterizations, including τ, inverted-τ (Maraston et al., 2010), delayed-τ (linearly increasing before eventual exponential decay; Simha et al., 2014; Behroozi, Wechsler & Conroy, 2013), and a log-normal SFH (Gladders et al., 2013; Dressler et al., 2016), which has been success-

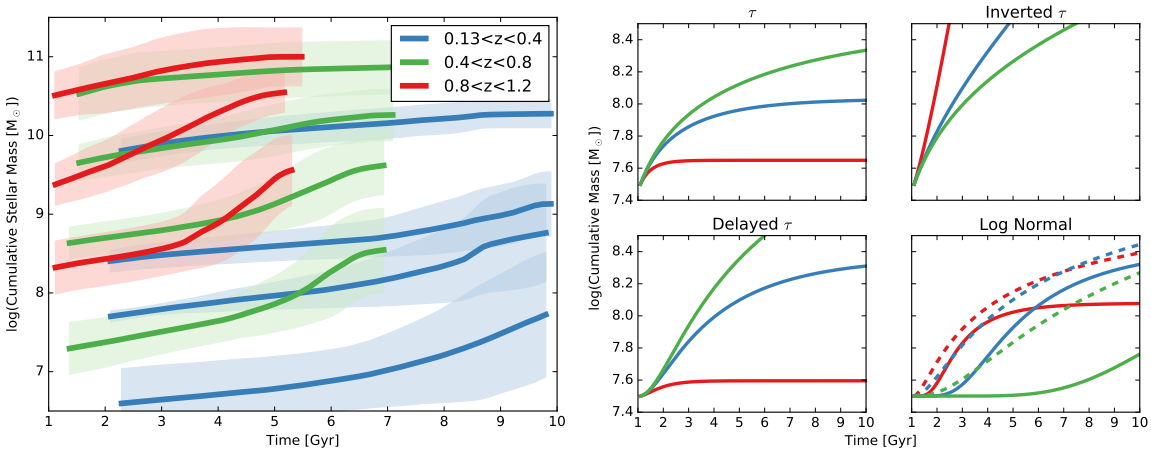

Figure 3.20: Left: Cumulative mass history from pixel-by-pixel SED fitting of XDF galaxies with spectroscopic redshifts. The curves show the average of galaxies in initial mass bins of one dex and redshift bins of 0.4. Shaded areas indicate 1-σ uncertainties. Right: Theoretical mass histories from common SFH parameterizations. Different colors show different values of τ. The dashed lines in the log-normal plot show different values for t_o.

ful in describing the universal star-formation rate density (SFRD) over cosmic time. Our non-parametric mass histories show the "stretched-S" pattern characteristic of the SFHs with delayed onset of star-formation, such as the delayed-τ and the log-normal parameterizations, but in practice we were unable to find good fits to any of the parameterizations. The delay of the onset of peak star-formation was too long in our non-parametric SFHs to be consistent with the models; all the model cumulative mass history parameterizations rose much more steeply or were unable to rise enough. We theorize that our pixel-by-pixel SFH suffers from our assumed age limits, spacing, and assumed SFH in each pixel. The assumed exponentially declining τ SFH may be particularly problematic, as the "frosting" of young stellar populations means the underlying mass formed earlier is hidden. This likely leads to the rapid build up seen in the cumulative mass history at a delayed onset time, when it really should be much more steady. We refit the spectroscopic redshift sample using delayed-τ SFH, but saw no qualitative difference in the integrated cumulative mass history.

Interestingly, the use of delayed-τ SFHs did not significantly alter the outshining bias found with exponentially declining SFHs signaling that, unless the star-formation history

of a galaxy is known *a priori*, the wide range of M_*/L ratios covered by any parameterized grid of SFHs will still lead to a bias due to outshining. This agrees with our previous work that found outshining still occurred when using two component burst models.

3.5 Conclusions

- Following Sorba & Sawicki (2015), we examined the ratio of the unresolved mass estimate to the pixel-by-pixel mass estimate as a function of sSFR. We found that a bias in the mass estimate of galaxies due to outshining still persists up to $z = 2.5$. Moreover, the bias appears to have two distinct components:

    1. At low sSFRs (less than approximately $10^{-9.5} yr^{-1}$), the ratio of unresolved to pixel-by-pixel mass changes roughly linearly with log(sSFR). The slope and intercept of a linear fit is commensurate with the results found for nearby galaxies in Sorba & Sawicki (2015).
    2. Above sSFR $= 10^{-9.5} yr^{-1}$, the mass ratio turns sharply downward, and can no longer be represented by the shallow linear trend found at lower redshifts. Because sSFRs tend to be larger at higher redshift, the sharply increasing bias implies that masses for some galaxies between redshifts 1.5 and 2.5 could systematically be underestimated by factors of 2-5.

- The piecewise form of the mass correction (shallow at low sSFRs and becoming much steeper as sSFR increases) naturally resolves a long-standing tension between the directly observed SFRD and that derived from the observed SMD. Correcting stellar mass functions from Huertas-Company et al. (2016) brings the derived SFRD much more in line with the directly observed SFRD compilation of Madau & Dickinson (2014).

- Correcting mass estimates for the bias found above slightly alters the slope of the star-forming main-sequence. It also reduces the intrinsic scatter about the star-forming

main-sequence, suggesting that star-formation in galaxies proceeds in a smooth fashion.

- Spatially integrated star formation histories strongly suggest that two parameter models such as log-normal (Gladders et al., 2013) or double power law (Behroozi, Wechsler & Conroy, 2013) provide better fits to a galaxy's SFH because they can naturally account for a rising and falling SFH at different times.

- Spatially resolved SED fitting is a powerful tool, and differences between resolved and unresolved fits highlight the importance of treating galaxies as composite structures, rather than one cohesive whole.

Chapter 4

Simulations for NIRISS

Wide field slitless spectroscopy will be used as an important tool in several future surveys. Its ability to create highly resolved line emission maps will yield a better understanding of how stellar mass forms in a galaxy. Cutting edge analysis software for wide field slitless spectra, such as the currently-in-development GRIZLI, should be tested and optimized now in order to make the most of future observations. We created mock spatially-distributed galaxy spectra using pixel-by-pixel SED fits of the Hubble Extreme Deep Field (XDF). We used these to make realistic NIRISS observations of the XDF using GRIZLI, and compare the true emission maps of several emission lines to those recovered by GRIZLI. GRIZLI tended to over-estimate the line emission flux, on average by a factor of 1.37, for Hα and OIII, but correctly estimated the line flux from Hβ on average. The fitting procedure used by GRIZLI assumed one continuum model spectrum could apply for the whole galaxy, but this assumption was found to be inadequate in several cases. Fitting just one continuum model spectrum to galaxies with inhomogeneous spatially distributed spectra led to poor continuum fits overall, and thus inaccuracies in line strength estimation. In cases such as this, it would be beneficial to implement a method for modelling a spatially varying continuum. Grism redshifts were found to perform well, with $\sigma_{NMAD} = 0.0012$, comparable to previous results.

4.1 Introduction

Wide field slitless spectroscopy (WFSS) is a technique whereby the light from every source in a field is dispersed into a spectrum by a low resolution grism. The entire field is imaged at once, and spectra for each pixel are obtained simultaneously. Each spectrum is oriented along the same dispersion direction, and thus the superposition of spectra can be a common issue in crowded fields. Despite the difficulty in disentangling slitless spectra, the technique is a powerful tool; unlike a multi-object spectrograph (MOS), WFSS has no loss of flux due to slits, and WFSS allows for a higher degree of multiplexing compared to an integral field unit (IFU) or MOS.

WFSS has been used prominently with the recent addition of the Wide Field Camera 3 (WFC3) to the Hubble Space Telescope, which supplemented the existing G800L grism with three more grisms (G280, G102, and G141). Several large-scale WFSS projects have since emerged including: the 3D-HST survey (van Dokkum et al., 2011; Brammer et al., 2012; Skelton et al., 2014), the WFC3 Infrared Spectroscopic Parallel Survey (WISPS; Atek et al., 2010), and the Grism Lens-Amplified Survey from Space (GLASS; Schmidt et al., 2014; Treu et al., 2015). The grism observations allow for the construction of spatially resolved line emission maps (Nelson et al., 2012; Schmidt et al., 2013; Wuyts et al., 2013), which can be used to place constraints on when and where stars form within a galaxy. For example, Nelson et al. (2013) use stacked Hα emission maps to show that the line emission is more extended than the stellar continuum, implying inside-out galaxy formation.

The advent of the James Webb Space Telescope (JWST) with its Near Infrared and Slitless Spectrograph (NIRISS) instrument will provide the next leap in slitless spectroscopy in the coming years. The NIRISS field of view is $2.2' \times 2.2'$ and is focused onto a 2048×2048 pixel detector, yielding a 65 mas/pix image scale. For WFSS, NIRISS two orthogonal grisms (GR150C and GR150R where the C and R stand for column and row) which both have a (first order) resolving power of approximately 150. The grisms give a spectral coverage of 0.8 to 2.2μm and are combined with several wide and medium band filters (F090W,

F115W, F150W, F200W, F140M, F158M) to limit the occurrences of overlapping spectra. For further technical details, refer to Doyon et al. (2012).

Additionally, two other notable future space missions will include slitless spectroscopy instruments. The Wide Field Infrared Survey Telescope (WFIRST; Spergel et al., 2015) will include a grism as part of its wide field instrument in order to obtain the large number of precise redshifts required to meet its scientific goals. The European Space Agency's next generation telescope Euclid (Racca et al., 2016; Laureijs et al., 2011) will also contain 4 grisms as part of it's near infrared spectrometer, providing spectra through two different filters in three different orientations.

Being able to accurately map the line emission in galaxies is crucial for advancing our understanding of galaxy evolution. Our pixel-by-pixel measurements of galaxies in the XDF provide us with the unique opportunity to test the capabilities of slitless spectrographs and fine tune analysis software using realistic mock observations. In this chapter, we detail simulations made for the NIRISS instrument on JWST. The mock observations were generated and examined with the currently-in-development Grism Redshift and Line (GRIZLI) software (Brammer in prep.) GRIZLI is planned to work for HST, JWST, and WFIRST, and realistic performance tests are necessary to locate areas that can be improved before the future missions launch. By identifying and addressing any possible issues before launch, we hope to ensure the awesome power of next generation telescopes will be able to be used to its full potential from the very first light observed.

4.2 Method

Starting with the XDF images from the previous chapter that had been convolved to the same PSF, we resampled these images to the NIRISS pixel scale. In order to maximize the number of galaxies in the image, we used a rotation angle of 45 degrees centered at a right ascension and declination of 53.162469 and -27.780373 degrees respectively. The re-sampled images were put through the same segmentation and SED fitting procedures as described

in Chapter 3. Note that it was necessary to fit spectral templates to the re-sampled pixels (rather than directly using our fits from the previous chapter) because the pixel mapping caused by the drizzling process is not one-to-one.

For each template SED, we found the emission line spectrum by calculating the SED once including nebular emission and once without (i.e. just the continuum) and subtracting the two (Byler et al., 2016). For each of the emission lines Hα, Hβ, and OIII, we determined the flux by integrating the residual emission spectrum about the central wavelengths of each line. We could then determine the line flux in each pixel by correcting the line flux of the best-fitting template SED for the luminosity distance to the galaxy and multiplying by the flux scaling derived from the fitting procedure. For the purposes of simulating mock observations, we took the best-fit spectrum for each pixel to be "reality". An example of the line emission maps for the whole field is shown in Figure 4.1, and those for one galaxy (ID 54454) are shown in Figure 4.2.

In order to turn our mock reality into simulated NIRISS observations, we used the currently-in-development Grism Redshift and Line (GRIZLI; v0.2.1) analysis software package (Brammer in prep.) GRIZLI is the successor to previous slitless spectra analysis pipelines created for HST such as aXe (Kümmel et al., 2009). GRIZLI enables one to model several overlapping spectra of hundreds or thousands of objects in exposures taken with one or more separate grisms. The mock survey was assumed to have an exposure time of 11460 seconds per grism per filter over 12 exposures (955s per exposure).

Using the (re-drizzled) F140W image as a reference image, we segmented each galaxy pixel as its own object and used GRIZLI to calculate a model dispersion beam for each object in each of the F115W, F150W, and F200W NIRISS filters at orientation angles of 0 and 90 degrees (representing the R and C grisms). It was necessary to manually adjust the parameter 'MMAG_EXTRACT_A' (which represents the minimum magnitude of an object for it to be dispersed by the grisms) in the NIRISS configuration file to 40.0 in order for beams to be calculated for the pixel objects, which obviously have a much lower flux than an entire galaxy. GRIZLI originally assigns a flat spectrum for each object. The

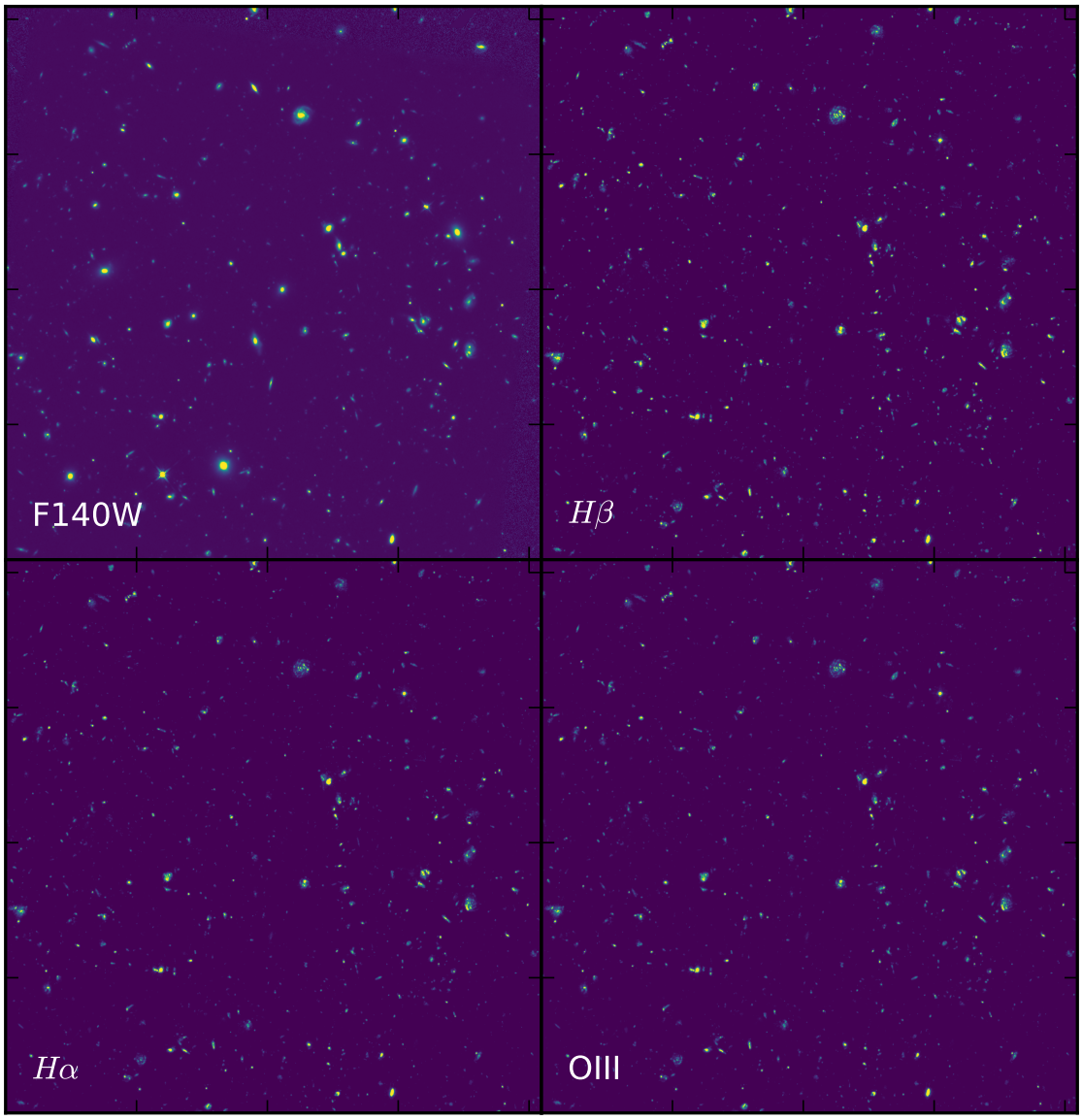

Figure 4.1: Emission line strength per pixel from the SED fits for entire mock field. The F140W image is the re-drizzled XDF observations, while the Hα, Hβ, and OIII images are synthesized from the SED fits to the multi-filter HST data.

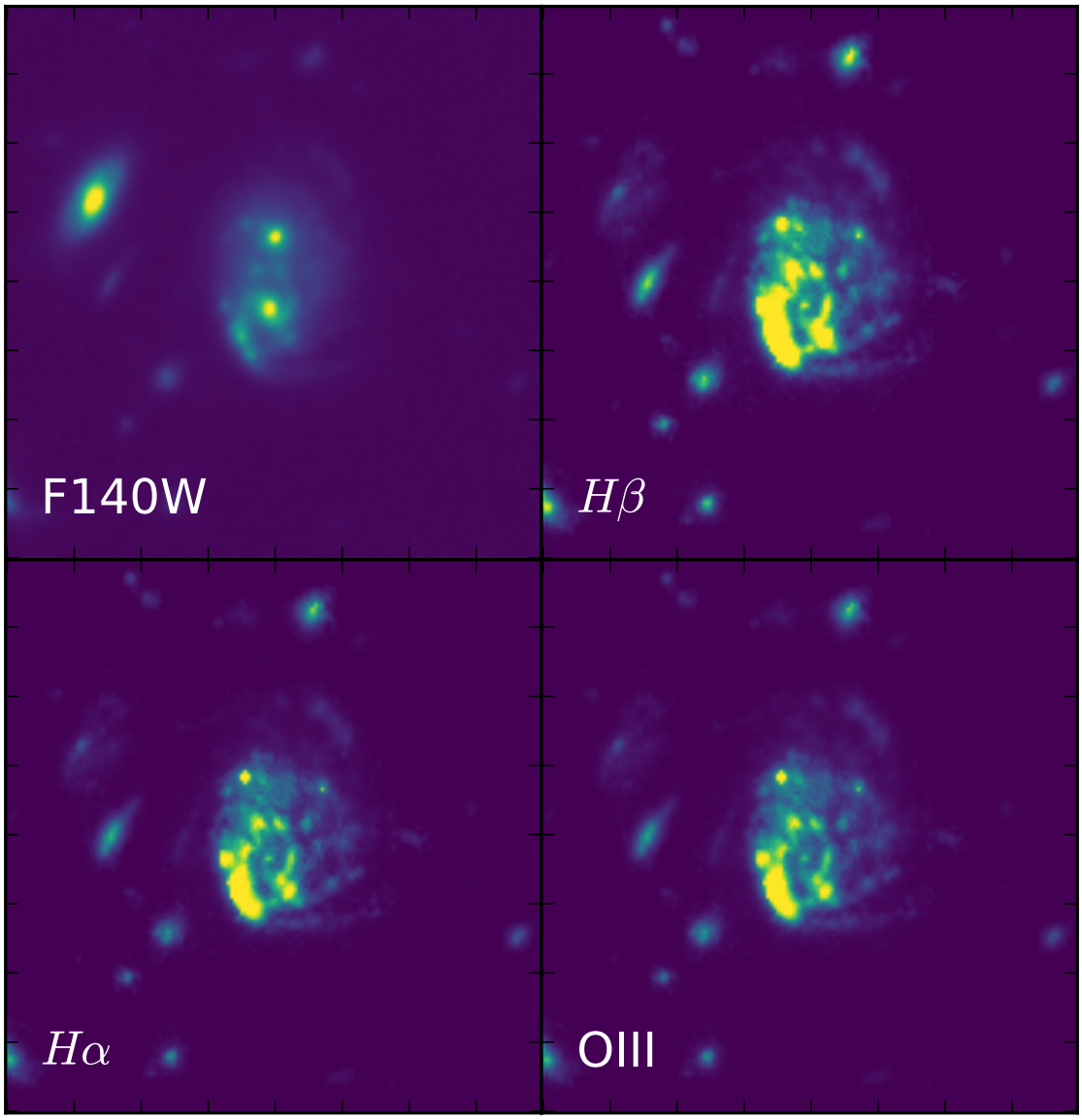

Figure 4.2: Emission line strength per pixel from the SED fits for galaxy 54454 (RA, Dec) = (53.14794797, -27.77392421). As in Figure 4.1, the F140W image is real data from the XDF, while the line images are our SED-fit-based models.

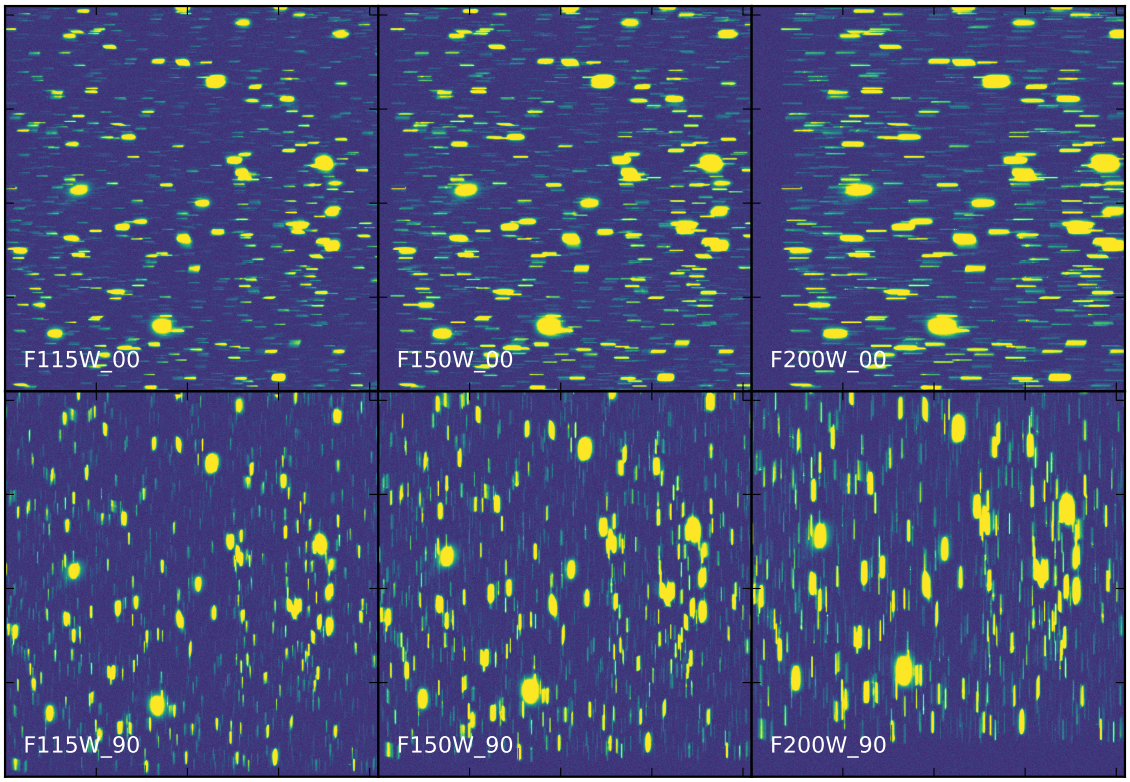

Figure 4.3: Mock observations created with GRIZLI.

model dispersion beams were updated with the "true" spectra from our SED fits, and noise from the sky and instrument were added according to GRIZLI's default settings. These six science images (3 filters, 2 grism orientations) thus constituted our mock observations and are shown in Figure 4.3.

The mock observations were reloaded into GRIZLI, again using the F140W image as a reference, but this time using a segmentation with each galaxy as its own object. For each galaxy in the redshift range $1.06 \leq z \leq 2.36$ (meaning both Hα and Hβ should appear within the observed spectra), and with a magnitude brighter than 26, we used GRIZLI's analysis tools to determine the galaxy's redshift and line fluxes. Each galaxy observed is represented by six "beams", one for each science image. For redshift, GRIZLI creates a coarse grid of 1D model templates (an intermediate age SED created with EAZY (Brammer, van Dokkum & Coppi, 2008), an old SSP from Conroy & van Dokkum (2012), a post-starburst template

from Muzzin et al. (2013), or a low metallicity LBG template from Erb et al. (2010)) where the grid spans $0.5 \leq z \leq 2.4$, and has $dz/(1+z) \sim 0.005$. The continuum templates are supplemented with line complex templates for OII + NeIII, OIII + Hβ, and Hα + SII + weaker red lines. These line complexes have fixed line ratios and are used to break redshift degeneracies. GRIZLI finds minima in the χ^2 distribution first on the coarse grid, and then on a finer grid allowing for more freedom in the individual line strengths. For each beam, the goodness of fit is computed by comparing the models in full 2D pixel space after removing contamination from nearby objects and background.

Obviously, it is important to have accurate segmentation maps for the contamination removal process to be effective. Fortunately in this work we have perfect segmentations due to the nature of our mock image creation process; we know exactly which pixels belong to each galaxy. The contamination from nearby neighbors is modelled as a flat continuum for faint sources (F140W magnitude greater than 24), and a second degree polynomial for brighter objects.

For spatially resolved line emission maps, GRIZLI subtracts the best-fit continuum spectra and generates drizzled line emission maps averaged over both grism orientations. Figure 4.4 shows an example of how GRIZLI fits a grism redshift and spectral template (continuum plus line emission) for galaxy 8133 which has an input redshift of 1.07. The top-most panel displays how the reduced χ^2 of the two dimensional residuals changes as the spectral template's redshift changes. The minimum lies at $z_{grism} = 1.0695$, extremely close to the input redshift. The bottom panel displays the flux in each beam as a function of wavelength, as well as the fitted continuum plus line emission in each beam. Here we can see that the Hα line emission (largest peak) appears slightly different between the two grism orientations. GRIZLI's final flux determination is an average of the two.

It is important to emphasize that the model continuum is assumed by GRIZLI to be the same throughout the entire galaxy (although scaled to match the flux profile of a reference image). As previous chapters have explained, galaxies are not comprised of one cohesive stellar population, but instead very different stellar populations (and thus different spectra)

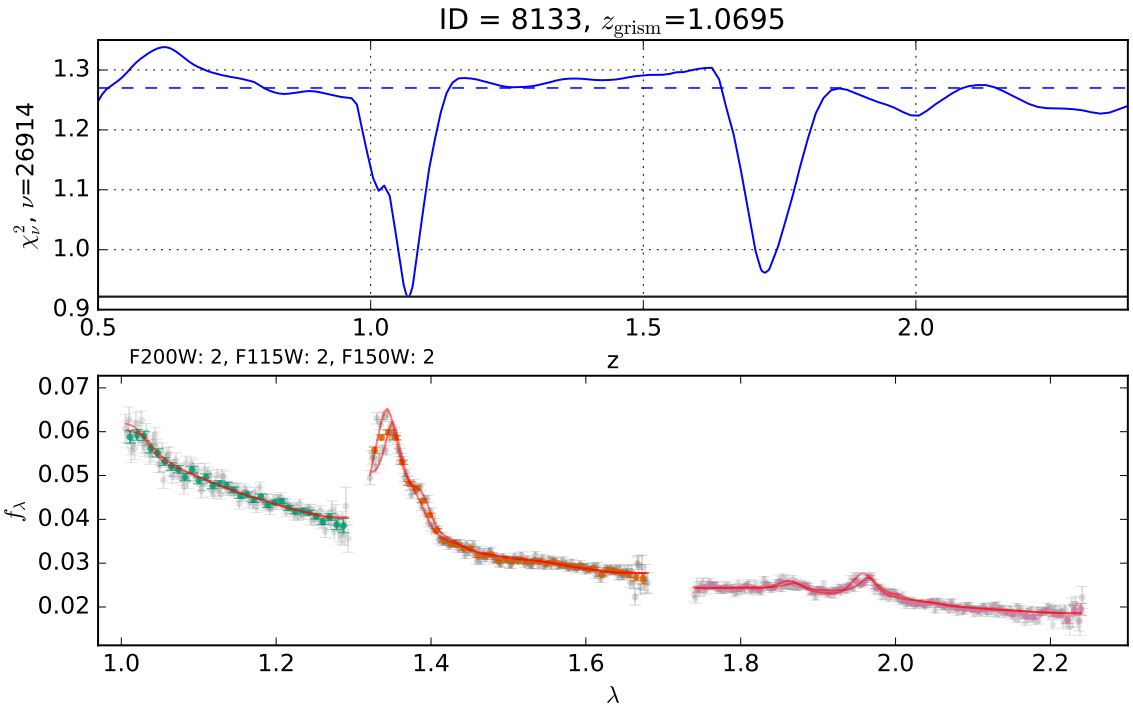

Figure 4.4: GRIZLI measurements for galaxy 8133. *Top:* Reduced χ^2 values for grism redshift estimation. *Bottom:* Observed flux in each beam (grey points), average flux (colored points), and best-fit 1D spectral template for each beam (red lines).

reside in disparate locations throughout the galaxy. A significant aim of this chapter is to test how the assumption of a single representative continuum throughout the galaxy affects line strength measurements, if at all.

4.3 Results

Shown in Figures 4.5, 4.6, and 4.7 are residual checks on GRIZLI's continuum and line emission estimation for three (typical) galaxies (8133, 21783, 54454). The top-most panel shows the difference between the observed flux through each filter and grism combination, and the modelled spectral continuum template and modelled contamination from nearby sources. Only emission lines should appear above the noise if the continuum is accurately modeled. The bottom panel shows how accurately GRIZLI recovers the two dimensional distribution of Hα. From left to right displays a false-color image with blue, green, and red roughly represented by rest-frame BVi wavelengths (actually the F105W, F125W and F140W images), followed by the true emission map input into GRIZLI, the recovered emission map, the difference between the two, and the ratio of the two. Because the emission map is measured by subtracting the continuum, how accurately the line flux is measured will depend on the best-fitting continuum model.

Beginning with galaxy 8133 (Figure 4.5), the grism residuals show that GRIZLI seems to do a good job at modelling the continuum of this galaxy. There is no presence of the dispersed beam in the residual images, and all that remains is bright Hα emission in the F150W filter and weaker sulphur lines in the F200W grism. Looking at the two dimensional emission map measured by GRIZLI, however, shows an excess of flux. Since the continuum appears to be well-modeled for this galaxy, the mismatch in Hα emission likely stems from how GRIZLI defines what flux to include in its emission map. For example, in Figure 4.4 one can see there is a second emission line (SII) contributing flux adjacent to Hα. GRIZLI could be falsely attributing some of the flux from SII to the Hα emission map, leading to the excess seen. For this galaxy, the difference between GRIZLI's integrated line flux and

the true integrated line flux is 2.36×10^{-17} erg/s/cm^2.

Galaxy 21783 (Figure 4.6) has a skewed morphology, with star-formation occurring in the lower-left quadrant and a redder population in the upper-right. We find that GRIZLI does not model the continuum for this galaxy as well as 8133. There are clear, side-by-side linear artifacts in each of the grism residuals, one showing an excess in the model and one showing a paucity. The model continuum is both too much and too little at the same time, implying that GRIZLI's use of one continuum model for the entire galaxy is not adequate in this situation. The different stellar populations need to be modeled separately. Also present in the F150W_00 image is the emission from a neighboring galaxy (22020), which seems to have an adequate continuum model. Examining the line emission maps, it again appears that GRIZLI tends to attribute too much flux to each pixel in the emission map, excepting one small region. For this galaxy, the difference between GRIZLI's integrated line flux and the true integrated line flux is 1.16×10^{-16} erg/s/cm^2.

An extreme example of spatially changing stellar populations, galaxy 54454 (Figure 4.7) provides an interesting test case of a galaxy pair where most of the Hα emission lies in the arms of the bottom-most galaxy. Other than one bright spot, the top-most galaxy contributes very little to the total emission. The grism residuals show strong linear artifacts, and their dual nature (one light, one dark) again suggest that accounting for the inherently two dimensional nature of galaxy observations will be a necessary aspect of grism spectroscopy. In this case, the continuum mismatch is strong enough to directly affect the Hα emission map, which displays an erroneous dual tail that is comparable to the emission from the rest of the galaxy. For this galaxy, the difference between GRIZLI's integrated line flux and the true integrated line flux is 1.93×10^{-16} erg/s/cm^2.

While optimizing GRIZLI's analysis procedure is beyond the scope of this work, a slight improvement to the continuum modeling process might alleviate some of the more drastic inaccuracies. In cases where the dual line residuals are present, a secondary refinement where the galaxy is further segmented into, say, blue and red pixels, and each of those subsets has their own continuum model might be enough.

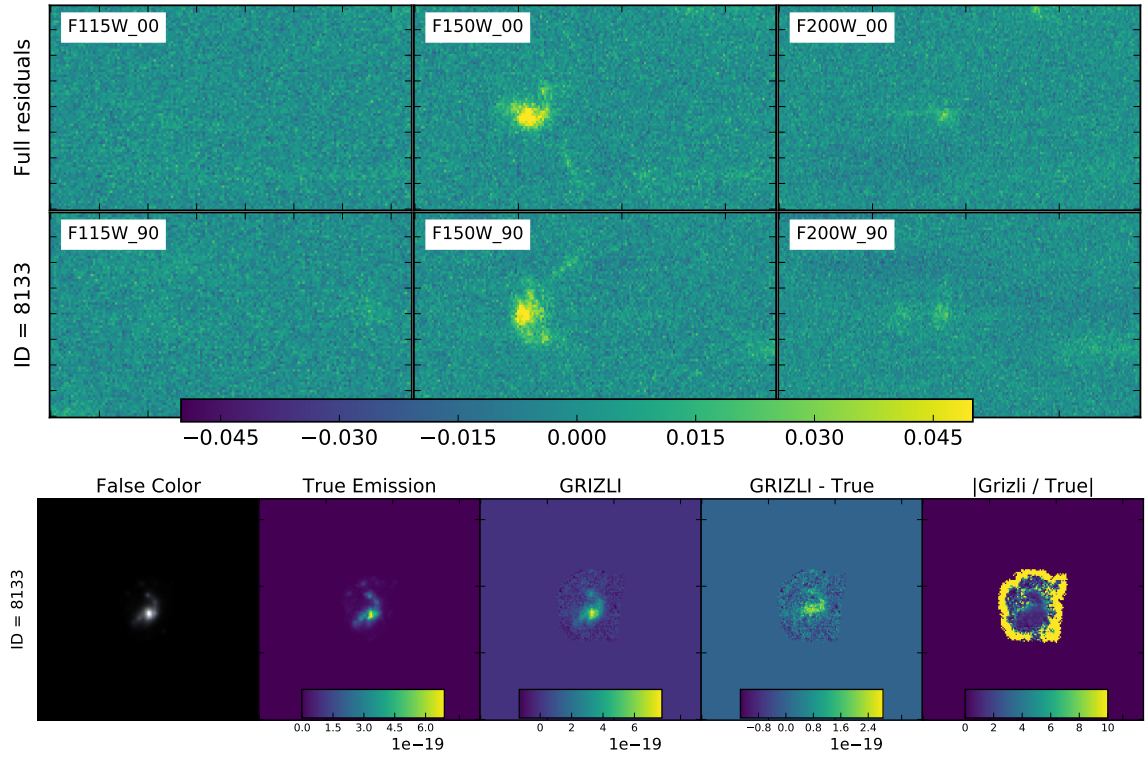

Figure 4.5: Comparisons of true input versus GRIZLI measurements. *Top:* 2D residuals of the observed flux minus the continuum model and contamination. Units are in 10^{-17} erg/s/cm^2. *Bottom:* 2D Hα comparison showing the false color image, true line flux input into the mock image, measured line emission map from GRIZLI, and difference and absolute ratio maps. Units are in erg/s/cm^2.

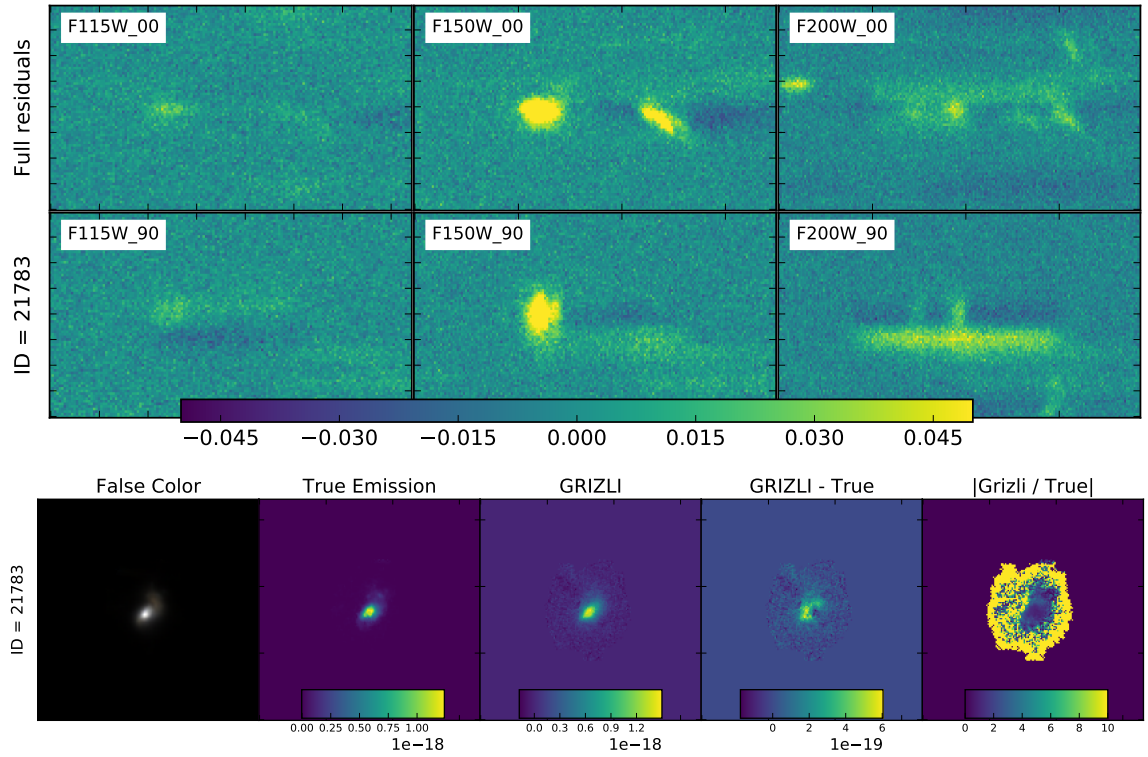

Figure 4.6: Same as Figure 4.5 except for galaxy 21783.

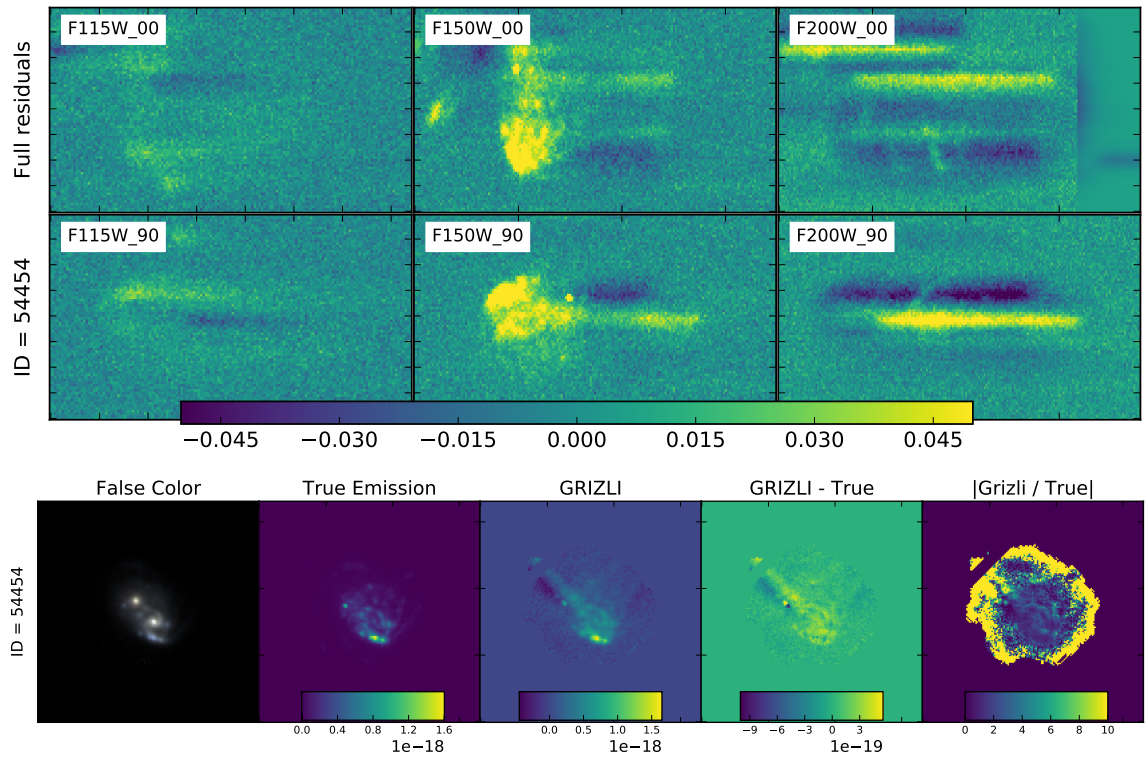

Figure 4.7: Same as Figure 4.5 except for galaxy 54454.

In addition to resolving line emission maps, NIRISS is capable of measuring grism redshifts. Typically, NIRISS observations will be supplemented by a large array of broadband photometry (both from JWST and from ancillary data). The broadband observations would be used to get a first estimate of the photometric redshift, and then NIRISS would be used to achieve greater accuracy from the observed emission lines. However, it is possible to use just the grism spectra observed by NIRISS to estimate redshift as well. GRIZLI does this by comparing the observed spectra to several template spectra, each representing a different galaxy type (e.g. old age, intermediate age, post-starburst). In Figure 4.8 we compare the input redshift and that measured by GRIZLI. We find a normalized median absolute deviation (σ_{NMAD}; Brammer, van Dokkum & Coppi, 2008) of 0.0012, commensurate with previously found values for grism redshifts (0.0012 to 0.0035 Brammer et al., 2012; Kriek et al., 2015). However, there are twelve catastrophic outliers (here defined as $\Delta z/(1+z) \geq 0.15$; Rafelski et al., 2015), or approximately 5%. This appreciable fraction emphasizes the need to supplement grism data with photometry, though see also discussions in Rafelski et al. (2015) and Kriek et al. (2015) regarding catastrophic grism redshifts.

In Figure 4.9 we show how the measured flux compares to the input flux for three emission lines: Hα, Hβ, and OIII. In concordance with the excess seen in the three displayed emission line maps, we find that GRIZLI tends to over-estimate the Hα line flux for all galaxies. It does not over-estimate Hβ, but does for OIII. The red dashed line in the top and bottom panels shows a best fitting slope of 1.37, or a 37% bias in flux estimation from GRIZLI. The accuracy of the Hβ line, combined with the excess emission shown for galaxy 8133 even when the continuum is well-modeled, mean that the excess must stem from how GRIZLI defines the flux in each line, rather than a fundamental short-coming in measuring the integrated flux from 2D grism spectra. Perhaps of note, Kriek et al. (2015) found that 3D-HST fluxes were greater than MOSDEF grism flux estimates by 13% on average, again suggesting a calibration difference. The Hα-Hβ ratio plotted in Figure 4.10 unsurprisingly shows that GRIZLI's estimation is on average above the true input ratio. The red dashed line here shows the same slope of 1.37 as in Figure 4.9.

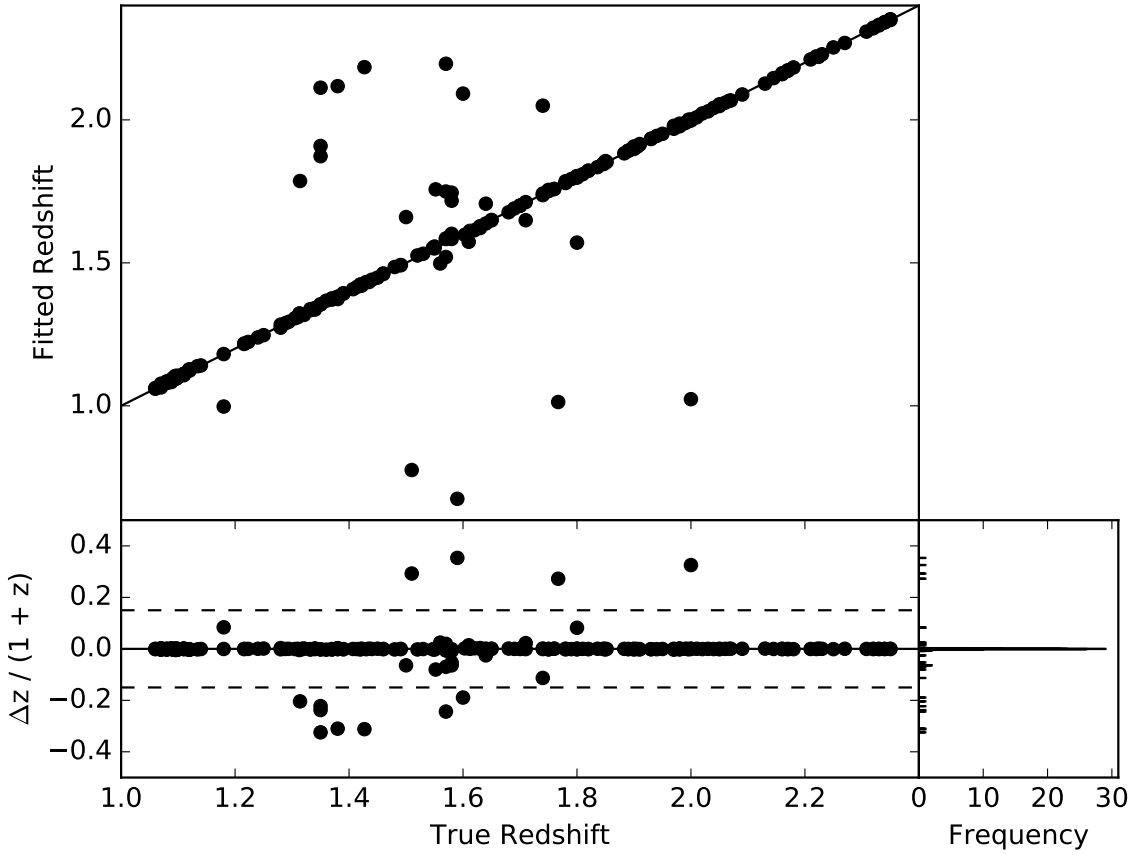

Figure 4.8: *Top:* Comparison of true input redshifts versus those fit by GRIZLI by fitting template spectra to the mock grism observations for 236 galaxies between $1.06 \leq z \leq 2.35$. *Bottom-Left:* Difference between true and fitted redshifts normalized by $1 + z_{true}$. Dashed lines of plus or minus 0.15 define catastrophic outliers. *Bottom-Right:* Histogram of difference plot showing the tight distribution around zero.

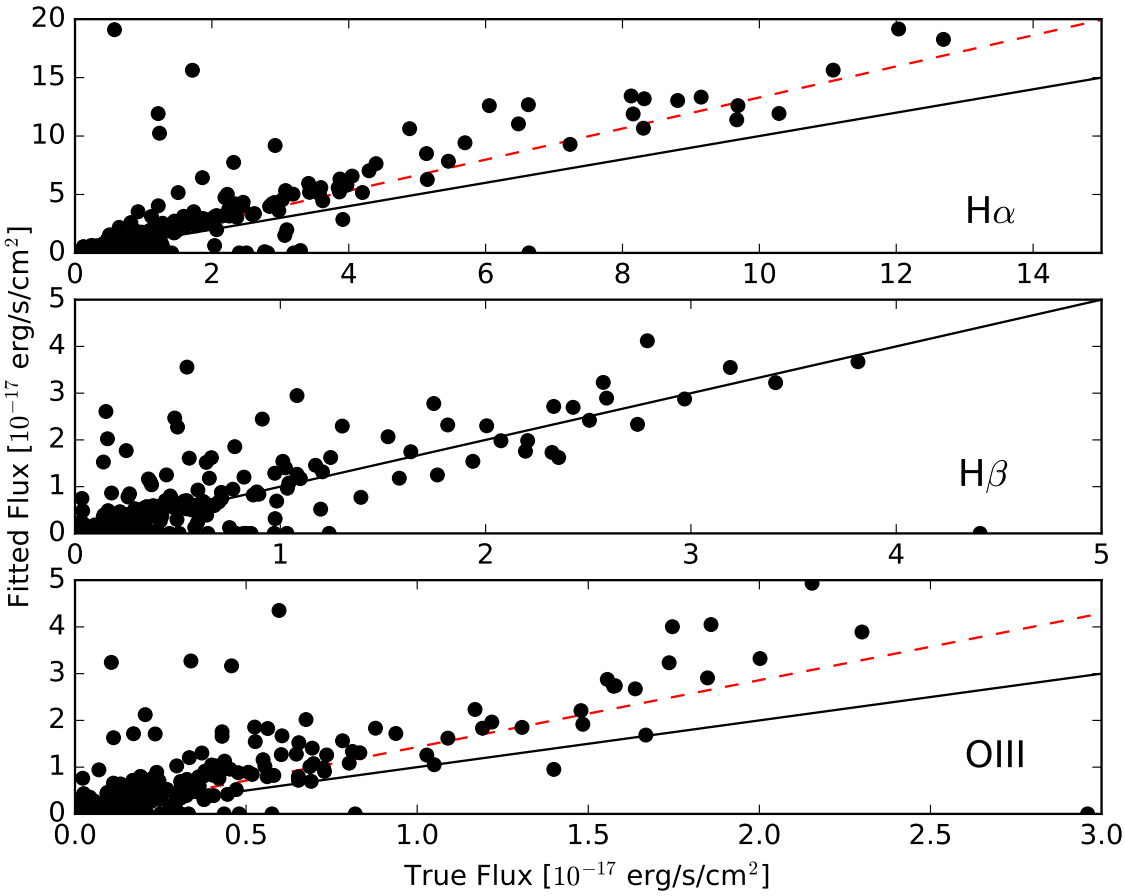

Figure 4.9: Comparison of true and measured emission line strength for, from top to bottom, Hα, Hβ, and OIII. Solid black lines display a one-to-one correspondence, and dashed red lines show a slope of 1.37.

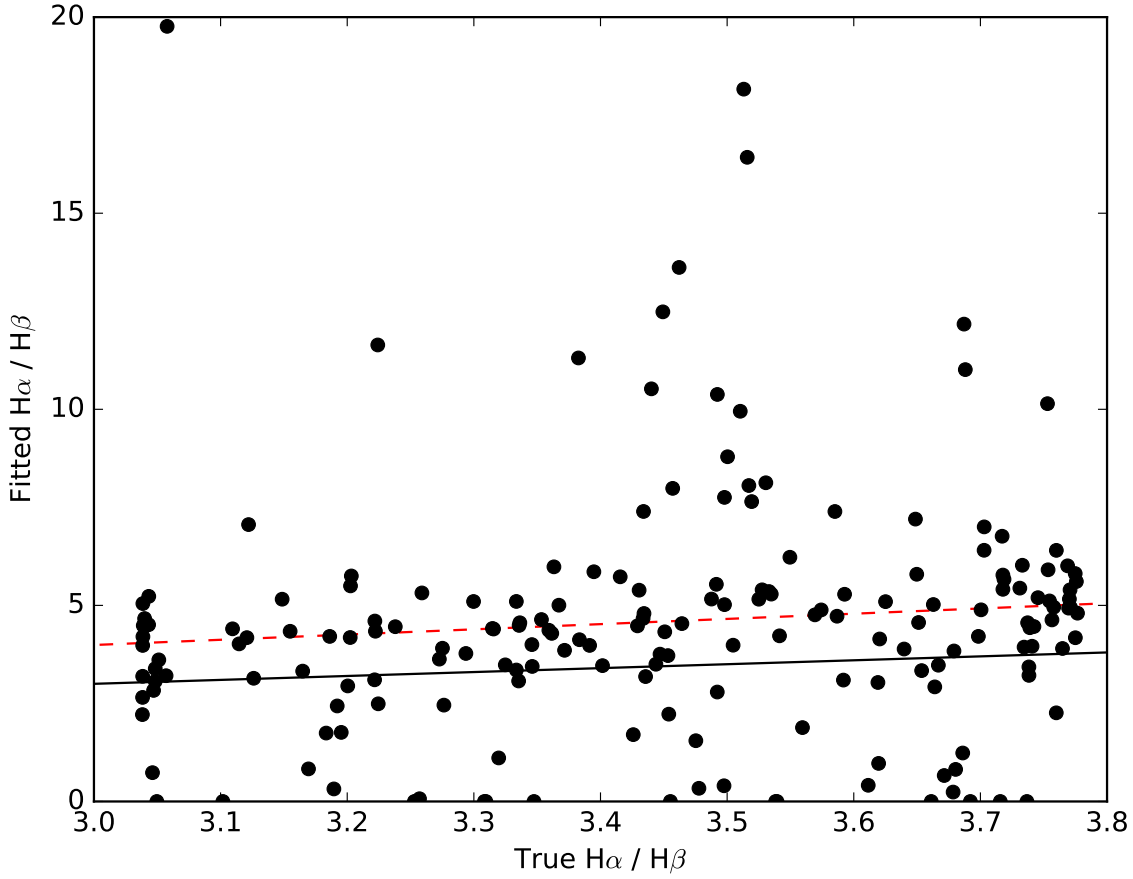

Figure 4.10: Comparison of true and fitted line ratio. Solid black line displays a one-to-one correspondence, and dashed red lines show a slope of 1.37.

Although these average offsets can be calibrated away, catastrophic failures caused by mismatched continuum models cannot. In the future, grism analysis should incorporate a method of allowing the continuum to vary across a galaxy so that different populations can be adequately modelled.

4.4 Conclusions

Grism spectroscopy is a powerful tool for astronomers, but it requires equally powerful analysis software. Through the use of realistic mock NIRISS observations, we tested the still-in-development software package GRIZLI. For galaxies with $1.06 < z < 2.36$ grism redshifts performed well, with a σ_{NMAD} of 0.0012, although with a 5% catastrophic outlier fraction. The use of supplementary broadband observations should help control the outliers, while the grisms greatly increase the accuracy of the photometric redshifts.

The continuum model GRIZLI calculates can significantly affect the measured integrated emission line flux, and greatly impacts the two-dimensional emission line maps. Often, the different spatial distribution of stellar populations within a galaxy mean that one continuum model cannot adequately model the entire galaxy. In such cases, it would be desirable for GRIZLI to implement a method of employing a spatially varying continuum.

The realistic "truth" images produced in this work are an important and necessary tool in the (ongoing) development of tools such as GRIZLI. In particular, one needs to treat galaxies as composite objects, especially for methods such as WFSS where a key feature is the ability to spatially resolve galaxies.

Chapter 5

How Future Space-Based Weak-Lensing Surveys Might Obtain Photometric Redshifts Independently

---

This chapter was originally published in 2011 in the Publications of the Astronomical Society of the Pacific, Volume 127, pp 777

DOI: 10.1086/660843

We study how the addition of on-board optical photometric bands to future space-based weak lensing instruments could affect the photometric redshift estimation of galaxies, and hence improve estimations of the dark energy parameters through weak lensing. Basing our study on the current proposed Euclid configuration and using a mock catalog of galaxy observations, various on-board options are tested and compared with the use of ground-based observations from the Large Synoptic Survey Telescope (LSST) and Pan-STARRS.

Comparisons are made through the use of the dark energy Figure of Merit, which provides a quantifiable measure of the change in the quality of the scientific results that can be obtained in each scenario. Effects of systematic offsets between LSST and Euclid photometric calibration are also studied. We find that adding two (U and G) or even one (U) on-board optical band-passes to the space-based infrared instrument greatly improves its photometric redshift performance, bringing it close to the level that would be achieved by combining observations from both space-based and ground-based surveys while freeing the space mission from reliance on external datasets.

5.1 Introduction

Over the past few years, it has been shown that approximately 74% of the energy density of the universe is in the form of dark energy (DE). Often represented as the cosmological constant Λ in Einstein's theory of general relativity, DE causes the expansion of the Universe to accelerate (see Copeland, Sami & Tsujikawa, 2006, for a review). A great deal of effort is being put into constraining the DE equation of state parameters in order to better understand the phenomenon. One promising method of placing high accuracy constraints on the DE parameters is through weak lensing, which involves measuring the shape of numerous galaxies over a large area of the sky (e.g. Blandford et al., 1991; Bartelmann & Schneider, 2001; Refregier, 2003).

An important source of error in the weak lensing analysis comes from uncertainties in the photometric redshift (photo-z) estimation to each galaxy, which is required to form a three dimensional map. While they are less accurate than spectroscopic redshifts (spec-zs), the extremely large area (20 000 deg^2) planned for future dark energy surveys necessitates the use of photo-zs (see Hildebrandt et al., 2010, for a summary of current photometric redshift techniques and capabilities). The effects of photo-z uncertainties on weak lensing were studied by Huterer et al. (2006), who placed stringent constraints on the degree of accuracy and precision required in order for the redshift estimations to be useful in tomography.

Indeed, current goals state that the standard deviation of the photo-zs must be less than $0.05(1+z)$ and that any bias in the photo-zs must be known to a degree of $0.002(1+z)$. Ma, Hu & Huterer (2006) found that in order to satisfy these criteria, a large spectroscopic survey (on the order of $\sim 10^5$ galaxies) must be carried out to properly calibrate the photometric redshifts. Several works since then have found that the amount of spectroscopy needed can be reduced by optimizing the spectroscopic survey to cover important redshift ranges (Ma & Bernstein, 2008; Sun et al., 2009; Bernstein & Huterer, 2010), while Bordoloi, Lilly & Amara (2010) studied how the photo-zs themselves can be used for calibration.

Because of confusion between breaks, photometric redshifts are especially prone to catastrophic outliers, which can greatly impact the weak lensing analysis (Sun et al., 2009; Bernstein & Huterer, 2010). It was found that the number of catastrophic outliers can be greatly reduced if ground-based photometry (u,g,r,i,z,y) is complimented with near-infrared (NIR) photometry (Abdalla et al., 2008; Nishizawa et al., 2010). To this aim, both WFIRST and Euclid, two space-based instruments that will study weak lensing, will include a NIR channel to facilitate accurate photometric redshifts. However, in their current state, neither instrument can obtain accurate photo-zs by itself. Instead, they must rely on complimentary observations from ground-based instruments (such as the proposed Large Synoptic Survey Telescope, LSST, or the Panoramic Survey Telescope and Rapid Response System, Pan-STARRS). Various complications may arise from trying to combine such a large amount of data from two or more observatories, and it may be beneficial if a space-based instrument could produce its own optical observations.

In this work, we study how future space-based weak lensing missions may benefit from the addition of on-board optical photometry. We do this in the context of the current Euclid design in order to ground our results in reality, but the conclusions could apply just as well to WFIRST or any other future weak lensing instrument. Euclid is comprised of both a visual (VIS) channel and a near infrared (NIR) channel. The proposed VIS channel is made of a very broad filter (RIZ) which covers the wavelength range 0.55-0.92μm and will be used primarily to measure galaxy shapes for weak lensing. The NIR photometric channel

includes three band-passes (Y, J, and H) and spans wavelengths from 1.0 to 1.6μm.

While one could design a highly-optimized, multi-element on-board filter system, our aim, instead, is to explore simple scenarios that result in relatively small perturbations to the current Euclid instrument and mission design. To this end we explore the impact of adding two on-board optical band-passes (U and G) to Euclid and compare them to the results one would obtain by augmenting Euclid observations with ground-based optical observations. In Section 2, we detail the method with which we simulate a catalog of observed galaxies and generate photometric redshifts for each of the galaxies. In Section 3 we present the photometric redshift distribution of various filter combinations and compare these with the expected results of combining observations from Euclid with either LSST or Pan-STARRS using the dark energy Figure of Merit (FoM). Finally, we discuss the effects of any systematic offsets between the Euclid and ground-based observations on the weak lensing analysis.

5.2 Method

5.2.1 Mock Catalog

In order to study the effect of space-based optical observations, we first needed a catalog of galaxies to be observed. Ideally, this catalog would have realistic redshift, color, and luminosity distributions in order to accurately model the galaxy population and its photometric redshift distribution. To this aim, we chose to use the COSMOS Mock Catalog (CMC; Jouvel et al., 2009). This catalog draws upon observations from the COSMOS Deep Field (Capak et al., 2007) and the photometric redshift catalog of those galaxies (Ilbert et al., 2009). By combining the best fitting redshift and extinction with observable properties such as galaxy type and half-light radius (Leauthaud et al., 2007), the CMC is by construction representative of a real galaxy survey.

The CMC best-fitting spectral energy distribution (SED) templates were generated similarly to Ilbert et al. (2009) which used template libraries of both Polletta et al. (2007) and

Bruzual & Charlot (2003). The Polletta et al. (2007) templates include SEDs of elliptical and spiral galaxies, whereas the Bruzual & Charlot (2003) templates model starburst galaxies with ages ranging from 3 to 0.03 Gyr. Additional extinction was applied to the templates using the Calzetti et al. (2000) extinction law with $E(B-V)$ values of 0, 0.05, 0.1, 0.15, 0.2, 0.35, 0.3, 0.4, and 0.5.

In summary, the CMC provides best-fitting spectra and observed properties of 538 000 galaxies from the COSMOS-ACS catalog and covers an effective area of 1.24 deg^2. It has a maximum redshift of $z = 3.64$ and a median redshift of 0.96. The COSMOS mock catalog is limited by the completeness of the COSMOS imaging ($i^+_{AB} \sim 26.2$ for 5σ detection, Capak et al. 2007).

5.2.2 Simulating Observations

The proposed observational strategy for Euclid involves taking 4 dithered exposures of each field, with the total integration time of each dither being approximately 700s (Duvet, 2010). Euclid is designed such that the VIS and NIR channels can observe simultaneously. In order to limit the number of moving parts during the VIS integration, the NIR spectrometer and the VIS channel will observe first (with an integration time of $\sim$ 540s) after which the NIR photometry bands will observe sequentially (integration times given in Table 5.1). All of our simulations for Euclid observations assume this observational strategy.

We studied photo-z performance with several Euclid U+G channel configurations as outlined in a recent CSA-sponsored study (Rowlands, Lin & Aldridge, 2011). We first assumed a best-case scenario where two dichroics split the VIS channel light such that the RIZ, G, and U filters can all observe simultaneously (i.e. three separate detectors). However, we also tested other scenarios: one where we removed one detector and dichroic and put the U and G filters on a filter exchanger so that they must share integration time, and another where all the filters are on an exchanger and all feed the same single detector. Finally, we also considered scenarios in which only one additional on-board filter — either U or G — is used.

Filter	Wavelength (nm)	Obs. Time (s)	Total Throughput (%)
U	300 - 440	542	0.35
G	440 - 550	542	0.5
RIZ	550 - 920	542	0.59
Y	920 - 1146	88.5	0.45
J	1146 - 1372	107.4	0.45
H	1372 - 2000	61.8	0.45

Table 5.1: Description of filters used in simulations for Euclid. Total Throughput is estimated to include all photon losses through the system. Each filter is approximated as a box function. The U and G observation times listed are for the scenario where each of these filters feeds a dedicated detector; U and G observation times are shorter for other scenarios, as described in the text.

Assuming that the best-fitting SED from a galaxy in the CMC is the "true" signal from the galaxy, we simulated the observed magnitude of each galaxy in each of the Euclid filters (properties shown in Table 5.1) by adding a random noise component to the "true" signal measured through each filter.

Our method of estimating noise follows closely that described in the appendix of Jouvel et al. (2010), but a brief outline is given here. First, we calculated the expected signal to noise ratio (S/N). For space-based observations, the S/N can be found by

$$\frac{S}{N} = \frac{e_{\rm signal}}{\sqrt{e_{\rm signal} + e_{\rm sky} + N_{\rm pix} N_{\rm exp} {e_{\rm RON}}^2 + N_{\rm pix} N_{\rm exp} t_{\rm obs} e_{\rm dark}}}. \tag{5.1}$$

Here, $e_{\rm signal}$ is the number of electrons produced in the device by the galaxy flux. The noise contributions in the denominator include Poissonian noise from the source as well as the background zodiacal light ($e_{\rm sky}$), the dark current caused by the thermal radiation of the instrument ($e_{\rm dark}$), and also the read-out noise of the detector ($e_{\rm RON}$) which follows a Gaussian statistic. $N_{\rm pix}$ is defined to be the number of pixels contained within a circular area of 1.4 times the observed full width at half maximum of the galaxy, and $N_{\rm exp}$ is the number of exposures (4 as planned in the Euclid survey) and $t_{\rm obs}$ is the exposure time. For the VIS channel, we use $e_{\rm dark}$=0.03 electrons per second, $e_{\rm RON}$ = 6 electrons, and assume

0.1 arcsecond pixels, whereas for the NIR we assume $e_{\rm dark}$=0.05 electrons per second, $e_{\rm RON}$ = 5 electrons, and 0.3 arcsecond pixels. The on-board optical U and G channel is assumed to have the same pixel scale as the NIR channel (0.3 arcsecond pixels), but the RON and dark current of the VIS channel.

Once the theoretical S/N is determined, we simply added an error term to the true magnitude of the galaxy which is drawn from a Gaussian distribution of mean $\mu = 0$ and standard deviation $\sigma = \frac{2.5}{\ln(10)}\frac{1}{S/N}$. In this way, realistic observational uncertainties are included in our final simulated observations, as is demonstrated in Figure 5.1. By comparing Figure 5.1 with results from other radiometric performance simulations of Euclid (the Euclid Reference Payload Concept Document (Duvet, 2010) predicts a S/N of 14.3 for the RIZ filter at a magnitude of 24.5, and 7.1 for the IR filters at magnitude 24), we are confident that our noise generation procedure produces reasonable results.

For ground-based LSST observations our error simulations followed a different approach. In accordance with Ivezic et al. (2008), the expected photometric error for a single observation of a galaxy is given by

$$\sigma_{LSST}{}^2 = \sigma_{sys}^2 + \sigma_{rand}^2 \tag{5.2}$$

where $\sigma_{sys} = 0.003$ and σ_{rand} is given by

$$\sigma_{rand}{}^2 = (0.04 - \gamma)x + \gamma x^2 \tag{5.3}$$

with $x = 10^{0.4(m-m_5)}$. Here m_5 is the 5σ depth for point sources in a given band and γ is based on factors such as the sky brightness and readout noise. Values for m_5 and γ can be found in Table 5.2. To account for repeat observations, σ_{rand} is divided by 10 to give the error after 100 observations. In a similar fashion to the space based observations above, an error term was added to each of the model magnitudes, which is drawn from a Gaussian distribution but now with $\sigma = \frac{\sigma_{LSST}}{10}$. Gaussian errors for Pan-STARRS are assumed to have the same form as those for LSST, but have been adjusted to match the sensitivities given in Abdalla et al. (2008) for a Pan-4 like scenario (Table 5.2).

Filter	m_5(LSST)	γ	m_{10}(Pan-4)
u	23.9	0.037	–
g	25.0	0.038	25.9
r	24.7	0.039	25.6
i	24.0	0.039	25.4
z	23.3	0.040	23.9
y	22.1	0.040	22.3

Table 5.2: The LSST parameters used in Equation 5.2 (Ivezic et al., 2008) as well as the 10σ magnitudes assumed for Pan-STARRS (Abdalla et al., 2008).

From the "true" signals of the CMC, we thus created a catalog of realistic observations for LSST, for Pan-STARRS, and for Euclid combined with a proposed on-board $U + G$ optical channel.

5.2.3 Photometric Redshifts

From the noisy observations, we then calculated a photometric redshift to each galaxy for various filter combinations. The photometric redshifts were estimated by comparing the simulated observed broadband photometry with a grid of the model SEDs from the CMC. While this creates a situation where our model SED templates perfectly match the "reality" of the CMC galaxies, and therefore over-estimates the photo-z quality, we feel this is an unavoidable approach. While some systematic effects of choice of SED templates are known (for example, the BC03 templates are thought to under-estimate stellar mass due to a poor treatment of the thermally pulsating asymptotic giant branch phase (Bruzual, 2007), most are not well understood. It would therefore be very difficult to realistically model the scatter and possible bias of the photometric redshift estimates as a consequence of our choice of model templates. We chose to instead focus on contributions to the photo-z error resulting from random photon statistics and possible systematic instrument calibration errors, but acknowledge that the photo-zs given here may be slightly worse in reality because of imperfect SED templates.

To calculate the photometric redshifts, we used the SEDfit software package (Sawicki,

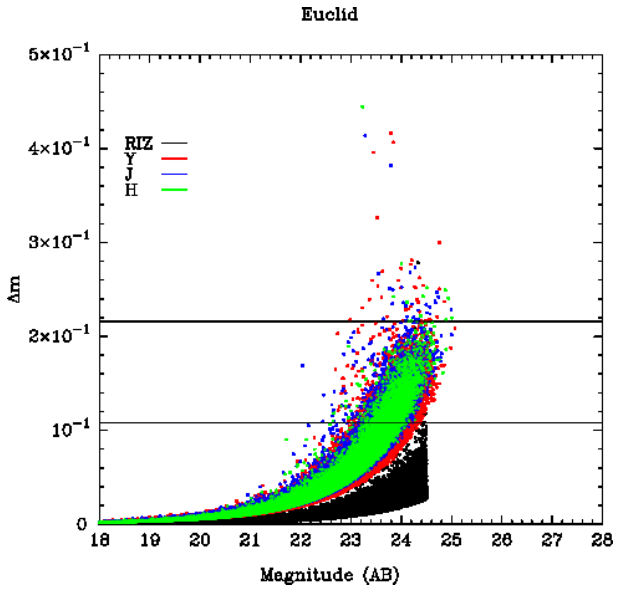

Figure 5.1: Uncertainty versus "observed" magnitude for objects with RIZ magnitude less than 24.5. Horizontal lines mark the 10-σ and 5-σ uncertainties.

2012a). This software redshifted the CMC model spectra onto a grid of redshifts spanning $0 \leq z \leq 6$ in steps of 0.02 and attenuated them using the Madau (1995) prescription for continuum and line blanketing due to intergalactic hydrogen along the line of sight. It then integrated the resultant observer-frame model spectra through filter transmission curves to produce model template broadband fluxes. In order to match the model template fluxes to the simulated observations, the observed fluxes of each object were compared with each template in the grid by computing the statistic

$$\chi^2 = \sum_i \frac{[f_{obs}(i) - s f_{tpt}(i)]^2}{\sigma^2(i)}, \tag{5.4}$$

where $f_{obs}(i)$ and σ(i) are the observed flux and its uncertainty in the ith filter, and $f_{tpt}(i)$ is the flux of the template in that filter. The variable s is the scaling between the observed and template fluxes, and can be computed analytically by minimizing the χ^2 statistic with respect to s giving

$$s = \frac{\sum_i f_{obs}(i) f_{tpt}(i)/\sigma^2(i)}{\sum_i f_{tpt}^2(i)/\sigma^2(i)} \tag{5.5}$$

(Sawicki 2002). For each object, the most likely redshift is determined by the smallest χ^2 value over all the templates. Error bars are generated by refitting the object 200 times with slightly perturbed photometry and finding the range in which 68% of the fits lie.

5.2.4 Figure of Merit

In order to objectively compare the different observational scenarios, we employ the DE Figure of Merit (FoM) proposed by the Dark Energy Task Force (DETF). This number is the inverse of the area of the 2-σ uncertainty ellipse in the plane of the DE parameters w_0 and w_a. The FoM is thus a statement on the precision of the DE measurements, not necessarily the accuracy.

We used the iCosmo package (Refregier et al., 2008) to calculate the FoM for each of our survey scenarios assuming a flat cosmology with fiducial cosmological parameters of $(\Omega_m, w_0, w_a, h, \Omega_b, \sigma_8, n_s, \Omega_\Lambda) = [0.3, -0.95, 0, 0.7, 0.045, 0.8, 1, 0.7]$, an intrinsic ellipticity dispersion of 0.25, and 10 tomographic redshift bins. The calculations are done using only the weak lensing power spectrum which is summed over $10 \leq \ell \leq 20000$, and the $w_0 - w_a$ uncertainty is marginalized over the other five parameters without any external priors.

To orient our comparisons, the Euclid Science Book (Refregier et al., 2010) states that the current FoM is on the order of 10, which is generated using WMAP observations combined with Baryon Acoustic Oscillation (BAO) and Type Ia supernova distance measurements, as well as a prior adopted in accordance with Big Bang Nucleosynthesis (Komatsu et al., 2009). This is the FoM value currently achieved by combining several available DE probes; in contrast, in the rest of the paper we presenting FoM values attainable from weak lensing observations alone, without the inclusion of other probes available now or in the future.

A FoM generated *solely* from a weak lensing survey using both space-based and ground-based observations is expected to be approximately 180 (see Table 4.1 in Euclid Science Book), over an order of magnitude greater than the current figure. However, values can vary depending on the parameters and methods used to estimate the expected FoM. For

example, Amara & Refregier (2007) obtain a FoM of only 50 for a survey with properties similar to what is expected with Euclid plus ground-based observations (20 000 deg^2 area, 35 gals/arcmin^2, median redshift of 0.9). Regardless, if all cosmological probes observable with Euclid are utilized then the FoM increases to ~ 400, and well over 1000 with the use of external prior constraints derived from Planck.

It is informative to discuss how various parameters of the photometric redshift distribution affect the FoM. Amara & Refregier (2007) have shown that the FoM is almost directly proportional to the number density of galaxies in the photometric redshift catalog. However there is a trade-off between a wide and a deep survey, as they show that the FoM also depends strongly on the median redshift of the photo-z distribution (FoM $\propto z_m^{1.2}$). The figure of merit also degrades as the precision of the photometric redshifts decreases (FoM $\propto 10^{-1.69\sigma_z}$) and as the fraction of objects with catastrophic redshift errors (F_{cata}) increases (FoM $\propto 10^{-0.75F_{cata}}$). It is clear that accurate and precise photo-zs are important if a respectable FoM is to be obtained.

5.3 Results

In this work, we used the above procedure to create a catalog of observations for each galaxy in the mock catalog, but limited ourselves to analyzing only those galaxies that have an AB magnitude less than 24.5 in the RIZ channel. We studied three options for a weak lensing survey: 1) using only the filters currently planned for the Euclid instrument (RIZ shape channel, Y, J and H), 2) the Euclid filters plus additional on-board optical filters U and G, and 3) the Euclid IR filters (Y, J, H) plus ground-based observations from either Pan-STARRS ($grizy$) or LSST ($ugrizy$). The first scenario was done strictly for comparison and is not expected to yield usable photometric redshifts since it has no optical observations. The second scenario we divided into several sub-cases in which we examined the impact of different exposure times with the two optical filters and also the effect of not using the RIZ shape channel for photometry. For the last case we preferentially used

LSST for the ground based observations, since we found similar although slightly worse photometric redshift results using Pan-STARRS (see also Abdalla et al. 2008). A summary of the scenarios and results is presented in Table 5.3. The median redshift for all cases is 0.8.

Scenario	Filters	Culling	N_{gal}	$\sigma_{\Delta z/1+z}$	F_{cata}	FoM
Euclid	RIZ, Y, J, H	N	32.2	0.951	0.3985	< 5
		Y	2.3	0.114	0.0126	< 5
Euclid + Optical	U, G, RIZ, Y, J, H	N	32.2	0.052	0.0043	122
		Y	31.6	0.037	0.0016	126
Euclid + Optical (50:50 U:G time split)	U, G, RIZ, Y, J, H	N	32.2	0.071	0.0090	113
		Y	30.8	0.046	0.0029	119
Euclid + U Only	U, RIZ, Y, J, H	N	32.2	0.126	0.0414	85
		Y	25.7	0.062	0.0063	100
Euclid + G Only	G, RIZ, Y, J, H	N	32.2	0.199	0.0919	58
		Y	19.7	0.059	0.0047	67
Euclid + Pan-1	g, r, i, z, y, Y, J, H	N	32.2	0.299	0.098	41
		Y	24.8	0.102	0.027	72
Euclid + Pan-4	g, r, i, z, y, Y, J, H	N	32.2	0.175	0.039	70
		Y	30.1	0.070	0.010	105
Euclid + LSST	$u, g, r, i, z, y, Y, J, H$	N	32.2	0.030	0.0011	131
		Y	32.2	0.024	0.0003	133
Euclid + LSST with ZP errors	$u, g, r, i, z, y, Y, J, H$	N	32.2	0.032	0.0011	130
		Y	32.2	0.025	0.0004	132

Table 5.3: Description and comparisons of various survey scenarios. Culling is defined as removing any objects with photo-z error bars greater than 0.5.

5.3.1 Euclid Alone

The currently proposed strategy for Euclid has chosen to rely on other ground-based projects to obtain optical measurements for photometric redshift estimation. The optical wavelength observations are required in order to obtain accurate low redshift photo-zs by detecting the various breaks in a galaxy's SED as they appear in our observer frame. It is well understood that without any optical band-passes, virtually no constraints can be placed on the redshifts of low-z galaxies. Thus, it is no surprise that the plot shown in Figure 5.2 contains a large number of catastrophic redshifts as galaxies with $z \leq 1$ are scattered upwards to higher redshifts. Note also that the standard deviation $\frac{\sigma_z}{1+z}$ is well above the required level of 0.05 at nearly all redshifts and the FoM is less than the present-day value. Obviously, results can be improved by culling galaxies that have low-quality photometric redshift estimates, as shown in Figure 5.3 where any galaxy with an uncertainty Δz_{phot} greater than 0.5 has been removed. Removal of poorly constrained galaxies can be a trade-off, as it tightens up the spread of the photo-zs and thus raises the FoM, but it also reduces the number density of galaxies which acts to lower the FoM. However, in this scenario, culling of poorly fit galaxies results in the removal of almost all galaxies needed for weak lensing in the target range of $0.3 \leq z \leq 2$, resulting in a poor FoM.

The point of this exercise is to emphasize that when it is said that Euclid will rely on ground-based observations, it is *fully* reliant in that a weak lensing DE survey will not be possible without optical photometry from other telescopes.

5.3.2 Addition of an On-board U and/or G Channel

Figure 5.4 shows the drastic improvement in photometric redshifts that can be found with the addition of two on-board optical band-passes to Euclid. The ability to discriminate low-z galaxies from high-z ones is invaluable. While the overall standard deviation is still rather high ($\frac{\sigma}{1+z} > 0.05$) due to the number of catastrophic failures at low redshift, a simple culling of untrustworthy galaxies ($\Delta z_{phot} < 0.5$) brings this down to below the required level

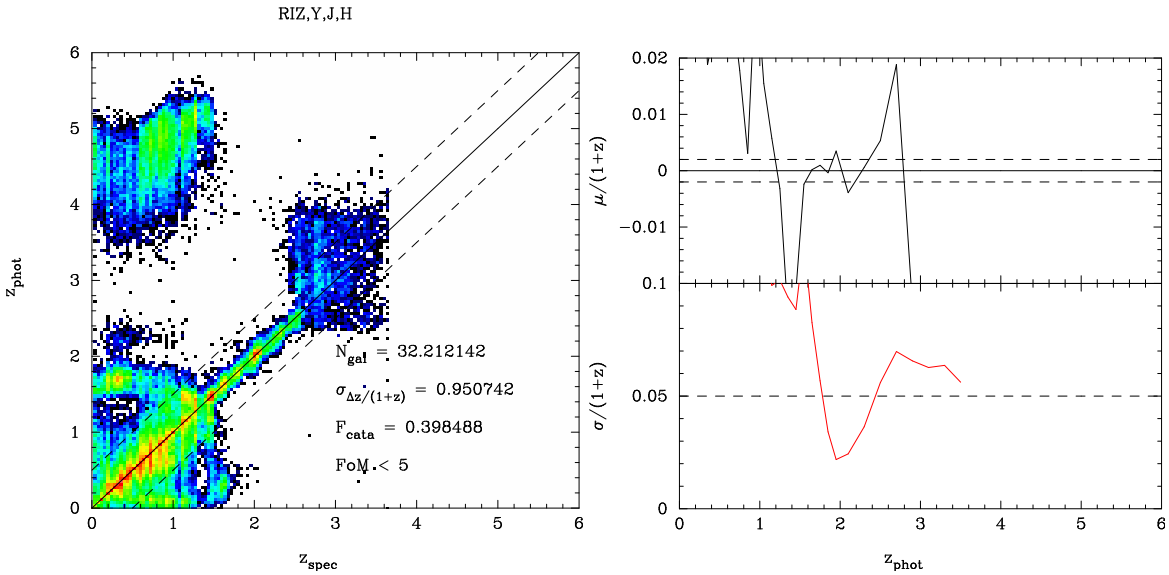

Figure 5.2: Left: Photometric redshift as a function of spectroscopic redshift using only Euclid's RIZ, Y, J and H band-passes. N_{gal} is the number density of galaxies per arcmin^2, $\sigma_{\Delta z/(1+z)}$ is the overall standard deviation for all galaxies, and F_{cata} is the fraction of catastrophic redshifts defined to be $\Delta z > 0.3$ (shown by the dashed diagonal lines). Right: Standard deviation (σ) and bias (μ) of the photometric redshifts scaled by $1 + z$ as a function of redshift; the bias does not include any corrections which may be possible through spectroscopic calibration. The dashed horizontal lines in the μ and σ panels show the scientific requirements for a weak lensing survey. The FoM for this scenario is less than 5.

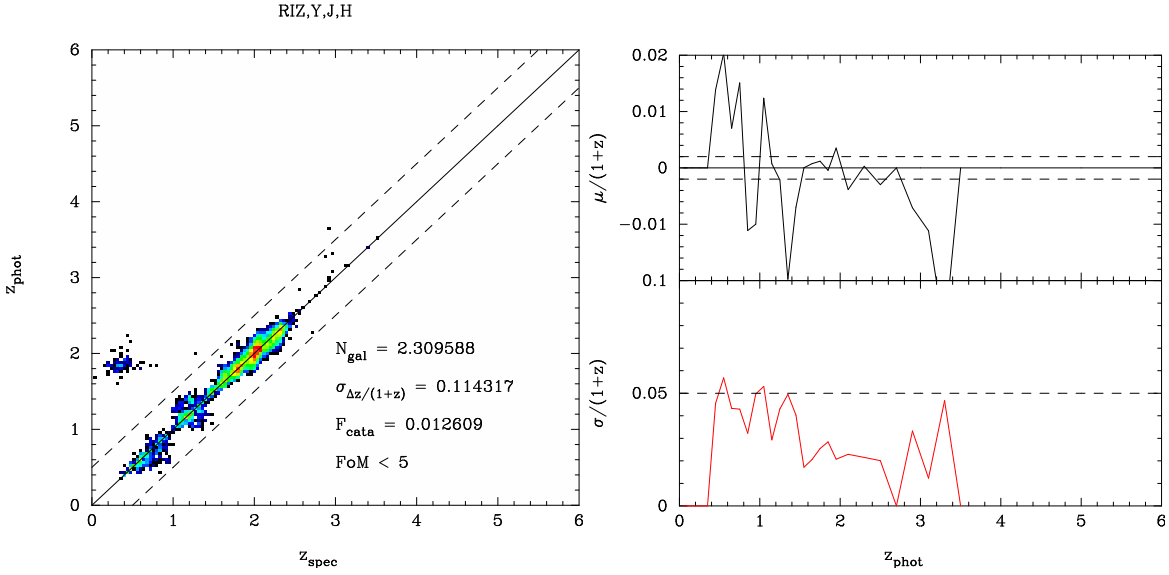

Figure 5.3: Same as Figure 5.2 except culling galaxies which have a poorly constrained photometric redshift with error bars greater than 0.5.

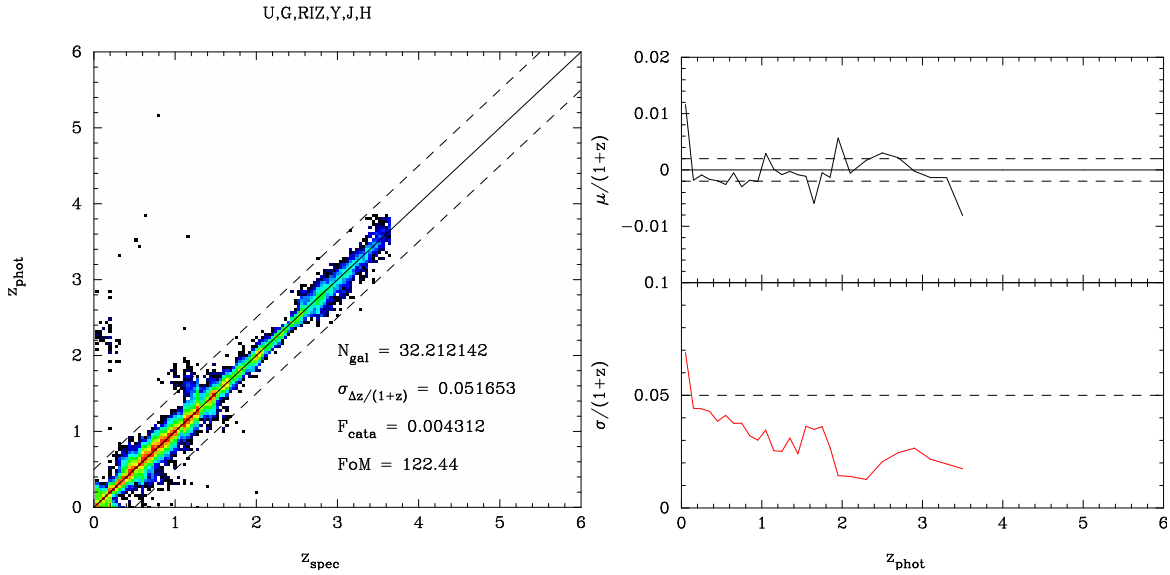

Figure 5.4: Same as Figure 5.2 except with the addition of U and G band-passes.

as shown in Figure 5.5. The right panels of Figures 5.4 and 5.5 demonstrate that even if the overall standard deviation is high, the standard deviation as a function of redshift can still be below the required value in the key redshift range for weak lensing ($0.3 \leq z \leq 2$). The resulting FoMs of 122 and 126 for the raw and culled scenarios respectively make it clear that the addition of on-board optical band-passes could make Euclid self-sufficient for weak lensing. Although observations from other instruments could of course still be used, Euclid would no longer be completely reliant on them.

In the above scenario, both the U and G filter feed dedicated detectors and so have the maximum exposure time available ($\sim$ 500s, the same as the RIZ shape channel). If the two optical bands cannot observe simultaneously, but instead have to share observation time as might be the case if a single detector plus a filter exchange mechanism were used, this will have a negative impact on the photometric redshift estimations. Figure 5.6 shows that the optimal time-sharing arrangement would be approximately an even division of time. The FoM has a maximum at near 50% observing time in each band of 118.84. The photometric redshift distribution of this best-case scenario is shown in Figure 5.7.

The FoM stays at roughly the same level ($115 < FoM < 119$) until the observing time

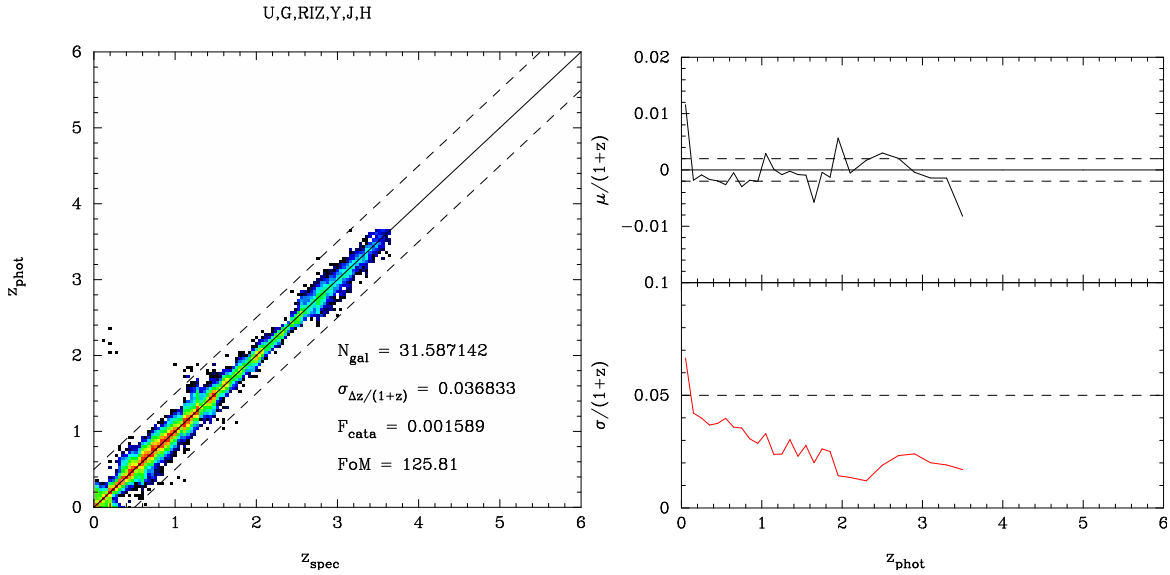

Figure 5.5: Same as Figure 5.2 except with the addition of U and G band-passes and culling galaxies with photo-z error bars greater than 0.5.

percentage drops below 30% in either band. At the extreme ends of sharing scenarios, it is clear that U band observations are more critical than G band observations, as the FoM with nothing but G is 67.4, much less than the FoM = 100.1 for solely U band observations. The larger FoM comes from the better constraints the U band can place on the lowest redshift galaxies. In order to determine if two optical filters are absolutely necessary, we also tested a scenario with a broad filter that combined the U and G wavelengths which resulted in a FoM of 87.86. While being able to estimate the photo-zs of low-redshift galaxies better than just the G band, the broadness of this merged filter led to ambiguity as to where the 4000Å break falls within the filter, and hence it was not able to break the degeneracy between low-z and high-z objects as well as simply the U filter. These results show that both a U and a G filter are required for optimal photometric redshifts. Note, however, that using just the U filter gives a fairly adequate FoM of $\sim$100 which, while not optimal, may prove to be the best compromise between the instrument's weight and complexity and the best obtainable DE constraints.

As a final scenario for Euclid, we tested the effects of splitting the broad shape channel RIZ filter into two separate filters, hereafter called R and Z and adding U and G filters

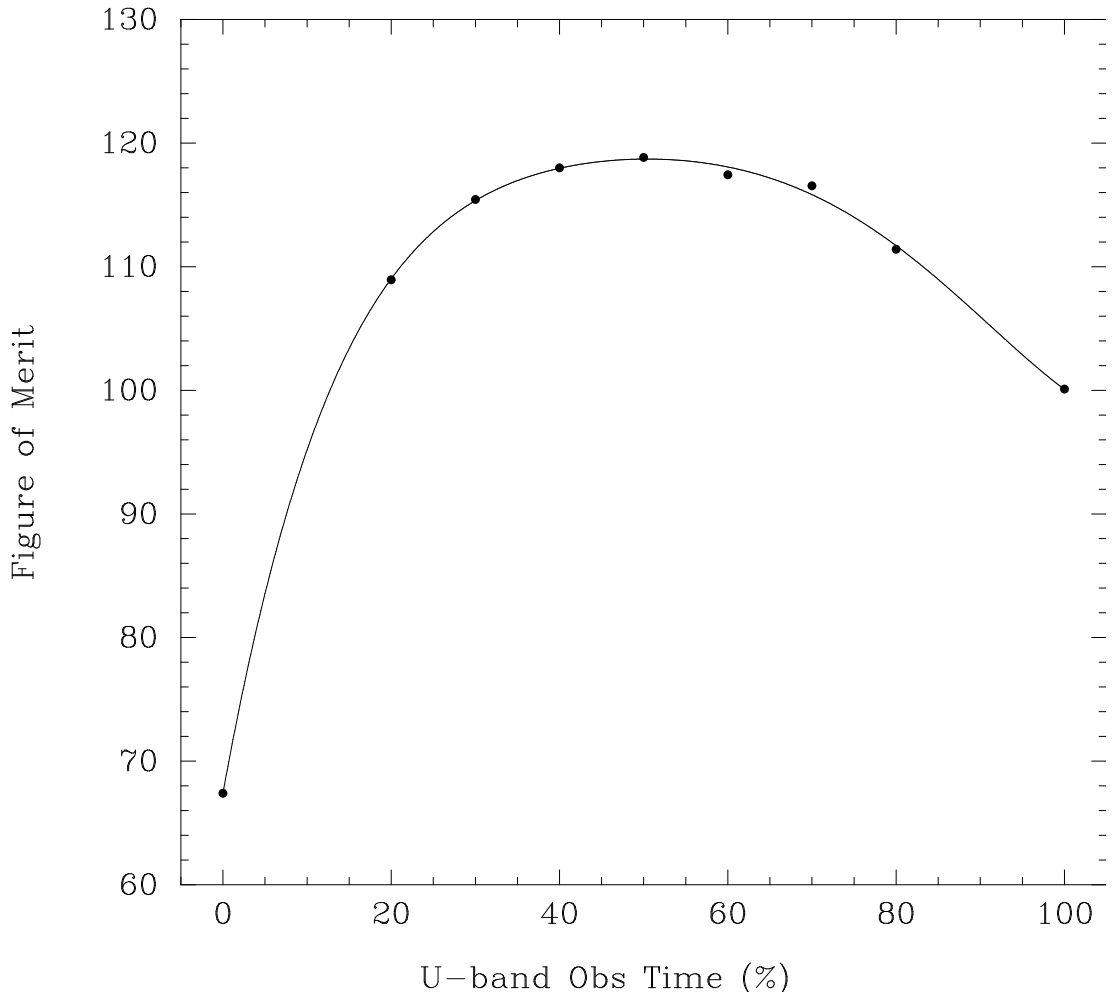

Figure 5.6: Demonstrating the effects of time sharing between the U and G filters. The plot shows how the FoM changes as the percentage of time spent observing in U-band increases. The G band observing percentage is 100 minus the U band percentage. The total observing time is 542s. The solid line is a fifth order polynomial fit to the data points.

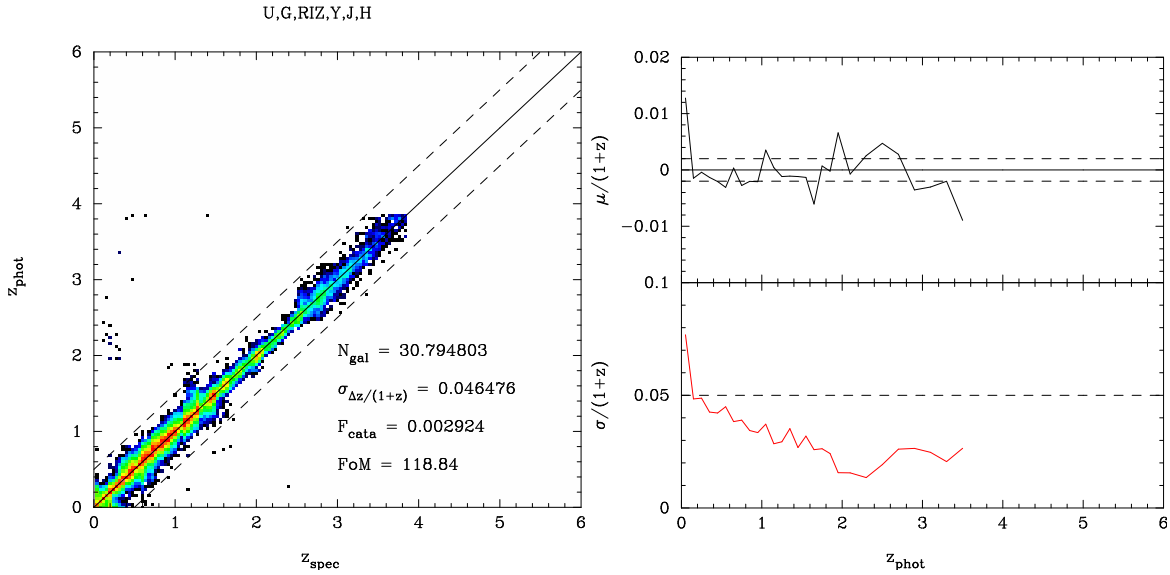

Figure 5.7: Same as Figure 5.2 except using band-passes U, G, RIZ, Y, J, H where the U and G bands each observe for only 271s (50% of the RIZ band) and galaxies with photo-z error bars greater than 0.5 have been culled.

as well. In this scenario, all the filters feed one detector and would be mounted on a filter wheel. Euclid's planned total observing time per dither is fixed at ∼700s, which was divided among the U, G, R and Z filters allowing ten seconds to account for the time taken to change filters. We found that using four filters (U, G, R, and Z) in this finite amount of time was not beneficial as the short observing time increased the signal to noise ratio. The best case we found used three filters (U, R, and Z) with the observing time split roughly evenly between the three although slightly favoring the U band (40%, 30% and 30% of the observing time in the U, R, and Z bands respectively). This layout yields a FoM of 105, lower than the scenarios with one broad shape channel and two optical bands, but slightly higher than one broad shape channel and the U band alone. However this figure is an upper limit at best, as it is uncertain if accurate shape measurements will be attainable in the R or Z band with this little observing time. If the shape channel were to be split up, a different survey strategy that allows more observation time per object may be preferable in order to increase the S/N in the observations, both for photometry and shape measurements

5.3.3 Euclid's IR plus Ground-Based Observations

For comparison, we now show what is expected to be obtainable with the use of ground-based telescopes plus the IR bands from Euclid. In these scenarios, all surveys are assumed to overlap completely and cover the same 20 000 deg^2 area. This yields a best-case result and if the overlap between Euclid's space-based survey and ground-based surveys turns out to be smaller, then the FoM would be negatively affected. In fact, the FoM scales linearly with the survey area (Amara & Refregier, 2007) so that if only half of the space-based survey overlaps with the ground-based component then the expected FoM will also be cut in half.

Figures 5.8 and 5.9 show the results for Pan-4 and LSST respectively. The Pan-4 scenario is slightly worse than the Euclid+UG case, while the LSST results are slightly better due to its deeper observations relative to Pan-STARRS. We will hence use the LSST observations for all future discussion. Abdalla et al. (2008) note that in order to obtain reliable photo-zs, shallower surveys such as DES or Pan-STARRS are not well matched to the Euclid survey, and show similar effects on the FoM due to the increased photo-z scatter from these shallower surveys.

In the interest of establishing a time frame for the desired lensing results, we investigated how long it would take LSST plus Euclid to reach the same FoM as the Euclid plus on-board optical scenario, and found that LSST needs to observe each galaxy at least 45 times to have the same FoM (126) as Euclid plus optical filters (approximately 6 months of observations with LSST). After this point, the FoM will increase as LSST makes more and more observations. We now have a simple means of estimating how many LSST observations are needed if Equation 5.2 turns out to be overly generous in reality. For example, if the LSST photometric errors turn out to be twice as large as predicted, then four times as many observations (i.e. 180 observations or $\sim$ 2 years) are needed to match the Euclid plus on-board optical FoM.

We also studied two scenarios that could detrimentally affect the LSST observations:

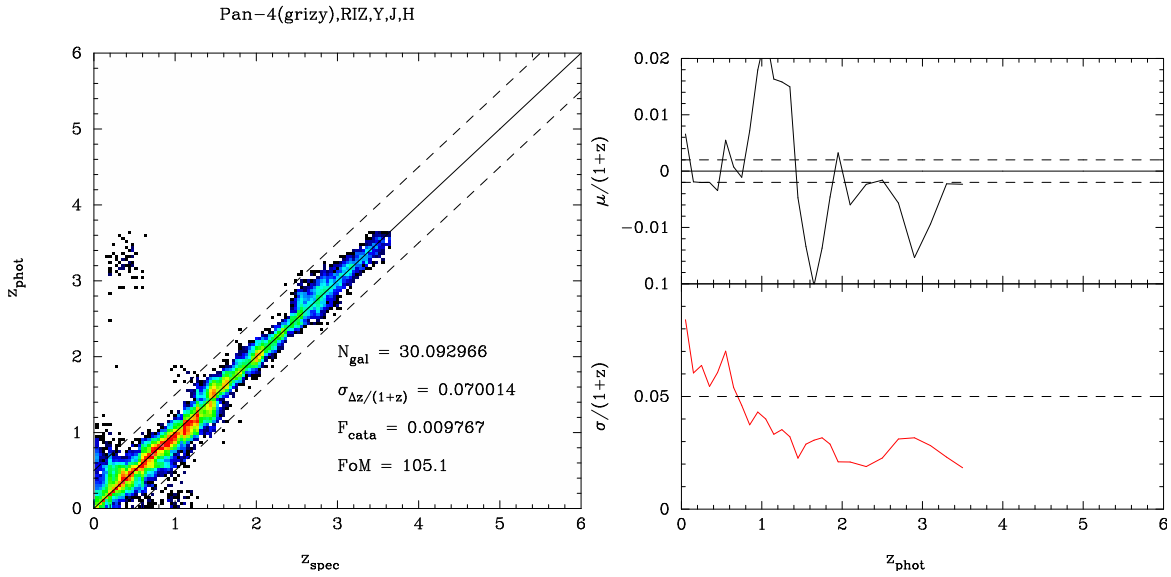

Figure 5.8: Same as Figure 5.2 except using band-passes from both Euclid and Pan-STARRS with all four mirrors and culling galaxies with photo-z error bars greater than 0.5.

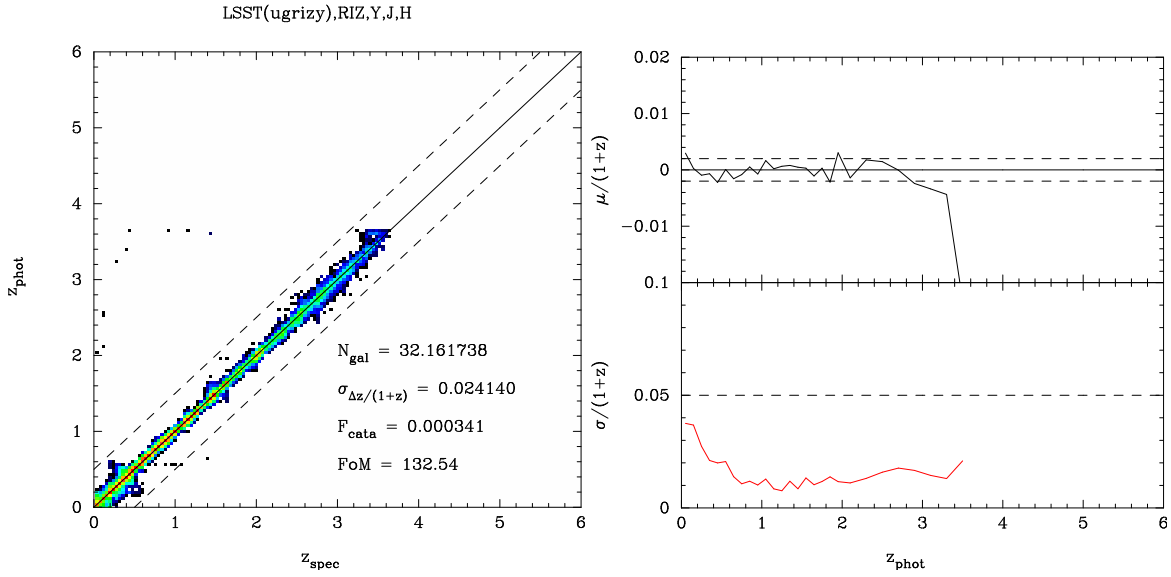

Figure 5.9: Same as Figure 5.2 except using band-passes from both Euclid and LSST and culling galaxies with photo-z error bars greater than 0.5.

Band	σ_{ZP}
u	0.05
g	0.02
r	0.02
i	0.02
z	0.03
y	0.03

Table 5.4: Standard deviations of distributions from which a random zero-point offset error was chosen to apply to each pointing from LSST

random photometric zero-point errors, and systematic zero-point offsets between ground and space observations.

The error formulation given in Equation 5.2 for LSST specifically does not include any terms for mis-calibration of the zero-point (ZP) magnitudes from field to field. To study how any field-to-field ZP errors could negatively affect the photo-zs, we use the Canada-France-Hawaii-Telescope Legacy Survey (CFHTLS; Erben et al., 2009; Hildebrandt et al., 2009) as a reference point. Each pointing of the LSST could have slight errors associated with the ZP calibration and so we divided our observational catalog into ~ 2000 fields, which is approximately the number of fields required for LSST to cover Euclid's 20 000 deg^2 survey. In each field we add a random Gaussian offset to the observed magnitudes in the various filters, where the standard deviations are similar to those found for CFHTLS (Hildebrandt, private communication) and are given in Table 5.4. This has the effect of increasing the spread in the photometric redshifts (shown in Figure 5.10) and thus slightly decreasing the FoM (though not significantly) to 132. The small deviations expected from field-to-field ZP errors are for the most part dominated by the random photometric errors. Additionally, the ZP errors are independent and thus add in quadrature with the photometric errors, leading to only slight effects in the best-fitting photometric redshifts. Their contribution is therefore almost negligible and we conclude that field-to-field ZP offsets in ground data are not likely to be an issue in DE weak lensing surveys.

There is also a possibility that the LSST ZP magnitudes could be systematically offset

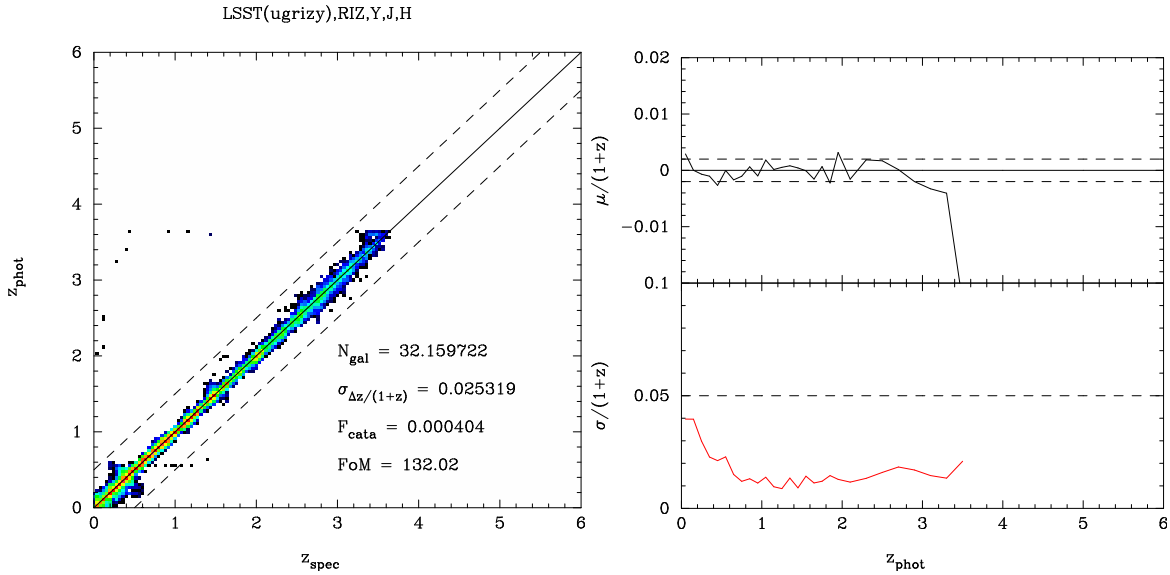

Figure 5.10: Same as Figure 5.9 except with random Gaussian errors added to simulate zero-point magnitude errors.

from the ZPs derived for the Euclid instrument. We found that this has the effect of worsening the photometric bias μ_z, specifically at redshifts greater than ~ 1.5 when the 4000Å break starts to fall between the LSST filters and Euclid's IR filters. Figure 5.11 demonstrates how this effect worsens as the systematic offset increases. The steep drop-off in bias (present in nearly all the figures) above redshift 3 is a result of our brightness restriction, leading to small numbers of galaxies at this redshift and a bias towards galaxies that are erroneously bright in the RIZ bandpass due to photometric errors. The drop-off should not be confused with a failure of LSST, as the sharp decline in bias is also seen in Figure 5.4.

The rise in photo-z bias can have detrimental effects to the weak lensing analysis, which requires the central redshift of each tomographic redshift bin to be known to better than $0.002(1+z)$. While many photo-z codes can correct for systematic offsets between bandpasses (e.g. Ilbert et al., 2006; Coe et al., 2006), this requires spectroscopic redshifts for comparison. This highlights the importance of a spectroscopic redshift survey in order to properly calibrate the photometric redshifts. Such a survey is not without its own difficulties in that it has to overcome cosmic variance (Van Waerbeke et al., 2006) and selection biases

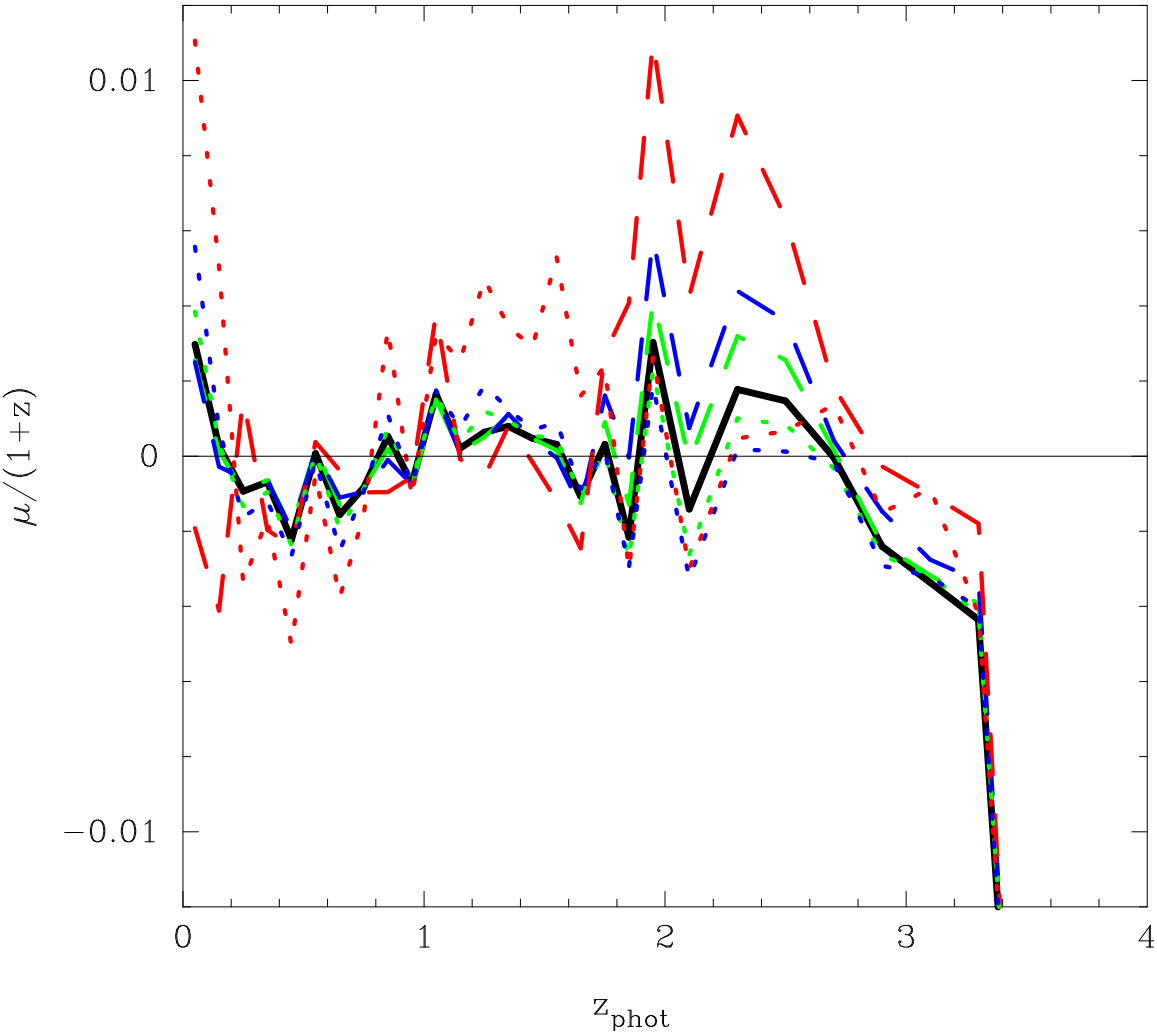

Figure 5.11: Effects of a systematic offset between the zero-point magnitudes of Euclid and LSST. The solid black curve is the ideal case of no offset, and the green, blue, and red curves show the result of increasing offsets of 0.01, 0.02 and 0.05 magnitude respectively. The dashed lines indicate that the four Euclid bands are offset by a negative amount relative to LSST magnitudes, while the dotted lines indicate a positive offset.

in order to obtain a fully representative sample. The calibration of any systematic ZP offsets might be greatly aided if the instruments shared similar band-passes, such as U or G, and avoided entirely if space-based surveys could be independent.

5.4 Conclusions

In this work, we have used the currently proposed Euclid design to study how future space-based weak lensing missions might be able to estimate photometric redshifts independently, i.e. without the use of complimentary ground-based observations. We found that the addition of two or even one optical band-passes to Euclid could greatly improve the fidelity of photometric redshifts the telescope can attain by itself. If the U and G filters are added, the constraints that Euclid will be able to place on dark energy from weak lensing (FoM = 119–126) are comparable to those using a combination of Euclid and ground-based LSST observations (FoM = 132). Additionally, quite acceptable dark energy constraints can be obtained if only the U bandpass is added to the baseline Euclid design (FoM = 100).

In their present form, to fulfill their weak lensing goals missions such as Euclid and WFIRST must rely on external ground-based observations. Including such ground-based observations entails many of the difficulties of combining two very large and different data sets, including, but not limited to, logistical complications, mis-match or potential delays in construction timescales, changes is planned survey designs, or data access limitations. Furthermore, if the survey area of the space-based observations does not overlap entirely with that of the ground-based survey, then the FoM will be negatively affected. For example, if Euclid and LSST only share 10,000deg^2, then the FoM obtainable by combining the observations will be only $\sim$66 instead of $\sim$132 in the case of full overlap. The addition of on-board optical imaging through two or even one filter would avoid most of such complications. It would allow future space-based instruments to meet their scientific requirements for weak lensing without having to risk relying on external data.

Chapter 6

Conclusions

Realistic spectral energy distribution models are an especially effective tool in the study of galaxies. Not only can they be compared to observations to determine galaxy properties such as stellar mass, star formation rate, or redshift, they can also be used to optimize future instruments to better achieve their scientific goals. For example, in this work (Chapter 5), we used model SEDs to create mock observations for the future space-based weak lensing mission Euclid. We demonstrated the importance of optical photometry for acquiring accurate photometric redshifts, and therefore the importance for weak lensing as a whole. Because of weak lensing's stringent requirements for accurate redshifts in order to map the three dimensional mass distribution of the universe, an addition of an optical channel to the Euclid spacecraft would have limited risk by allowing the telescope to be self-sufficient. Euclid relies on optical data from ground-based telescopes, most notably LSST, in order to meet its scientific requirements. Although there will be no optical channel aboard Euclid, the results of this chapter have contributed to the proposed Cosmological Advanced Survey Telescope for Optical and ultraviolet Research (CASTOR; Côté & Scott, 2014; Côte et al., 2012), a space-based survey mission that would provide panoramic, high-resolution imaging of 1/8th of the sky in UV and optical bandpasses.

While using model SEDs can inform future observing strategies through the creation of a mock reality, it must be remembered that they are only models. They are our current best

representation of galaxy SEDs, but they are not reality. It is thus important to analyze how our model assumptions could lead to erroneous or biased results. In Chapter 2, we examined how fitting broadband observations to model spectra as if the galaxy was a homogeneous entity led to an outshining bias. We studied observations of 67 nearby galaxies taken through the Sloan Digital Sky Survey, fitting model SEDs once to the integrated light from the entire galaxy, and once to each individual pixel in the galaxy and summing the parts. The unresolved mass estimates were found to underestimate the pixel-by-pixel mass estimates, and the underestimation was discovered to be correlated with specific star formation rate, increasing from no difference at sSFRs of 10^{-12} yr^{-1}, to approximately 25% (0.12 dex) at sSFRs of 10^{-8} yr^{-1}. The increasing disparity in mass estimation with increasing sSFR strongly implies that it is the presence of young stars causing the disagreement, rather than dust as previously conjectured by Zibetti, Charlot & Rix (2009). Although the presence of dust lanes was found to affect the resolved mass estimates of individual galaxies by up to 45% (0.3 dex), it did not significantly affect the average mass estimate of an ensemble of galaxies. The presence of young stars on top of an older stellar population causes the model SED fitting procedure to preferentially fit only the much brighter young stars, thus missing mass from the older population. The pixel-by-pixel analysis was able to disentangle the separate populations by spatially resolving them. By artificially degrading the resolution of the galaxies, we were able to determine that a physical scale of nearly 3 kpc (comparable to the width of spiral arms) is required to adequately resolve the separate populations and overcome the outshining bias. For projects that are unable to do so, we derived a statistical correction that could be applied to unresolved galaxy masses to correct for outshining: $m_{resolved} = \frac{m_{unresolved}}{-0.0057\log(sSFR)+0.34}$ where the sSFR is in units of yr^{-1}.

Because outshining is caused by contrasting older and younger stellar populations, it was not immediately apparent if the results for nearby galaxies would hold true for galaxies at higher redshifts, where star formation is more intense, but there has been less time to build up the mass of an older population. In Chapter 3 we applied similar pixel-by-pixel procedures to galaxies in the Hubble Extreme Deep Field, and compared resolved and unresolved

mass estimates for galaxies up to redshift 2.5. We discovered that resolved mass estimates continued to be lower than resolved mass estimates, and that the underestimation continued to increase with sSFR. Moreover, the discrepancy displayed two distinct components, changing linearly with log(sSFR) before dropping steeply above sSFRs of $10^{-9.5}$ yr^{-1}. By sSFRs of 10^{-8} yr^{-1}, the resolved mass was only one half or one third (up to low as one fifth) that of the resolved mass measurement. When galactic stellar mass functions were corrected using these results, the resulting derived star formation rate density more closely resembled the directly observed one, resolving a decade old puzzle (Hopkins & Hernquist, 2006; Wilkins, Trentham & Hopkins, 2008). Additionally, it was found that correcting the mass of galaxies for these results slightly altered the slope of the star-forming main sequence, and reduced the intrinsic scatter about the main sequence, implying that star-formation is not quite as stochastic as was previously thought. Through examination of the star formation histories implied by the pixel-by-pixel fits, we confirmed previous results (Behroozi, Wechsler & Conroy, 2013; Dressler et al., 2016) that SFHs are better modelled by two parameter models that can account for a rising SFR early in the galaxy's history, rather than the ubiquitous exponentially declining τ models. Although promising, these conclusions may not be verified until JWST provides us with rest-frame near-infrared observations of high redshift galaxies, confirming that the mass in older stars is adequately accounted for.

Coming full circle, in Chapter 4 we applied our new knowledge of the importance of spatially resolved SEDs to test analysis software for upcoming wide field slitless spectrographs such as NIRISS on JWST. We again used model SEDs to create mock observations, only this time accounting for stellar population spatial distributions as correctly as possible. Our mock observations made it clear that it will be necessary for grism analysis tools to allow continuum models for galaxies to vary within a galaxy. Assuming one uniform continuum spectrum per galaxy led to large residual fluxes and hence inaccurate line flux estimation. However, redshift estimation was not affected and remained accurate to $0.0012(1 + z)$, in line with previous results (Brammer et al., 2012).

In order to obtain the most accurate stellar mass measurements, galaxies should be

treated as composite objects. However, the depth and resolution required to do so are, forgive the pun, astronomical. Fortunately, we are on the brink of a momentous era for astronomy. In the coming decade, several powerful new survey missions will come online, including JWST, LSST, Euclid, and WFIRST among others. The unprecedented capability of these instruments will provide highly accurate observations for huge swaths of the sky. To use these observations to the fullest, we must accept that galaxy images are inherently two dimensional, and be prepared to handle the increased complexity of spatially resolved analysis.

Bibliography

Abadi M. G., Moore B., Bower R. G., 1999, Monthly Notices of the Royal Astronomical Society, Volume 308, Issue 4, pp. 947-954., 308, 947

Abdalla F. B., Amara A., Capak P., Cypriano E. S., Lahav O., Rhodes J., 2008, Monthly Notices of the Royal Astronomical Society, Volume 387, Issue 3, pp. 969-986., 387, 969

Abraham R. G., Ellis R. S., Fabian A. C., Tanvir N. R., Glazebrook K., 1999, Monthly Notices of the Royal Astronomical Society, Volume 303, Issue 4, pp. 641-658., 303, 641

Abramson L. E., Kelson D. D., Dressler A., Poggianti B. M., Gladders M. D., Oemler A., Vulcani B., 2014, The Astrophysical Journal Letters, Volume 785, Issue 2, article id. L36, 6 pp. (2014)., 785

Alard C., Lupton R. H., 1998, The Astrophysical Journal, Volume 503, Issue 1, pp. 325-331., 503, 325

Allen P. D., Driver S. P., Graham A. W., Cameron E., Liske J., De Propris R., 2006, Monthly Notices of the Royal Astronomical Society, Volume 371, Issue 1, pp. 2-18., 371, 2

Amara A., Refregier A., 2007, Monthly Notices of the Royal Astronomical Society, Volume 381, Issue 3, pp. 1018-1026., 381, 1018

Atek H. et al., 2010, The Astrophysical Journal, Volume 723, Issue 1, pp. 104-115 (2010)., 723, 104

Baldry I. K., Glazebrook K., Brinkmann J., Ivezić Ž., Lupton R. H., Nichol R. C., Szalay A. S., 2004, The Astrophysical Journal, Volume 600, Issue 2, pp. 681-694., 600, 681

Balogh M. L., Baldry I. K., Nichol R., Miller C., Bower R., Glazebrook K., 2004, The Astrophysical Journal, Volume 615, Issue 2, pp. L101-L104., 615, L101

Balogh M. L., Navarro J. F., Morris S. L., 2000, The Astrophysical Journal, Volume 540, Issue 1, pp. 113-121., 540, 113

Barden M., Häußler B., Peng C. Y., McIntosh D. H., Guo Y., 2012, Monthly Notices of the Royal Astronomical Society, Volume 422, Issue 1, pp. 449-468., 422, 449

Bartelmann M., Schneider P., 2001, Physics Reports, Volume 340, Issue 4-5, p. 291-472., 340, 291

Becker A. C., Homrighausen D., Connolly A. J., Genovese C. R., Owen R., Bickerton S. J., Lupton R. H., 2012, Monthly Notices of the Royal Astronomical Society, Volume 425, Issue 2, pp. 1341-1349., 425, 1341

Behroozi P. S., Conroy C., Wechsler R. H., 2010, The Astrophysical Journal, Volume 717, Issue 1, pp. 379-403 (2010)., 717, 379

Behroozi P. S., Wechsler R. H., Conroy C., 2013, The Astrophysical Journal, Volume 770, Issue 1, article id. 57, 36 pp. (2013)., 770

Bell E. F. et al., 2004, The Astrophysical Journal, Volume 600, Issue 1, pp. L11-L14., 600, L11

Bell E. F., McIntosh D. H., Katz N., Weinberg M. D., 2003, The Astrophysical Journal Supplement Series, Volume 149, Issue 2, pp. 289-312., 149, 289

Benitez N., 2000, The Astrophysical Journal, Volume 536, Issue 2, pp. 571-583., 536, 571

Benitez N. et al., 2004, The Astrophysical Journal Supplement Series, Volume 150, Issue 1, pp. 1-18., 150, 1

Bernardi M., Hyde J. B., Sheth R. K., Miller C. J., Nichol R. C., 2007, The Astronomical Journal, 133, 1741

Bernstein G., Huterer D., 2010, Monthly Notices of the Royal Astronomical Society, Volume 401, Issue 2, pp. 1399-1408., 401, 1399

Bertin E., Arnouts S., 1996, Astronomy and Astrophysics Supplement Series, 117, 393

Bertin ., Mellier ., Radovich ., Missonnier ., Didelon ., Morin ., 2002, Astronomical Data Analysis Software and Systems XI, 281

Blandford R. D., Saust A. B., Brainerd T. G., Villumsen J. V., 1991, Monthly Notices of the Royal Astronomical Society, 251, 600

Blanton M. R. et al., 2005, The Astronomical Journal, 129, 2562

Bolzonella M. et al., 2010, Astronomy and Astrophysics, Volume 524, id.A76, 17 pp., 524

Bordoloi R., Lilly S. J., Amara A., 2010, Monthly Notices of the Royal Astronomical Society, Volume 406, Issue 2, pp. 881-895., 406, 881

Brammer G. et al., 2012, The Astrophysical Journal Supplement, Volume 200, Issue 2, article id. 13, 19 pp. (2012)., 200

Brammer G. B., van Dokkum P. G., Coppi P., 2008, The Astrophysical Journal, Volume 686, Issue 2, article id. 1503-1513, pp. (2008)., 686

Brammer G. B. et al., 2009, The Astrophysical Journal Letters, Volume 706, Issue 1, pp. L173-L177 (2009)., 706, L173

Bromm V., Coppi P. S., Larson R. B., 2002, The Astrophysical Journal, Volume 564, Issue 1, pp. 23-51., 564, 23

Bruzual G., 2007, eprint arXiv:astro-ph/0703052

Bruzual G., Charlot S., 2003, Monthly Notices of the Royal Astronomical Society, Volume 344, Issue 4, pp. 1000-1028., 344, 1000

Bruzual A. G., Charlot S., 1993, The Astrophysical Journal, 405, 538

Byler N., Dalcanton J. J., Conroy C., Johnson B. D., 2016, eprint arXiv:1611.08305

Calzetti D., Armus L., Bohlin R. C., Kinney A. L., Koornneef J., StorchiBergmann T., 2000, The Astrophysical Journal, 533, 682

Capak P. et al., 2007, The Astrophysical Journal Supplement Series, Volume 172, Issue 1, pp. 99-116., 172, 99

Cappellari M., Copin Y., 2003, Monthly Notice of the Royal Astronomical Society, Volume 342, Issue 2, pp. 345-354., 342, 345

Chabrier G., 2003, Publications of the Astronomical Society of the Pacific, 115, 763

Chapman S. C., Windhorst R., Odewahn S., Yan H., Conselice C., 2003, The Astrophysical Journal, Volume 599, Issue 1, pp. 92-104., 599, 92

Charlot S., Fall S. M., 2000, The Astrophysical Journal, Volume 539, Issue 2, pp. 718-731., 539, 718

Coe D., Benitez N., Sanchez S. F., Jee M., Bouwens R., Ford H., 2006, The Astronomical Journal, Volume 132, Issue 2, pp. 926-959., 132, 926

Collister A. A., Lahav O., 2004, The Publications of the Astronomical Society of the Pacific, Volume 116, Issue 818, pp. 345-351., 116, 345

Conroy C., 2013, Annual Review of Astronomy and Astrophysics, 51, 393

Conroy C., Gunn J. E., 2010, The Astrophysical Journal, 712, 833

Conroy C., Gunn J. E., White M., 2009, The Astrophysical Journal, 699, 486

Conroy C., van Dokkum P., 2012, The Astrophysical Journal, Volume 747, Issue 1, article id. 69, 22 pp. (2012)., 747

Conroy C., van Dokkum P., 2016, The Astrophysical Journal, Volume 827, Issue 1, article id. 9, pp. (2016)., 827

Conroy C., Wechsler R. H., 2008, The Astrophysical Journal, Volume 696, Issue 1, pp. 620-635 (2009)., 696, 620

Conselice C. J., Bershady M. A., Dickinson M., Papovich C., 2003, The Astronomical Journal, 126, 1183

Copeland E. J., Sami M., Tsujikawa S., 2006, International Journal of Modern Physics D, Volume 15, Issue 11, pp. 1753-1935 (2006)., 15, 1753

Côté P., Scott A., 2014, in Proceedings of the SPIE, Volume 9144, id. 914403 6 pp. (2014)., Takahashi T., den Herder J.-W. A., Bautz M., eds., Vol. 9144, p. 914403

Côte P. et al., 2012, in Space Telescopes and Instrumentation 2012: Optical, Infrared, and Millimeter Wave. Proceedings of the SPIE, Volume 8442, article id. 844215, 18 pp. (2012)., Clampin M. C., Fazio G. G., MacEwen H. A., Oschmann J. M., eds., Vol. 8442, p. 844215

Courteau S. et al., 2014, Reviews of Modern Physics, vol. 86, Issue 1, pp. 47-119, 86, 47

Cowie L. L., Songaila A., Hu E. M., Cohen J. G., 1996, The Astronomical Journal, 112, 839

Daddi E. et al., 2007, The Astrophysical Journal, 670, 156

Davis M., Geller M. J., 1976, The Astrophysical Journal, 208, 13

Dekel A., Birnboim Y., 2006, Monthly Notices of the Royal Astronomical Society, Volume 368, Issue 1, pp. 2-20., 368, 2

Di Matteo T., Springel V., Hernquist L., 2005, Nature, Volume 433, Issue 7026, pp. 604-607 (2005)., 433, 604

Doyon R. et al., 2012, in Space Telescopes and Instrumentation 2012: Optical, Infrared, and Millimeter Wave. Proceedings of the SPIE, Volume 8442, article id. 84422R, 13 pp. (2012)., Clampin M. C., Fazio G. G., MacEwen H. A., Oschmann J. M., eds., Vol. 8442, p. 84422R

Dressler A., 1980, The Astrophysical Journal, 236, 351

Dressler A. et al., 2016, eprint arXiv:1607.02143

Drory N., Bender R., Hopp U., 2004, The Astrophysical Journal, 616, L103

Duvet L., 2010, European Space Agency SRE-PA/2010.030 "Euclid Reference Payload Concept"

Efremov Y. N., 1995, The Astronomical Journal, 110, 2757

Eisenstein D. J. et al., 2011, The Astronomical Journal, 142, 72

Eldridge J. J., Stanway E. R., 2009, Monthly Notices of the Royal Astronomical Society, Volume 400, Issue 2, pp. 1019-1028., 400, 1019

Erb D. K., Pettini M., Shapley A. E., Steidel C. C., Law D. R., Reddy N. A., 2010, The Astrophysical Journal, Volume 719, Issue 2, pp. 1168-1190 (2010)., 719, 1168

Erben T. et al., 2009, Astronomy and Astrophysics, Volume 493, Issue 3, 2009, pp.1197-1222, 493, 1197

Faber S. M., Jackson R. E., 1976, Velocity dispersions and mass-to-light ratios for elliptical galaxies

Feulner G., Gabasch A., Salvato M., Drory N., Hopp U., Bender R., 2005, The Astrophysical Journal, 633, L9

Gallazzi A., Bell E. F., 2009, The Astrophysical Journal Supplement, Volume 185, Issue 2, pp. 253-272 (2009)., 185, 253

Gallazzi A., Charlot S., Brinchmann J., White S. D. M., Tremonti C. A., 2005, Monthly Notices of the Royal Astronomical Society, 362, 41

Gil de Paz A. et al., 2007, The Astrophysical Journal Supplement Series, 173, 185

Gladders M. D., Oemler A., Dressler A., Poggianti B., Vulcani B., Abramson L., 2013, The Astrophysical Journal, Volume 770, Issue 1, article id. 64, 13 pp. (2013)., 770

Grogin N. A. et al., 2011, The Astrophysical Journal Supplement, Volume 197, Issue 2, article id. 35, 39 pp. (2011)., 197

Gunn J. E., Gott, J. Richard I., 1972, The Astrophysical Journal, 176, 1

Gusev A. S., Egorov O. V., Sakhibov F., 2013, Monthly Notices of the Royal Astronomical Society, 437, 1337

Heavens A., Panter B., Jimenez R., Dunlop J., 2004, Nature, Volume 428, Issue 6983, pp. 625-627 (2004)., 428, 625

Hildebrandt H. et al., 2010, Astronomy and Astrophysics, Volume 523, id.A31, 21 pp., 523

Hildebrandt H., Pielorz J., Erben T., van Waerbeke L., Simon P., Capak P., 2009, Astronomy and Astrophysics, Volume 498, Issue 3, 2009, pp.725-736, 498, 725

Hopkins P. F., Hernquist L., 2006, The Astrophysical Journal Supplement Series, Volume 166, Issue 1, pp. 1-36., 166, 1

Hubble E. P., 1926, The Astrophysical Journal, 64, 321

Huertas-Company M. et al., 2016, Monthly Notices of the Royal Astronomical Society, Volume 462, Issue 4, p.4495-4516, 462, 4495

Huterer D., Takada M., Bernstein G., Jain B., 2006, Monthly Notices of the Royal Astronomical Society, Volume 366, Issue 1, pp. 101-114., 366, 101

Ilbert O. et al., 2006, Astronomy and Astrophysics, Volume 457, Issue 3, October III 2006, pp.841-856, 457, 841

Ilbert O. et al., 2009, The Astrophysical Journal, Volume 690, Issue 2, pp. 1236-1249 (2009)., 690, 1236

Ilbert O. et al., 2013, Astronomy & Astrophysics, Volume 556, id.A55, 19 pp., 556

Ilbert O. et al., 2010, The Astrophysical Journal, 709, 644

Illingworth G. D. et al., 2013, The Astrophysical Journal Supplement, Volume 209, Issue 1, article id. 6, 13 pp. (2013)., 209

Ivezic Z. et al., 2008, eprint arXiv:0805.2366

Johnston R., Vaccari M., Jarvis M., Smith M., Giovannoli E., Häußler B., Prescott M., 2015, Monthly Notices of the Royal Astronomical Society, Volume 453, Issue 3, p.2540-2557, 453, 2540

Jouvel S. et al., 2010, Astronomy & Astrophysics, Volume 532, id.A25, 24 pp., 532

Jouvel S. et al., 2009, Astronomy and Astrophysics, Volume 504, Issue 2, 2009, pp.359-371, 504, 359

Kannappan S. J., Gawiser E., 2007, The Astrophysical Journal, Volume 657, Issue 1, pp. L5-L8., 657, L5

Kauffmann G. et al., 2003, Monthly Notices of the Royal Astronomical Society, 341, 33

Kennicutt, R. J., Hodge P., 1982, The Astrophysical Journal, 253, 101

Koekemoer A. M. et al., 2011, The Astrophysical Journal Supplement, Volume 197, Issue 2, article id. 36, 36 pp. (2011)., 197

Komatsu E. et al., 2009, The Astrophysical Journal Supplement, Volume 180, Issue 2, pp. 330-376 (2009)., 180, 330

Komatsu E. et al., 2011, The Astrophysical Journal Supplement Series, 192, 18

Kriek M. et al., 2010, The Astrophysical Journal, 722, L64

Kriek M. et al., 2015, The Astrophysical Journal Supplement Series, Volume 218, Issue 2, article id. 15, 27 pp. (2015)., 218

Kriek M. et al., 2008, The Astrophysical Journal, Volume 677, Issue 1, article id. 219-237, pp. (2008)., 677

Krist J., 1995, Astronomical Data Analysis Software and Systems IV, ASP Conference Series, Vol. 77, 1995, R.A. Shaw, H.E. Payne, and J.J.E. Hayes, eds., p. 349., 77, 349

Krist J. E., Hook R. N., Stoehr F., 2011, in Proceedings of the SPIE, Volume 8127, id. 81270J (2011)., Kahan M. A., ed., Vol. 8127, p. 81270J

Kroupa P., 2001, Monthly Notices of the Royal Astronomical Society, Volume 322, Issue 2, pp. 231-246., 322, 231

Kümmel M., Walsh J. R., Pirzkal N., Kuntschner H., Pasquali A., 2009, Publications of the Astronomical Society of Pacific, Volume 121, Issue 875, pp. 59-72 (2009)., 121, 59

Kurczynski P. et al., 2016, The Astrophysical Journal Letters, Volume 820, Issue 1, article id. L1, 6 pp. (2016)., 820

Larson R. B., Tinsley B. M., Caldwell C. N., 1980, The Astrophysical Journal, 237, 692

Laureijs R. et al., 2011, eprint arXiv:1110.3193

Law D. R., Shapley A. E., Steidel C. C., Reddy N. A., Christensen C. R., Erb D. K., 2012, Nature, 487, 338

Leauthaud A. et al., 2007, The Astrophysical Journal Supplement Series, Volume 172, Issue 1, pp. 219-238., 172, 219

Lee H.-c., Worthey G., Trager S. C., Faber S. M., 2007, The Astrophysical Journal, Volume 664, Issue 1, pp. 215-225., 664, 215

Lee S.-K., Ferguson H. C., Somerville R. S., Wiklind T., Giavalisco M., 2010, The Astrophysical Journal, Volume 725, Issue 2, pp. 1644-1651 (2010)., 725, 1644

Lee S.-K., Idzi R., Ferguson H. C., Somerville R. S., Wiklind T., Giavalisco M., 2009, The Astrophysical Journal Supplement, Volume 184, Issue 1, pp. 100-132 (2009)., 184, 100

Lovekin C. C., 2012, Monthly Notices of the Royal Astronomical Society, Volume 415, Issue 4, pp. 3887-3894., 415, 3887

Lundgren B. F. et al., 2014, The Astrophysical Journal, Volume 780, Issue 1, article id. 34, 18 pp. (2014)., 780

Ma Z., Bernstein G., 2008, The Astrophysical Journal, Volume 682, Issue 1, article id. 39-48, pp. (2008)., 682

Ma Z., Hu W., Huterer D., 2006, The Astrophysical Journal, Volume 636, Issue 1, pp. 21-29., 636, 21

Madau P., 1995, The Astrophysical Journal, 441, 18

Madau P., Dickinson M., 2014, Annual Review of Astronomy and Astrophysics, vol. 52, p.415-486, 52, 415

Madau P., Ferguson H. C., Dickinson M. E., Giavalisco M., Steidel C. C., Fruchter A., 1996, Monthly Notices of the Royal Astronomical Society, Volume 283, Issue 4, pp. 1388-1404., 283, 1388

Maeder A., Meynet G., 2012, Reviews of Modern Physics, 84, 25

Mannucci F., Cresci G., Maiolino R., Marconi A., Gnerucci A., 2010, Monthly Notices of the Royal Astronomical Society, 408, 2115

Maraston C., 2005, Monthly Notices of the Royal Astronomical Society, 362, 799

Maraston C., Daddi E., Renzini A., Cimatti A., Dickinson M., Papovich C., Pasquali A., Pirzkal N., 2006, The Astrophysical Journal, 652, 85

Maraston C. et al., 2013, Monthly Notices of the Royal Astronomical Society, 435, 2764

Maraston C., Pforr J., Renzini A., Daddi E., Dickinson M., Cimatti A., Tonini C., 2010, Monthly Notices of the Royal Astronomical Society, 407, 830

Marchesini D., van Dokkum P. G., Förster Schreiber N. M., Franx M., Labbé I., Wuyts S., 2009, The Astrophysical Journal, 701, 1765

Martin D. C. et al., 2007, The Astrophysical Journal Supplement Series, Volume 173, Issue 2, pp. 342-356., 173, 342

Mendel J. T., Simard L., Palmer M., Ellison S. L., Patton D. R., 2014, The Astrophysical Journal Supplement, Volume 210, Issue 1, article id. 3, 21 pp. (2014)., 210

Moster B. P., Somerville R. S., Maulbetsch C., van den Bosch F. C., Macciò A. V., Naab T., Oser L., 2010, The Astrophysical Journal, Volume 710, Issue 2, pp. 903-923 (2010)., 710, 903

Munshi D., Valageas P., Van Waerbeke L., Heavens A., 2008, Physics Reports, Volume 462, Issue 3, p. 67-121., 462, 67

Muzzin A. et al., 2013, The Astrophysical Journal, Volume 777, Issue 1, article id. 18, 30 pp. (2013)., 777

Muzzin A., Marchesini D., van Dokkum P. G., Labbé I., Kriek M., Franx M., 2009, The Astrophysical Journal, Volume 701, Issue 2, pp. 1839-1864 (2009)., 701, 1839

Nelson E. J. et al., 2013, The Astrophysical Journal Letters, Volume 763, Issue 1, article id. L16, 6 pp. (2013)., 763

Nelson E. J. et al., 2012, The Astrophysical Journal Letters, Volume 747, Issue 2, article id. L28, 6 pp. (2012)., 747

Nishizawa A. J., Takada M., Hamana T., Furusawa H., 2010, The Astrophysical Journal, Volume 718, Issue 2, pp. 1252-1265 (2010)., 718, 1252

Noll S., Burgarella D., Giovannoli E., Buat V., Marcillac D., Muñoz-Mateos J. C., 2009, Astronomy and Astrophysics, 507, 1793

Oemler A., 1974, The Astrophysical Journal, 194, 1

Oke J. B., 1974, The Astrophysical Journal Supplement Series, 27, 21

Papovich C., Dickinson M., Ferguson H. C., 2001, The Astrophysical Journal, 559, 620

Patton D. R., Torrey P., Ellison S. L., Mendel J. T., Scudder J. M., 2013, Monthly Notices of the Royal Astronomical Society: Letters, Volume 433, Issue 1, p.L59-L63, 433, L59

Paxton B., Bildsten L., Dotter A., Herwig F., Lesaffre P., Timmes F., 2011, The Astrophysical Journal Supplement, Volume 192, Issue 1, article id. 3, 35 pp. (2011)., 192

Pérez-González P. G. et al., 2008, The Astrophysical Journal, Volume 675, Issue 1, article id. 234-261, pp. (2008)., 675

PérezGonzález P. G. et al., 2008, The Astrophysical Journal, 675, 234

Pforr J., Maraston C., Tonini C., 2012, Monthly Notices of the Royal Astronomical Society, Volume 422, Issue 4, pp. 3285-3326., 422, 3285

Pirzkal N. et al., 2005, The Astrophysical Journal, Volume 622, Issue 1, pp. 319-332., 622, 319

Polletta M. et al., 2007, The Astrophysical Journal, Volume 663, Issue 1, pp. 81-102., 663, 81

Racca G. D. et al., 2016, Proceedings of the SPIE, Volume 9904, id. 99040O 23 pp. (2016)., 9904

Rafelski M. et al., 2015, The Astronomical Journal, Volume 150, Issue 1, article id. 31, 25 pp. (2015)., 150

Reddy N. A., Steidel C. C., 2009, The Astrophysical Journal, Volume 692, Issue 1, pp. 778-803 (2009)., 692, 778

Reddy N. A., Steidel C. C., Fadda D., Yan L., Pettini M., Shapley A. E., Erb D. K., Adelberger K. L., 2006, The Astrophysical Journal, 644, 792

Refregier A., 2003, Annual Review of Astronomy &Astrophysics, vol. 41, pp.645-668, 41, 645

Refregier A., Amara A., Kitching T., Rassat A., 2008, iCosmo: an Interactive Cosmology Package

Refregier A., Amara A., Kitching T. D., Rassat A., Scaramella R., Weller J., Consortium f. t. E. I., 2010, eprint arXiv:1001.0061

Rowlands N., Lin H., Aldridge D., 2011, Com Dev Executive Report RPT/CSA/50148/1005 "Dark Energy Mission Contribution Study"

Salpeter E. E., 1955, The Astrophysical Journal, 121, 161

Sanders D. B., Soifer B. T., Elias J. H., Madore B. F., Matthews K., Neugebauer G., Scoville N. Z., 1988, The Astrophysical Journal, 325, 74

Savaglio S. et al., 2005, The Astrophysical Journal, 635, 260

Sawicki M., 2012a, Publications of the Astronomical Society of the Pacific, 124, 1208

Sawicki M., 2012b, Monthly Notices of the Royal Astronomical Society, 421, 2187

Sawicki M., Thompson D., 2006, The Astrophysical Journal, Volume 648, Issue 1, pp. 299-309., 648, 299

Sawicki M., Yee H. K. C., 1997, The Astronomical Journal, Volume 115, Issue 4, pp. 1329-1339., 115, 1329

Sawicki M., Yee H. K. C., 1998, The Astronomical Journal, Volume 115, Issue 4, pp. 1329-1339., 115, 1329

Schawinski K. et al., 2014, Monthly Notices of the Royal Astronomical Society, Volume 440, Issue 1, p.889-907, 440, 889

Schlafly E. F., Finkbeiner D. P., 2011, The Astrophysical Journal, 737, 103

Schlegel D. J., Finkbeiner D. P., Davis M., 1998, The Astrophysical Journal, 500, 525

Schmidt K. B. et al., 2013, Monthly Notices of the Royal Astronomical Society, Volume 432, Issue 1, p.285-300, 432, 285

Schmidt K. B. et al., 2014, The Astrophysical Journal Letters, Volume 782, Issue 2, article id. L36, 8 pp. (2014)., 782

Seigar M. S., James P. A., 1998, Monthly Notices of the Royal Astronomical Society, 299, 685

Shapley A. E., Steidel C. C., Erb D. K., Reddy N. A., Adelberger K. L., Pettini M., Barmby P., Huang J., 2005, The Astrophysical Journal, Volume 626, Issue 2, pp. 698-722., 626, 698

Simard L., Mendel J. T., Patton D. R., Ellison S. L., McConnachie A. W., 2011, The Astrophysical Journal Supplement, Volume 196, Issue 1, article id. 11, 20 pp. (2011)., 196

Simha V., Weinberg D. H., Conroy C., Dave R., Fardal M., Katz N., Oppenheimer B. D., 2014, eprint arXiv:1404.0402

Skelton R. E. et al., 2014, The Astrophysical Journal Supplement Series, Volume 214, Issue 2, article id. 24, 49 pp. (2014)., 214

Skrutskie M. F. et al., 2006, The Astronomical Journal, 131, 1163

Soille P. J., Ansoult M. M., 1990, Signal Processing, 20, 171

Sorba R., Sawicki M., 2010, The Astrophysical Journal, 721, 1056

Sorba R., Sawicki M., 2015, Monthly Notices of the Royal Astronomical Society, Volume 452, Issue 1, p.235-245, 452, 235

Spergel D. et al., 2015, eprint arXiv:1503.03757

Springel V., Di Matteo T., Hernquist L., 2005, Monthly Notices of the Royal Astronomical Society, Volume 361, Issue 3, pp. 776-794., 361, 776

Stacy A., Bromm V., Lee A. T., 2016, Monthly Notices of the Royal Astronomical Society, Volume 462, Issue 2, p.1307-1328, 462, 1307

Strateva I. et al., 2001, The Astronomical Journal, Volume 122, Issue 4, pp. 1861-1874., 122, 1861

Sun L., Fan Z. H., Tao C., Kneib J. P., Jouvel S., Tilquin A., 2009, The Astrophysical Journal, Volume 699, Issue 2, pp. 958-967 (2009)., 699, 958

Taylor E. N., Franx M., Brinchmann J., van der Wel A., van Dokkum P. G., 2010, The Astrophysical Journal, 722, 1

Taylor E. N. et al., 2009, The Astrophysical Journal Supplement, Volume 183, Issue 2, pp. 295-319 (2009)., 183, 295

Taylor E. N. et al., 2011, Monthly Notices of the Royal Astronomical Society, 418, 1587

Tomczak A. R. et al., 2014, The Astrophysical Journal, Volume 783, Issue 2, article id. 85, 15 pp. (2014)., 783

Treu T. et al., 2015, The Astrophysical Journal, Volume 812, Issue 2, article id. 114, 21 pp. (2015)., 812

Trujillo I. et al., 2006, The Astrophysical Journal, 650, 18

Tully R. B., Fisher J. R., 1977, Astronomy and Astrophysics, 54, 661

van der Wel A. et al., 2012, The Astrophysical Journal Supplement, Volume 203, Issue 2, article id. 24, 12 pp. (2012)., 203

van der Wel A., Franx M., Wuyts S., van Dokkum P. G., Huang J., Rix H.-W., Illingworth G. D., 2006, The Astrophysical Journal, Volume 652, Issue 1, pp. 97-106., 652, 97

van Dokkum P. G. et al., 2011, The Astrophysical Journal Letters, Volume 743, Issue 1, article id. L15, 6 pp. (2011)., 743

Van Waerbeke L., White M., Hoekstra H., Heymans C., 2006, Astroparticle Physics, Volume 26, Issue 2, p. 91-101., 26, 91

Weiner B. J. et al., 2005, The Astrophysical Journal, Volume 620, Issue 2, pp. 595-617., 620, 595

Welikala N. et al., 2011, eprint arXiv:1112.2657

Whitaker K. E. et al., 2014, The Astrophysical Journal, Volume 795, Issue 2, article id. 104, 20 pp. (2014)., 795

Whitaker K. E., van Dokkum P. G., Brammer G., Franx M., 2012, The Astrophysical Journal Letters, Volume 754, Issue 2, article id. L29, 6 pp. (2012)., 754

Wilkins S. M., Trentham N., Hopkins A. M., 2008, Monthly Notices of the Royal Astronomical Society, Volume 385, Issue 2, pp. 687-694., 385, 687

Williams R. J., Quadri R. F., Franx M., van Dokkum P., Toft S., Kriek M., Labbé I., 2010, The Astrophysical Journal, 713, 738

Willmer C. N. A. et al., 2006, The Astrophysical Journal, Volume 647, Issue 2, pp. 853-873., 647, 853

Witt A. N., Gordon K. D., 2000, The Astrophysical Journal, Volume 528, Issue 2, pp. 799-816., 528, 799

Wuyts S. et al., 2012, The Astrophysical Journal, Volume 753, Issue 2, article id. 114, 25 pp. (2012)., 753

Wuyts S. et al., 2011, The Astrophysical Journal, Volume 738, Issue 1, article id. 106, 18 pp. (2011)., 738

Wuyts S. et al., 2013, The Astrophysical Journal, Volume 779, Issue 2, article id. 135, 16 pp. (2013)., 779

Yang X., Mo H. J., van den Bosch F. C., Zhang Y., Han J., 2012, The Astrophysical Journal, Volume 752, Issue 1, article id. 41, 33 pp. (2012)., 752

Zibetti S., Charlot S., Rix H.-W., 2009, Monthly Notices of the Royal Astronomical Society, 400, 1181

Zibetti S., Gallazzi A., Charlot S., Pierini D., Pasquali A., 2013, Monthly Notices of the Royal Astronomical Society, Volume 428, Issue 2, p.1479-1497, 428, 1479

Zou H. et al., 2011, The Astronomical Journal, 142, 16

Appendices

Appendix A

Appendix A: Property Maps of SDSS Galaxies

False color images (ugi), 4000Å break strength, stellar mass, star-formation rate, and extinction maps for galaxies in the SDSS used in Chapter 2.

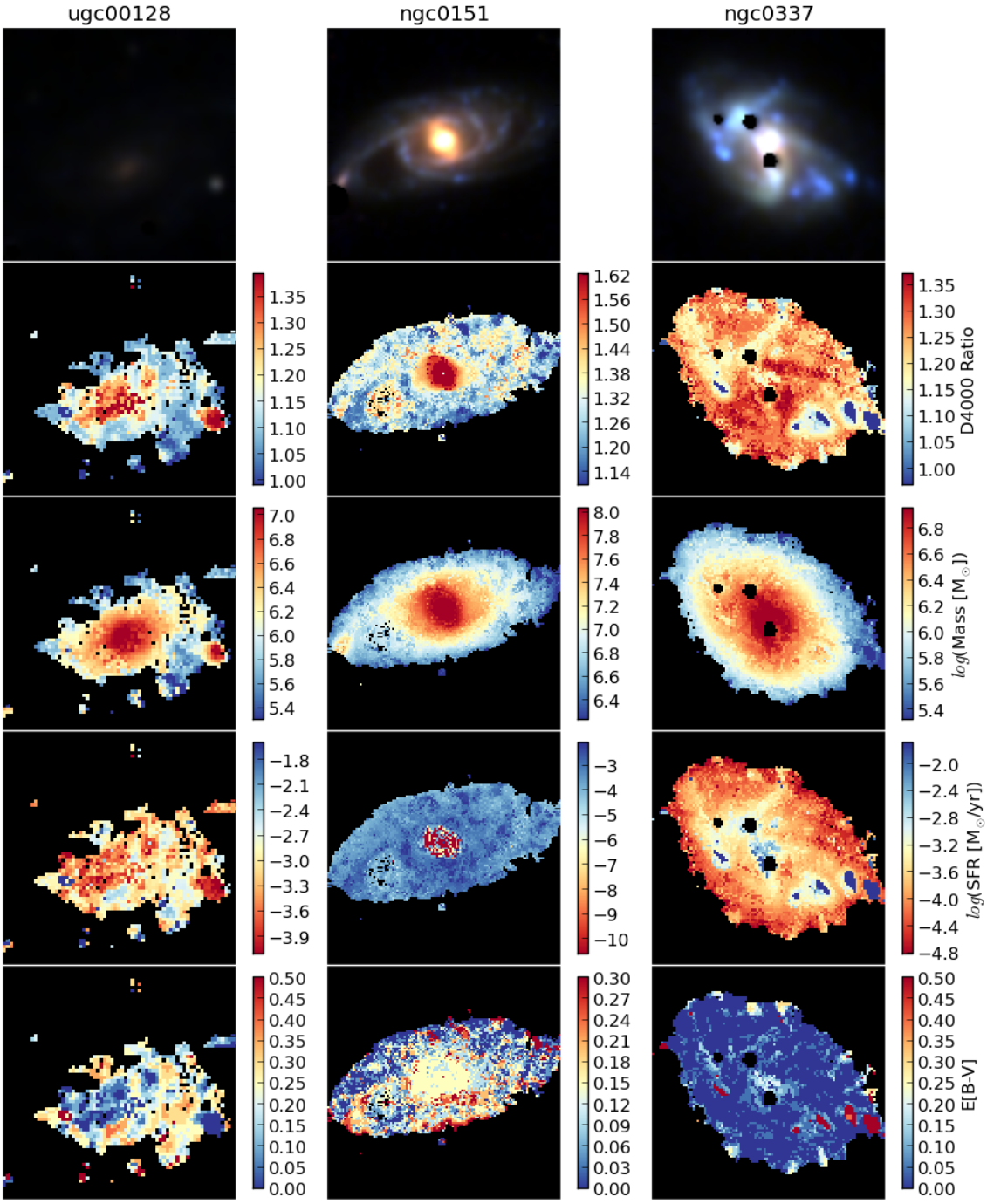
ugc00128
ngc0151
ngc0337
1.35 1.30 1.25 1.20 1.15 1.10 1.05 1.00
1.62 1.56 1.50 1.44 1.38 1.32 1.26 1.20 1.14
1.35 1.30 1.25 1.20 1.15 1.10 1.05 1.00
D4000 Ratio
7.0 6.8 6.6 6.4 6.2 6.0 5.8 5.6 5.4
8.0 7.8 7.6 7.4 7.2 7.0 6.8 6.6 6.4
6.8 6.6 6.4 6.2 6.0 5.8 5.6 5.4
log(Mass [M⊙])
−1.8 −2.1 −2.4 −2.7 −3.0 −3.3 −3.6 −3.9
−3 −4 −5 −6 −7 −8 −9 −10
−2.0 −2.4 −2.8 −3.2 −3.6 −4.0 −4.4 −4.8
log(SFR [M⊙/yr])
0.50 0.45 0.40 0.35 0.30 0.25 0.20 0.15 0.10 0.05 0.00
0.30 0.27 0.24 0.21 0.18 0.15 0.12 0.09 0.06 0.03 0.00
0.50 0.45 0.40 0.35 0.30 0.25 0.20 0.15 0.10 0.05 0.00
E[B-V]

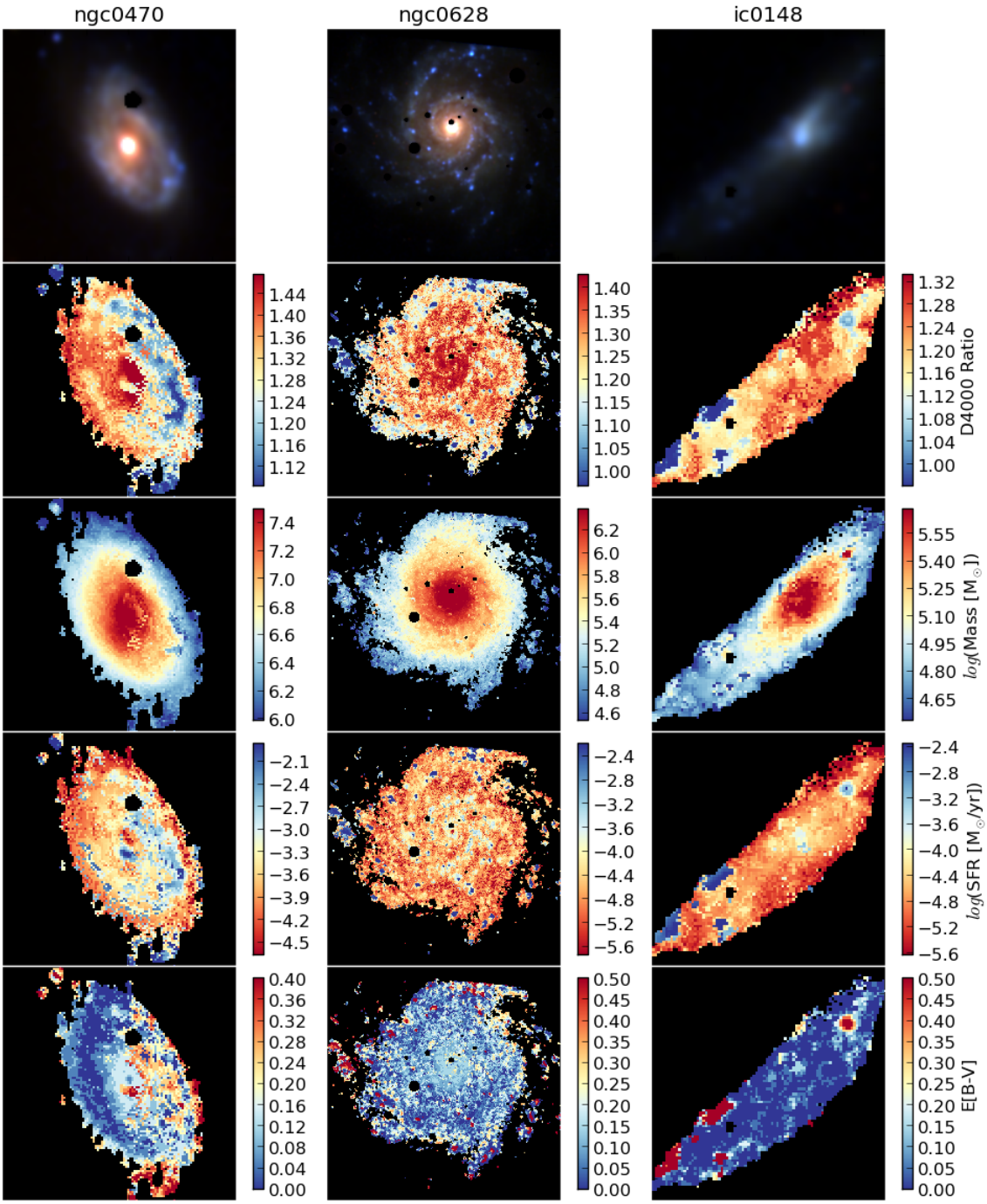
ngc0470
ngc0628
ic0148
1.44 1.40 1.36 1.32 1.28 1.24 1.20 1.16 1.12
1.40 1.35 1.30 1.25 1.20 1.15 1.10 1.05 1.00
1.32 1.28 1.24 1.20 1.16 1.12 1.08 1.04 1.00
D4000 Ratio
7.4 7.2 7.0 6.8 6.6 6.4 6.2 6.0
6.2 6.0 5.8 5.6 5.4 5.2 5.0 4.8 4.6
5.55 5.40 5.25 5.10 4.95 4.80 4.65
log(Mass [M⊙])
−2.1 −2.4 −2.7 −3.0 −3.3 −3.6 −3.9 −4.2 −4.5
−2.4 −2.8 −3.2 −3.6 −4.0 −4.4 −4.8 −5.2 −5.6
−2.4 −2.8 −3.2 −3.6 −4.0 −4.4 −4.8 −5.2 −5.6
log(SFR [M⊙/yr])
0.40 0.36 0.32 0.28 0.24 0.20 0.16 0.12 0.08 0.04 0.00
0.50 0.45 0.40 0.35 0.30 0.25 0.20 0.15 0.10 0.05 0.00
0.50 0.45 0.40 0.35 0.30 0.25 0.20 0.15 0.10 0.05 0.00
E[B-V]

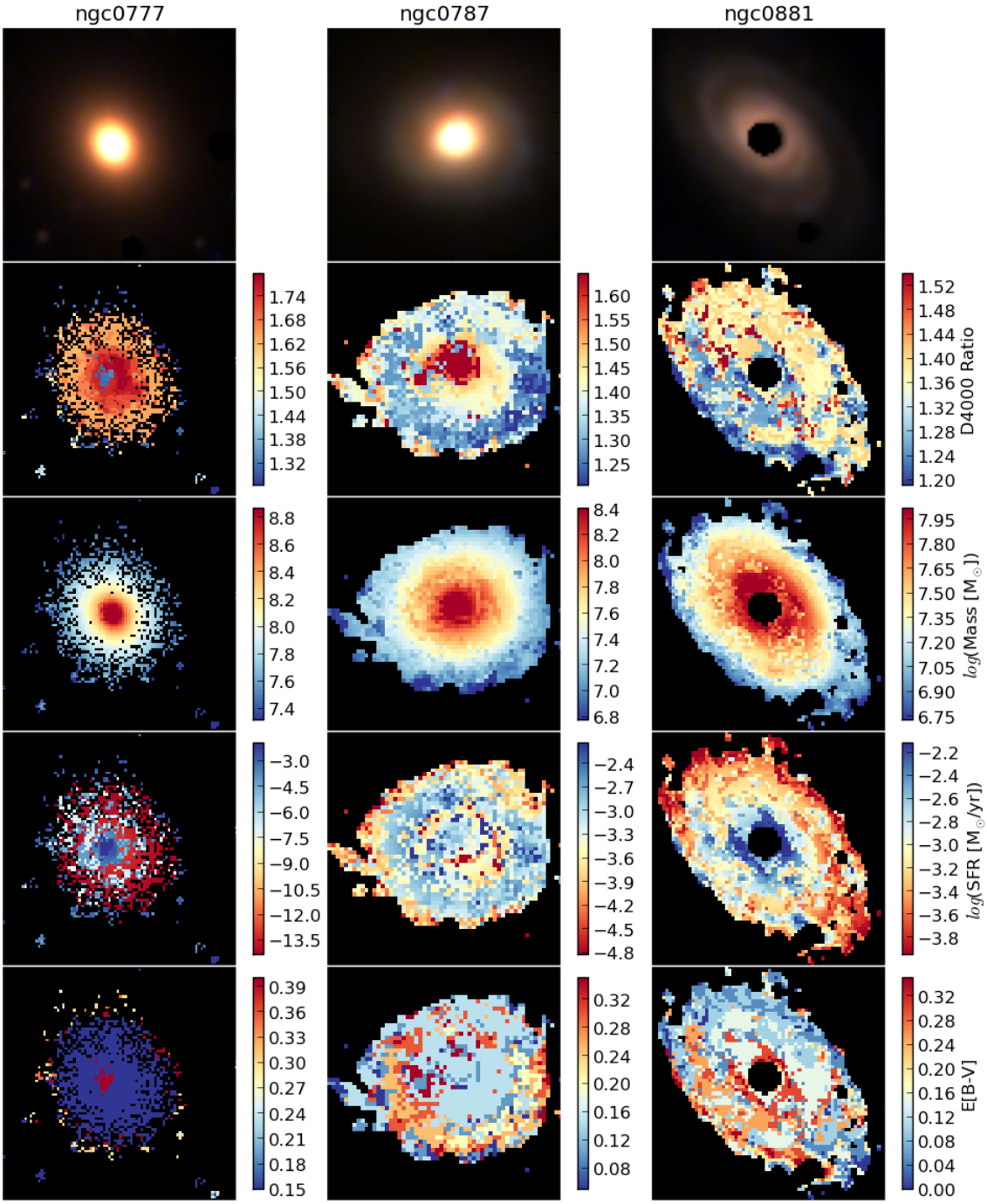
ngc0777
ngc0787
ngc0881
1.74
1.68
1.62
1.56
1.50
1.44
1.38
1.32
1.60
1.55
1.50
1.45
1.40
1.35
1.30
1.25
1.52
1.48
1.44
1.40
1.36
1.32
1.28
1.24
1.20
D4000 Ratio
8.8
8.6
8.4
8.2
8.0
7.8
7.6
7.4
8.4
8.2
8.0
7.8
7.6
7.4
7.2
7.0
6.8
7.95
7.80
7.65
7.50
7.35
7.20
7.05
6.90
6.75
log(Mass [M⊙])
−3.0
−4.5
−6.0
−7.5
−9.0
−10.5
−12.0
−13.5
−2.4
−2.7
−3.0
−3.3
−3.6
−3.9
−4.2
−4.5
−4.8
−2.2
−2.4
−2.6
−2.8
−3.0
−3.2
−3.4
−3.6
−3.8
log(SFR [M⊙/yr])
0.39
0.36
0.33
0.30
0.27
0.24
0.21
0.18
0.15
0.32
0.28
0.24
0.20
0.16
0.12
0.08
0.32
0.28
0.24
0.20
0.16
0.12
0.08
0.04
0.00
E[B-V]

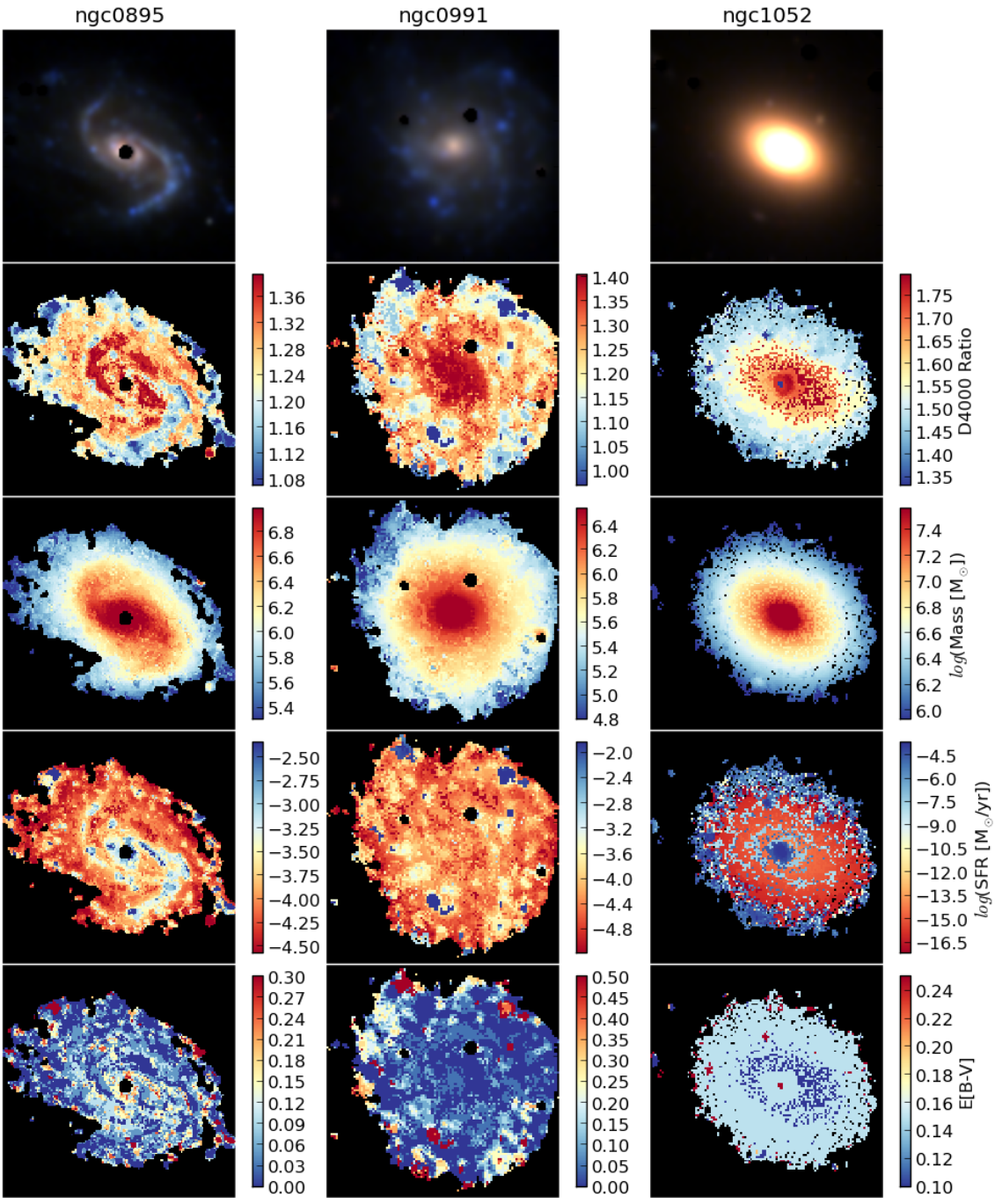
ngc0895
ngc0991
ngc1052
1.36 1.32 1.28 1.24 1.20 1.16 1.12 1.08
1.40 1.35 1.30 1.25 1.20 1.15 1.10 1.05 1.00
1.75 1.70 1.65 1.60 1.55 1.50 1.45 1.40 1.35
D4000 Ratio
6.8 6.6 6.4 6.2 6.0 5.8 5.6 5.4
6.4 6.2 6.0 5.8 5.6 5.4 5.2 5.0 4.8
7.4 7.2 7.0 6.8 6.6 6.4 6.2 6.0
log(Mass [M⊙])
−2.50 −2.75 −3.00 −3.25 −3.50 −3.75 −4.00 −4.25 −4.50
−2.0 −2.4 −2.8 −3.2 −3.6 −4.0 −4.4 −4.8
−4.5 −6.0 −7.5 −9.0 −10.5 −12.0 −13.5 −15.0 −16.5
log(SFR [M⊙/yr])
0.30 0.27 0.24 0.21 0.18 0.15 0.12 0.09 0.06 0.03 0.00
0.50 0.45 0.40 0.35 0.30 0.25 0.20 0.15 0.10 0.05 0.00
0.24 0.22 0.20 0.18 0.16 0.14 0.12 0.10
E[B-V]

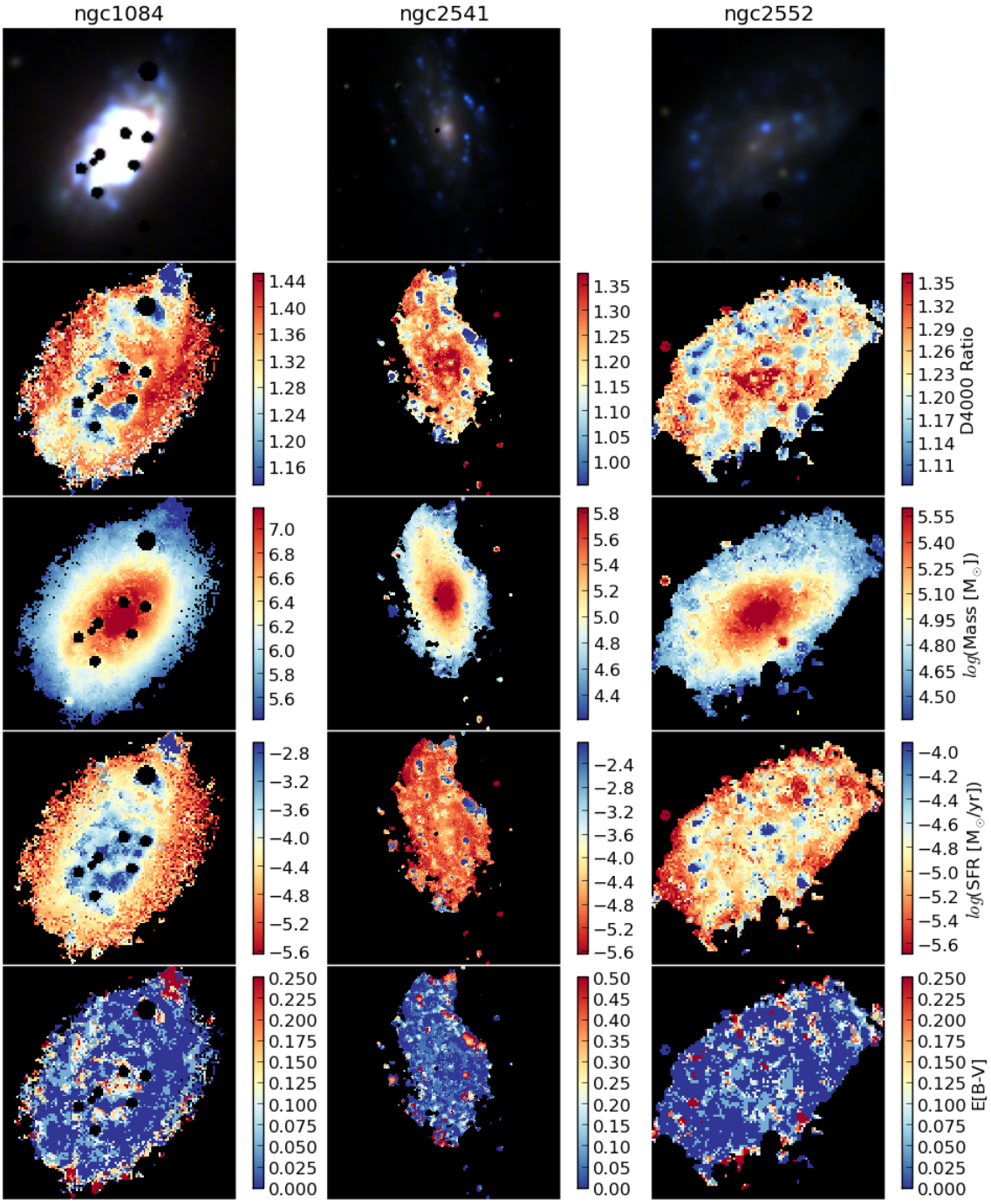
ngc1084
ngc2541
ngc2552
1.44 1.40 1.36 1.32 1.28 1.24 1.20 1.16
1.35 1.30 1.25 1.20 1.15 1.10 1.05 1.00
1.35 1.32 1.29 1.26 1.23 1.20 1.17 1.14 1.11
D4000 Ratio
7.0 6.8 6.6 6.4 6.2 6.0 5.8 5.6
5.8 5.6 5.4 5.2 5.0 4.8 4.6 4.4
5.55 5.40 5.25 5.10 4.95 4.80 4.65 4.50
log(Mass [M⊙])
−2.8 −3.2 −3.6 −4.0 −4.4 −4.8 −5.2 −5.6
−2.4 −2.8 −3.2 −3.6 −4.0 −4.4 −4.8 −5.2 −5.6
−4.0 −4.2 −4.4 −4.6 −4.8 −5.0 −5.2 −5.4 −5.6
log(SFR [M⊙/yr])
0.250 0.225 0.200 0.175 0.150 0.125 0.100 0.075 0.050 0.025 0.000
0.50 0.45 0.40 0.35 0.30 0.25 0.20 0.15 0.10 0.05 0.00
0.250 0.225 0.200 0.175 0.150 0.125 0.100 0.075 0.050 0.025 0.000
E[B-V]

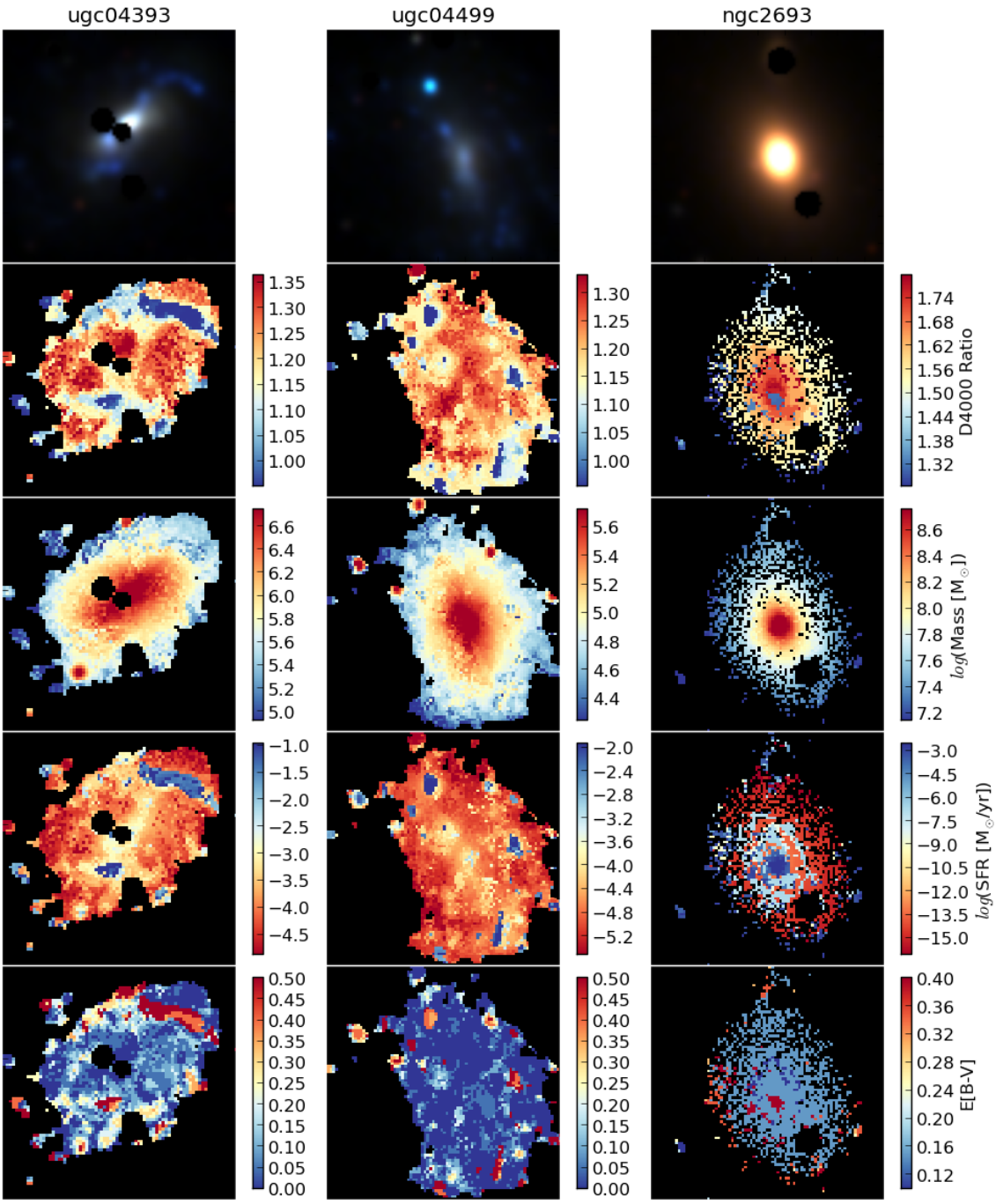
ugc04393
ugc04499
ngc2693
1.35 1.30 1.25 1.20 1.15 1.10 1.05 1.00
1.30 1.25 1.20 1.15 1.10 1.05 1.00
1.74 1.68 1.62 1.56 1.50 1.44 1.38 1.32
D4000 Ratio
6.6 6.4 6.2 6.0 5.8 5.6 5.4 5.2 5.0
5.6 5.4 5.2 5.0 4.8 4.6 4.4
8.6 8.4 8.2 8.0 7.8 7.6 7.4 7.2
log(Mass [M⊙])
−1.0 −1.5 −2.0 −2.5 −3.0 −3.5 −4.0 −4.5
−2.0 −2.4 −2.8 −3.2 −3.6 −4.0 −4.4 −4.8 −5.2
−3.0 −4.5 −6.0 −7.5 −9.0 −10.5 −12.0 −13.5 −15.0
log(SFR [M⊙/yr])
0.50 0.45 0.40 0.35 0.30 0.25 0.20 0.15 0.10 0.05 0.00
0.50 0.45 0.40 0.35 0.30 0.25 0.20 0.15 0.10 0.05 0.00
0.40 0.36 0.32 0.28 0.24 0.20 0.16 0.12
E[B-V]

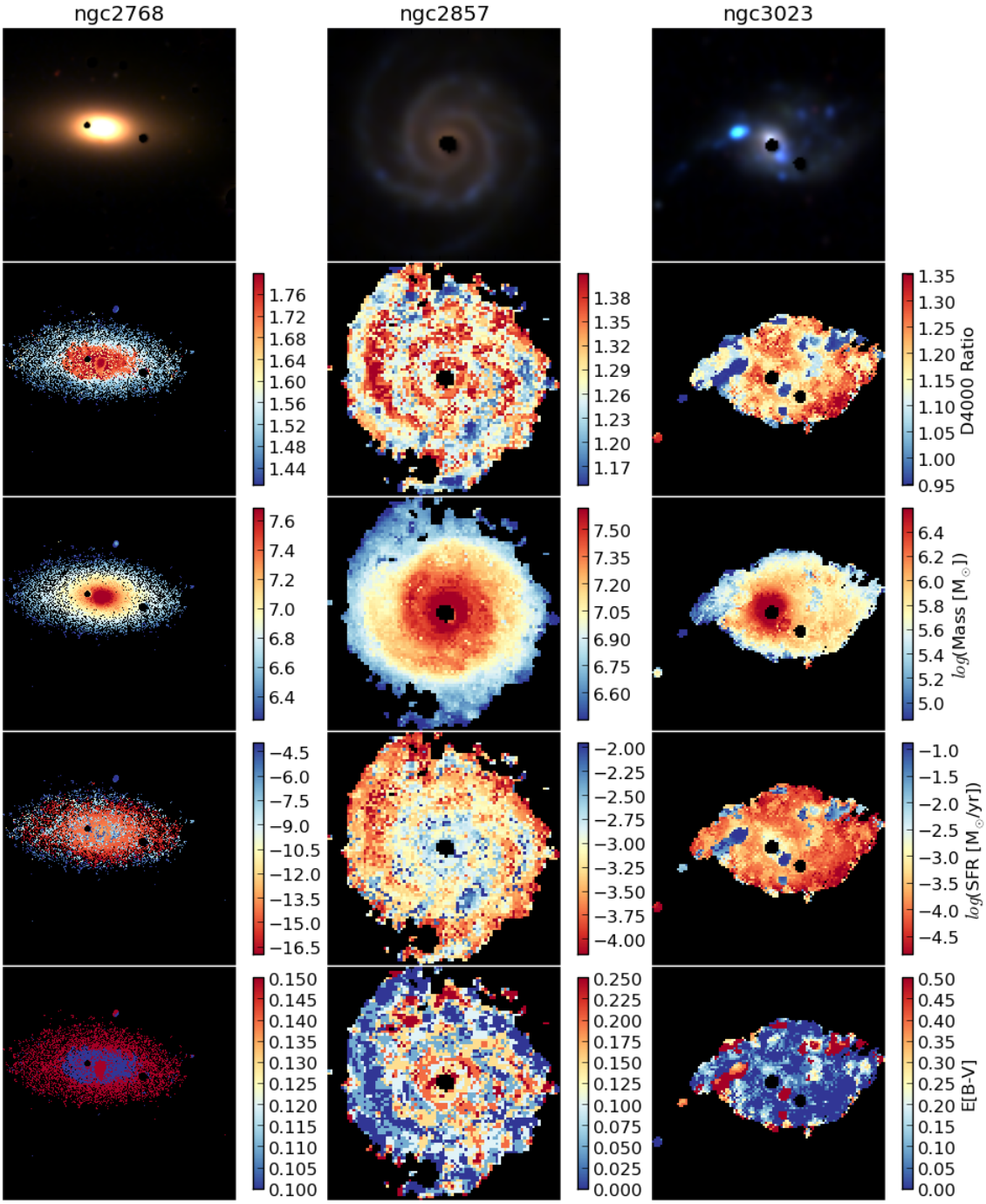
ngc2768
ngc2857
ngc3023
1.76 1.72 1.68 1.64 1.60 1.56 1.52 1.48 1.44
1.38 1.35 1.32 1.29 1.26 1.23 1.20 1.17
1.35 1.30 1.25 1.20 1.15 1.10 1.05 1.00 0.95
D4000 Ratio
7.6 7.4 7.2 7.0 6.8 6.6 6.4
7.50 7.35 7.20 7.05 6.90 6.75 6.60
6.4 6.2 6.0 5.8 5.6 5.4 5.2 5.0
log(Mass [M⊙])
−4.5 −6.0 −7.5 −9.0 −10.5 −12.0 −13.5 −15.0 −16.5
−2.00 −2.25 −2.50 −2.75 −3.00 −3.25 −3.50 −3.75 −4.00
−1.0 −1.5 −2.0 −2.5 −3.0 −3.5 −4.0 −4.5
log(SFR [M⊙/yr])
0.150 0.145 0.140 0.135 0.130 0.125 0.120 0.115 0.110 0.105 0.100
0.250 0.225 0.200 0.175 0.150 0.125 0.100 0.075 0.050 0.025 0.000
0.50 0.45 0.40 0.35 0.30 0.25 0.20 0.15 0.10 0.05 0.00
E[B-V]

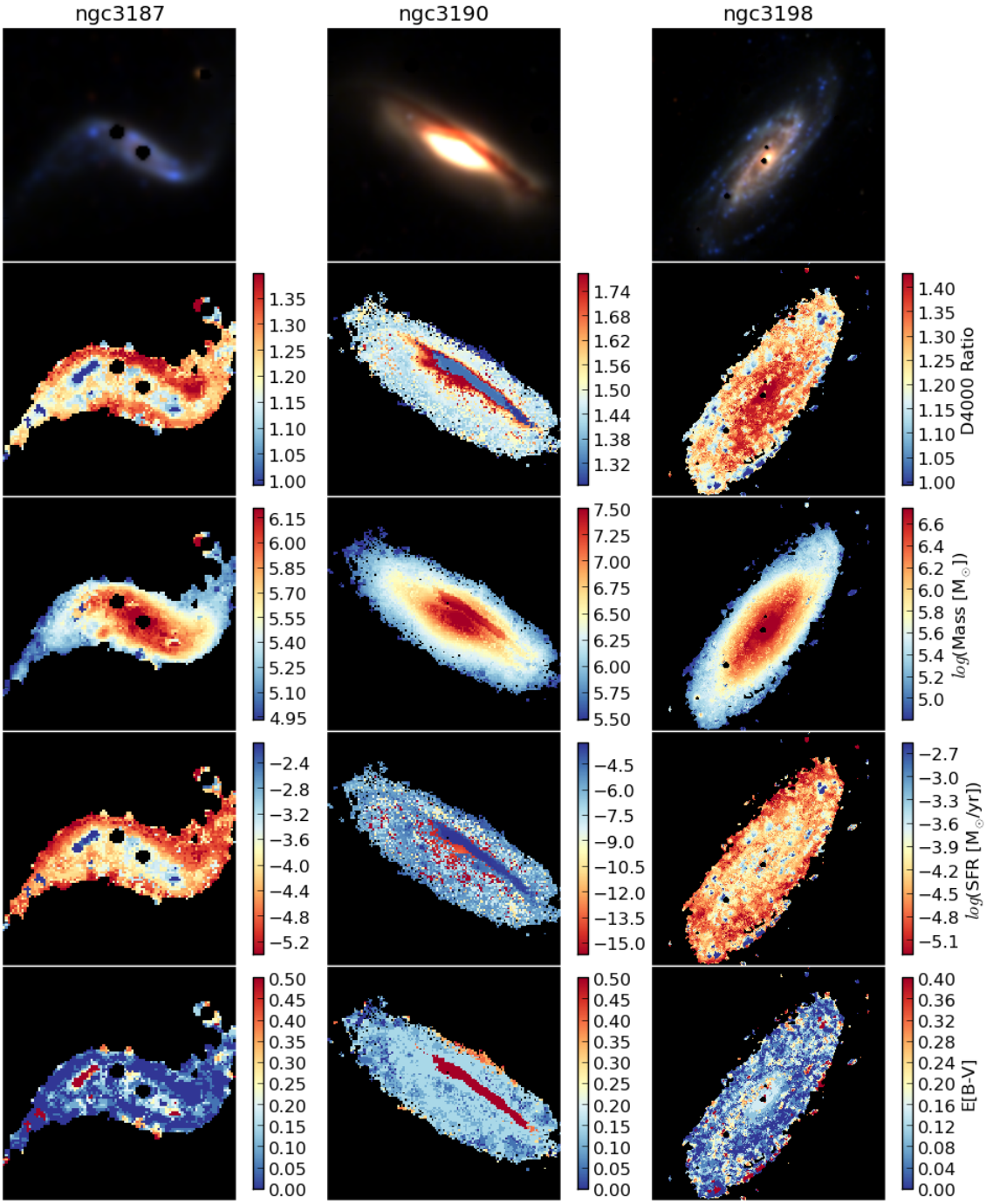
ngc3187
ngc3190
ngc3198
1.35 1.30 1.25 1.20 1.15 1.10 1.05 1.00
1.74 1.68 1.62 1.56 1.50 1.44 1.38 1.32
1.40 1.35 1.30 1.25 1.20 1.15 1.10 1.05 1.00
D4000 Ratio
6.15 6.00 5.85 5.70 5.55 5.40 5.25 5.10 4.95
7.50 7.25 7.00 6.75 6.50 6.25 6.00 5.75 5.50
6.6 6.4 6.2 6.0 5.8 5.6 5.4 5.2 5.0
log(Mass [M⊙])
−2.4 −2.8 −3.2 −3.6 −4.0 −4.4 −4.8 −5.2
−4.5 −6.0 −7.5 −9.0 −10.5 −12.0 −13.5 −15.0
−2.7 −3.0 −3.3 −3.6 −3.9 −4.2 −4.5 −4.8 −5.1
log(SFR [M⊙/yr])
0.50 0.45 0.40 0.35 0.30 0.25 0.20 0.15 0.10 0.05 0.00
0.50 0.45 0.40 0.35 0.30 0.25 0.20 0.15 0.10 0.05 0.00
0.40 0.36 0.32 0.28 0.24 0.20 0.16 0.12 0.08 0.04 0.00
E[B-V]

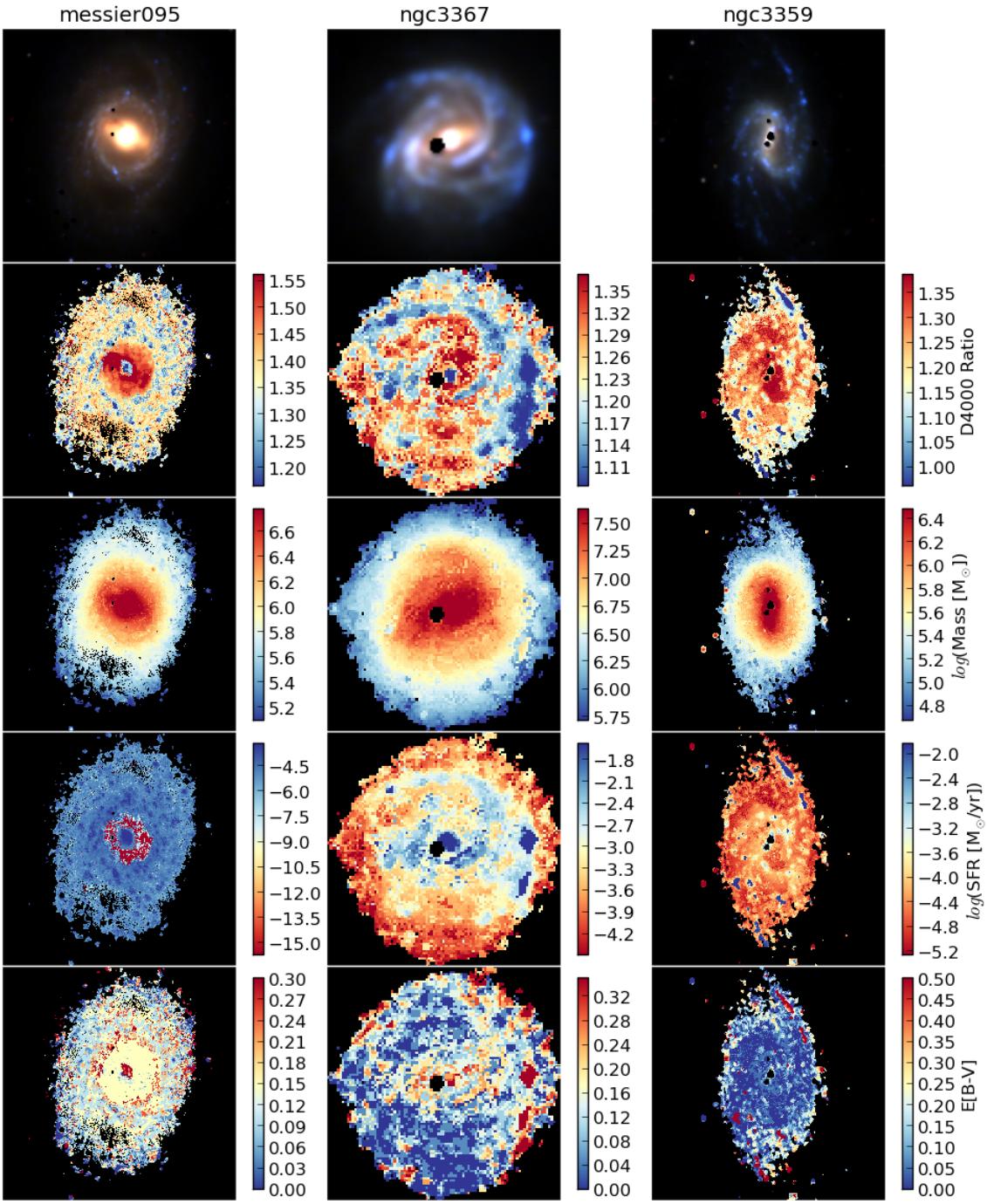
messier095
ngc3367
ngc3359
1.55 1.50 1.45 1.40 1.35 1.30 1.25 1.20
1.35 1.32 1.29 1.26 1.23 1.20 1.17 1.14 1.11
1.35 1.30 1.25 1.20 1.15 1.10 1.05 1.00
D4000 Ratio
6.6 6.4 6.2 6.0 5.8 5.6 5.4 5.2
7.50 7.25 7.00 6.75 6.50 6.25 6.00 5.75
6.4 6.2 6.0 5.8 5.6 5.4 5.2 5.0 4.8
log(Mass [M⊙])
−4.5 −6.0 −7.5 −9.0 −10.5 −12.0 −13.5 −15.0
−1.8 −2.1 −2.4 −2.7 −3.0 −3.3 −3.6 −3.9 −4.2
−2.0 −2.4 −2.8 −3.2 −3.6 −4.0 −4.4 −4.8 −5.2
log(SFR [M⊙/yr])
0.30 0.27 0.24 0.21 0.18 0.15 0.12 0.09 0.06 0.03 0.00
0.32 0.28 0.24 0.20 0.16 0.12 0.08 0.04 0.00
0.50 0.45 0.40 0.35 0.30 0.25 0.20 0.15 0.10 0.05 0.00
E[B-V]

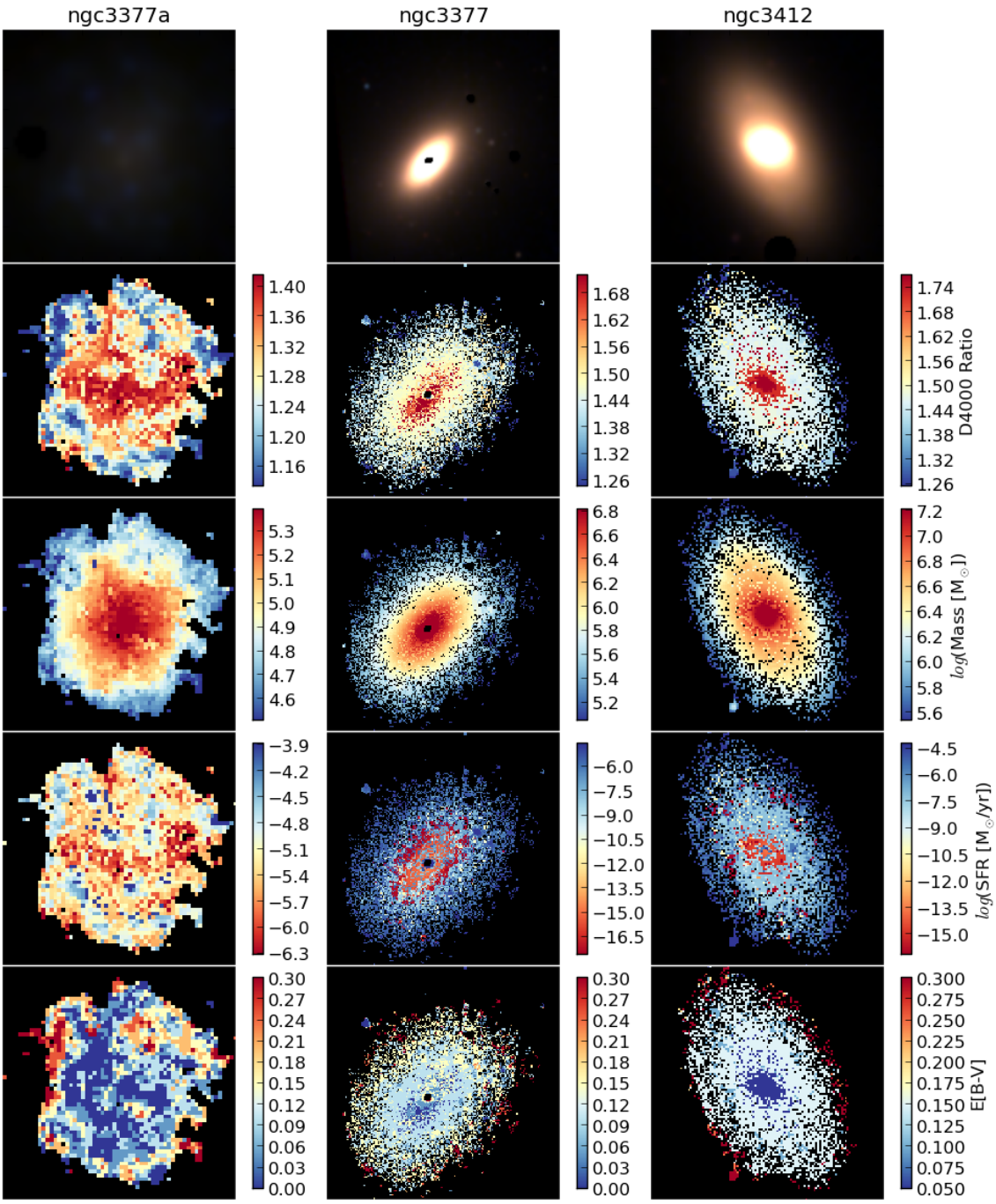
ngc3377a
ngc3377
ngc3412
1.40
1.36
1.32
1.28
1.24
1.20
1.16
1.68
1.62
1.56
1.50
1.44
1.38
1.32
1.26
1.74
1.68
1.62
1.56
1.50
1.44
1.38
1.32
1.26
D4000 Ratio
5.3
5.2
5.1
5.0
4.9
4.8
4.7
4.6
6.8
6.6
6.4
6.2
6.0
5.8
5.6
5.4
5.2
7.2
7.0
6.8
6.6
6.4
6.2
6.0
5.8
5.6
log(Mass [M⊙])
−3.9
−4.2
−4.5
−4.8
−5.1
−5.4
−5.7
−6.0
−6.3
−6.0
−7.5
−9.0
−10.5
−12.0
−13.5
−15.0
−16.5
−4.5
−6.0
−7.5
−9.0
−10.5
−12.0
−13.5
−15.0
log(SFR [M⊙/yr])
0.30
0.27
0.24
0.21
0.18
0.15
0.12
0.09
0.06
0.03
0.00
0.30
0.27
0.24
0.21
0.18
0.15
0.12
0.09
0.06
0.03
0.00
0.300
0.275
0.250
0.225
0.200
0.175
0.150
0.125
0.100
0.075
0.050
E[B-V]

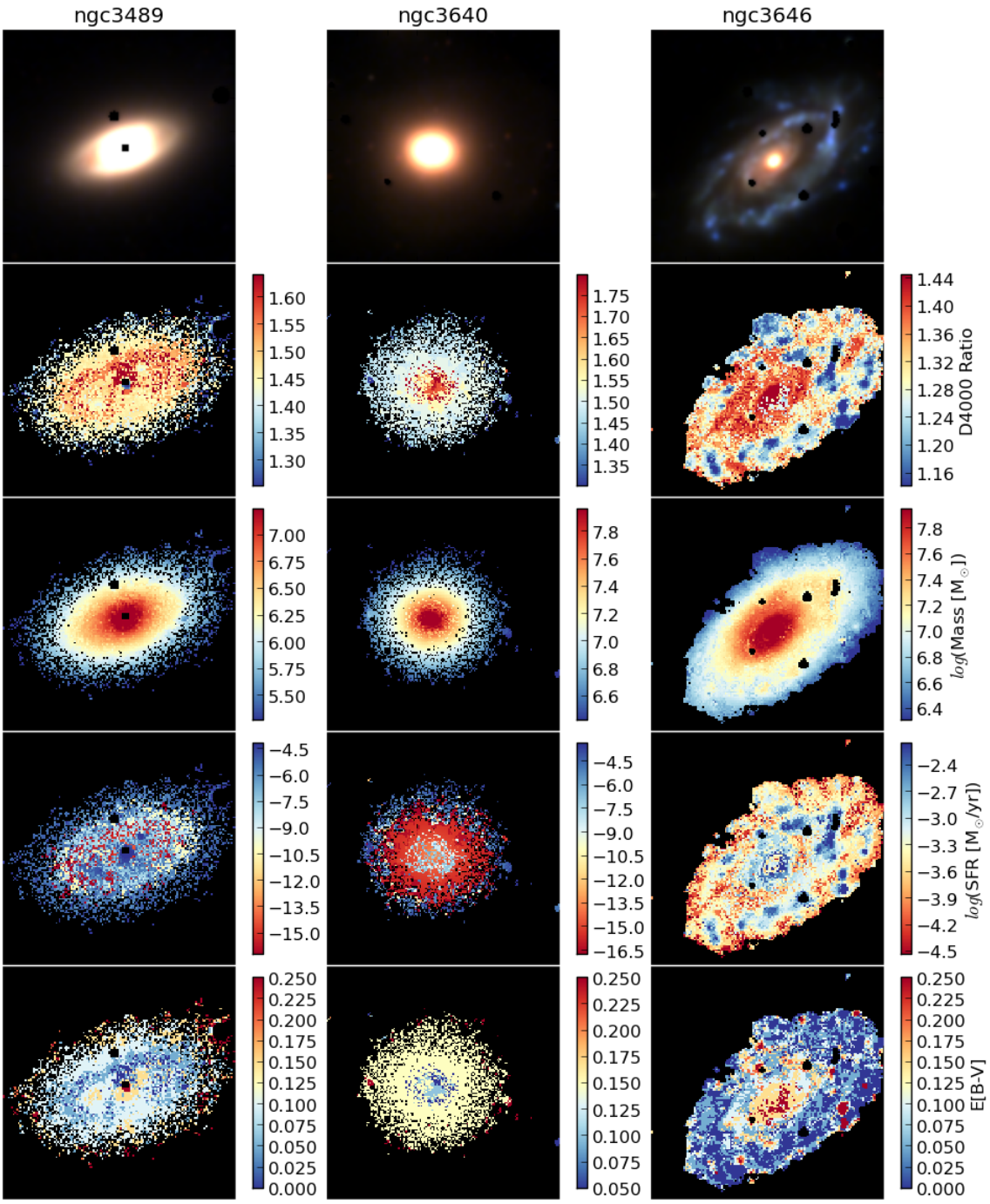
ngc3489
ngc3640
ngc3646
1.60
1.55
1.50
1.45
1.40
1.35
1.30
1.75
1.70
1.65
1.60
1.55
1.50
1.45
1.40
1.35
1.44
1.40
1.36
1.32
1.28
1.24
1.20
1.16
D4000 Ratio
7.00
6.75
6.50
6.25
6.00
5.75
5.50
7.8
7.6
7.4
7.2
7.0
6.8
6.6
7.8
7.6
7.4
7.2
7.0
6.8
6.6
6.4
log(Mass [M⊙])
−4.5
−6.0
−7.5
−9.0
−10.5
−12.0
−13.5
−15.0
−4.5
−6.0
−7.5
−9.0
−10.5
−12.0
−13.5
−15.0
−16.5
−2.4
−2.7
−3.0
−3.3
−3.6
−3.9
−4.2
−4.5
log(SFR [M⊙/yr])
0.250
0.225
0.200
0.175
0.150
0.125
0.100
0.075
0.050
0.025
0.000
0.250
0.225
0.200
0.175
0.150
0.125
0.100
0.075
0.050
0.250
0.225
0.200
0.175
0.150
0.125
0.100
0.075
0.050
0.025
0.000
E[B-V]

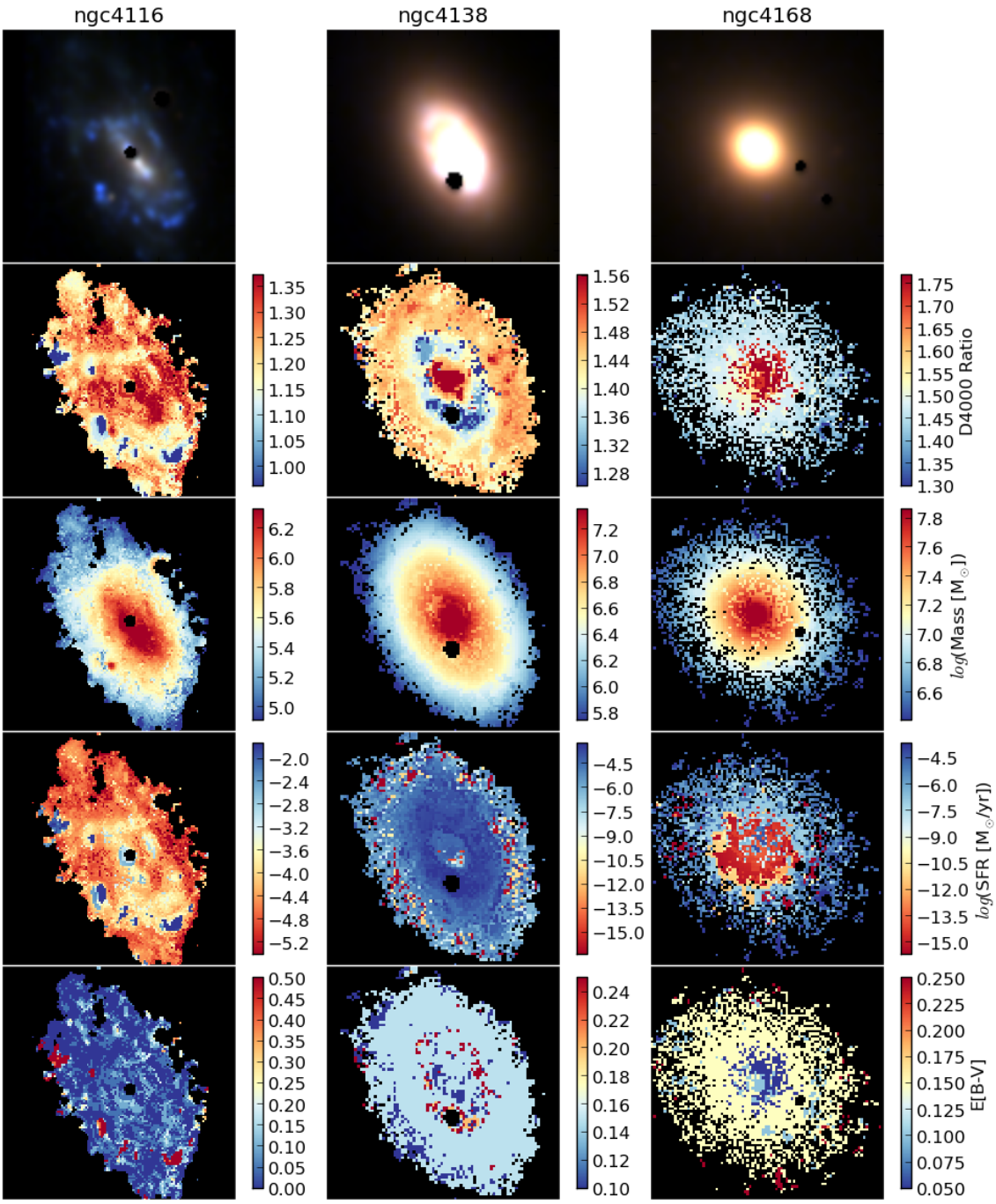
ngc4116
ngc4138
ngc4168
1.35 1.30 1.25 1.20 1.15 1.10 1.05 1.00
1.56 1.52 1.48 1.44 1.40 1.36 1.32 1.28
1.75 1.70 1.65 1.60 1.55 1.50 1.45 1.40 1.35 1.30
D4000 Ratio
6.2 6.0 5.8 5.6 5.4 5.2 5.0
7.2 7.0 6.8 6.6 6.4 6.2 6.0 5.8
7.8 7.6 7.4 7.2 7.0 6.8 6.6
log(Mass [M⊙])
−2.0 −2.4 −2.8 −3.2 −3.6 −4.0 −4.4 −4.8 −5.2
−4.5 −6.0 −7.5 −9.0 −10.5 −12.0 −13.5 −15.0
−4.5 −6.0 −7.5 −9.0 −10.5 −12.0 −13.5 −15.0
log(SFR [M⊙/yr])
0.50 0.45 0.40 0.35 0.30 0.25 0.20 0.15 0.10 0.05 0.00
0.24 0.22 0.20 0.18 0.16 0.14 0.12 0.10
0.250 0.225 0.200 0.175 0.150 0.125 0.100 0.075 0.050
E[B-V]

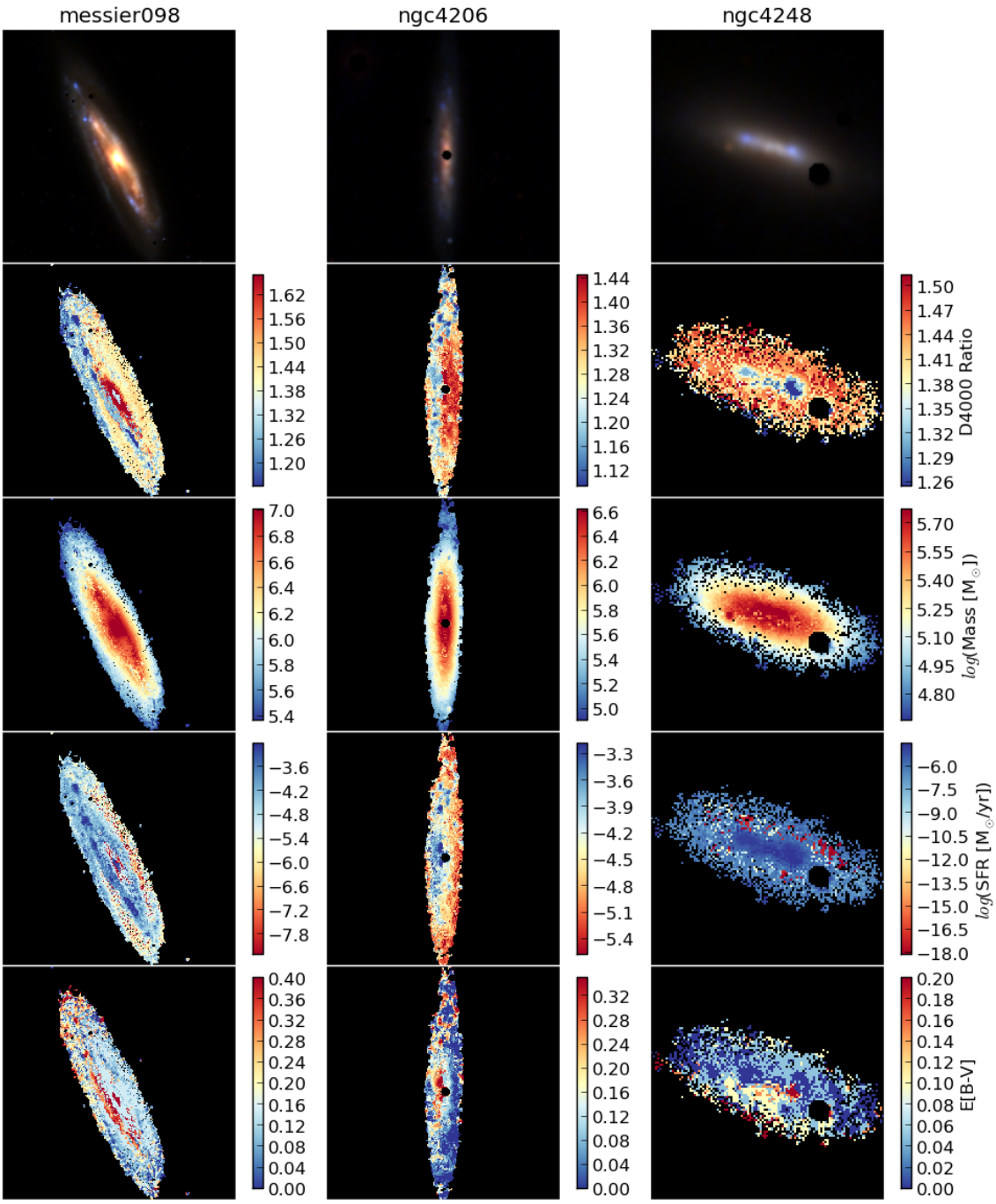
messier098
ngc4206
ngc4248
1.62 1.56 1.50 1.44 1.38 1.32 1.26 1.20
1.44 1.40 1.36 1.32 1.28 1.24 1.20 1.16 1.12
1.50 1.47 1.44 1.41 1.38 1.35 1.32 1.29 1.26
D4000 Ratio
7.0 6.8 6.6 6.4 6.2 6.0 5.8 5.6 5.4
6.6 6.4 6.2 6.0 5.8 5.6 5.4 5.2 5.0
5.70 5.55 5.40 5.25 5.10 4.95 4.80
log(Mass [M⊙])
−3.6 −4.2 −4.8 −5.4 −6.0 −6.6 −7.2 −7.8
−3.3 −3.6 −3.9 −4.2 −4.5 −4.8 −5.1 −5.4
−6.0 −7.5 −9.0 −10.5 −12.0 −13.5 −15.0 −16.5 −18.0
log(SFR [M⊙/yr])
0.40 0.36 0.32 0.28 0.24 0.20 0.16 0.12 0.08 0.04 0.00
0.32 0.28 0.24 0.20 0.16 0.12 0.08 0.04 0.00
0.20 0.18 0.16 0.14 0.12 0.10 0.08 0.06 0.04 0.02 0.00
E[B-V]

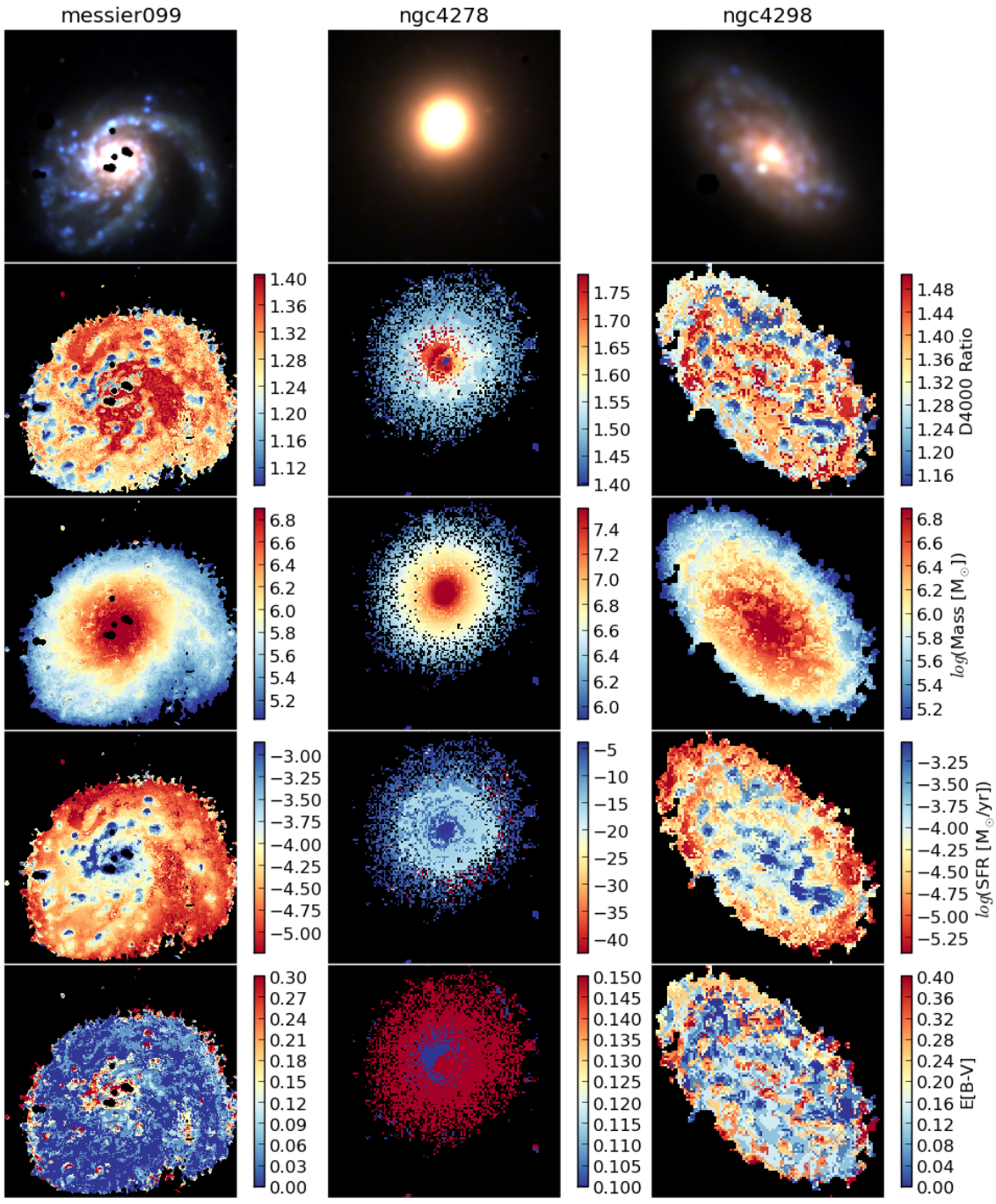
messier099
ngc4278
ngc4298
1.40 1.36 1.32 1.28 1.24 1.20 1.16 1.12
1.75 1.70 1.65 1.60 1.55 1.50 1.45 1.40
1.48 1.44 1.40 1.36 1.32 1.28 1.24 1.20 1.16
D4000 Ratio
6.8 6.6 6.4 6.2 6.0 5.8 5.6 5.4 5.2
7.4 7.2 7.0 6.8 6.6 6.4 6.2 6.0
6.8 6.6 6.4 6.2 6.0 5.8 5.6 5.4 5.2
log(Mass [M⊙])
−3.00 −3.25 −3.50 −3.75 −4.00 −4.25 −4.50 −4.75 −5.00
−5 −10 −15 −20 −25 −30 −35 −40
−3.25 −3.50 −3.75 −4.00 −4.25 −4.50 −4.75 −5.00 −5.25
log(SFR [M⊙/yr])
0.30 0.27 0.24 0.21 0.18 0.15 0.12 0.09 0.06 0.03 0.00
0.150 0.145 0.140 0.135 0.130 0.125 0.120 0.115 0.110 0.105 0.100
0.40 0.36 0.32 0.28 0.24 0.20 0.16 0.12 0.08 0.04 0.00
E[B-V]

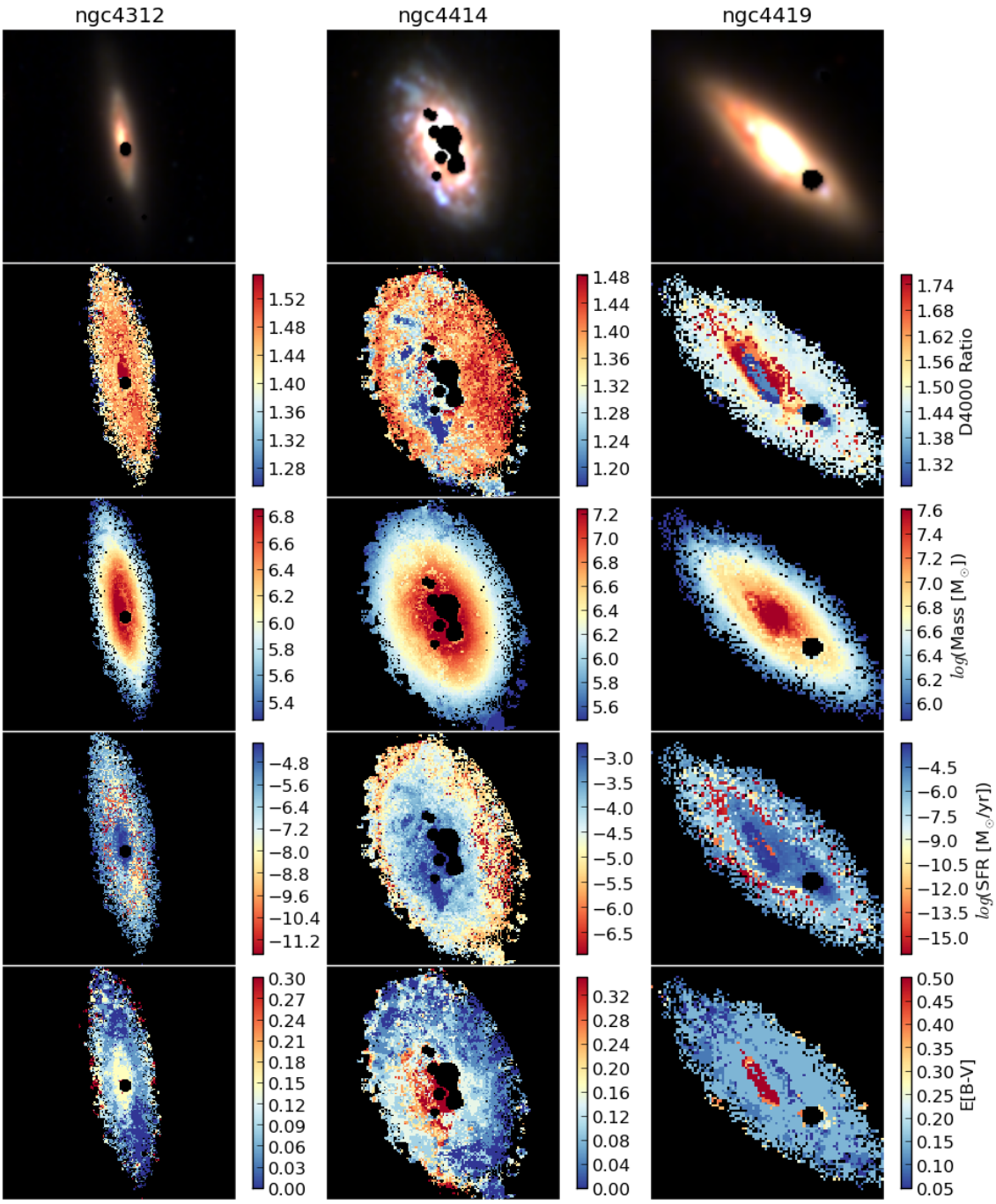
ngc4312
ngc4414
ngc4419
1.52 1.48 1.44 1.40 1.36 1.32 1.28
1.48 1.44 1.40 1.36 1.32 1.28 1.24 1.20
1.74 1.68 1.62 1.56 1.50 1.44 1.38 1.32
D4000 Ratio
6.8 6.6 6.4 6.2 6.0 5.8 5.6 5.4
7.2 7.0 6.8 6.6 6.4 6.2 6.0 5.8 5.6
7.6 7.4 7.2 7.0 6.8 6.6 6.4 6.2 6.0
log(Mass [M⊙])
−4.8 −5.6 −6.4 −7.2 −8.0 −8.8 −9.6 −10.4 −11.2
−3.0 −3.5 −4.0 −4.5 −5.0 −5.5 −6.0 −6.5
−4.5 −6.0 −7.5 −9.0 −10.5 −12.0 −13.5 −15.0
log(SFR [M⊙/yr])
0.30 0.27 0.24 0.21 0.18 0.15 0.12 0.09 0.06 0.03 0.00
0.32 0.28 0.24 0.20 0.16 0.12 0.08 0.04 0.00
0.50 0.45 0.40 0.35 0.30 0.25 0.20 0.15 0.10 0.05
E[B-V]

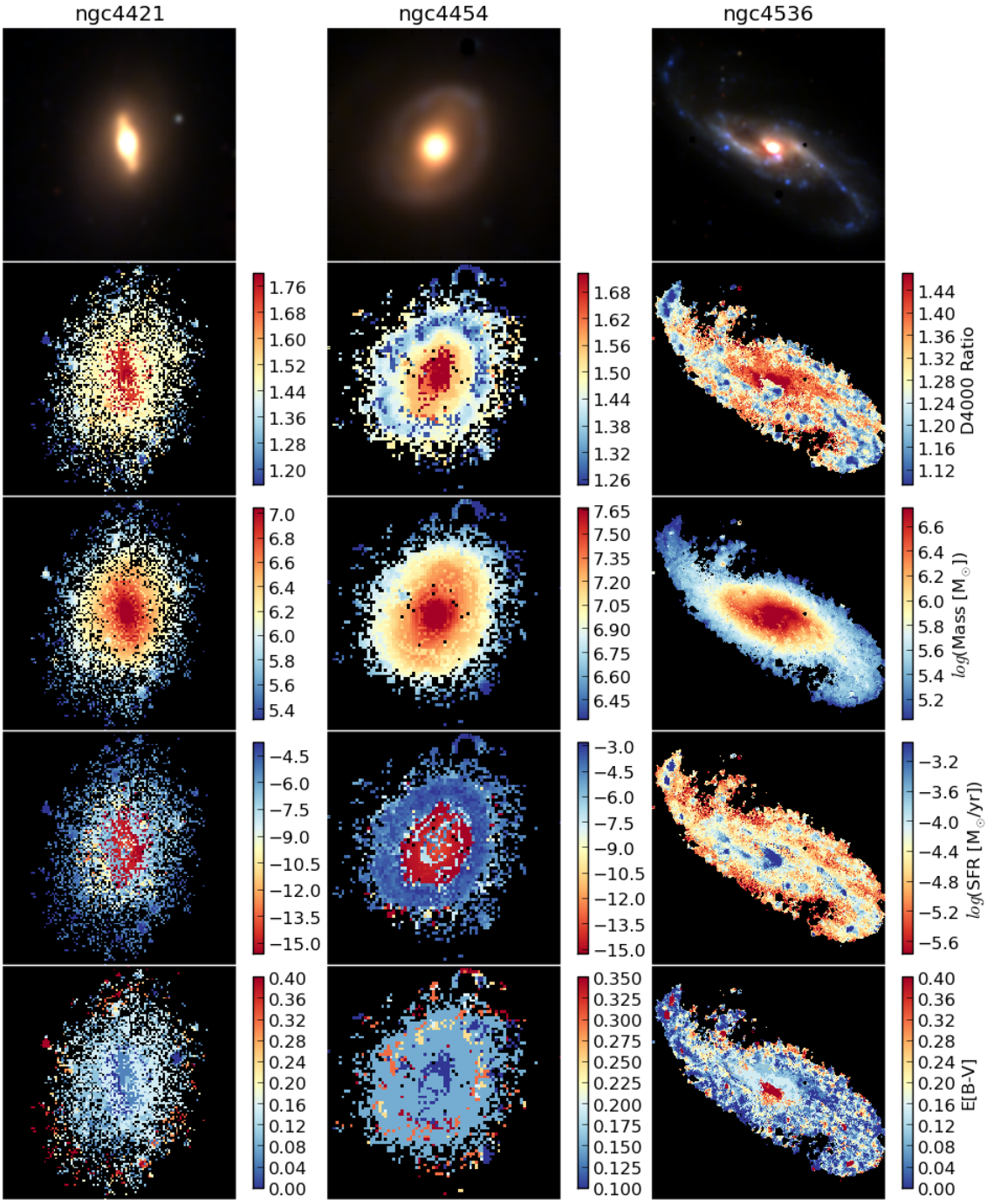
ngc4421
ngc4454
ngc4536
1.76 1.68 1.60 1.52 1.44 1.36 1.28 1.20
1.68 1.62 1.56 1.50 1.44 1.38 1.32 1.26
1.44 1.40 1.36 1.32 1.28 1.24 1.20 1.16 1.12
D4000 Ratio
7.0 6.8 6.6 6.4 6.2 6.0 5.8 5.6 5.4
7.65 7.50 7.35 7.20 7.05 6.90 6.75 6.60 6.45
6.6 6.4 6.2 6.0 5.8 5.6 5.4 5.2
log(Mass [M⊙])
−4.5 −6.0 −7.5 −9.0 −10.5 −12.0 −13.5 −15.0
−3.0 −4.5 −6.0 −7.5 −9.0 −10.5 −12.0 −13.5 −15.0
−3.2 −3.6 −4.0 −4.4 −4.8 −5.2 −5.6
log(SFR [M⊙/yr])
0.40 0.36 0.32 0.28 0.24 0.20 0.16 0.12 0.08 0.04 0.00
0.350 0.325 0.300 0.275 0.250 0.225 0.200 0.175 0.150 0.125 0.100
0.40 0.36 0.32 0.28 0.24 0.20 0.16 0.12 0.08 0.04 0.00
E[B-V]

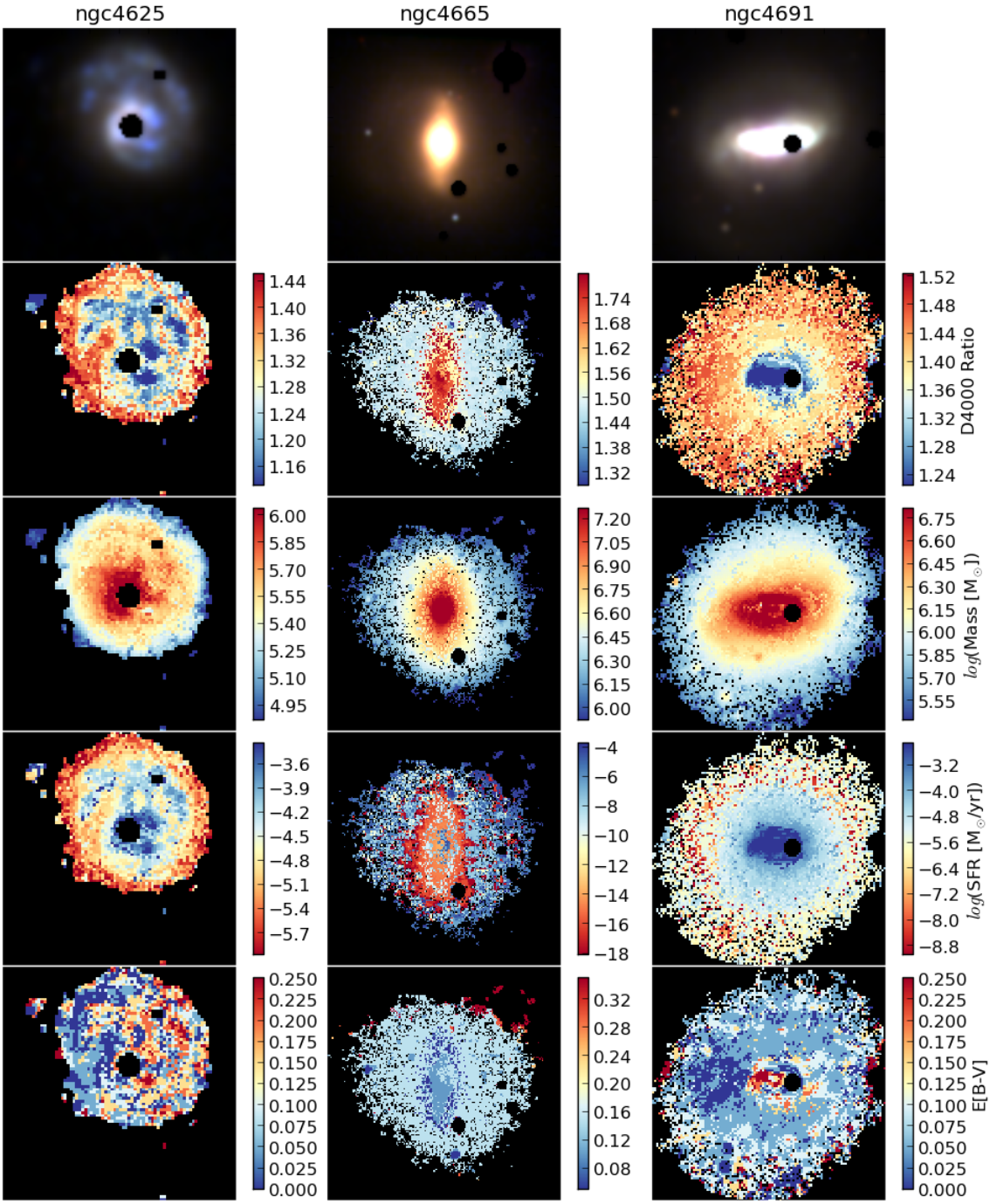
ngc4625
ngc4665
ngc4691
1.44 1.40 1.36 1.32 1.28 1.24 1.20 1.16
1.74 1.68 1.62 1.56 1.50 1.44 1.38 1.32
1.52 1.48 1.44 1.40 1.36 1.32 1.28 1.24
D4000 Ratio
6.00 5.85 5.70 5.55 5.40 5.25 5.10 4.95
7.20 7.05 6.90 6.75 6.60 6.45 6.30 6.15 6.00
6.75 6.60 6.45 6.30 6.15 6.00 5.85 5.70 5.55
log(Mass [M⊙])
−3.6 −3.9 −4.2 −4.5 −4.8 −5.1 −5.4 −5.7
−4 −6 −8 −10 −12 −14 −16 −18
−3.2 −4.0 −4.8 −5.6 −6.4 −7.2 −8.0 −8.8
log(SFR [M⊙/yr])
0.250 0.225 0.200 0.175 0.150 0.125 0.100 0.075 0.050 0.025 0.000
0.32 0.28 0.24 0.20 0.16 0.12 0.08
0.250 0.225 0.200 0.175 0.150 0.125 0.100 0.075 0.050 0.025 0.000
E[B-V]

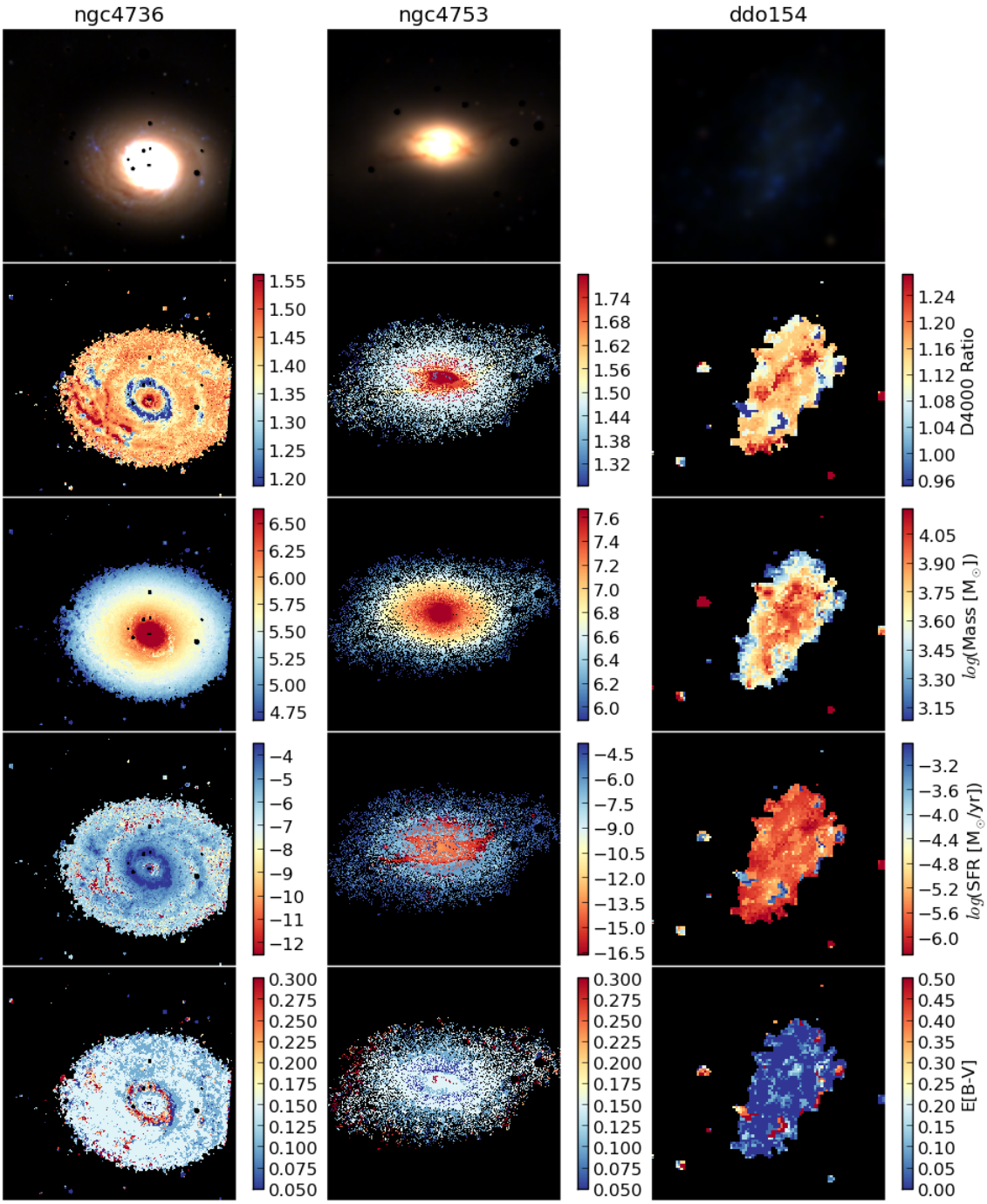
ngc4736
ngc4753
ddo154
1.55 1.50 1.45 1.40 1.35 1.30 1.25 1.20
1.74 1.68 1.62 1.56 1.50 1.44 1.38 1.32
1.24 1.20 1.16 1.12 1.08 1.04 1.00 0.96
D4000 Ratio
6.50 6.25 6.00 5.75 5.50 5.25 5.00 4.75
7.6 7.4 7.2 7.0 6.8 6.6 6.4 6.2 6.0
4.05 3.90 3.75 3.60 3.45 3.30 3.15
log(Mass [M⊙])
−4 −5 −6 −7 −8 −9 −10 −11 −12
−4.5 −6.0 −7.5 −9.0 −10.5 −12.0 −13.5 −15.0 −16.5
−3.2 −3.6 −4.0 −4.4 −4.8 −5.2 −5.6 −6.0
log(SFR [M⊙/yr])
0.300 0.275 0.250 0.225 0.200 0.175 0.150 0.125 0.100 0.075 0.050
0.300 0.275 0.250 0.225 0.200 0.175 0.150 0.125 0.100 0.075 0.050
0.50 0.45 0.40 0.35 0.30 0.25 0.20 0.15 0.10 0.05 0.00
E[B-V]

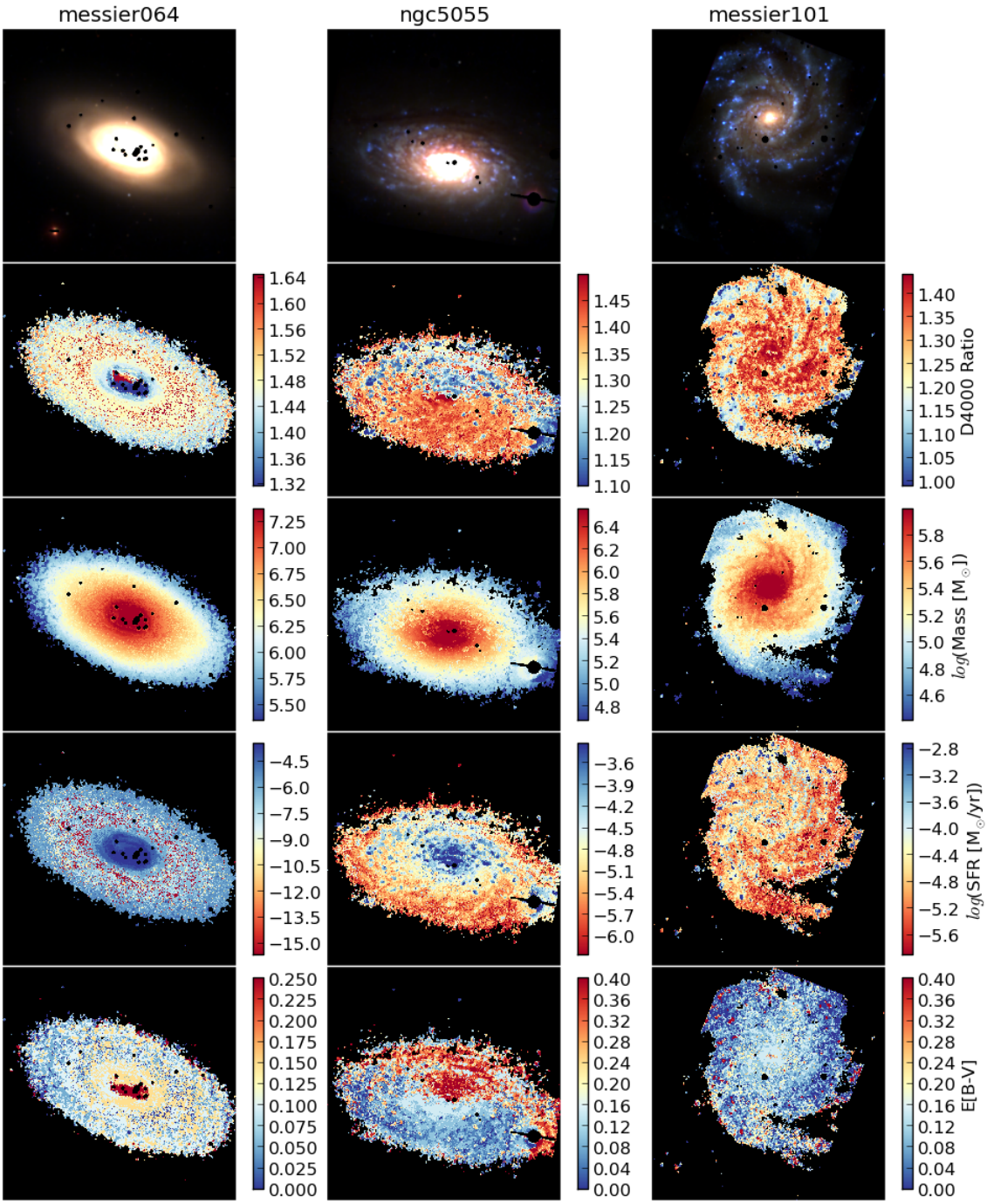
messier064
ngc5055
messier101
1.64 1.60 1.56 1.52 1.48 1.44 1.40 1.36 1.32
1.45 1.40 1.35 1.30 1.25 1.20 1.15 1.10
1.40 1.35 1.30 1.25 1.20 1.15 1.10 1.05 1.00
D4000 Ratio
7.25 7.00 6.75 6.50 6.25 6.00 5.75 5.50
6.4 6.2 6.0 5.8 5.6 5.4 5.2 5.0 4.8
5.8 5.6 5.4 5.2 5.0 4.8 4.6
log(Mass [M⊙])
−4.5 −6.0 −7.5 −9.0 −10.5 −12.0 −13.5 −15.0
−3.6 −3.9 −4.2 −4.5 −4.8 −5.1 −5.4 −5.7 −6.0
−2.8 −3.2 −3.6 −4.0 −4.4 −4.8 −5.2 −5.6
log(SFR [M⊙/yr])
0.250 0.225 0.200 0.175 0.150 0.125 0.100 0.075 0.050 0.025 0.000
0.40 0.36 0.32 0.28 0.24 0.20 0.16 0.12 0.08 0.04 0.00
0.40 0.36 0.32 0.28 0.24 0.20 0.16 0.12 0.08 0.04 0.00
E[B-V]

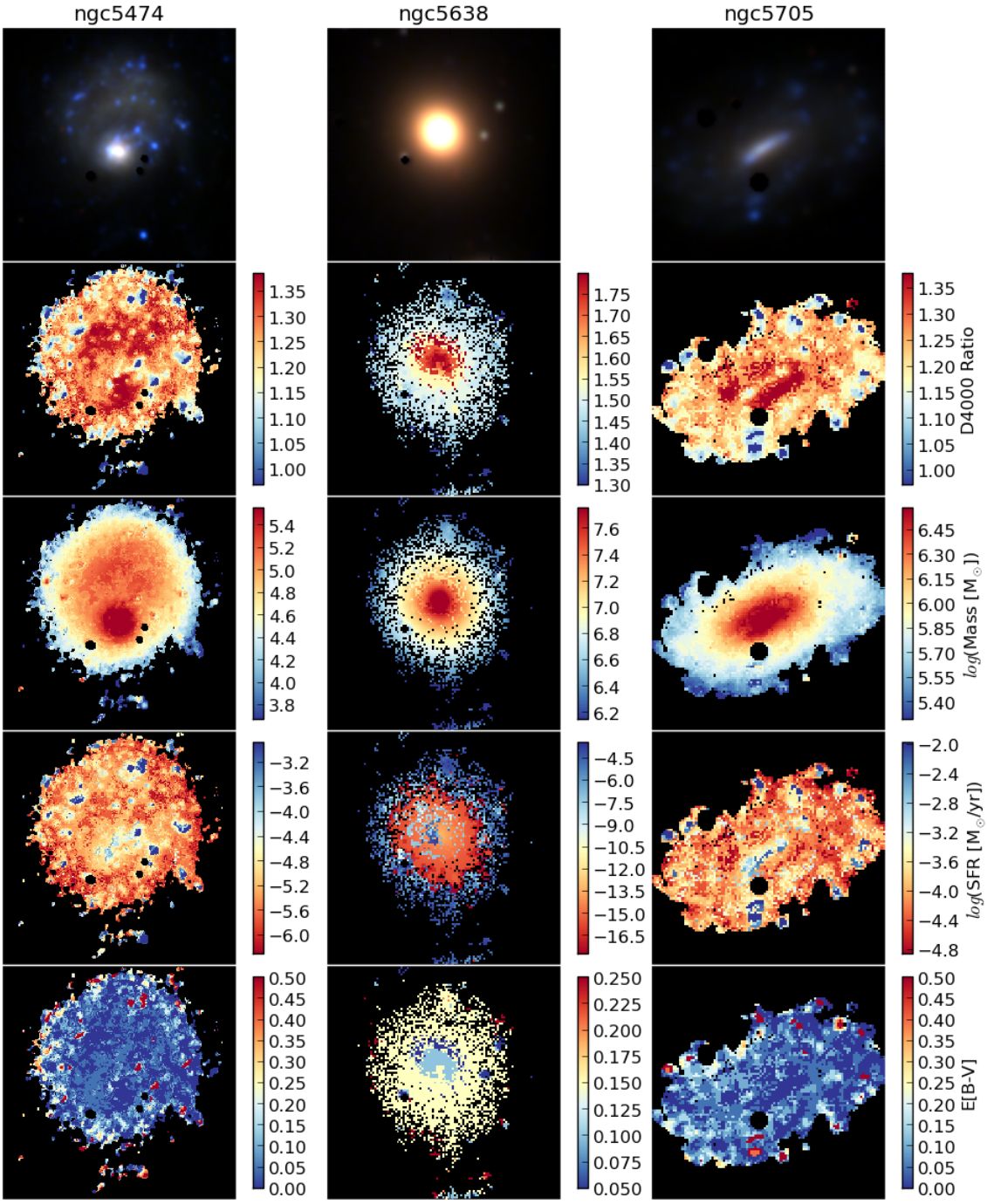
ngc5474
ngc5638
ngc5705
1.35 1.30 1.25 1.20 1.15 1.10 1.05 1.00
1.75 1.70 1.65 1.60 1.55 1.50 1.45 1.40 1.35 1.30
1.35 1.30 1.25 1.20 1.15 1.10 1.05 1.00
D4000 Ratio
5.4 5.2 5.0 4.8 4.6 4.4 4.2 4.0 3.8
7.6 7.4 7.2 7.0 6.8 6.6 6.4 6.2
6.45 6.30 6.15 6.00 5.85 5.70 5.55 5.40
log(Mass [M⊙])
−3.2 −3.6 −4.0 −4.4 −4.8 −5.2 −5.6 −6.0
−4.5 −6.0 −7.5 −9.0 −10.5 −12.0 −13.5 −15.0 −16.5
−2.0 −2.4 −2.8 −3.2 −3.6 −4.0 −4.4 −4.8
log(SFR [M⊙/yr])
0.50 0.45 0.40 0.35 0.30 0.25 0.20 0.15 0.10 0.05 0.00
0.250 0.225 0.200 0.175 0.150 0.125 0.100 0.075 0.050
0.50 0.45 0.40 0.35 0.30 0.25 0.20 0.15 0.10 0.05 0.00
E[B-V]

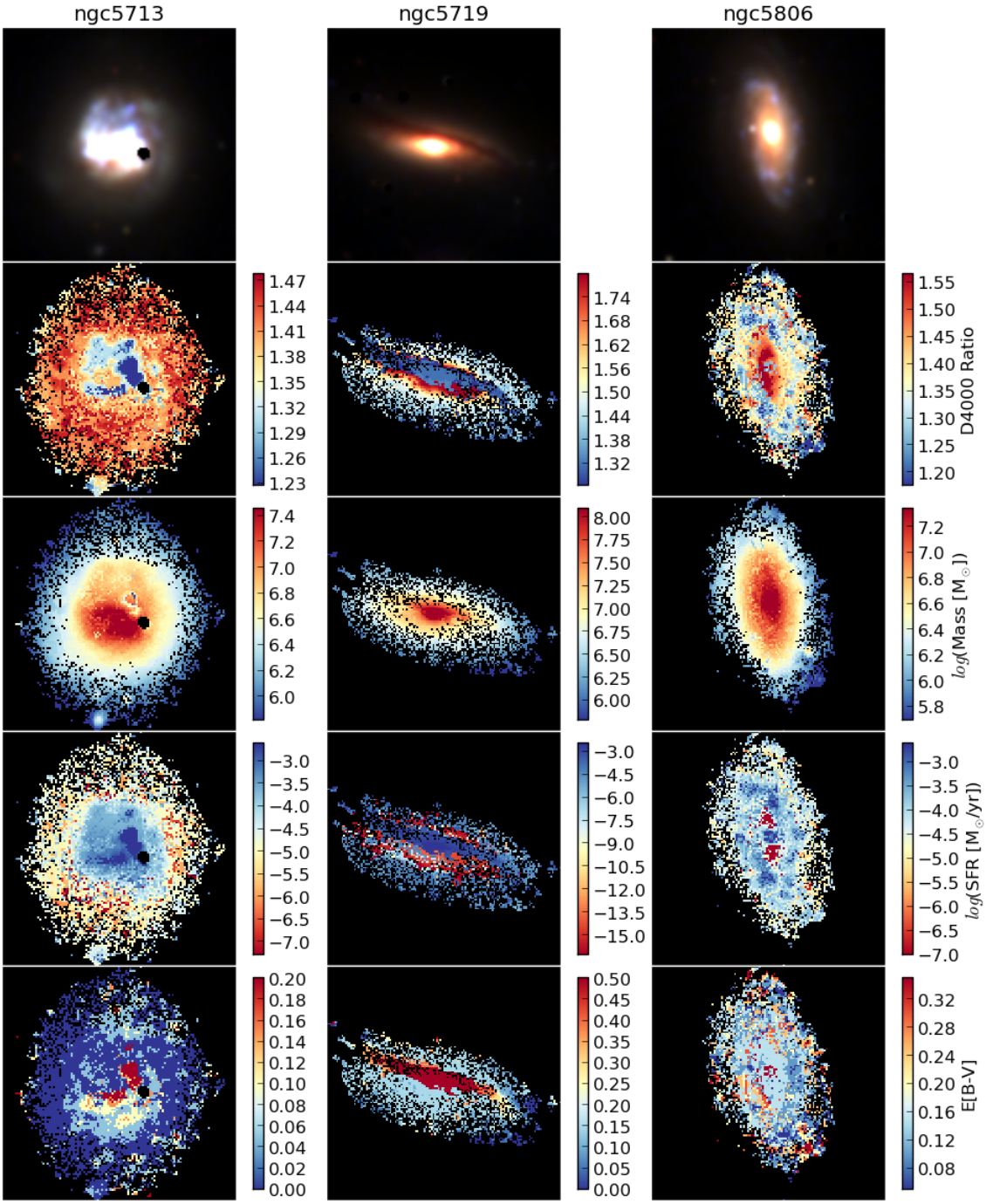
ngc5713
ngc5719
ngc5806
1.47
1.44
1.41
1.38
1.35
1.32
1.29
1.26
1.23
1.74
1.68
1.62
1.56
1.50
1.44
1.38
1.32
1.55
1.50
1.45
1.40
1.35
1.30
1.25
1.20
D4000 Ratio
7.4
7.2
7.0
6.8
6.6
6.4
6.2
6.0
8.00
7.75
7.50
7.25
7.00
6.75
6.50
6.25
6.00
7.2
7.0
6.8
6.6
6.4
6.2
6.0
5.8
log(Mass [M⊙])
−3.0
−3.5
−4.0
−4.5
−5.0
−5.5
−6.0
−6.5
−7.0
−3.0
−4.5
−6.0
−7.5
−9.0
−10.5
−12.0
−13.5
−15.0
−3.0
−3.5
−4.0
−4.5
−5.0
−5.5
−6.0
−6.5
−7.0
log(SFR [M⊙/yr])
0.20
0.18
0.16
0.14
0.12
0.10
0.08
0.06
0.04
0.02
0.00
0.50
0.45
0.40
0.35
0.30
0.25
0.20
0.15
0.10
0.05
0.00
0.32
0.28
0.24
0.20
0.16
0.12
0.08
E[B-V]

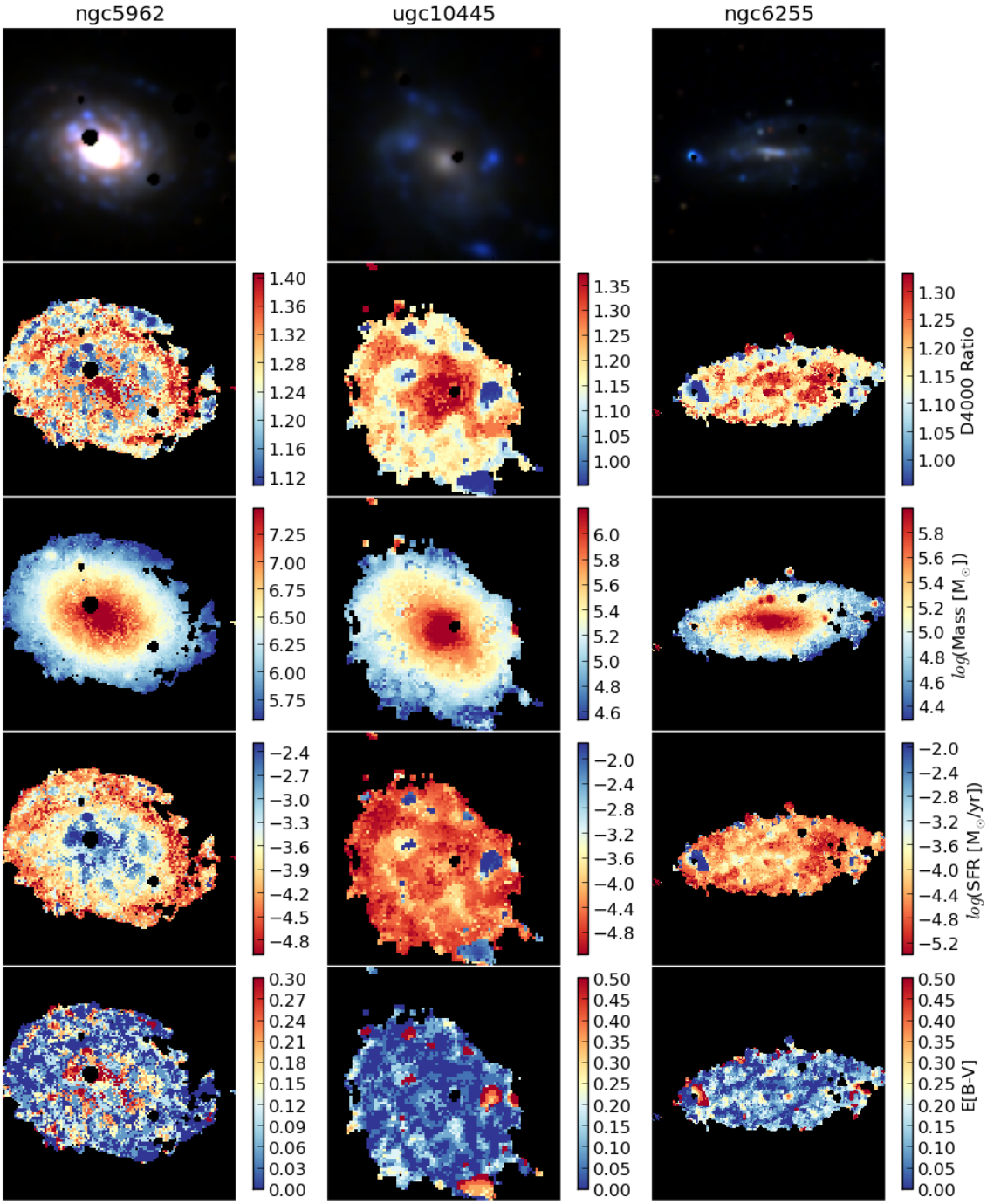
ngc5962
ugc10445
ngc6255
1.40 1.36 1.32 1.28 1.24 1.20 1.16 1.12
1.35 1.30 1.25 1.20 1.15 1.10 1.05 1.00
1.30 1.25 1.20 1.15 1.10 1.05 1.00
D4000 Ratio
7.25 7.00 6.75 6.50 6.25 6.00 5.75
6.0 5.8 5.6 5.4 5.2 5.0 4.8 4.6
5.8 5.6 5.4 5.2 5.0 4.8 4.6 4.4
log(Mass [M⊙])
−2.4 −2.7 −3.0 −3.3 −3.6 −3.9 −4.2 −4.5 −4.8
−2.0 −2.4 −2.8 −3.2 −3.6 −4.0 −4.4 −4.8
−2.0 −2.4 −2.8 −3.2 −3.6 −4.0 −4.4 −4.8 −5.2
log(SFR [M⊙/yr])
0.30 0.27 0.24 0.21 0.18 0.15 0.12 0.09 0.06 0.03 0.00
0.50 0.45 0.40 0.35 0.30 0.25 0.20 0.15 0.10 0.05 0.00
0.50 0.45 0.40 0.35 0.30 0.25 0.20 0.15 0.10 0.05 0.00
E[B-V]

Appendix B

Appendix B: Property Maps of XDF Galaxies

False color images (rest-frame *ugr*) made using a logarithmic scale, stellar mass, and star-formation rate maps for galaxies in the XDF with spectroscopic redshifts used in Chapter 3.

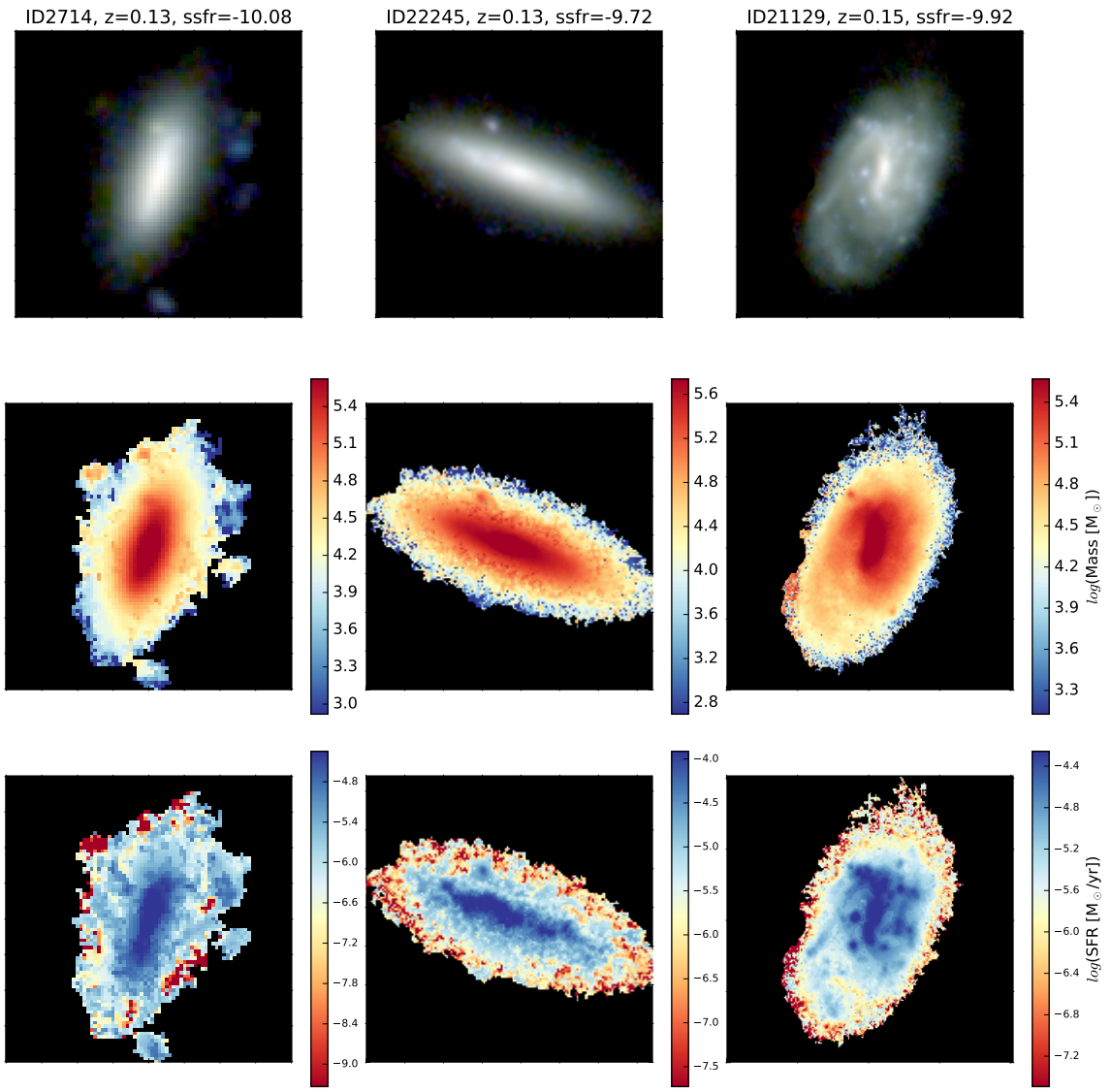
ID2714, z=0.13, ssfr=-10.08
ID22245, z=0.13, ssfr=-9.72
ID21129, z=0.15, ssfr=-9.92
5.4
5.1
4.8
4.5
4.2
3.9
3.6
3.3
3.0
5.6
5.2
4.8
4.4
4.0
3.6
3.2
2.8
5.4
5.1
4.8
4.5
4.2
3.9
3.6
3.3
log(Mass [M⊙])
−4.8
−5.4
−6.0
−6.6
−7.2
−7.8
−8.4
−9.0
−4.0
−4.5
−5.0
−5.5
−6.0
−6.5
−7.0
−7.5
−4.4
−4.8
−5.2
−5.6
−6.0
−6.4
−6.8
−7.2
log(SFR [M⊙/yr])

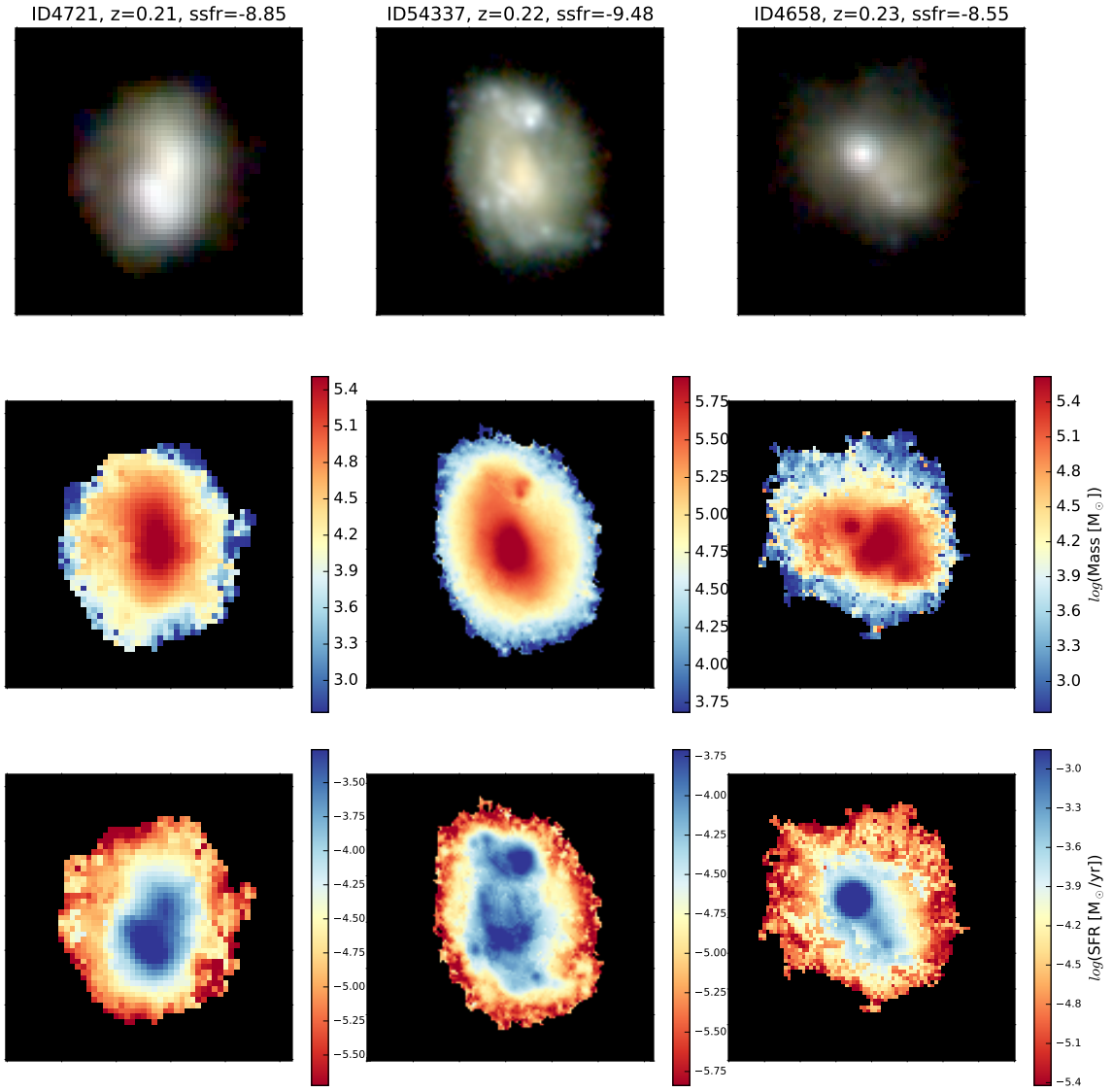
ID4721, z=0.21, ssfr=-8.85
ID54337, z=0.22, ssfr=-9.48
ID4658, z=0.23, ssfr=-8.55
5.4
5.1
4.8
4.5
4.2
3.9
3.6
3.3
3.0
5.75
5.50
5.25
5.00
4.75
4.50
4.25
4.00
3.75
log(Mass [M⊙])
−3.50
−3.75
−4.00
−4.25
−4.50
−4.75
−5.00
−5.25
−5.50
−3.75
−4.00
−4.25
−4.50
−4.75
−5.00
−5.25
−5.50
−5.75
log(SFR [M⊙/yr])

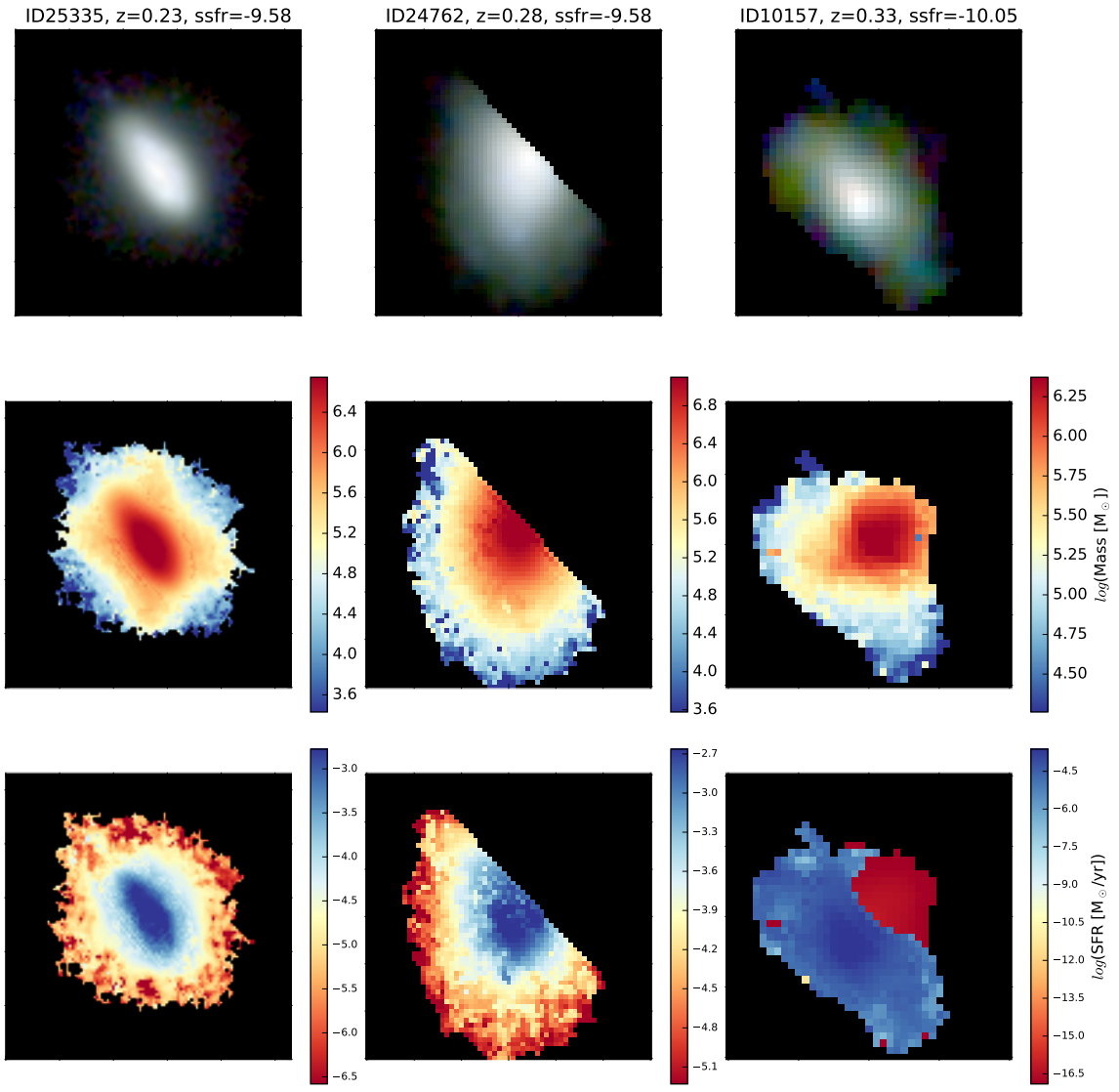
ID25335, z=0.23, ssfr=-9.58
ID24762, z=0.28, ssfr=-9.58
ID10157, z=0.33, ssfr=-10.05
log(Mass [M⊙])
log(SFR [M⊙/yr])

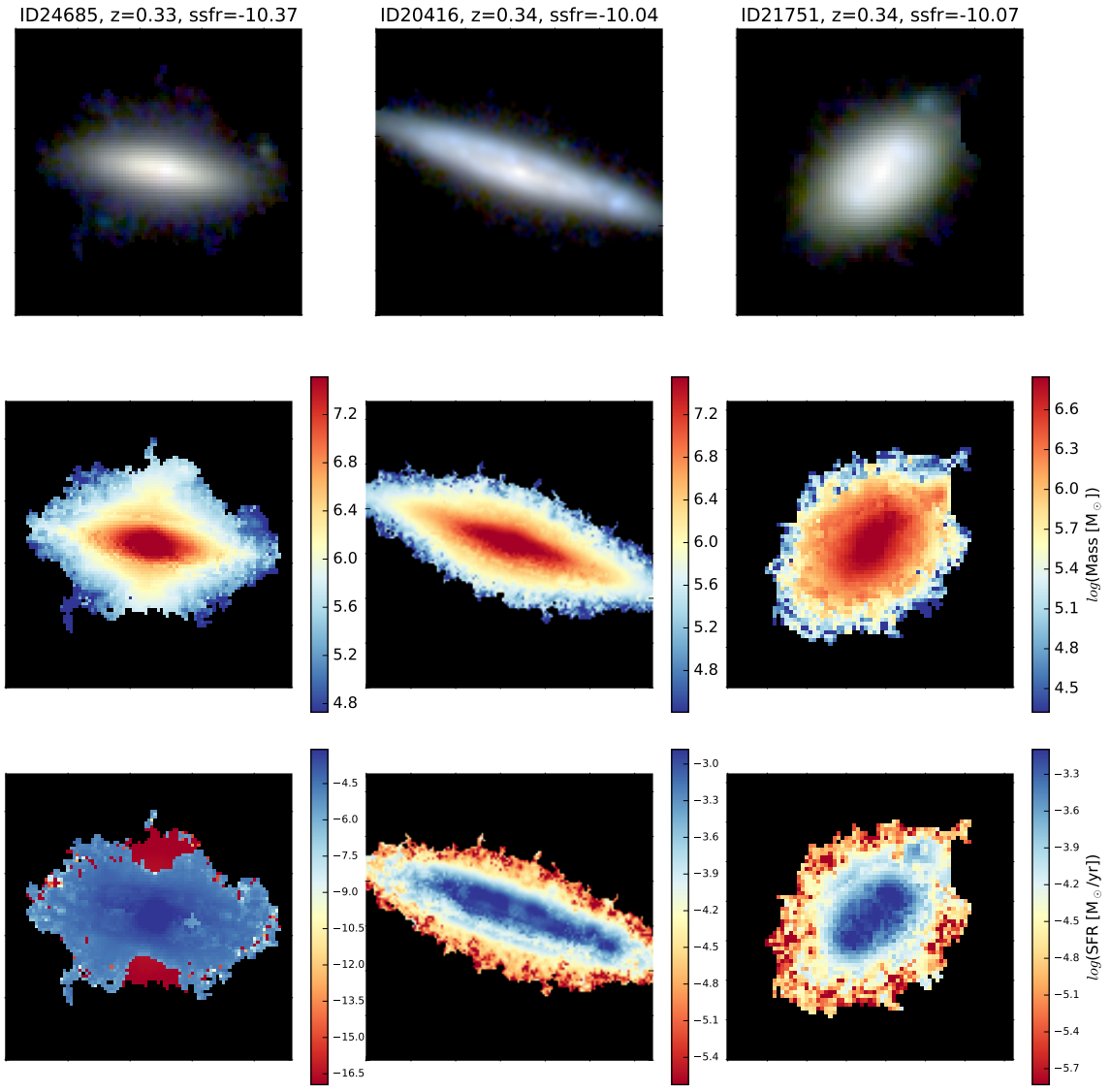
ID24685, z=0.33, ssfr=-10.37
ID20416, z=0.34, ssfr=-10.04
ID21751, z=0.34, ssfr=-10.07
7.2
6.8
6.4
6.0
5.6
5.2
4.8
7.2
6.8
6.4
6.0
5.6
5.2
4.8
6.6
6.3
6.0
5.7
5.4
5.1
4.8
4.5
log(Mass [M⊙])
−4.5
−6.0
−7.5
−9.0
−10.5
−12.0
−13.5
−15.0
−16.5
−3.0
−3.3
−3.6
−3.9
−4.2
−4.5
−4.8
−5.1
−5.4
−3.3
−3.6
−3.9
−4.2
−4.5
−4.8
−5.1
−5.4
−5.7
log(SFR [M⊙/yr])

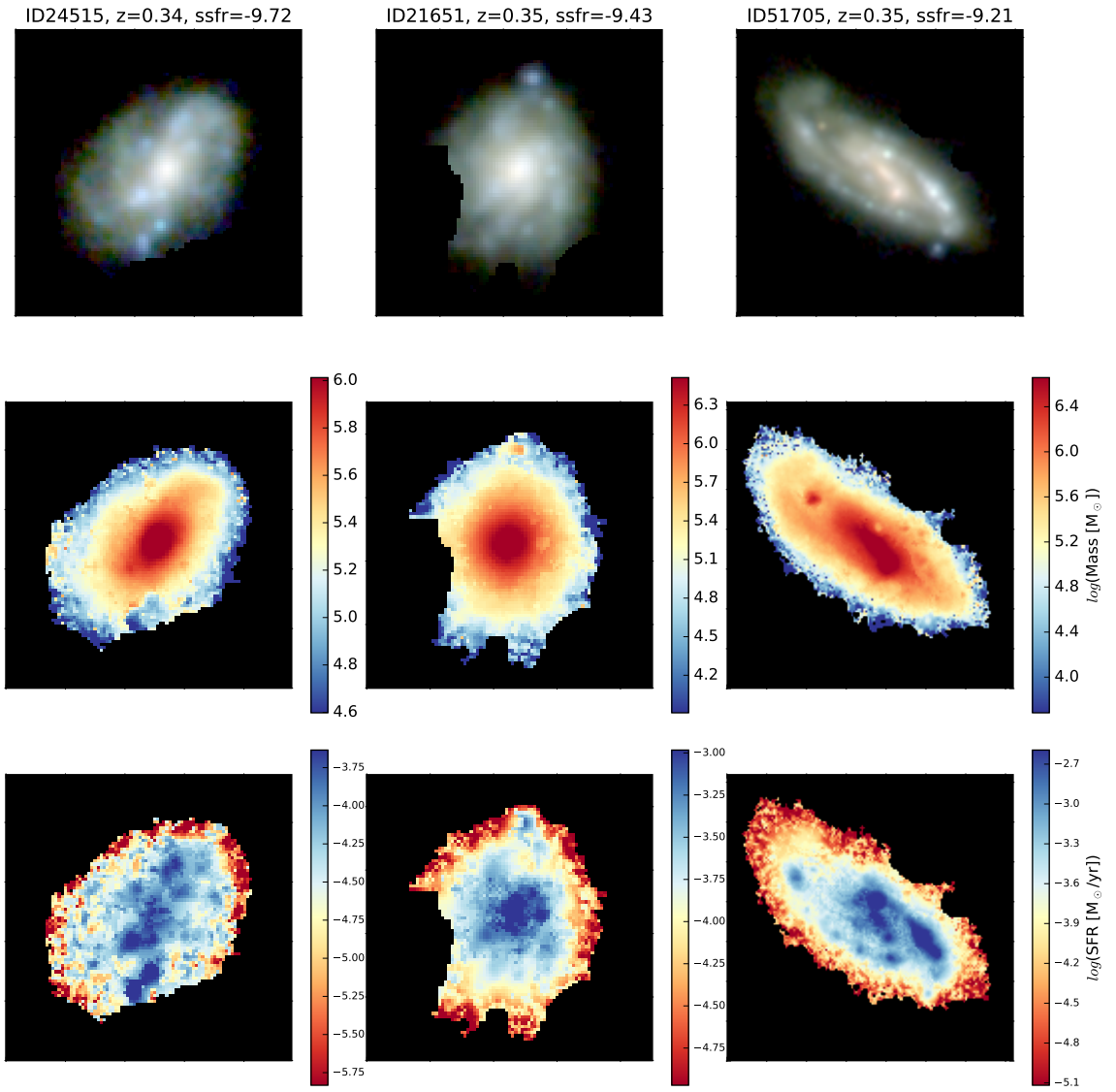
ID24515, z=0.34, ssfr=-9.72
ID21651, z=0.35, ssfr=-9.43
ID51705, z=0.35, ssfr=-9.21
6.0
5.8
5.6
5.4
5.2
5.0
4.8
4.6
6.3
6.0
5.7
5.4
5.1
4.8
4.5
4.2
6.4
6.0
5.6
5.2
4.8
4.4
4.0
log(Mass [M⊙])
−3.75
−4.00
−4.25
−4.50
−4.75
−5.00
−5.25
−5.50
−5.75
−3.00
−3.25
−3.50
−3.75
−4.00
−4.25
−4.50
−4.75
−2.7
−3.0
−3.3
−3.6
−3.9
−4.2
−4.5
−4.8
−5.1
log(SFR [M⊙/yr])

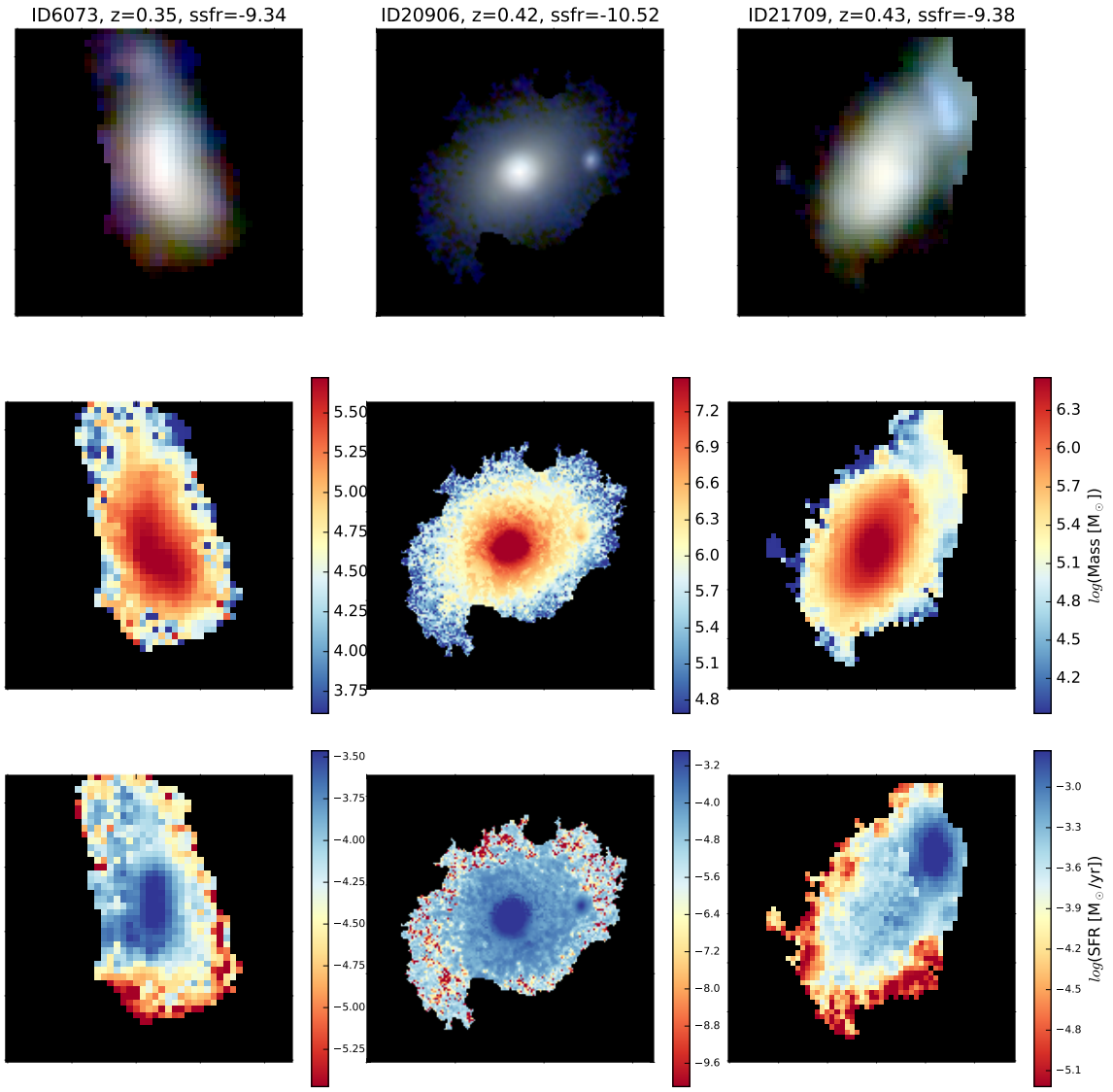
ID6073, z=0.35, ssfr=-9.34
ID20906, z=0.42, ssfr=-10.52
ID21709, z=0.43, ssfr=-9.38
5.50
5.25
5.00
4.75
4.50
4.25
4.00
3.75
7.2
6.9
6.6
6.3
6.0
5.7
5.4
5.1
4.8
6.3
6.0
5.7
5.4
5.1
4.8
4.5
4.2
log(Mass [M⊙])
−3.50
−3.75
−4.00
−4.25
−4.50
−4.75
−5.00
−5.25
−3.2
−4.0
−4.8
−5.6
−6.4
−7.2
−8.0
−8.8
−9.6
−3.0
−3.3
−3.6
−3.9
−4.2
−4.5
−4.8
−5.1
log(SFR [M⊙/yr])

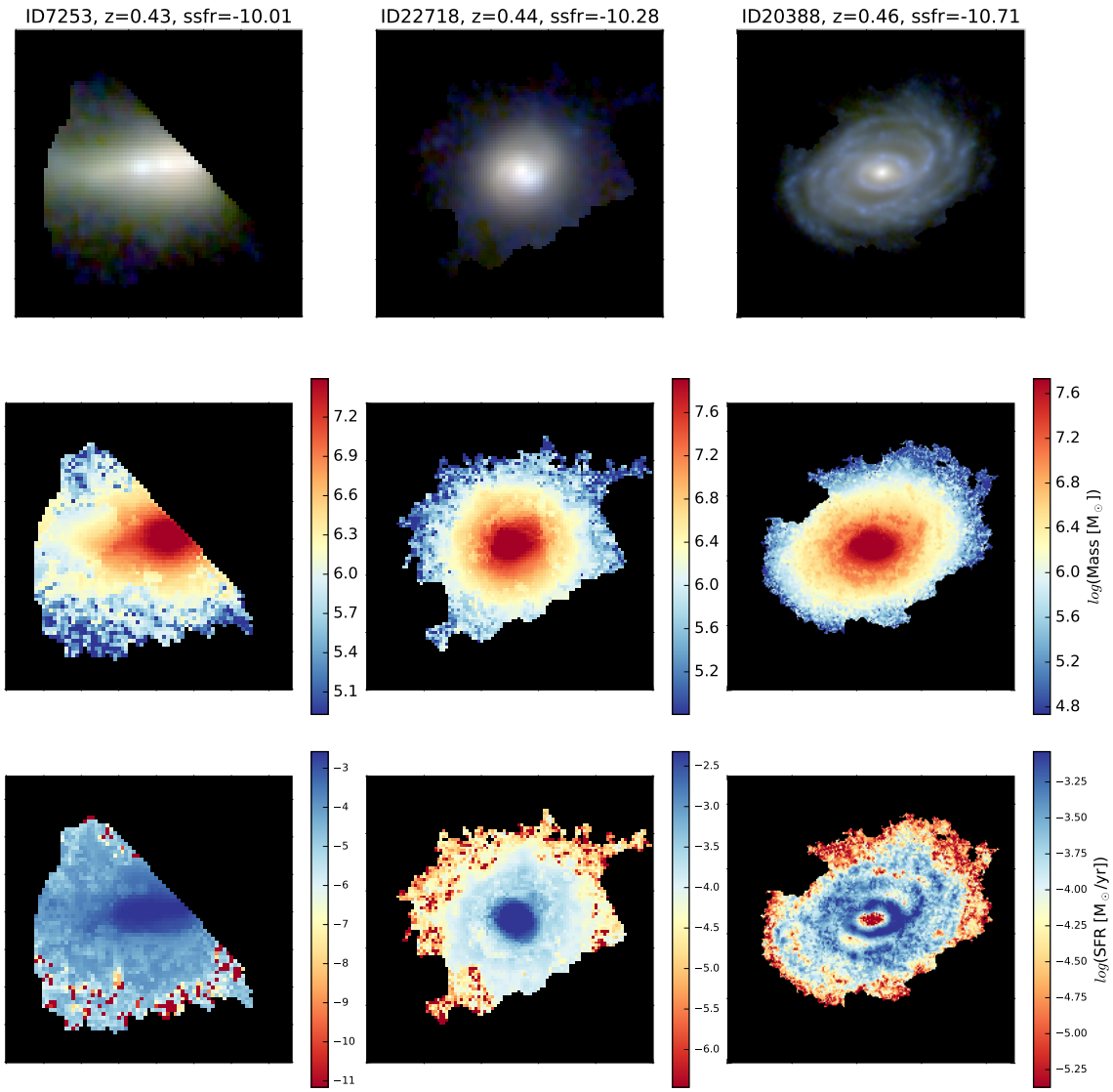
ID7253, z=0.43, ssfr=-10.01
ID22718, z=0.44, ssfr=-10.28
ID20388, z=0.46, ssfr=-10.71
7.2
6.9
6.6
6.3
6.0
5.7
5.4
5.1
7.6
7.2
6.8
6.4
6.0
5.6
5.2
7.6
7.2
6.8
6.4
6.0
5.6
5.2
4.8
log(Mass [M⊙])
−3
−4
−5
−6
−7
−8
−9
−10
−11
−2.5
−3.0
−3.5
−4.0
−4.5
−5.0
−5.5
−6.0
−3.25
−3.50
−3.75
−4.00
−4.25
−4.50
−4.75
−5.00
−5.25
log(SFR [M⊙/yr])

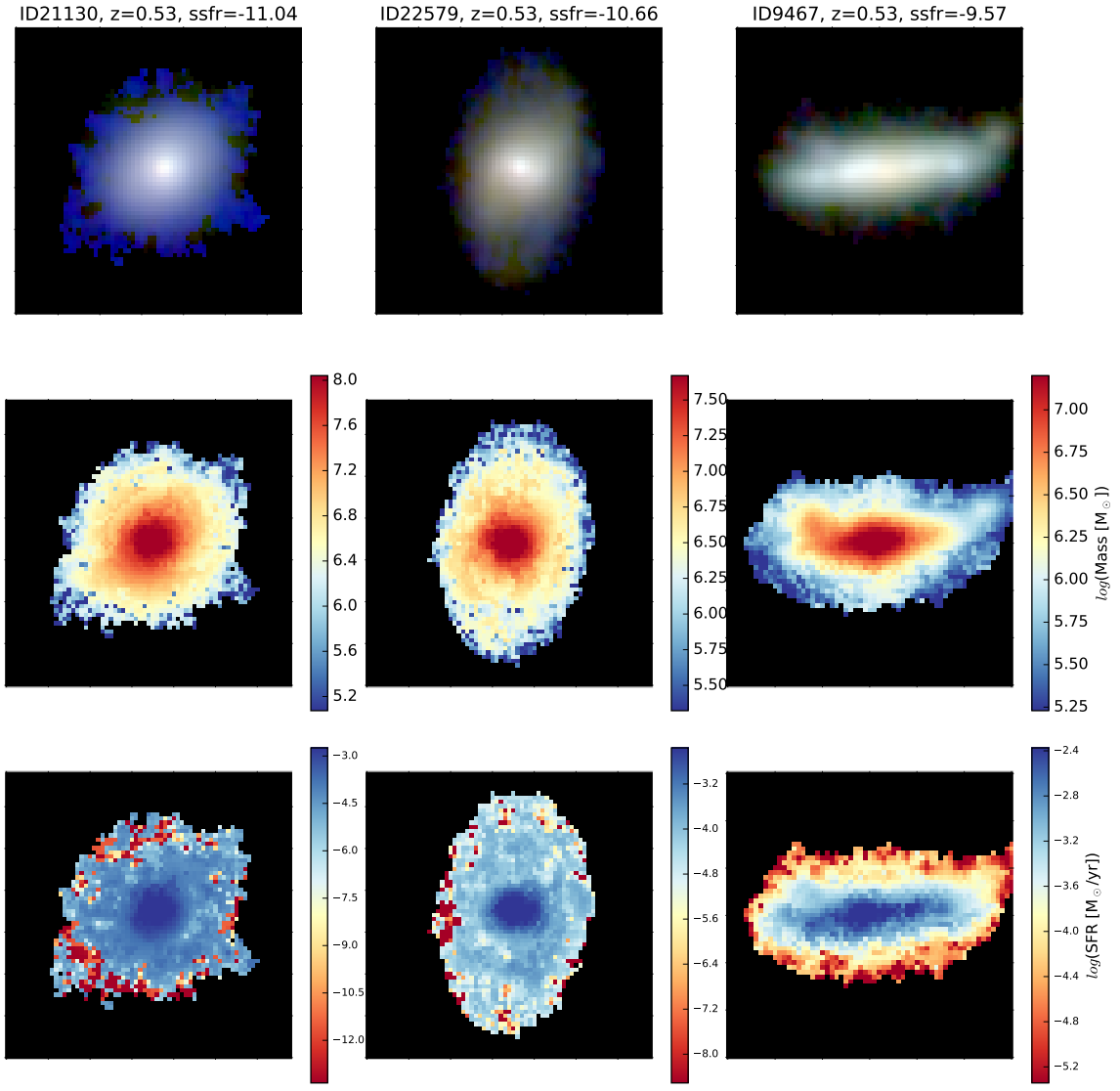
ID21130, z=0.53, ssfr=-11.04
ID22579, z=0.53, ssfr=-10.66
ID9467, z=0.53, ssfr=-9.57
log(Mass [M⊙])
log(SFR [M⊙/yr])

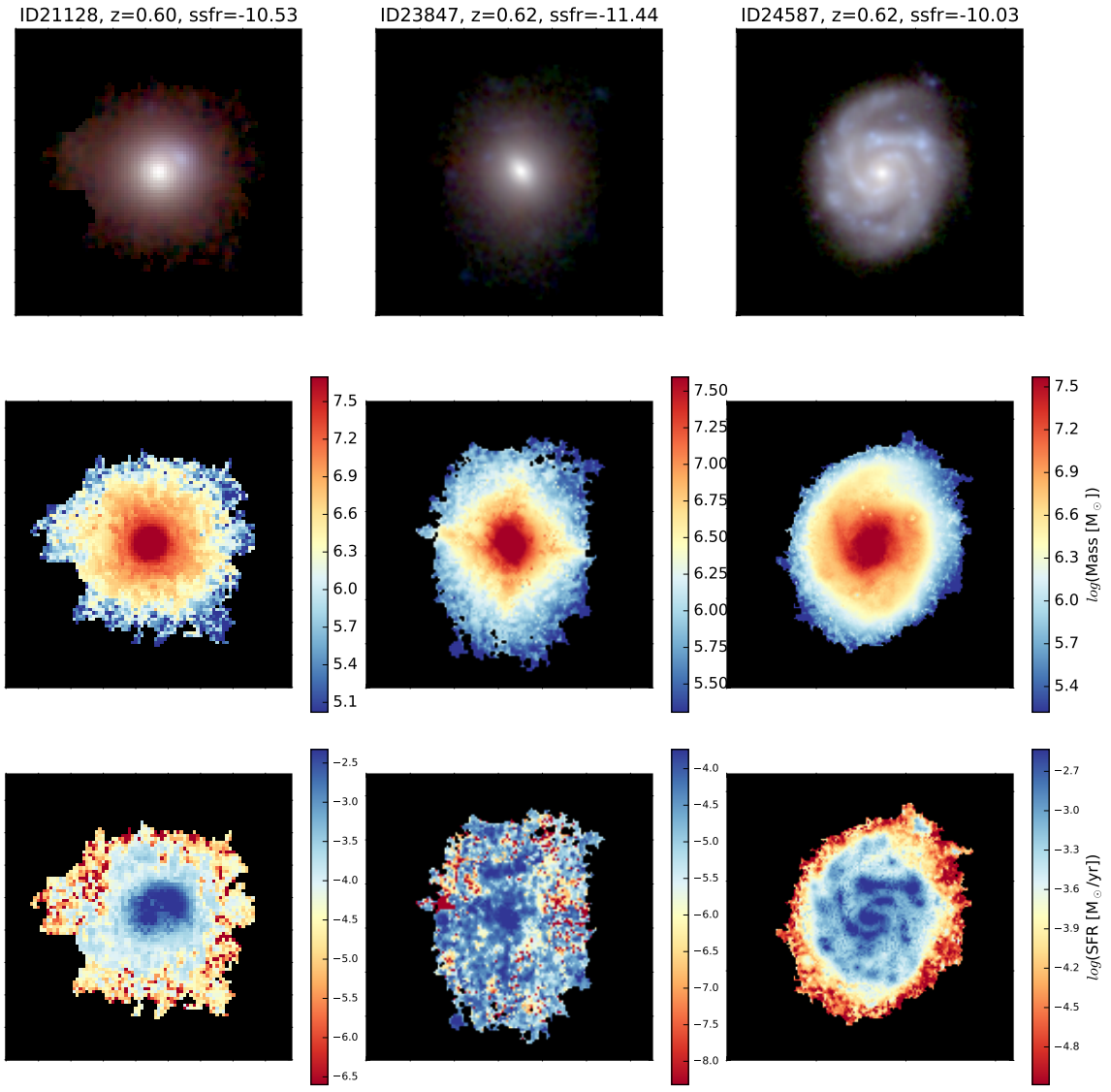
ID21128, z=0.60, ssfr=-10.53
ID23847, z=0.62, ssfr=-11.44
ID24587, z=0.62, ssfr=-10.03
7.5
7.2
6.9
6.6
6.3
6.0
5.7
5.4
5.1
7.50
7.25
7.00
6.75
6.50
6.25
6.00
5.75
5.50
7.5
7.2
6.9
6.6
6.3
6.0
5.7
5.4
log(Mass [M⊙])
−2.5
−3.0
−3.5
−4.0
−4.5
−5.0
−5.5
−6.0
−6.5
−4.0
−4.5
−5.0
−5.5
−6.0
−6.5
−7.0
−7.5
−8.0
−2.7
−3.0
−3.3
−3.6
−3.9
−4.2
−4.5
−4.8
log(SFR [M⊙/yr])

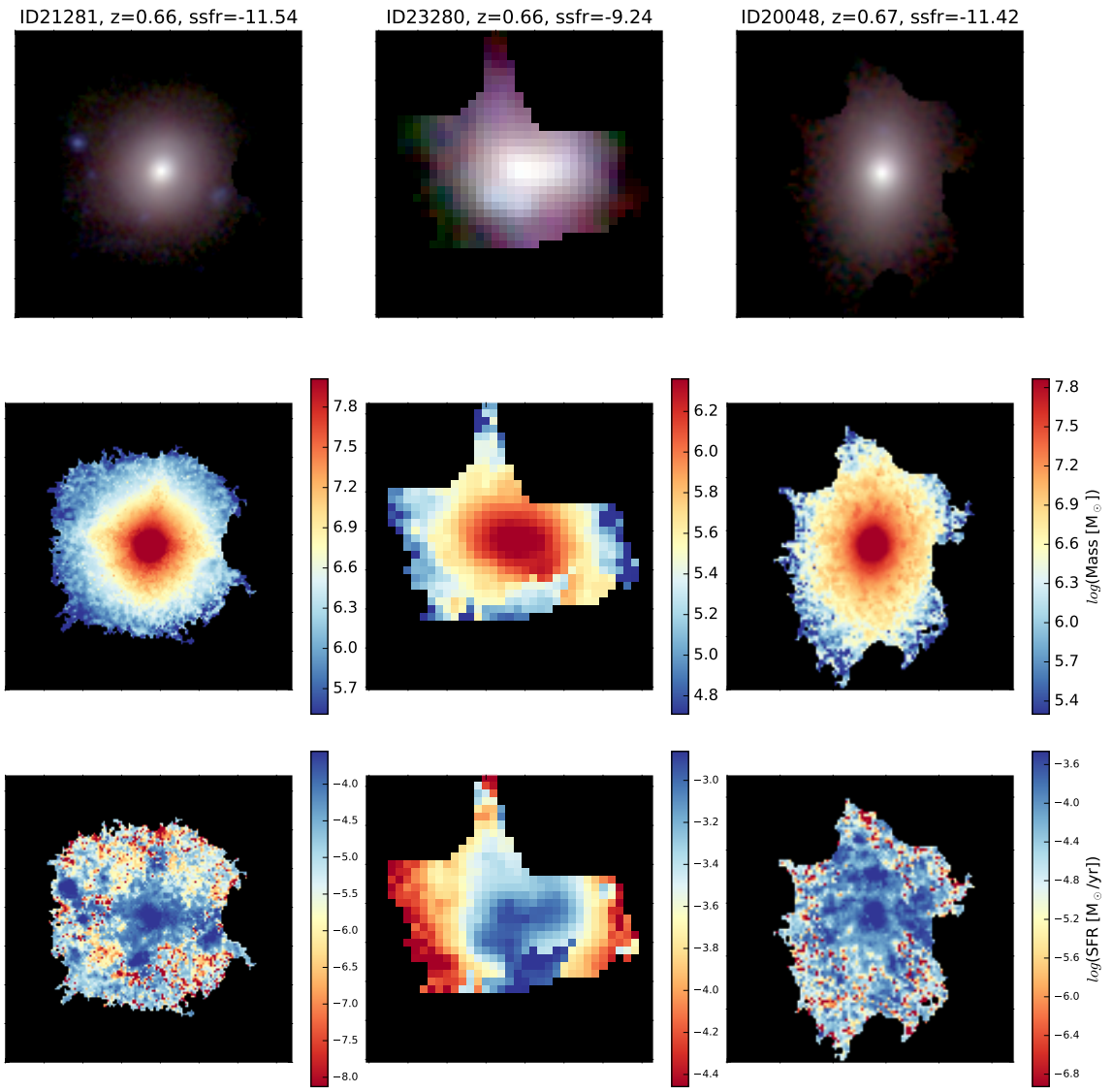
ID21281, z=0.66, ssfr=-11.54
ID23280, z=0.66, ssfr=-9.24
ID20048, z=0.67, ssfr=-11.42
7.8
7.5
7.2
6.9
6.6
6.3
6.0
5.7
6.2
6.0
5.8
5.6
5.4
5.2
5.0
4.8
7.8
7.5
7.2
6.9
6.6
6.3
6.0
5.7
5.4
log(Mass [M⊙])
−4.0
−4.5
−5.0
−5.5
−6.0
−6.5
−7.0
−7.5
−8.0
−3.0
−3.2
−3.4
−3.6
−3.8
−4.0
−4.2
−4.4
−3.6
−4.0
−4.4
−4.8
−5.2
−5.6
−6.0
−6.4
−6.8
log(SFR [M⊙/yr])

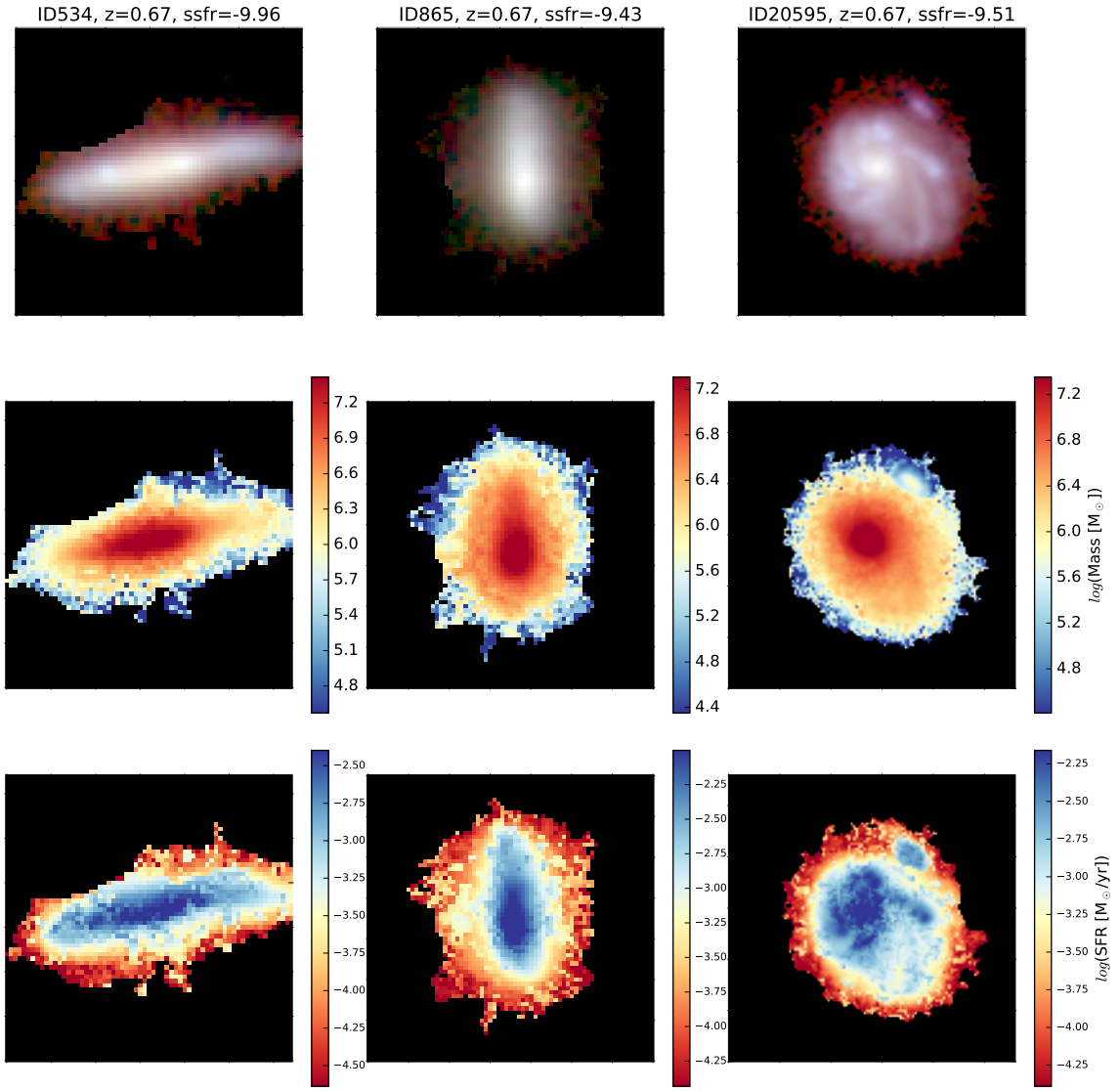
ID534, z=0.67, ssfr=-9.96
ID865, z=0.67, ssfr=-9.43
ID20595, z=0.67, ssfr=-9.51
7.2
6.9
6.6
6.3
6.0
5.7
5.4
5.1
4.8
7.2
6.8
6.4
6.0
5.6
5.2
4.8
4.4
7.2
6.8
6.4
6.0
5.6
5.2
4.8
log(Mass [M⊙])
−2.50
−2.75
−3.00
−3.25
−3.50
−3.75
−4.00
−4.25
−4.50
−2.25
−2.50
−2.75
−3.00
−3.25
−3.50
−3.75
−4.00
−4.25
−2.25
−2.50
−2.75
−3.00
−3.25
−3.50
−3.75
−4.00
−4.25
log(SFR [M⊙/yr])

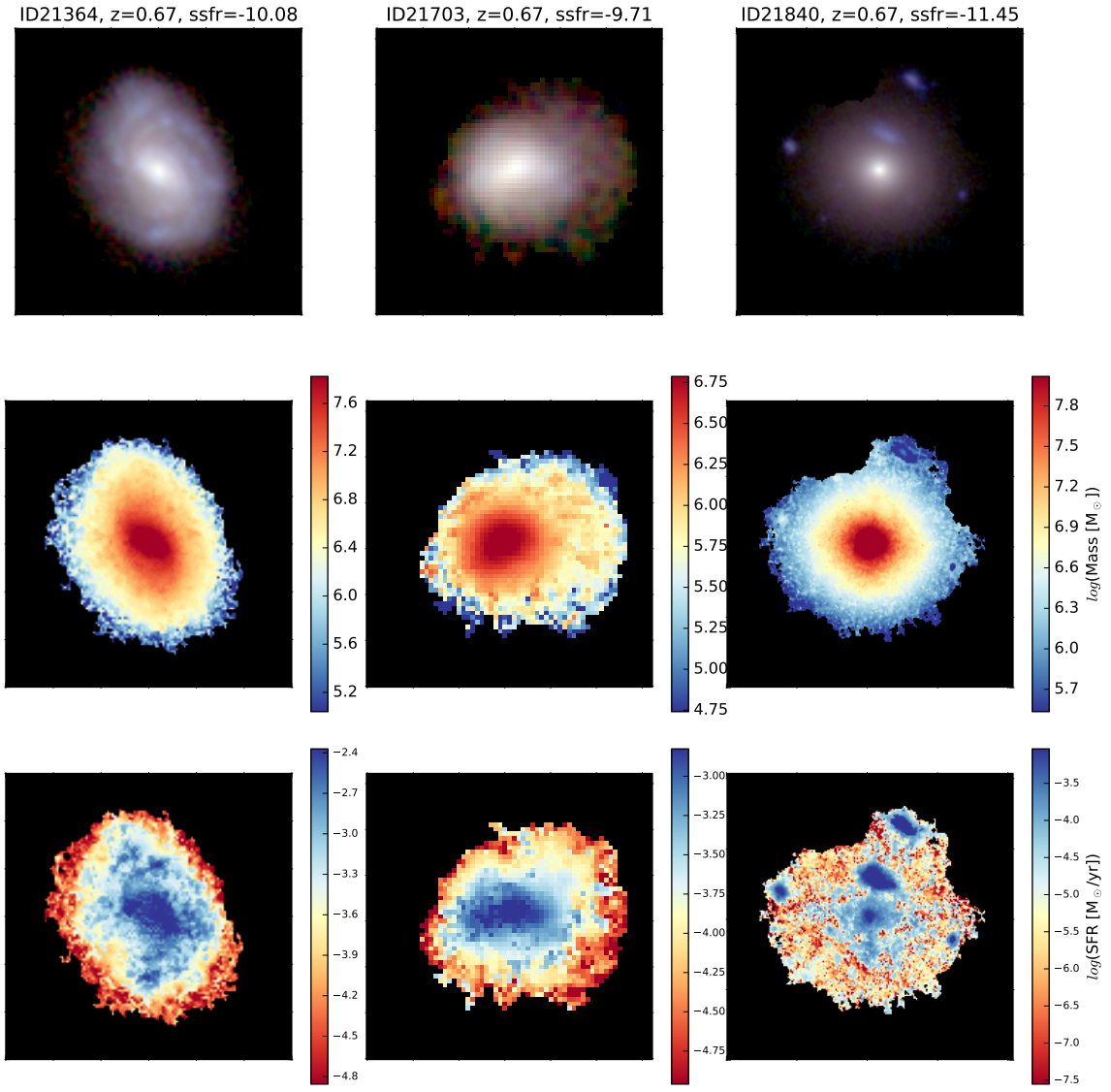
ID21364, z=0.67, ssfr=-10.08
ID21703, z=0.67, ssfr=-9.71
ID21840, z=0.67, ssfr=-11.45
7.6
7.2
6.8
6.4
6.0
5.6
5.2
6.75
6.50
6.25
6.00
5.75
5.50
5.25
5.00
4.75
7.8
7.5
7.2
6.9
6.6
6.3
6.0
5.7
log(Mass [M⊙])
−2.4
−2.7
−3.0
−3.3
−3.6
−3.9
−4.2
−4.5
−4.8
−3.00
−3.25
−3.50
−3.75
−4.00
−4.25
−4.50
−4.75
−3.5
−4.0
−4.5
−5.0
−5.5
−6.0
−6.5
−7.0
−7.5
log(SFR [M⊙/yr])

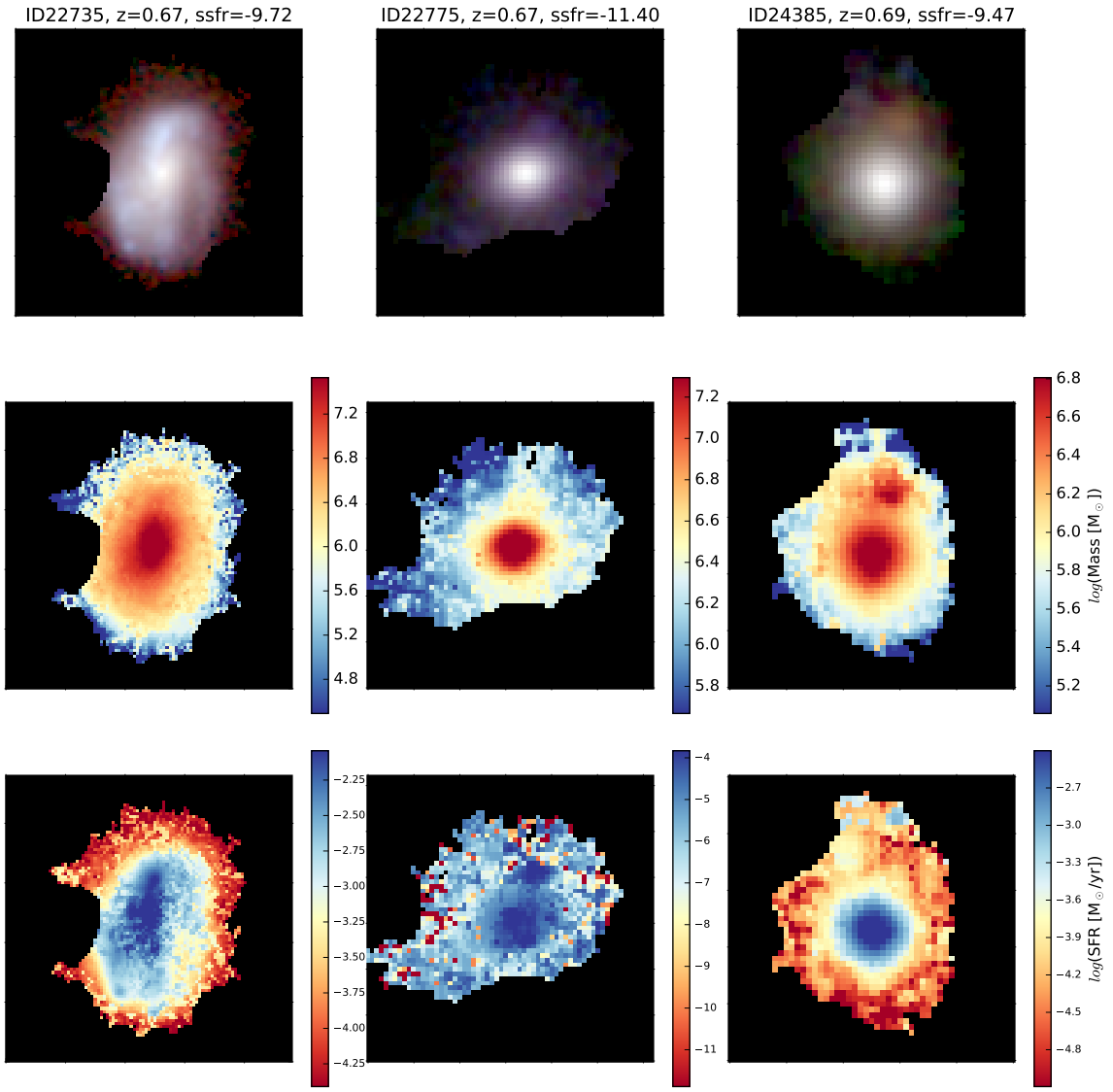
ID22735, z=0.67, ssfr=-9.72
ID22775, z=0.67, ssfr=-11.40
ID24385, z=0.69, ssfr=-9.47
log(Mass [M⊙])
log(SFR [M⊙/yr])

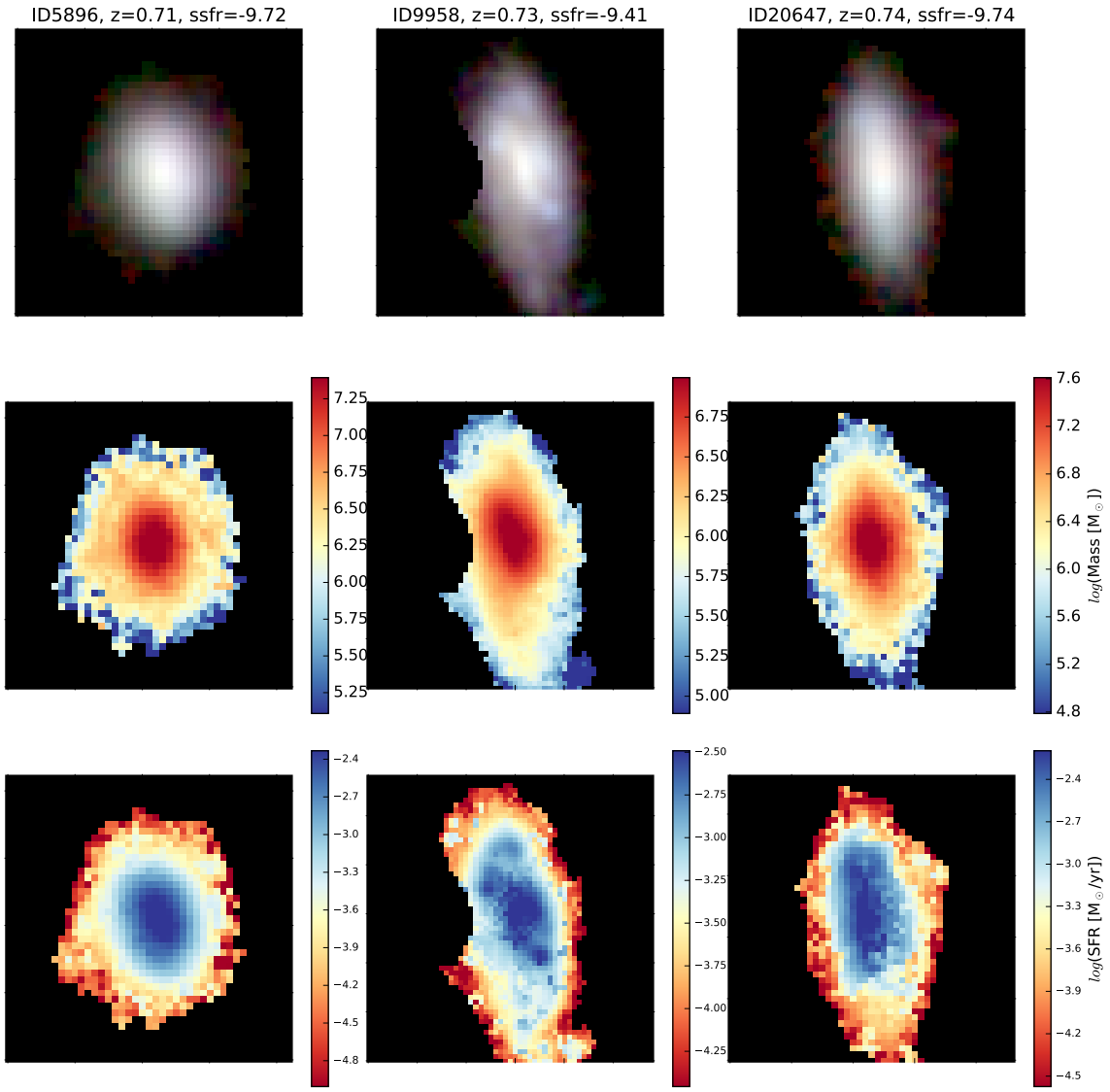
ID5896, z=0.71, ssfr=-9.72
ID9958, z=0.73, ssfr=-9.41
ID20647, z=0.74, ssfr=-9.74
log(Mass [M⊙])
log(SFR [M⊙/yr])

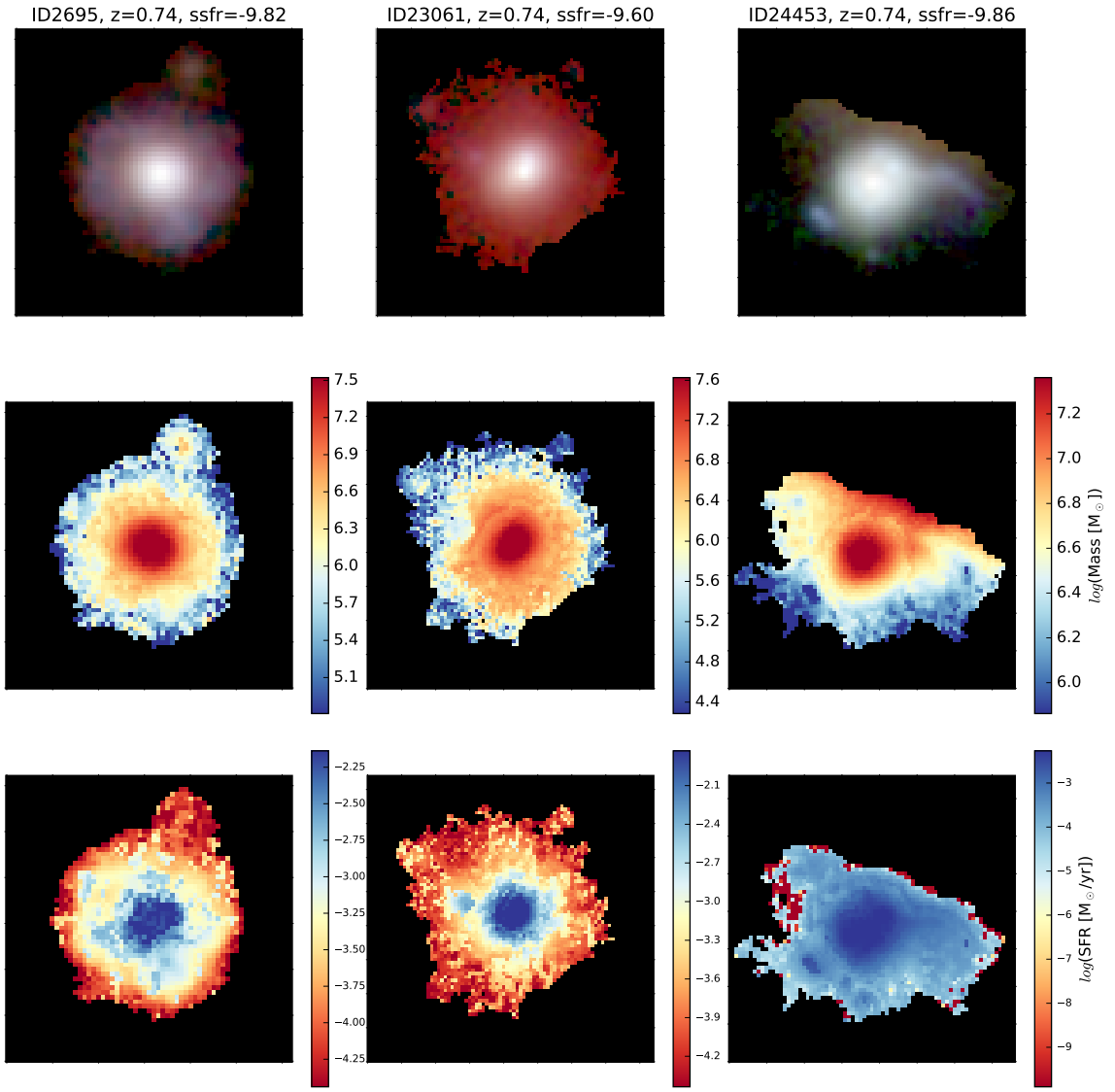
ID2695, z=0.74, ssfr=-9.82
ID23061, z=0.74, ssfr=-9.60
ID24453, z=0.74, ssfr=-9.86
7.5
7.2
6.9
6.6
6.3
6.0
5.7
5.4
5.1
7.6
7.2
6.8
6.4
6.0
5.6
5.2
4.8
4.4
7.2
7.0
6.8
6.6
6.4
6.2
6.0
log(Mass [M⊙])
−2.25
−2.50
−2.75
−3.00
−3.25
−3.50
−3.75
−4.00
−4.25
−2.1
−2.4
−2.7
−3.0
−3.3
−3.6
−3.9
−4.2
−3
−4
−5
−6
−7
−8
−9
log(SFR [M⊙/yr])

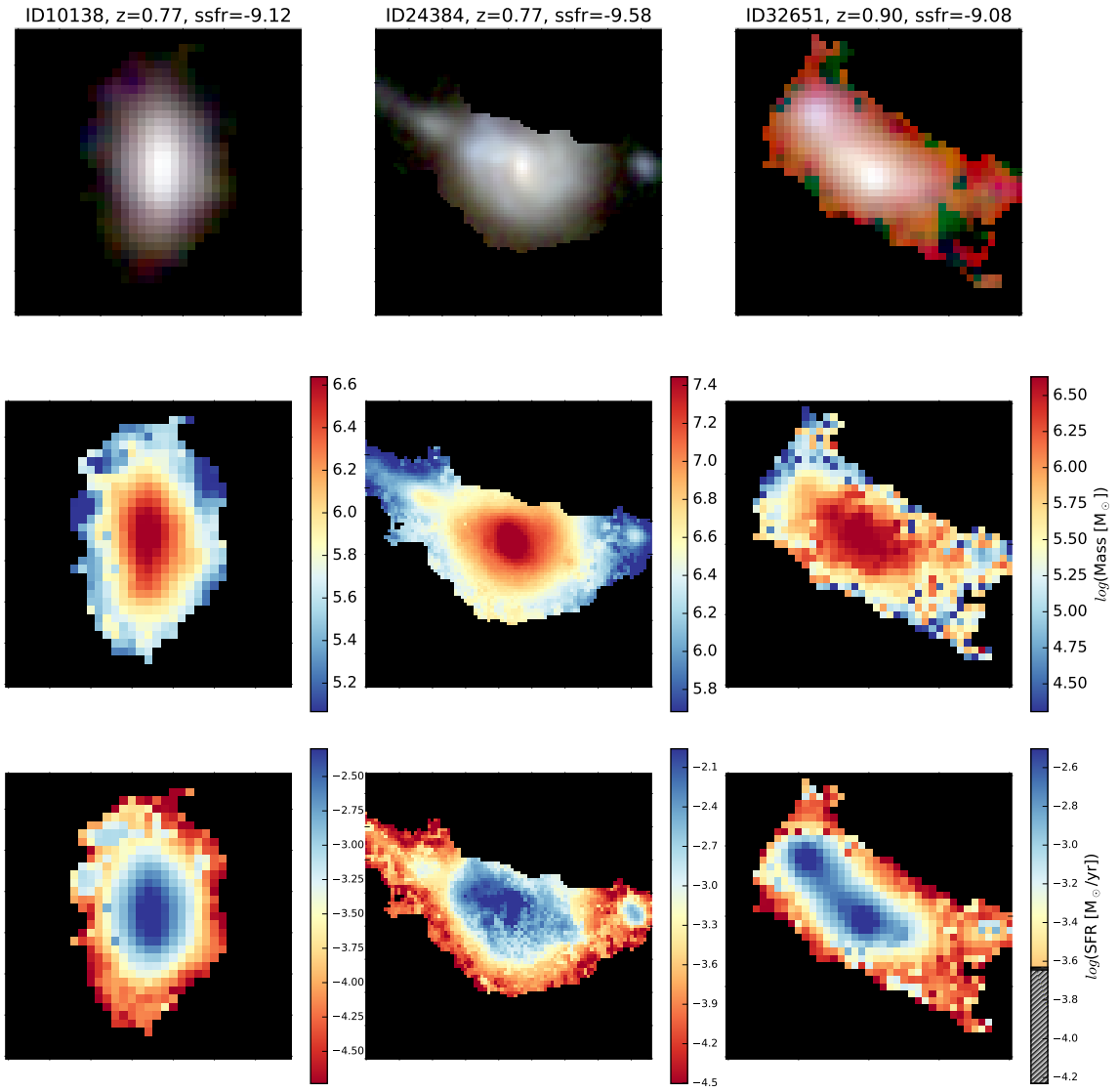
ID10138, z=0.77, ssfr=-9.12
ID24384, z=0.77, ssfr=-9.58
ID32651, z=0.90, ssfr=-9.08
log(Mass [M⊙])
log(SFR [M⊙/yr])

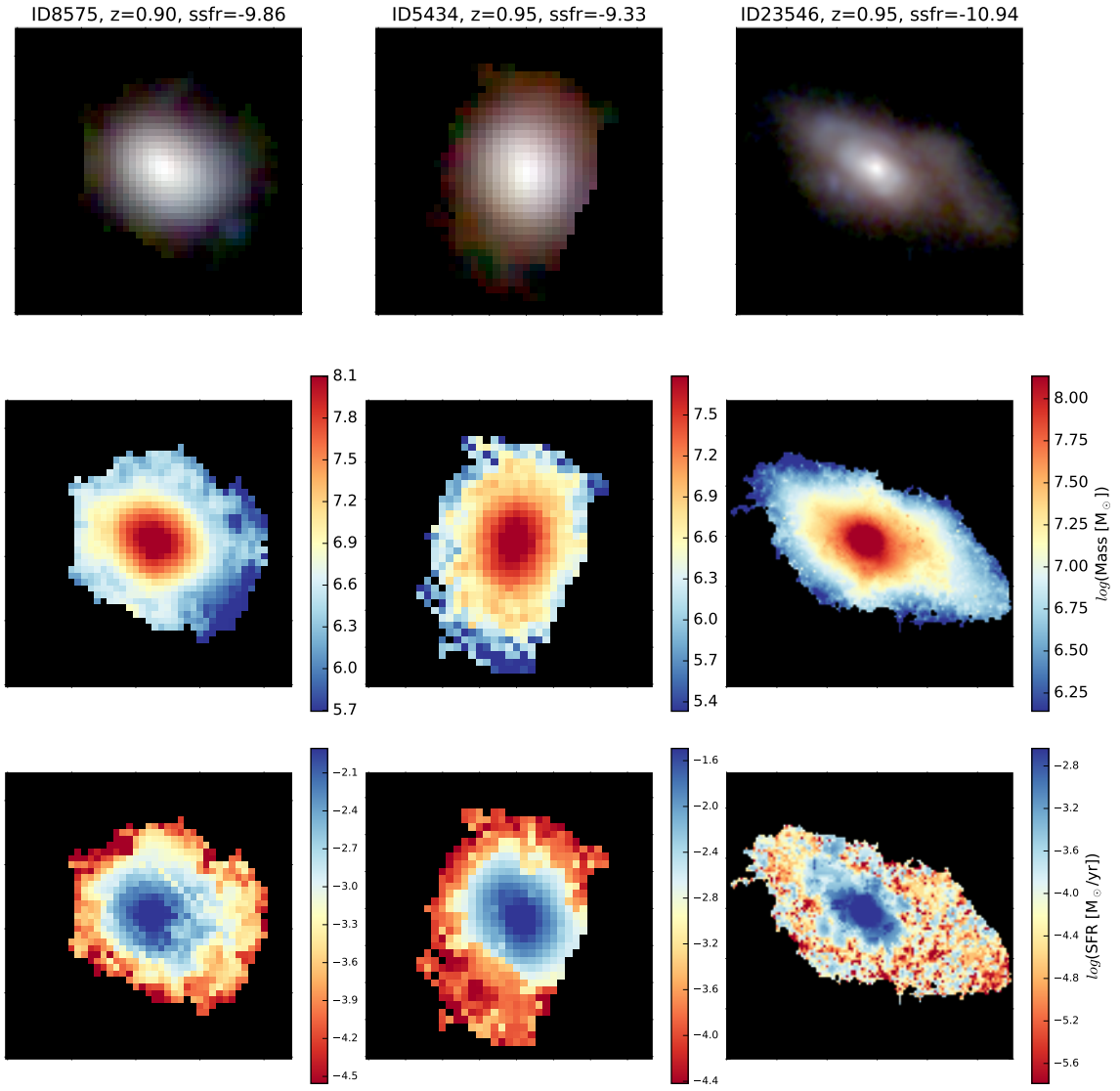
ID8575, z=0.90, ssfr=-9.86
ID5434, z=0.95, ssfr=-9.33
ID23546, z=0.95, ssfr=-10.94
8.1
7.8
7.5
7.2
6.9
6.6
6.3
6.0
5.7
7.5
7.2
6.9
6.6
6.3
6.0
5.7
5.4
8.00
7.75
7.50
7.25
7.00
6.75
6.50
6.25
log(Mass [M⊙])
−2.1
−2.4
−2.7
−3.0
−3.3
−3.6
−3.9
−4.2
−4.5
−1.6
−2.0
−2.4
−2.8
−3.2
−3.6
−4.0
−4.4
−2.8
−3.2
−3.6
−4.0
−4.4
−4.8
−5.2
−5.6
log(SFR [M⊙/yr])

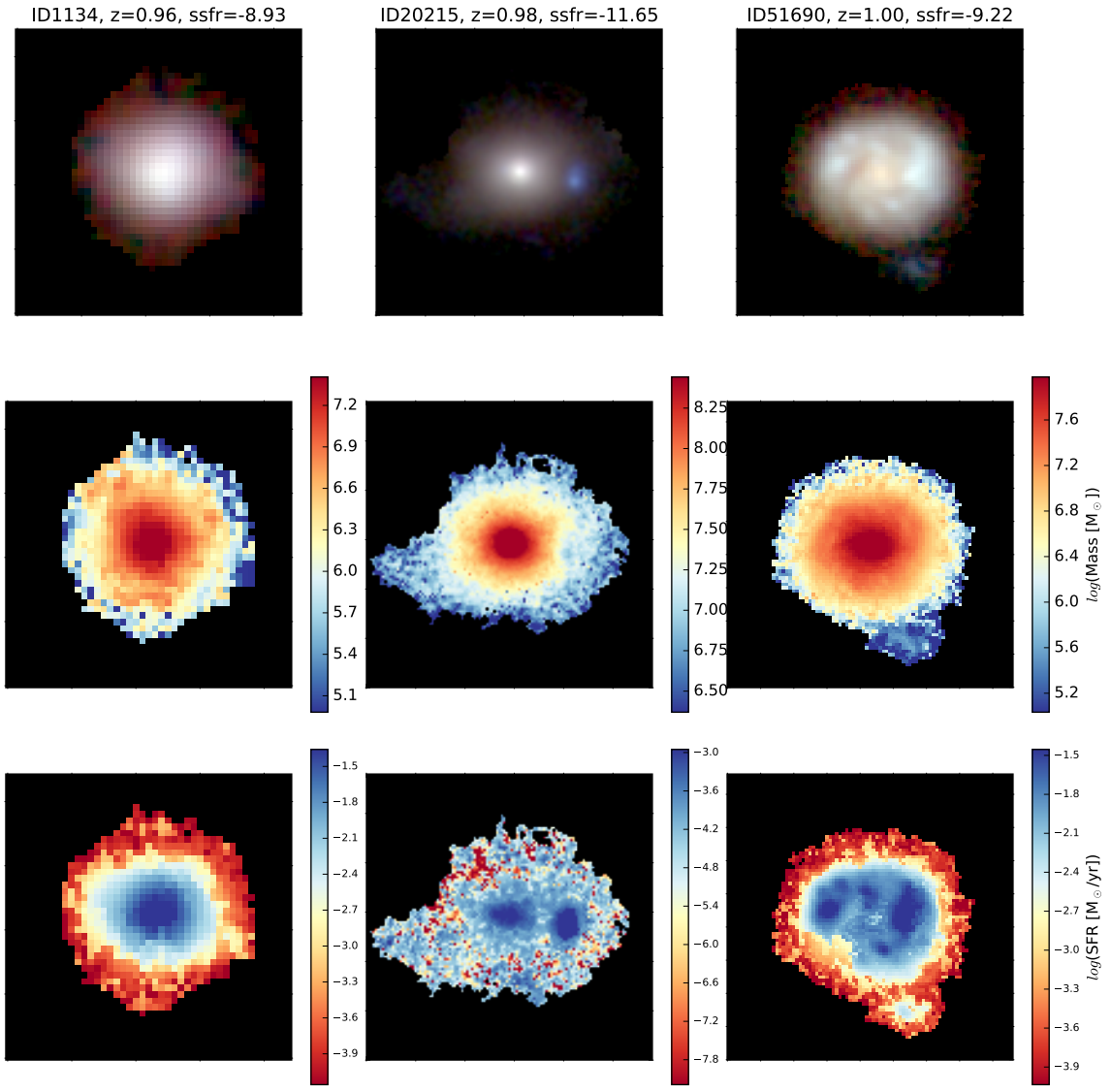
ID1134, z=0.96, ssfr=-8.93
ID20215, z=0.98, ssfr=-11.65
ID51690, z=1.00, ssfr=-9.22
7.2
6.9
6.6
6.3
6.0
5.7
5.4
5.1
8.25
8.00
7.75
7.50
7.25
7.00
6.75
6.50
7.6
7.2
6.8
6.4
6.0
5.6
5.2
log(Mass [M⊙])
−1.5
−1.8
−2.1
−2.4
−2.7
−3.0
−3.3
−3.6
−3.9
−3.0
−3.6
−4.2
−4.8
−5.4
−6.0
−6.6
−7.2
−7.8
log(SFR [M⊙/yr])

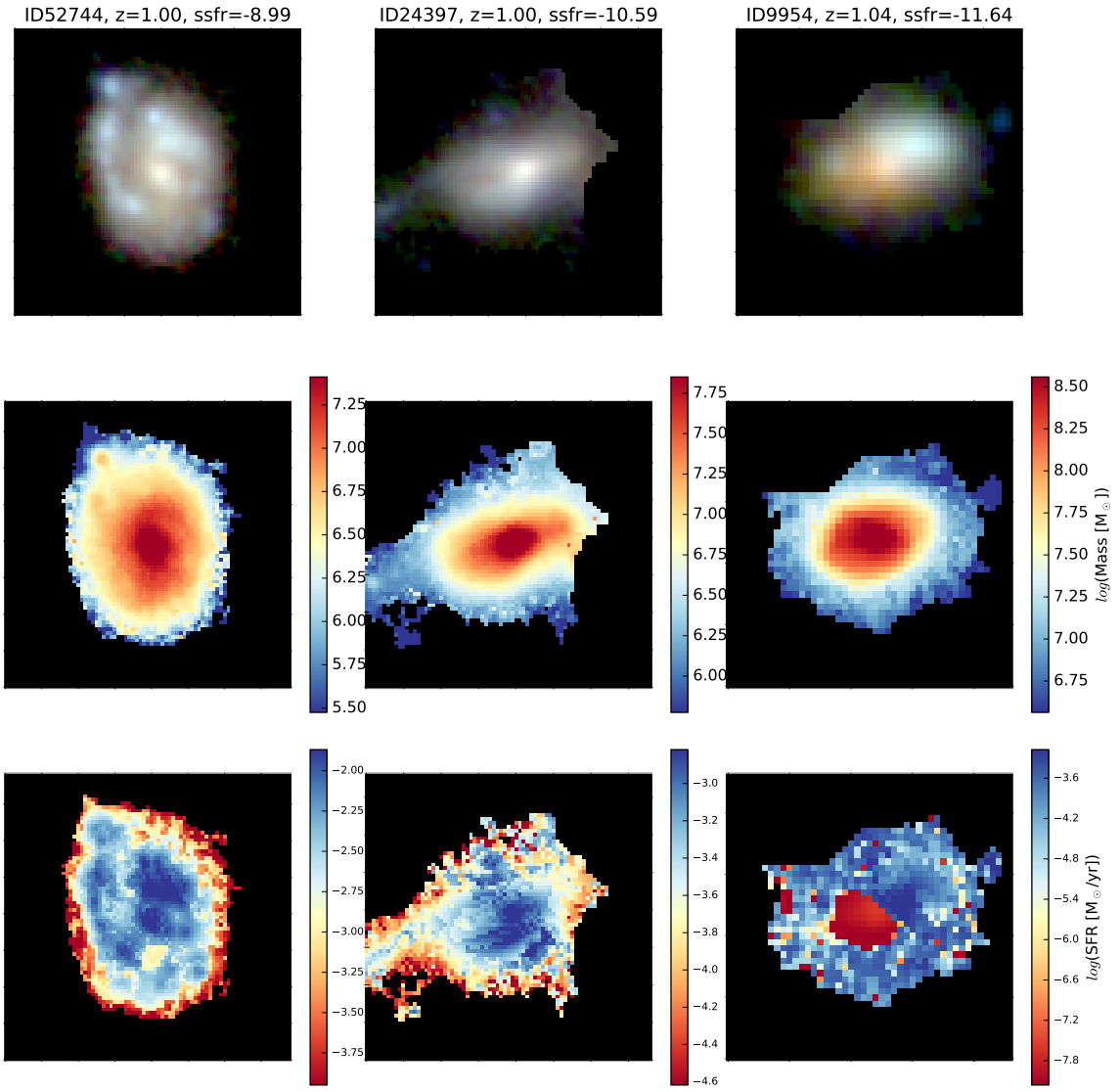
ID52744, z=1.00, ssfr=-8.99
ID24397, z=1.00, ssfr=-10.59
ID9954, z=1.04, ssfr=-11.64
log(Mass [M⊙])
log(SFR [M⊙/yr])

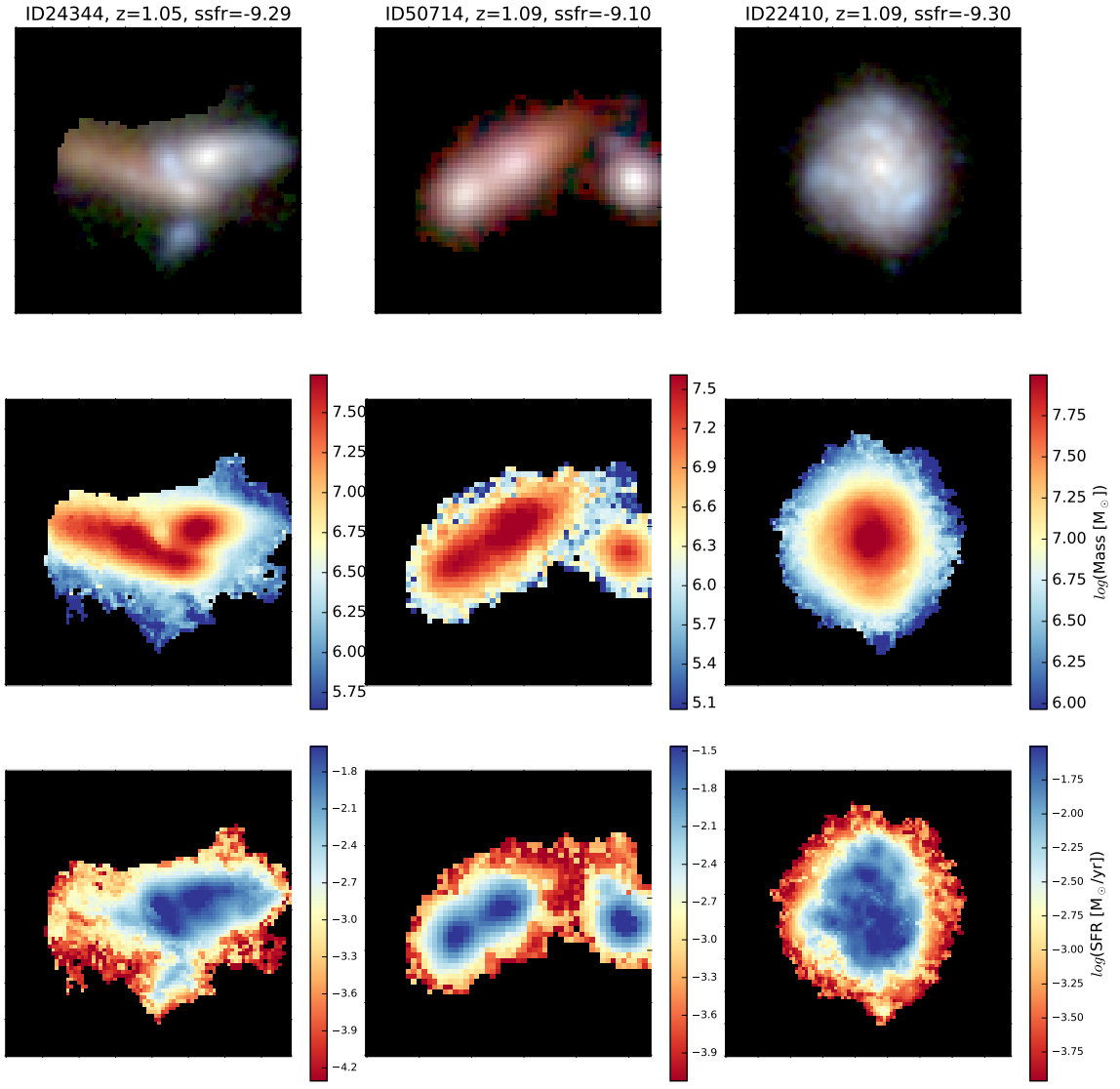
ID24344, z=1.05, ssfr=-9.29
ID50714, z=1.09, ssfr=-9.10
ID22410, z=1.09, ssfr=-9.30
log(Mass [M⊙])
log(SFR [M⊙/yr])

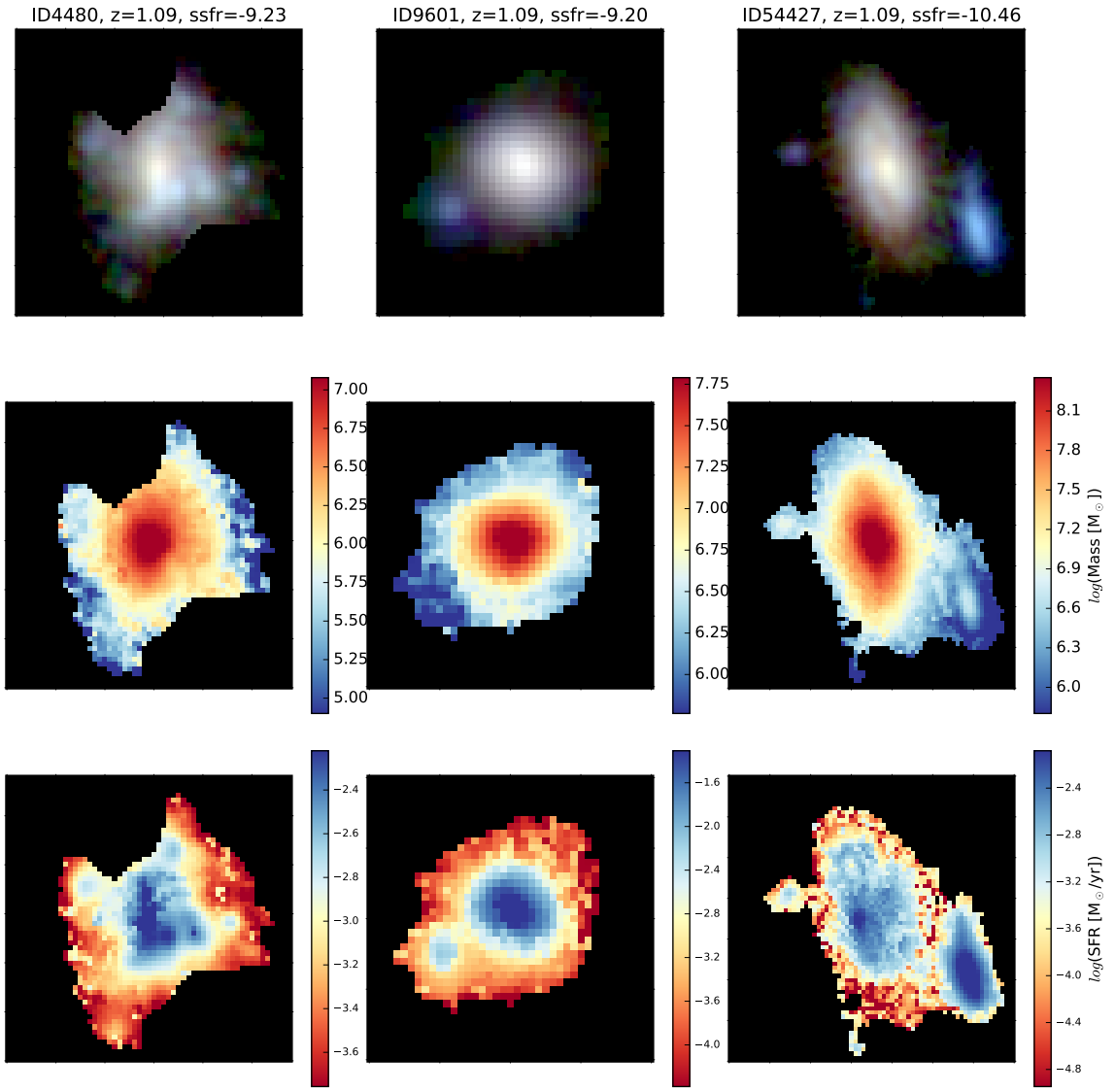
ID4480, z=1.09, ssfr=-9.23
ID9601, z=1.09, ssfr=-9.20
ID54427, z=1.09, ssfr=-10.46
7.00
6.75
6.50
6.25
6.00
5.75
5.50
5.25
5.00
7.75
7.50
7.25
7.00
6.75
6.50
6.25
6.00
8.1
7.8
7.5
7.2
6.9
6.6
6.3
6.0
log(Mass [M⊙])
−2.4
−2.6
−2.8
−3.0
−3.2
−3.4
−3.6
−1.6
−2.0
−2.4
−2.8
−3.2
−3.6
−4.0
−2.4
−2.8
−3.2
−3.6
−4.0
−4.4
−4.8
log(SFR [M⊙/yr])

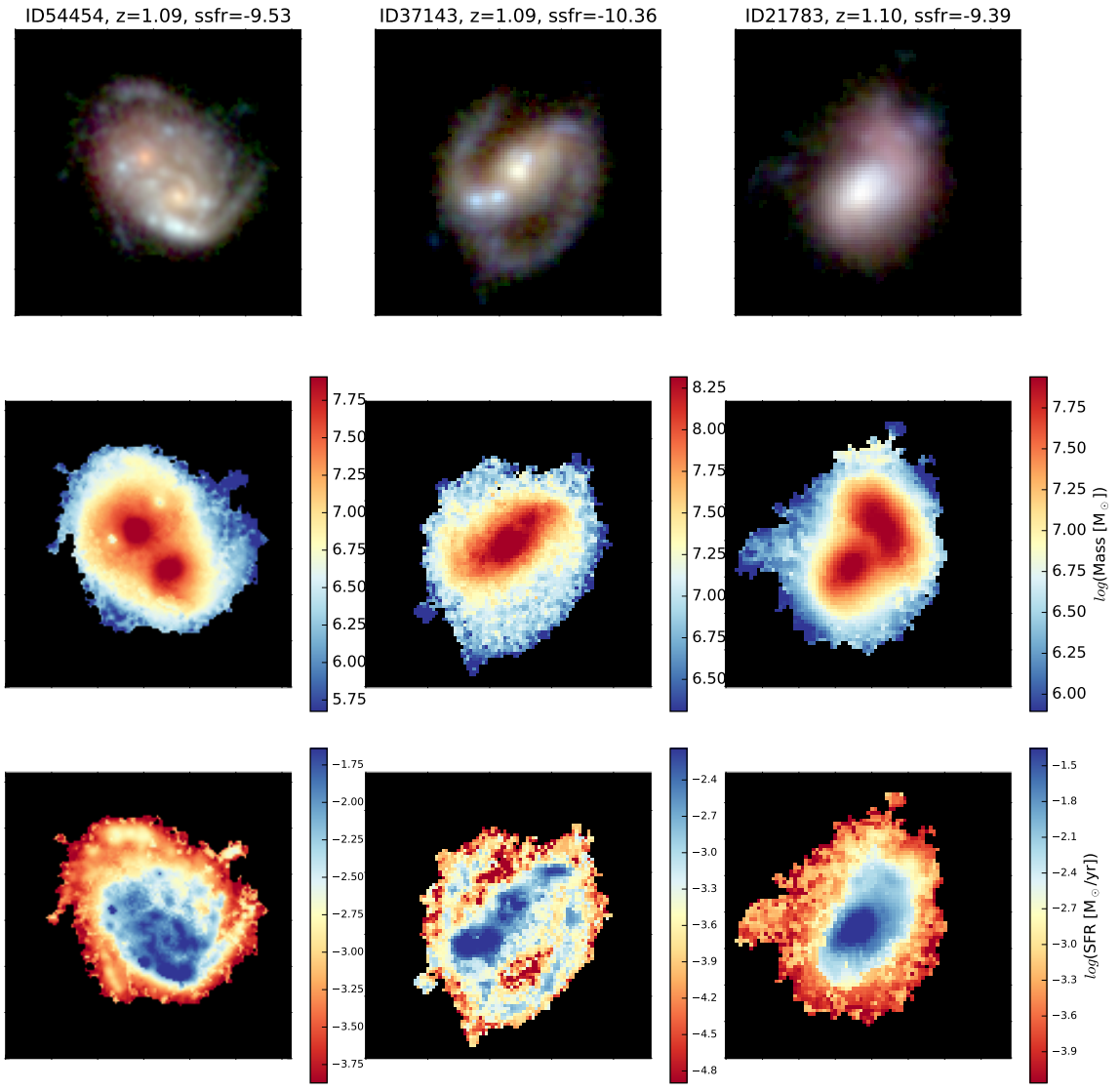
ID54454, z=1.09, ssfr=-9.53
ID37143, z=1.09, ssfr=-10.36
ID21783, z=1.10, ssfr=-9.39
log(Mass [M⊙])
log(SFR [M⊙/yr])

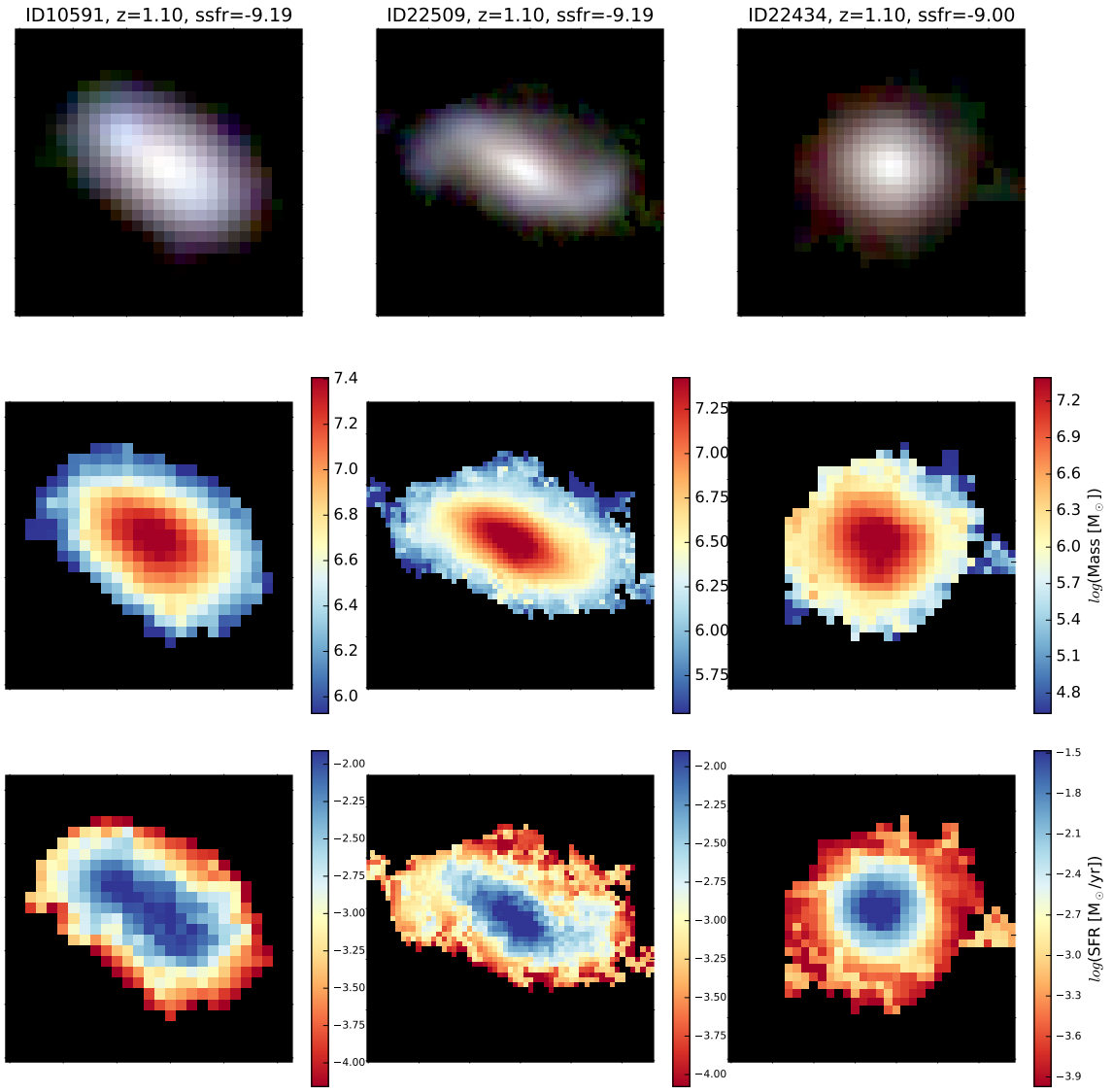
ID10591, z=1.10, ssfr=-9.19
ID22509, z=1.10, ssfr=-9.19
ID22434, z=1.10, ssfr=-9.00
7.4
7.2
7.0
6.8
6.6
6.4
6.2
6.0
7.25
7.00
6.75
6.50
6.25
6.00
5.75
7.2
6.9
6.6
6.3
6.0
5.7
5.4
5.1
4.8
log(Mass [M⊙])
−2.00
−2.25
−2.50
−2.75
−3.00
−3.25
−3.50
−3.75
−4.00
−1.5
−1.8
−2.1
−2.4
−2.7
−3.0
−3.3
−3.6
−3.9
log(SFR [M⊙/yr])

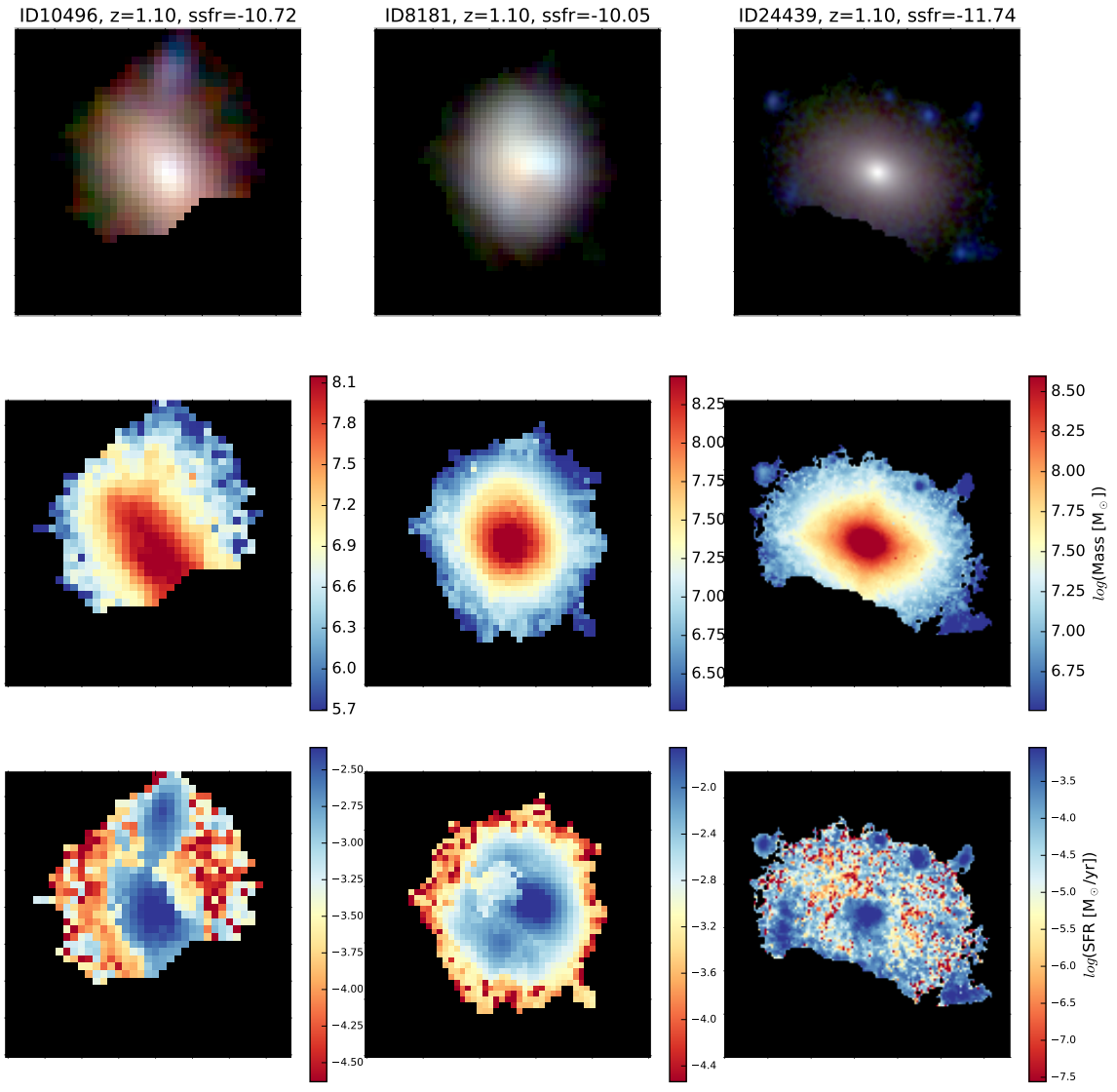
ID10496, z=1.10, ssfr=-10.72
ID8181, z=1.10, ssfr=-10.05
ID24439, z=1.10, ssfr=-11.74
8.1
7.8
7.5
7.2
6.9
6.6
6.3
6.0
5.7
8.25
8.00
7.75
7.50
7.25
7.00
6.75
6.50
8.50
8.25
8.00
7.75
7.50
7.25
7.00
6.75
log(Mass [M⊙])
−2.50
−2.75
−3.00
−3.25
−3.50
−3.75
−4.00
−4.25
−4.50
−2.0
−2.4
−2.8
−3.2
−3.6
−4.0
−4.4
−3.5
−4.0
−4.5
−5.0
−5.5
−6.0
−6.5
−7.0
−7.5
log(SFR [M⊙/yr])

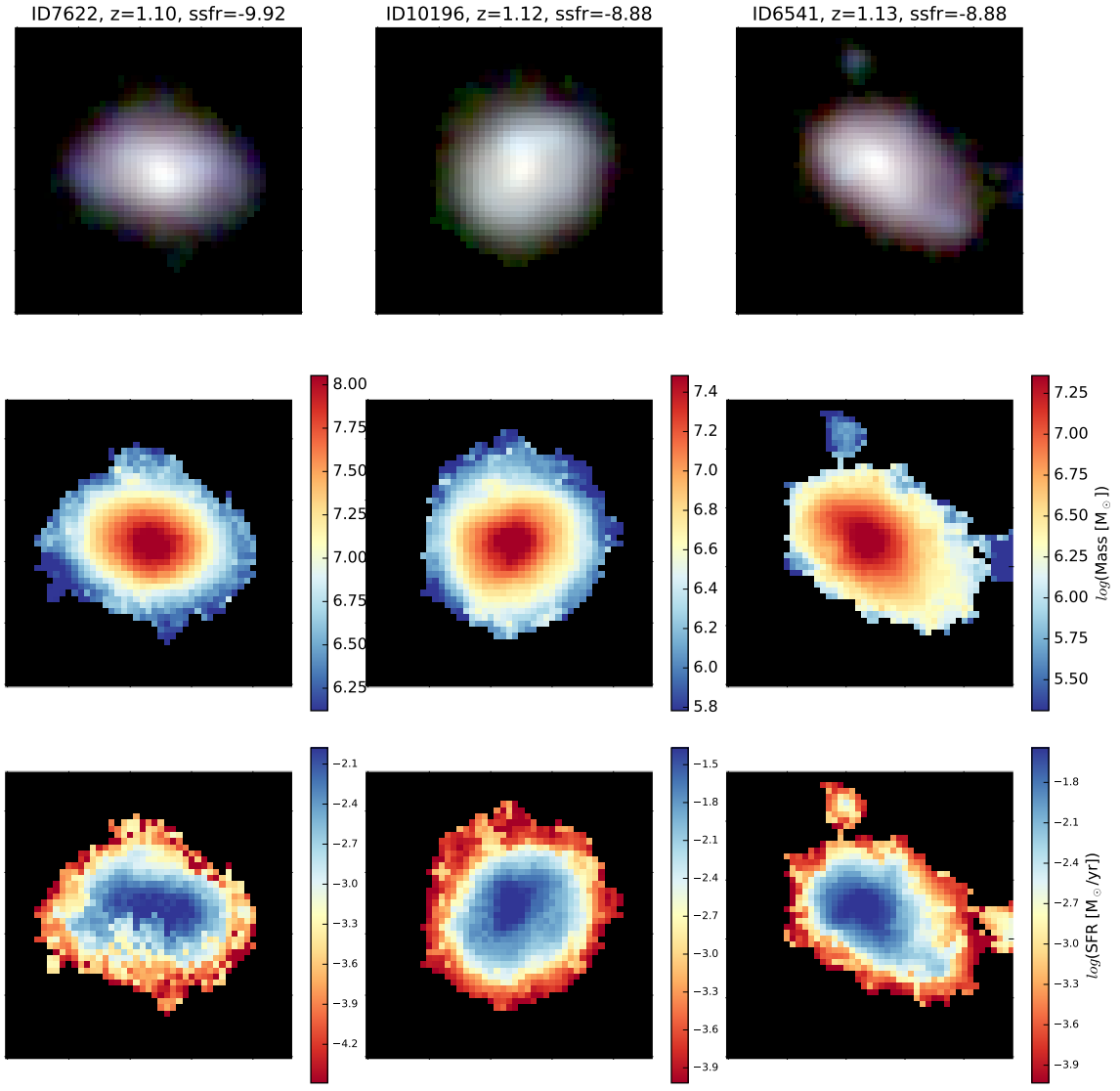
ID7622, z=1.10, ssfr=-9.92
ID10196, z=1.12, ssfr=-8.88
ID6541, z=1.13, ssfr=-8.88
8.00
7.75
7.50
7.25
7.00
6.75
6.50
6.25
7.4
7.2
7.0
6.8
6.6
6.4
6.2
6.0
5.8
7.25
7.00
6.75
6.50
6.25
6.00
5.75
5.50
log(Mass [M⊙])
−2.1
−2.4
−2.7
−3.0
−3.3
−3.6
−3.9
−4.2
−1.5
−1.8
−2.1
−2.4
−2.7
−3.0
−3.3
−3.6
−3.9
−1.8
−2.1
−2.4
−2.7
−3.0
−3.3
−3.6
−3.9
log(SFR [M⊙/yr])

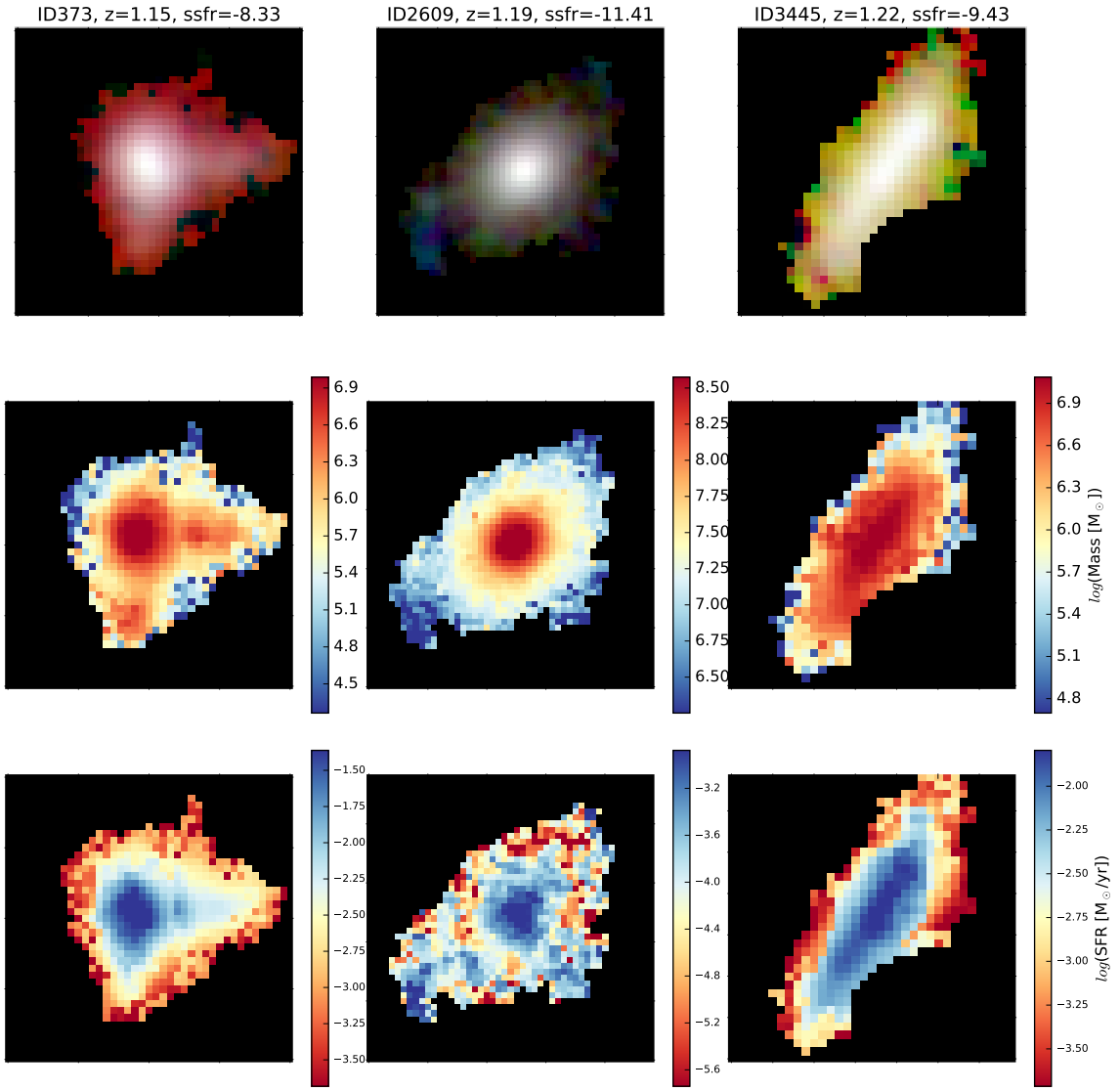
ID373, z=1.15, ssfr=-8.33
ID2609, z=1.19, ssfr=-11.41
ID3445, z=1.22, ssfr=-9.43
6.9
6.6
6.3
6.0
5.7
5.4
5.1
4.8
4.5
8.50
8.25
8.00
7.75
7.50
7.25
7.00
6.75
6.50
6.9
6.6
6.3
6.0
5.7
5.4
5.1
4.8
log(Mass [M⊙])
−1.50
−1.75
−2.00
−2.25
−2.50
−2.75
−3.00
−3.25
−3.50
−3.2
−3.6
−4.0
−4.4
−4.8
−5.2
−5.6
−2.00
−2.25
−2.50
−2.75
−3.00
−3.25
−3.50
log(SFR [M⊙/yr])

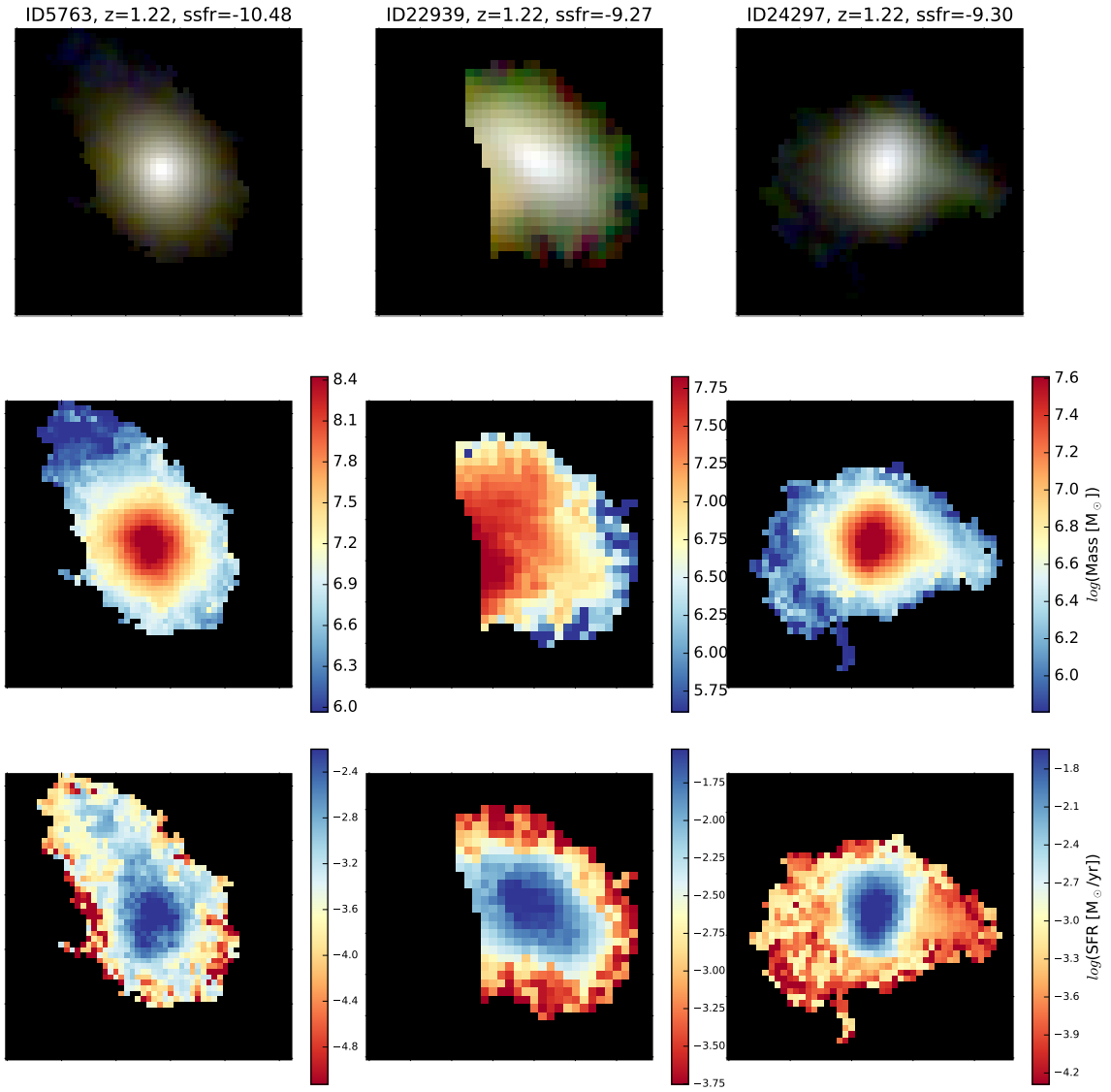
ID5763, z=1.22, ssfr=-10.48
ID22939, z=1.22, ssfr=-9.27
ID24297, z=1.22, ssfr=-9.30
8.4
8.1
7.8
7.5
7.2
6.9
6.6
6.3
6.0
7.75
7.50
7.25
7.00
6.75
6.50
6.25
6.00
5.75
7.6
7.4
7.2
7.0
6.8
6.6
6.4
6.2
6.0
log(Mass [M⊙])
−2.4
−2.8
−3.2
−3.6
−4.0
−4.4
−4.8
−1.75
−2.00
−2.25
−2.50
−2.75
−3.00
−3.25
−3.50
−3.75
−1.8
−2.1
−2.4
−2.7
−3.0
−3.3
−3.6
−3.9
−4.2
log(SFR [M⊙/yr])

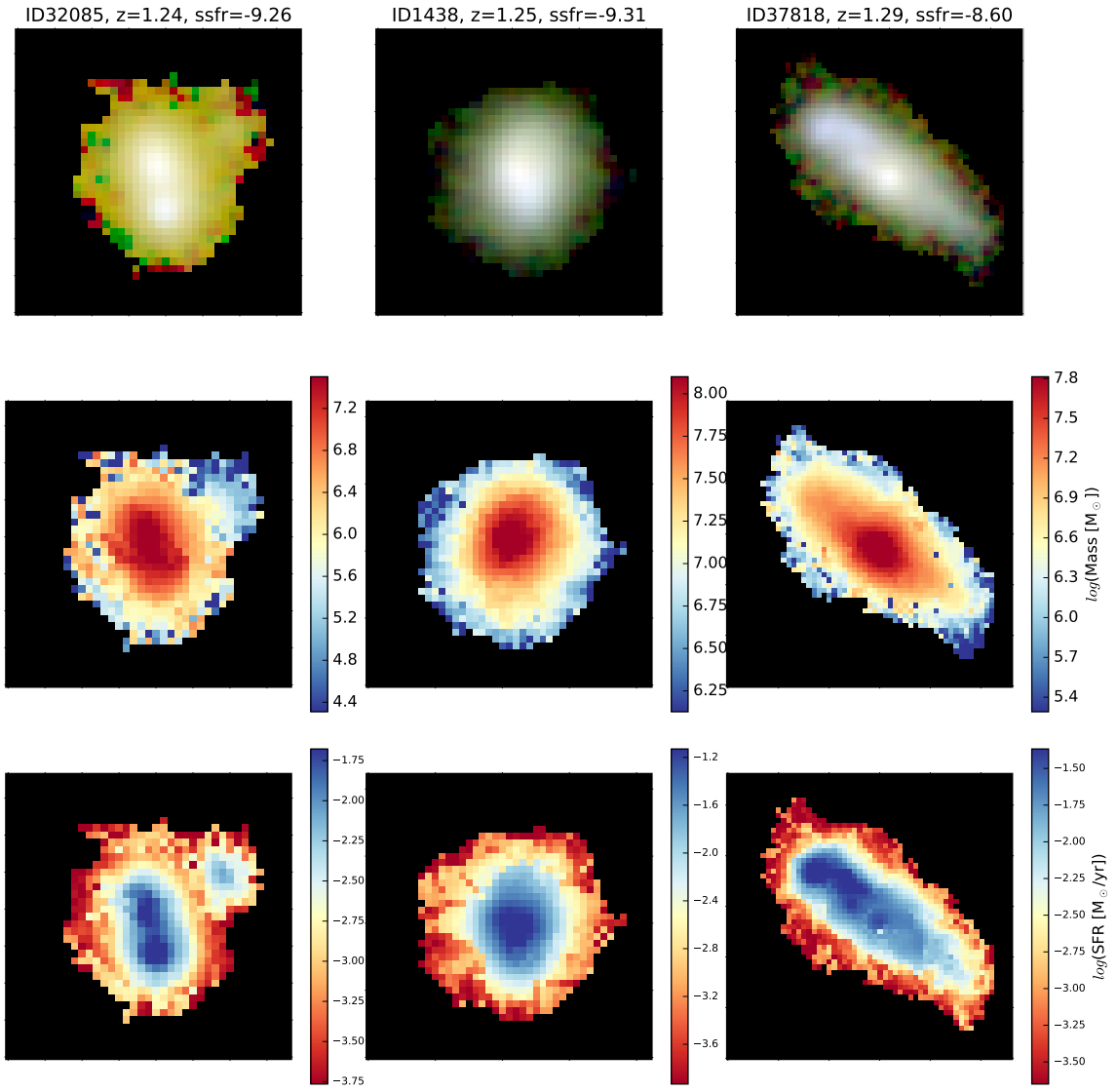
ID32085, z=1.24, ssfr=-9.26
ID1438, z=1.25, ssfr=-9.31
ID37818, z=1.29, ssfr=-8.60
7.2
6.8
6.4
6.0
5.6
5.2
4.8
4.4
8.00
7.75
7.50
7.25
7.00
6.75
6.50
6.25
7.8
7.5
7.2
6.9
6.6
6.3
6.0
5.7
5.4
log(Mass [M⊙])
−1.75
−2.00
−2.25
−2.50
−2.75
−3.00
−3.25
−3.50
−3.75
−1.2
−1.6
−2.0
−2.4
−2.8
−3.2
−3.6
−1.50
−1.75
−2.00
−2.25
−2.50
−2.75
−3.00
−3.25
−3.50
log(SFR [M⊙/yr])

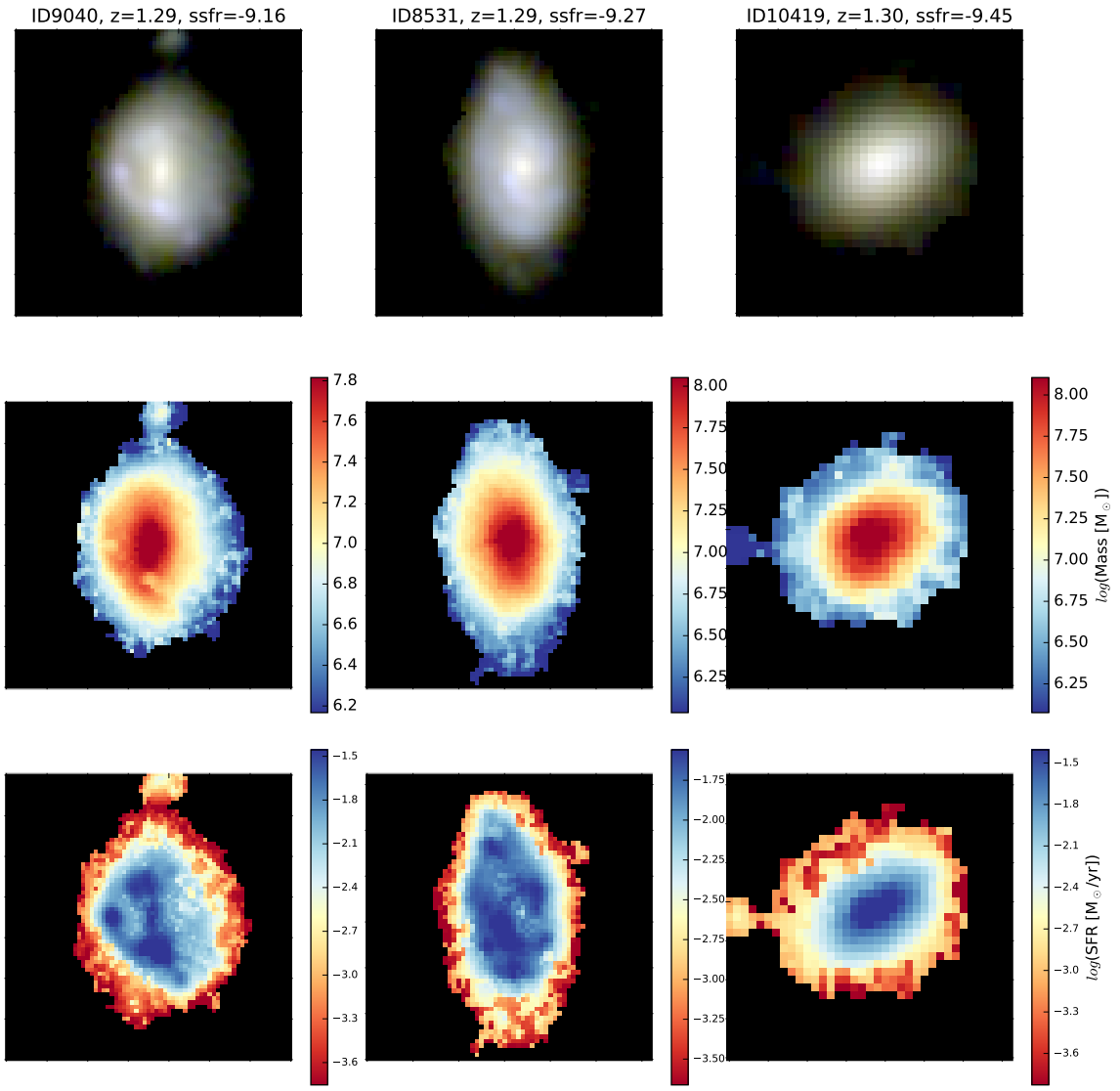
ID9040, z=1.29, ssfr=-9.16
ID8531, z=1.29, ssfr=-9.27
ID10419, z=1.30, ssfr=-9.45
7.8
7.6
7.4
7.2
7.0
6.8
6.6
6.4
6.2
8.00
7.75
7.50
7.25
7.00
6.75
6.50
6.25
8.00
7.75
7.50
7.25
7.00
6.75
6.50
6.25
log(Mass [M⊙])
−1.5
−1.8
−2.1
−2.4
−2.7
−3.0
−3.3
−3.6
−1.75
−2.00
−2.25
−2.50
−2.75
−3.00
−3.25
−3.50
−1.5
−1.8
−2.1
−2.4
−2.7
−3.0
−3.3
−3.6
log(SFR [M⊙/yr])

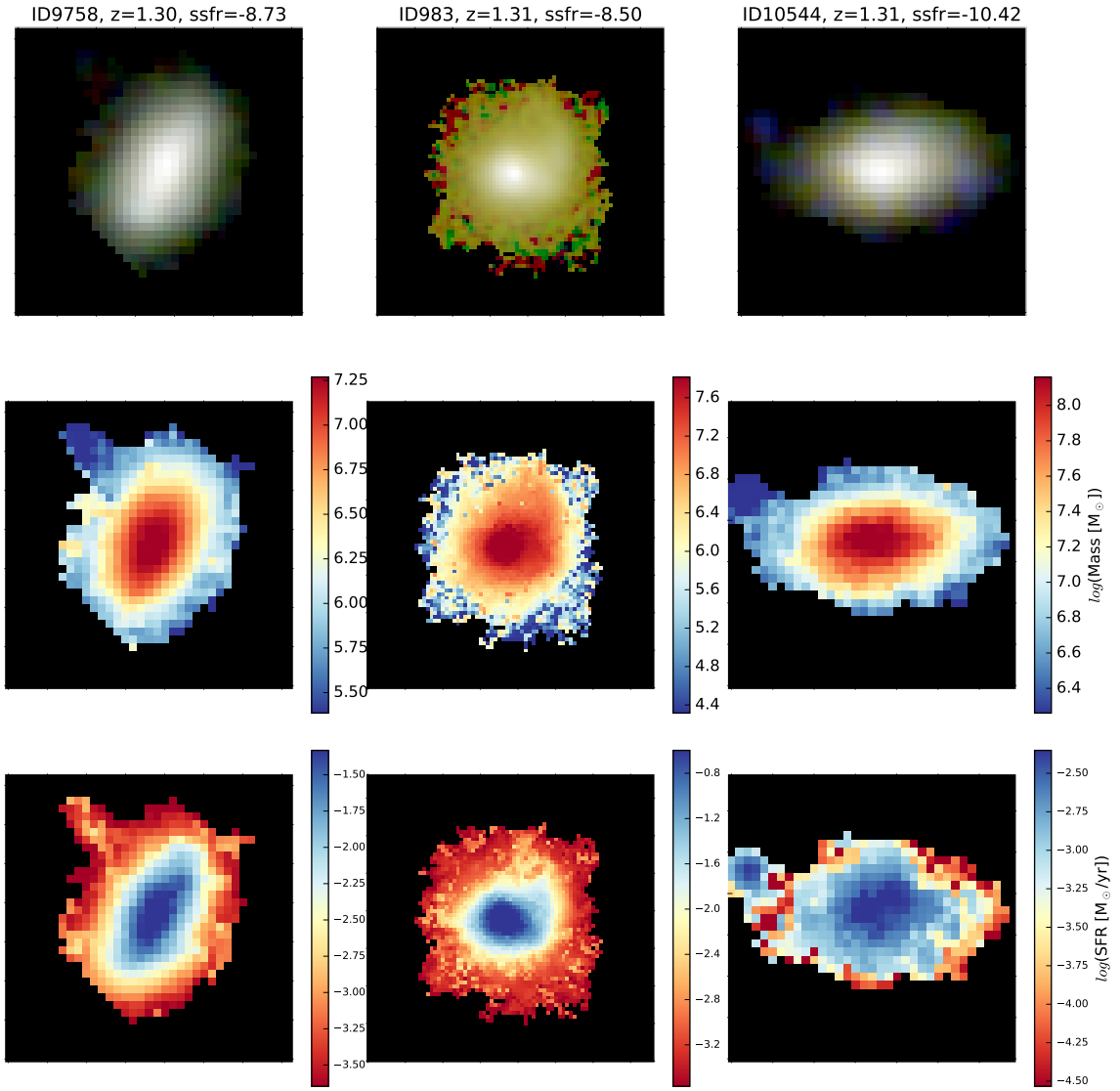
ID9758, z=1.30, ssfr=-8.73
ID983, z=1.31, ssfr=-8.50
ID10544, z=1.31, ssfr=-10.42
7.25
7.00
6.75
6.50
6.25
6.00
5.75
5.50
7.6
7.2
6.8
6.4
6.0
5.6
5.2
4.8
4.4
8.0
7.8
7.6
7.4
7.2
7.0
6.8
6.6
6.4
log(Mass [M⊙])
−1.50
−1.75
−2.00
−2.25
−2.50
−2.75
−3.00
−3.25
−3.50
−0.8
−1.2
−1.6
−2.0
−2.4
−2.8
−3.2
−2.50
−2.75
−3.00
−3.25
−3.50
−3.75
−4.00
−4.25
−4.50
log(SFR [M⊙/yr])

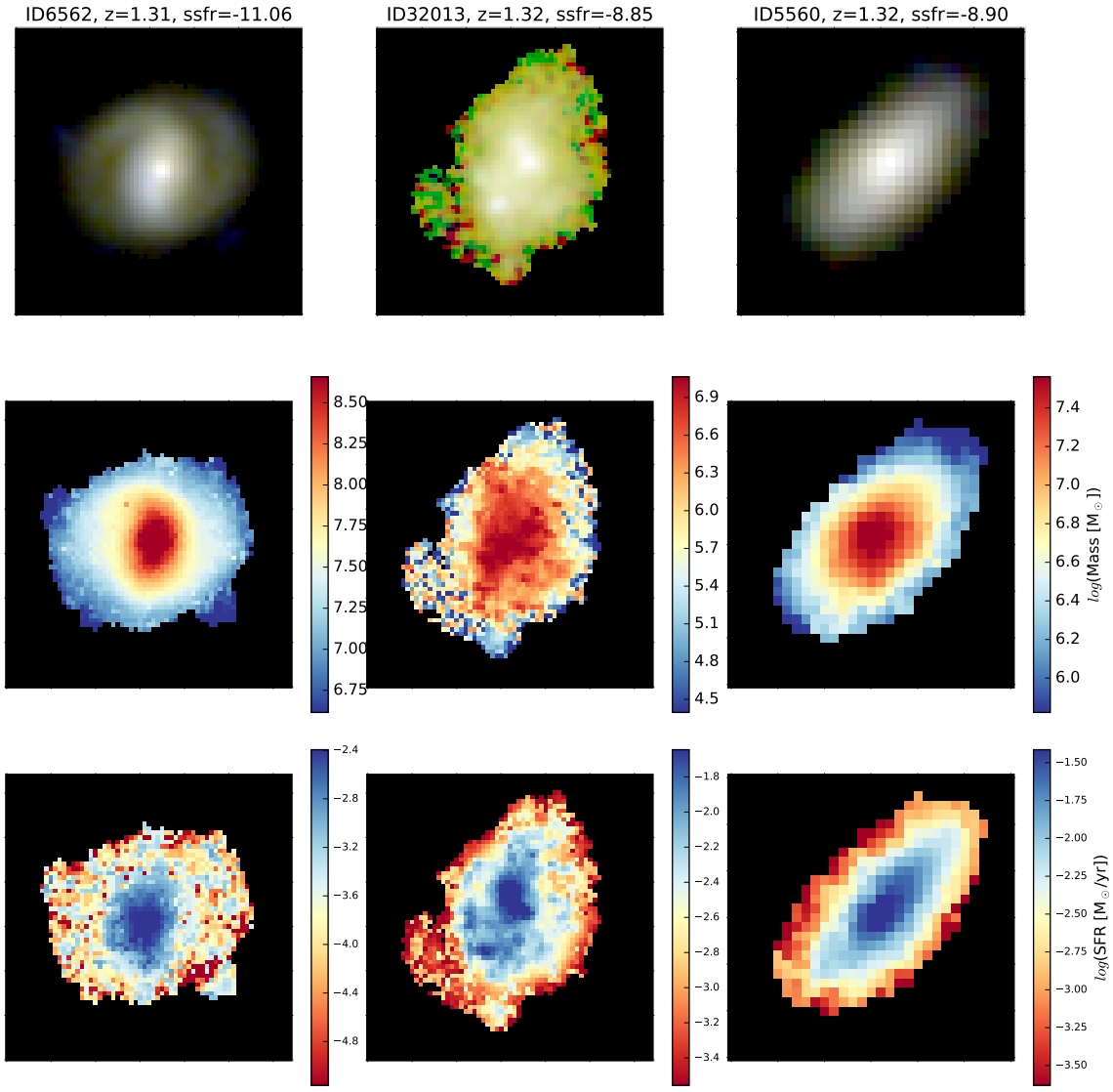
ID6562, z=1.31, ssfr=-11.06
ID32013, z=1.32, ssfr=-8.85
ID5560, z=1.32, ssfr=-8.90
8.50
8.25
8.00
7.75
7.50
7.25
7.00
6.75
6.9
6.6
6.3
6.0
5.7
5.4
5.1
4.8
4.5
7.4
7.2
7.0
6.8
6.6
6.4
6.2
6.0
log(Mass [M⊙])
−2.4
−2.8
−3.2
−3.6
−4.0
−4.4
−4.8
−1.8
−2.0
−2.2
−2.4
−2.6
−2.8
−3.0
−3.2
−3.4
−1.50
−1.75
−2.00
−2.25
−2.50
−2.75
−3.00
−3.25
−3.50
log(SFR [M⊙/yr])

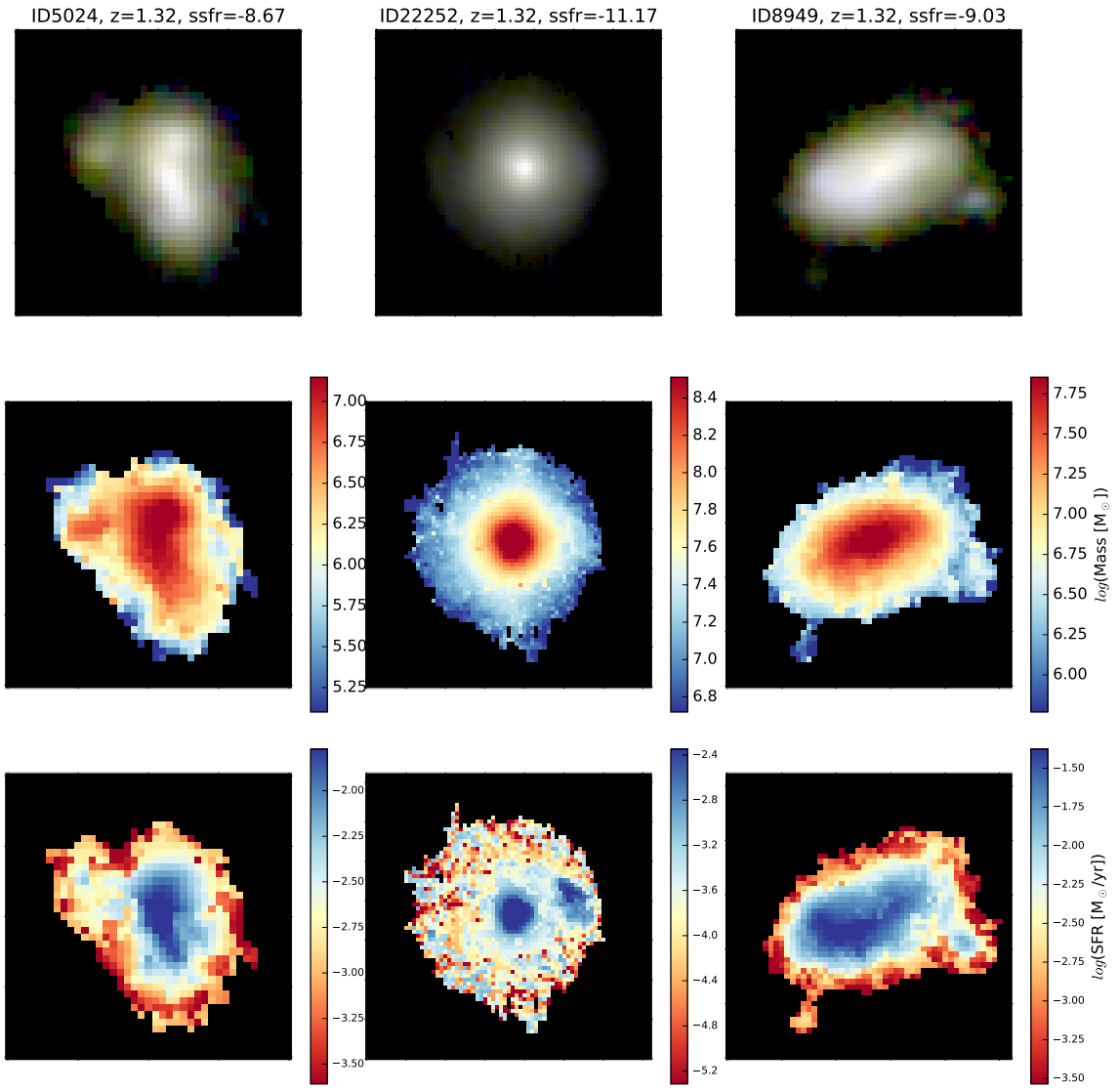
ID5024, z=1.32, ssfr=-8.67
ID22252, z=1.32, ssfr=-11.17
ID8949, z=1.32, ssfr=-9.03
log(Mass [M⊙])
log(SFR [M⊙/yr])

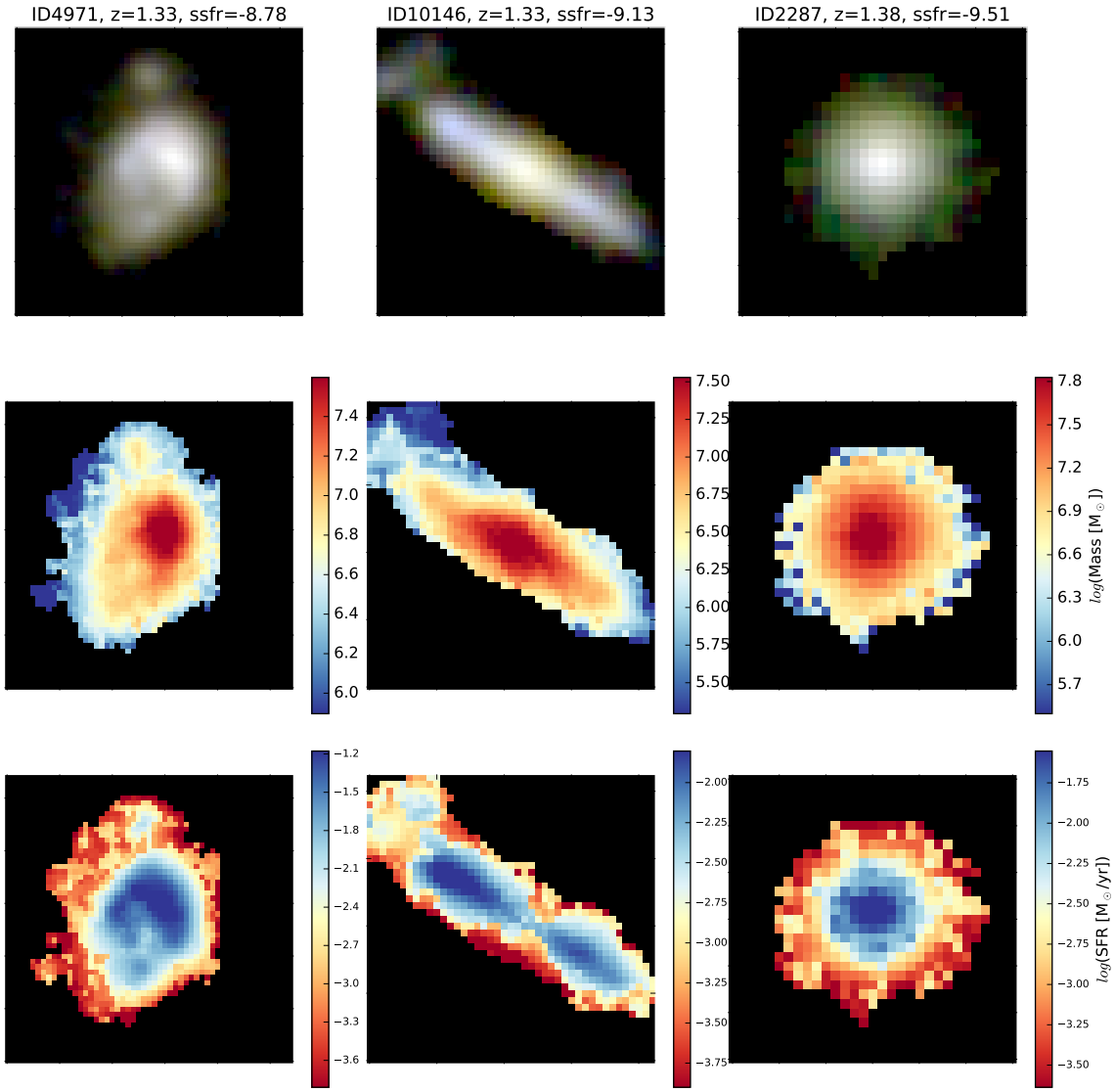
ID4971, z=1.33, ssfr=-8.78
ID10146, z=1.33, ssfr=-9.13
ID2287, z=1.38, ssfr=-9.51
7.4
7.2
7.0
6.8
6.6
6.4
6.2
6.0
7.50
7.25
7.00
6.75
6.50
6.25
6.00
5.75
5.50
7.8
7.5
7.2
6.9
6.6
6.3
6.0
5.7
log(Mass [M⊙])
−1.2
−1.5
−1.8
−2.1
−2.4
−2.7
−3.0
−3.3
−3.6
−2.00
−2.25
−2.50
−2.75
−3.00
−3.25
−3.50
−3.75
−1.75
−2.00
−2.25
−2.50
−2.75
−3.00
−3.25
−3.50
log(SFR [M⊙/yr])

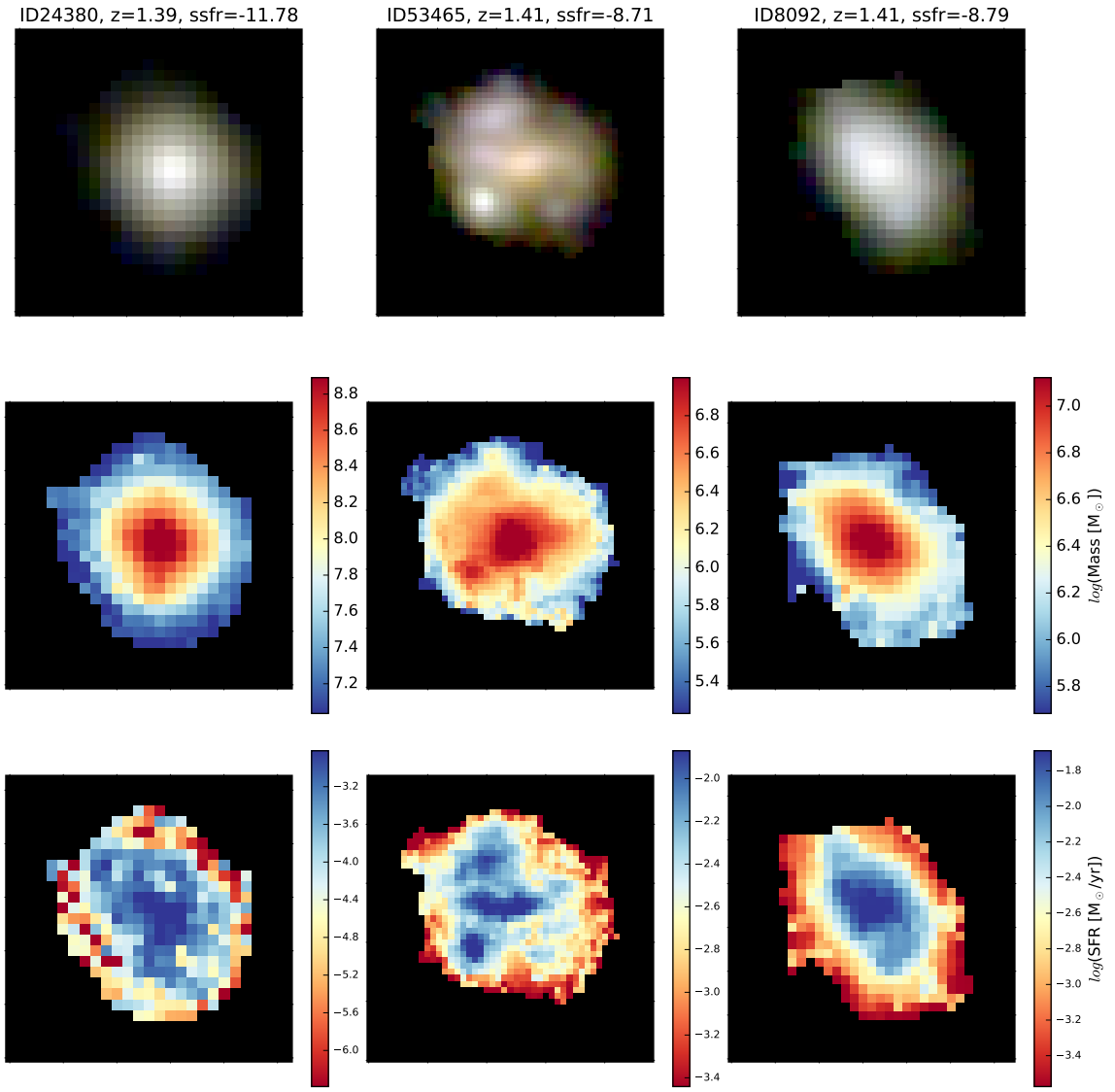
ID24380, z=1.39, ssfr=-11.78
ID53465, z=1.41, ssfr=-8.71
ID8092, z=1.41, ssfr=-8.79
8.8
8.6
8.4
8.2
8.0
7.8
7.6
7.4
7.2
6.8
6.6
6.4
6.2
6.0
5.8
5.6
5.4
7.0
6.8
6.6
6.4
6.2
6.0
5.8
log(Mass [M⊙])
−3.2
−3.6
−4.0
−4.4
−4.8
−5.2
−5.6
−6.0
−2.0
−2.2
−2.4
−2.6
−2.8
−3.0
−3.2
−3.4
−1.8
−2.0
−2.2
−2.4
−2.6
−2.8
−3.0
−3.2
−3.4
log(SFR [M⊙/yr])

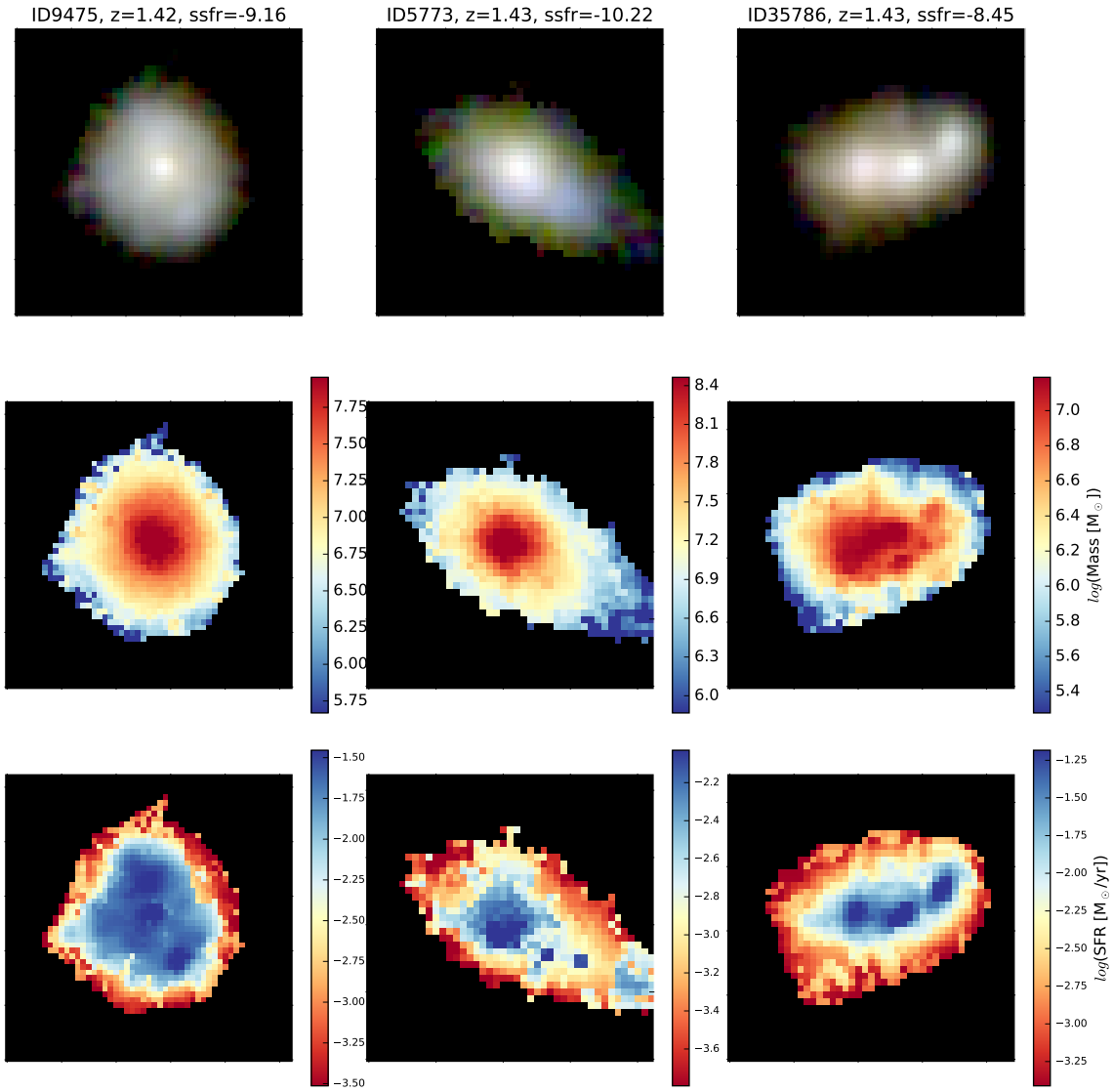
ID9475, z=1.42, ssfr=-9.16
ID5773, z=1.43, ssfr=-10.22
ID35786, z=1.43, ssfr=-8.45
7.75
7.50
7.25
7.00
6.75
6.50
6.25
6.00
5.75
8.4
8.1
7.8
7.5
7.2
6.9
6.6
6.3
6.0
7.0
6.8
6.6
6.4
6.2
6.0
5.8
5.6
5.4
log(Mass [M⊙])
−1.50
−1.75
−2.00
−2.25
−2.50
−2.75
−3.00
−3.25
−3.50
−2.2
−2.4
−2.6
−2.8
−3.0
−3.2
−3.4
−3.6
−1.25
−1.50
−1.75
−2.00
−2.25
−2.50
−2.75
−3.00
−3.25
log(SFR [M⊙/yr])

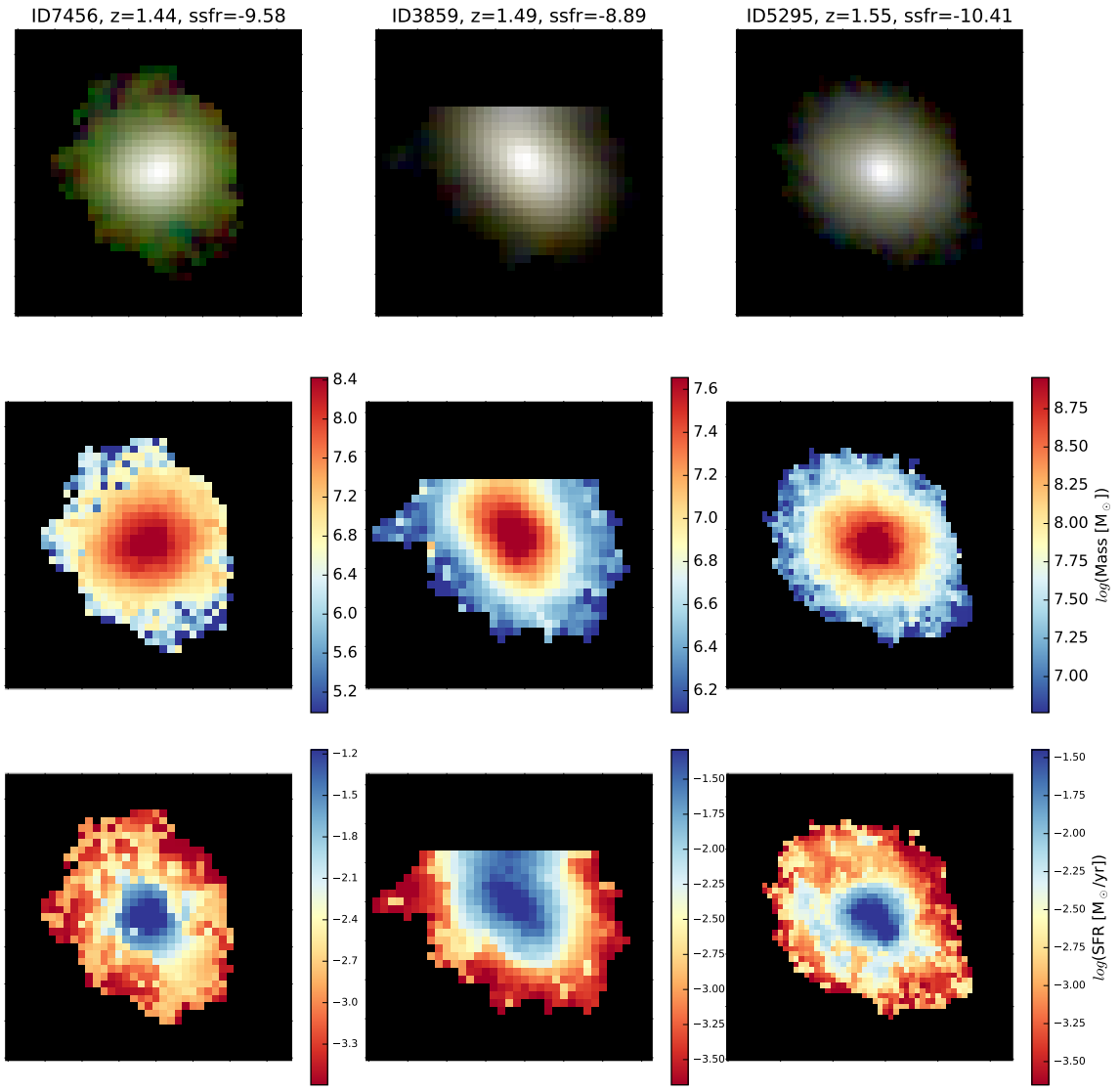
ID7456, z=1.44, ssfr=-9.58
ID3859, z=1.49, ssfr=-8.89
ID5295, z=1.55, ssfr=-10.41
8.4
8.0
7.6
7.2
6.8
6.4
6.0
5.6
5.2
7.6
7.4
7.2
7.0
6.8
6.6
6.4
6.2
8.75
8.50
8.25
8.00
7.75
7.50
7.25
7.00
log(Mass [M⊙])
−1.2
−1.5
−1.8
−2.1
−2.4
−2.7
−3.0
−3.3
−1.50
−1.75
−2.00
−2.25
−2.50
−2.75
−3.00
−3.25
−3.50
−1.50
−1.75
−2.00
−2.25
−2.50
−2.75
−3.00
−3.25
−3.50
log(SFR [M⊙/yr])

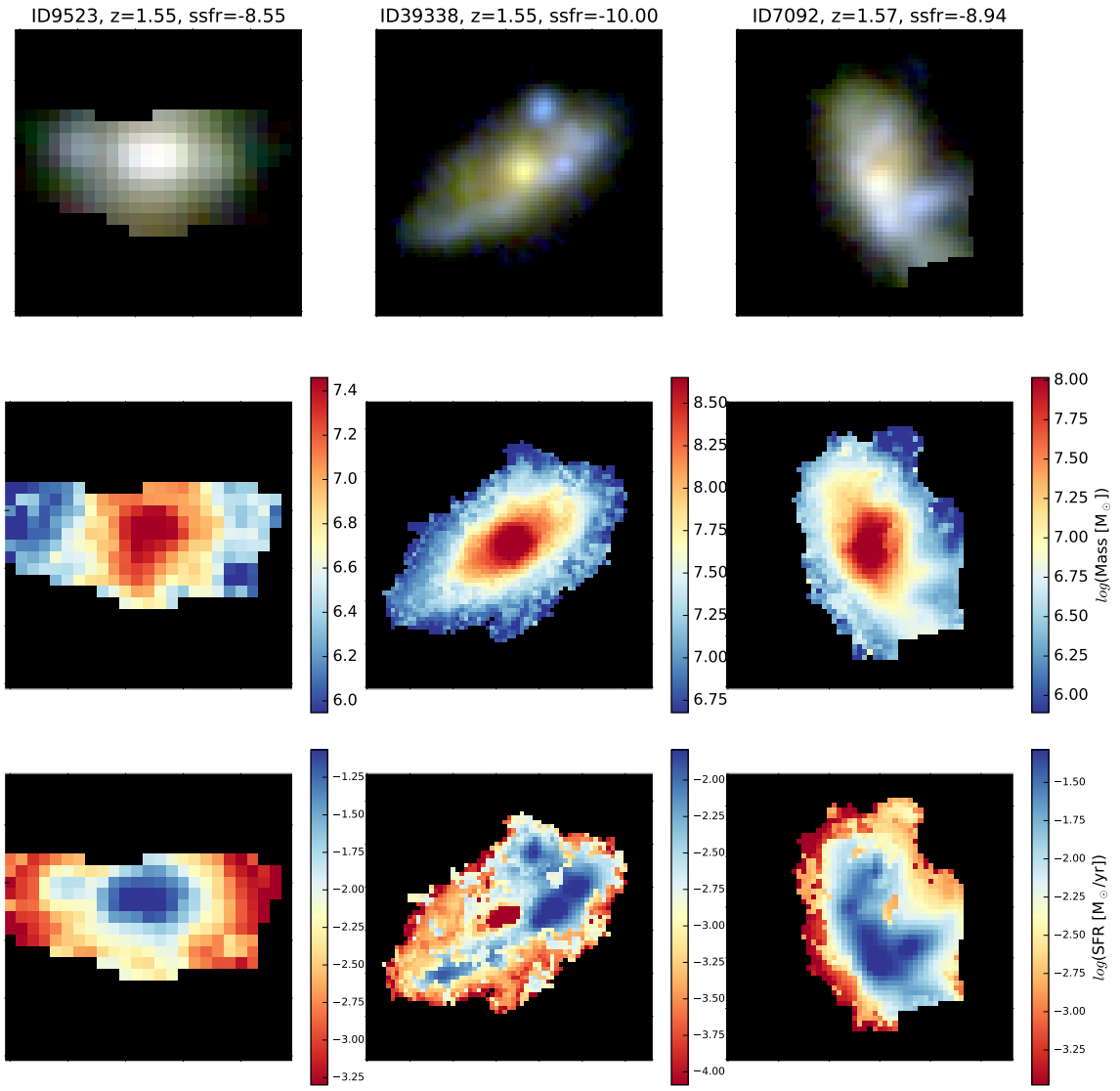
ID9523, z=1.55, ssfr=-8.55
ID39338, z=1.55, ssfr=-10.00
ID7092, z=1.57, ssfr=-8.94
log(Mass [M⊙])
log(SFR [M⊙/yr])

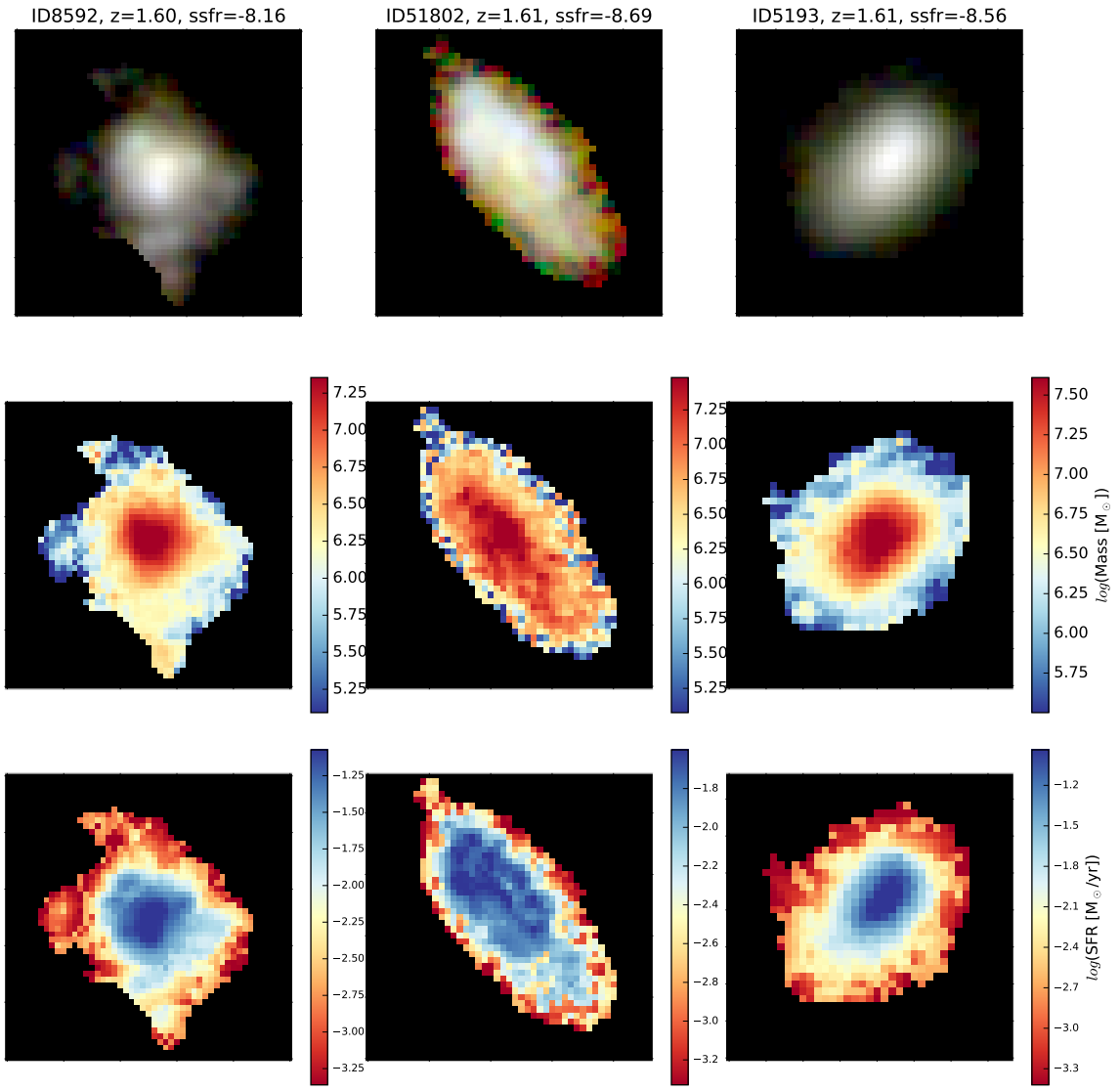
ID8592, z=1.60, ssfr=-8.16
ID51802, z=1.61, ssfr=-8.69
ID5193, z=1.61, ssfr=-8.56
log(Mass [M⊙])
log(SFR [M⊙/yr])

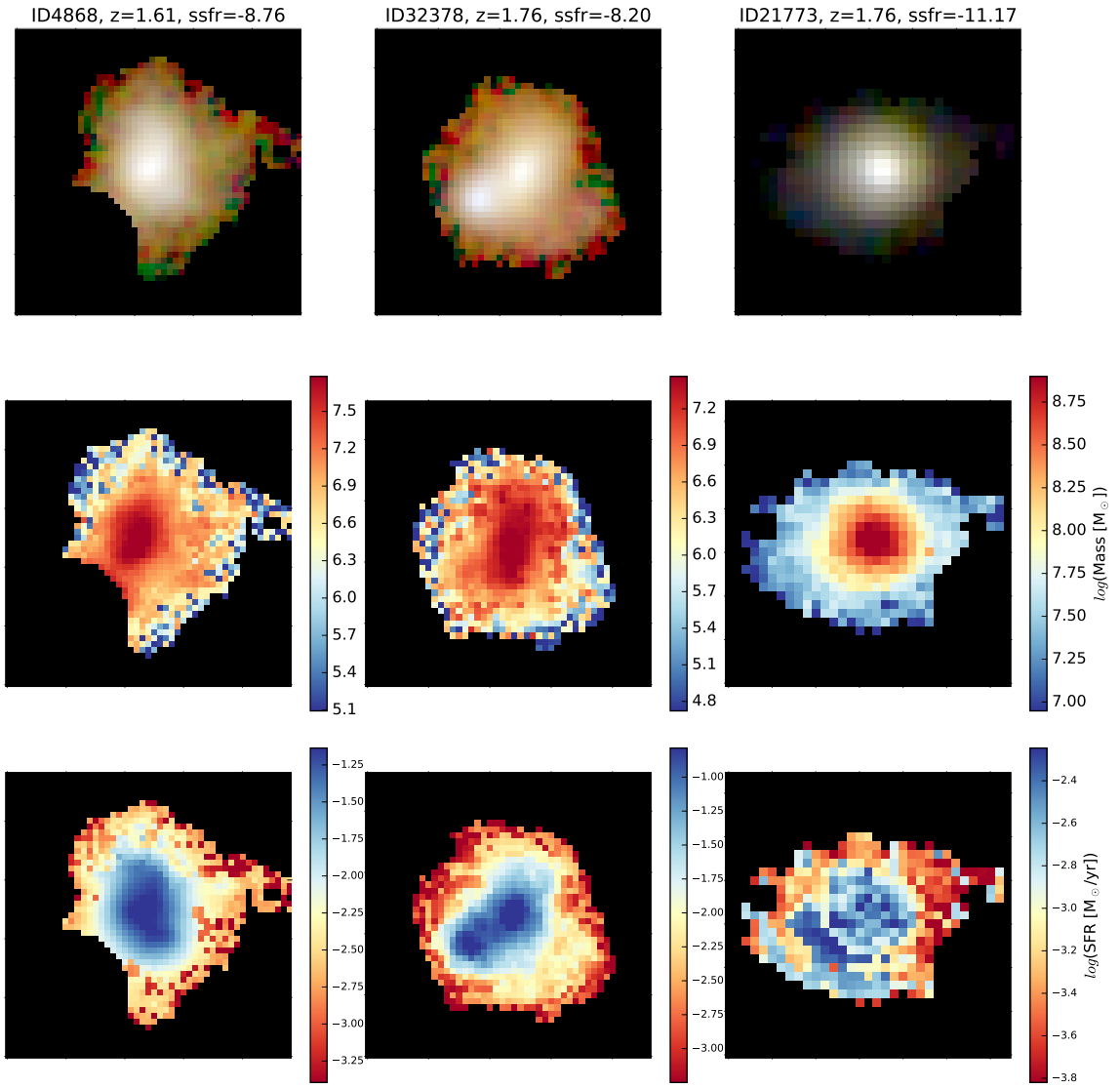
ID4868, z=1.61, ssfr=-8.76
ID32378, z=1.76, ssfr=-8.20
ID21773, z=1.76, ssfr=-11.17
log(Mass [M⊙])
log(SFR [M⊙/yr])

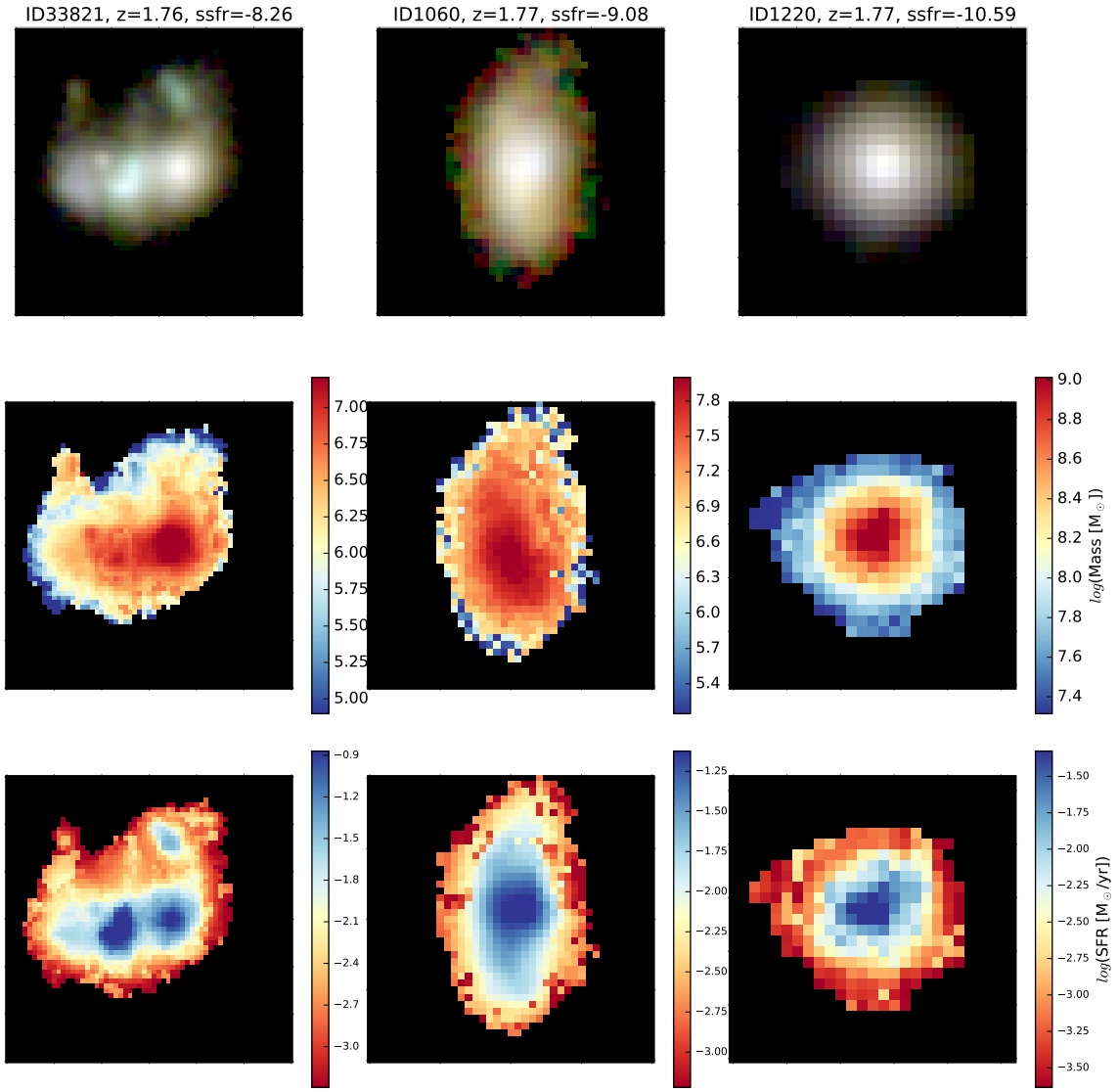
ID33821, z=1.76, ssfr=-8.26
ID1060, z=1.77, ssfr=-9.08
ID1220, z=1.77, ssfr=-10.59
7.00
6.75
6.50
6.25
6.00
5.75
5.50
5.25
5.00
7.8
7.5
7.2
6.9
6.6
6.3
6.0
5.7
5.4
9.0
8.8
8.6
8.4
8.2
8.0
7.8
7.6
7.4
log(Mass [M⊙])
−0.9
−1.2
−1.5
−1.8
−2.1
−2.4
−2.7
−3.0
−1.25
−1.50
−1.75
−2.00
−2.25
−2.50
−2.75
−3.00
−1.50
−1.75
−2.00
−2.25
−2.50
−2.75
−3.00
−3.25
−3.50
log(SFR [M⊙/yr])

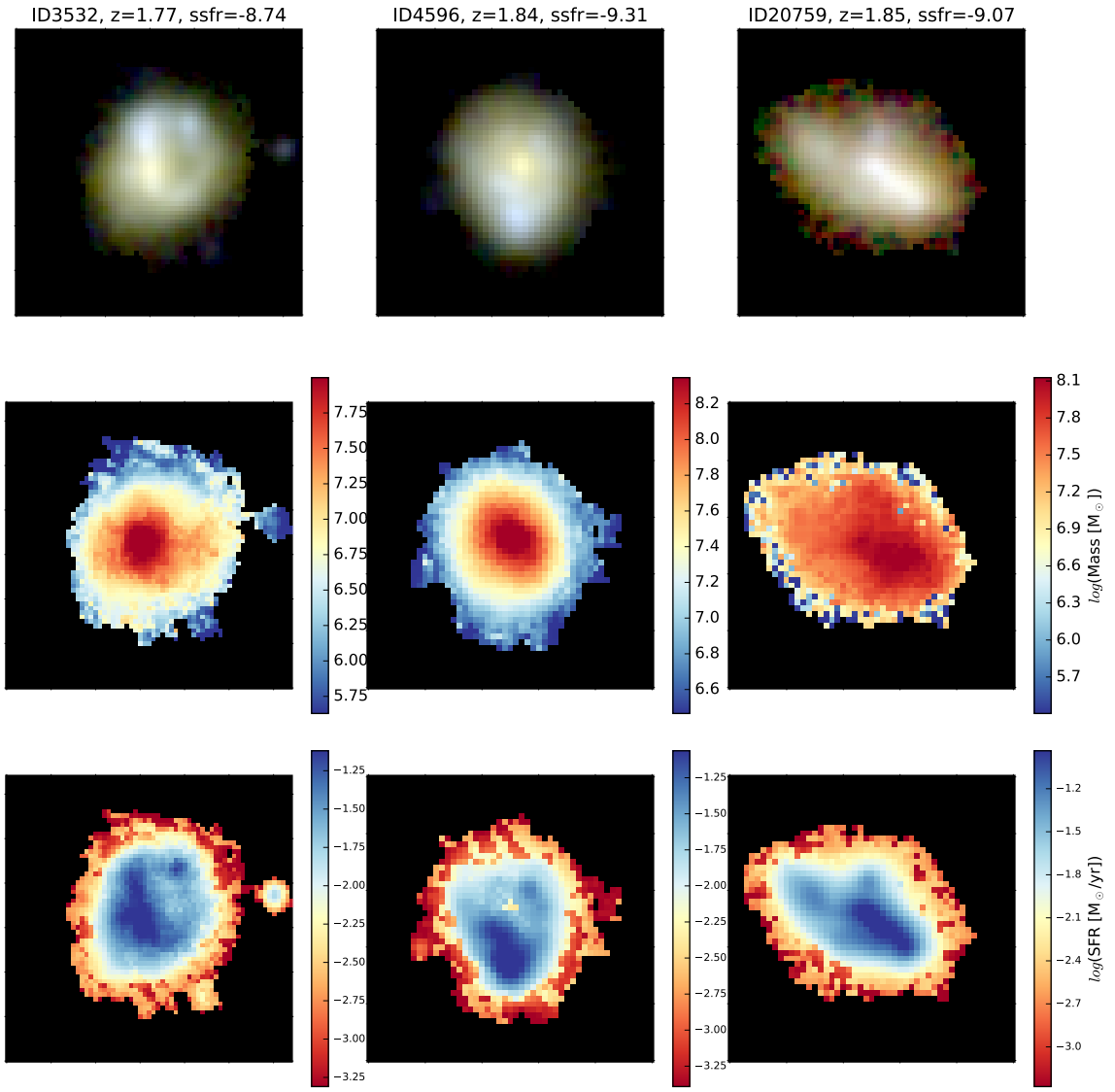
ID3532, z=1.77, ssfr=-8.74
ID4596, z=1.84, ssfr=-9.31
ID20759, z=1.85, ssfr=-9.07
log(Mass [M⊙])
log(SFR [M⊙/yr])

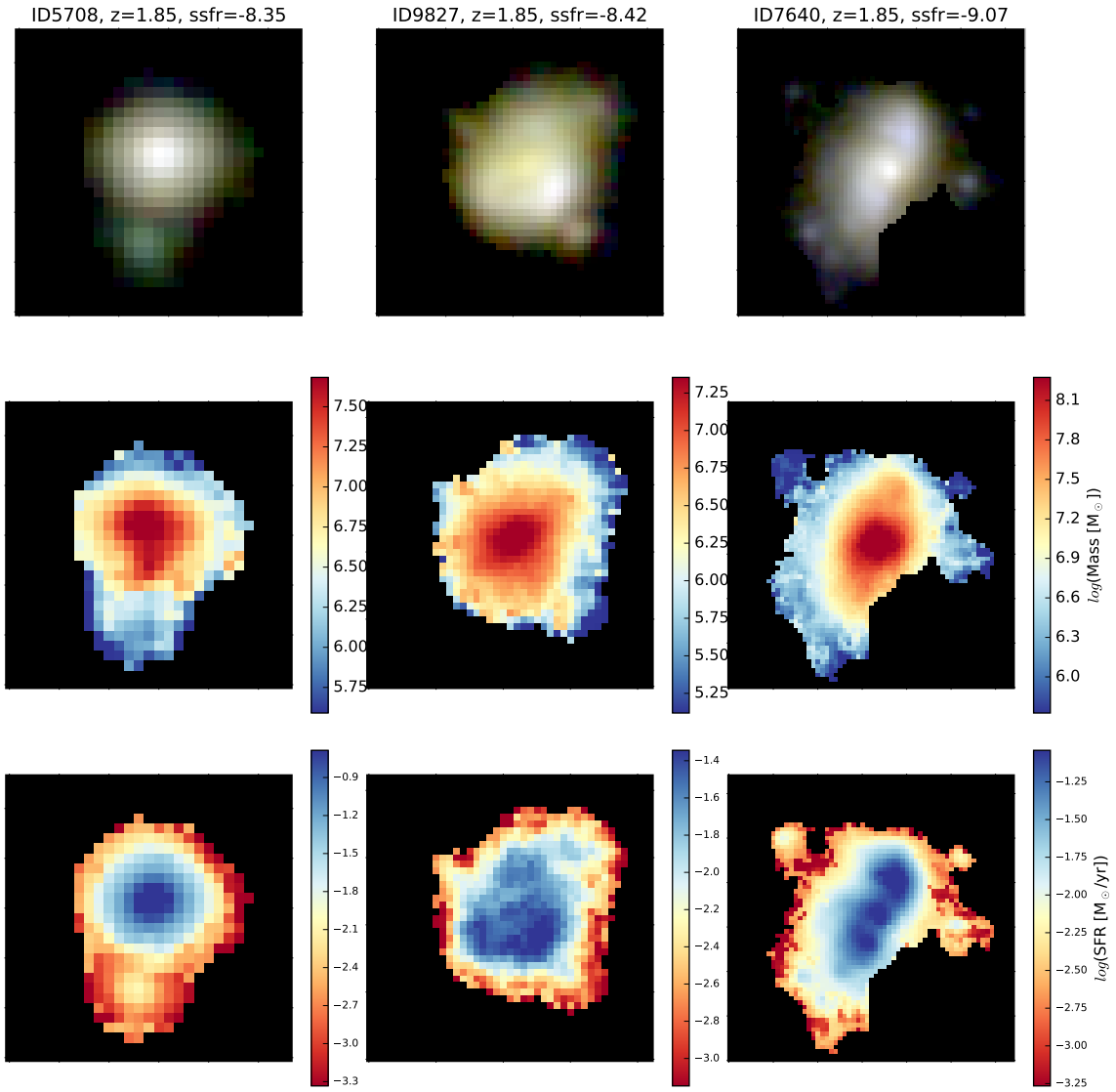
ID5708, z=1.85, ssfr=-8.35
ID9827, z=1.85, ssfr=-8.42
ID7640, z=1.85, ssfr=-9.07
log(Mass [M⊙])
log(SFR [M⊙/yr])

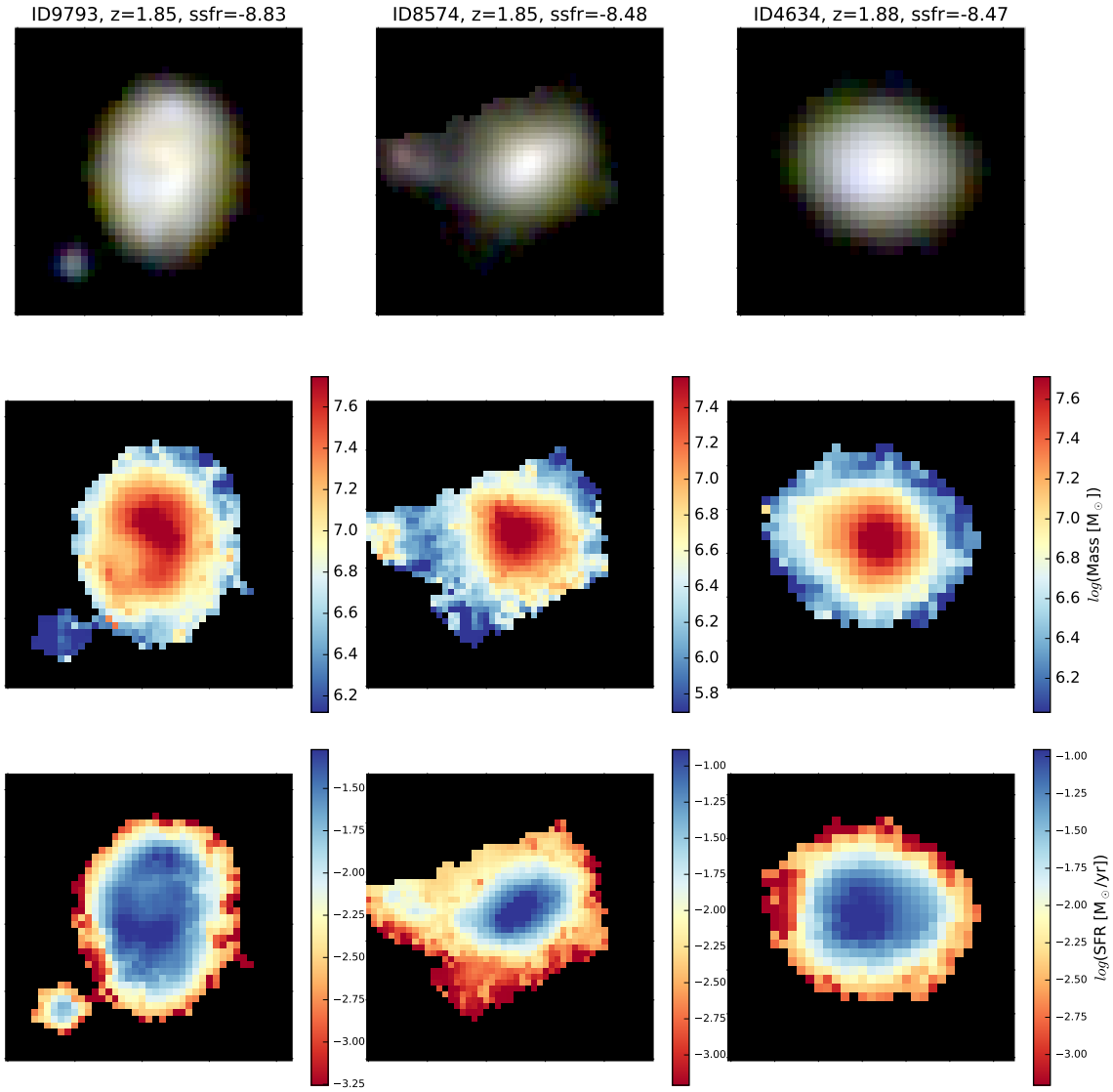
ID9793, z=1.85, ssfr=-8.83
ID8574, z=1.85, ssfr=-8.48
ID4634, z=1.88, ssfr=-8.47
log(Mass [M⊙])
log(SFR [M⊙/yr])

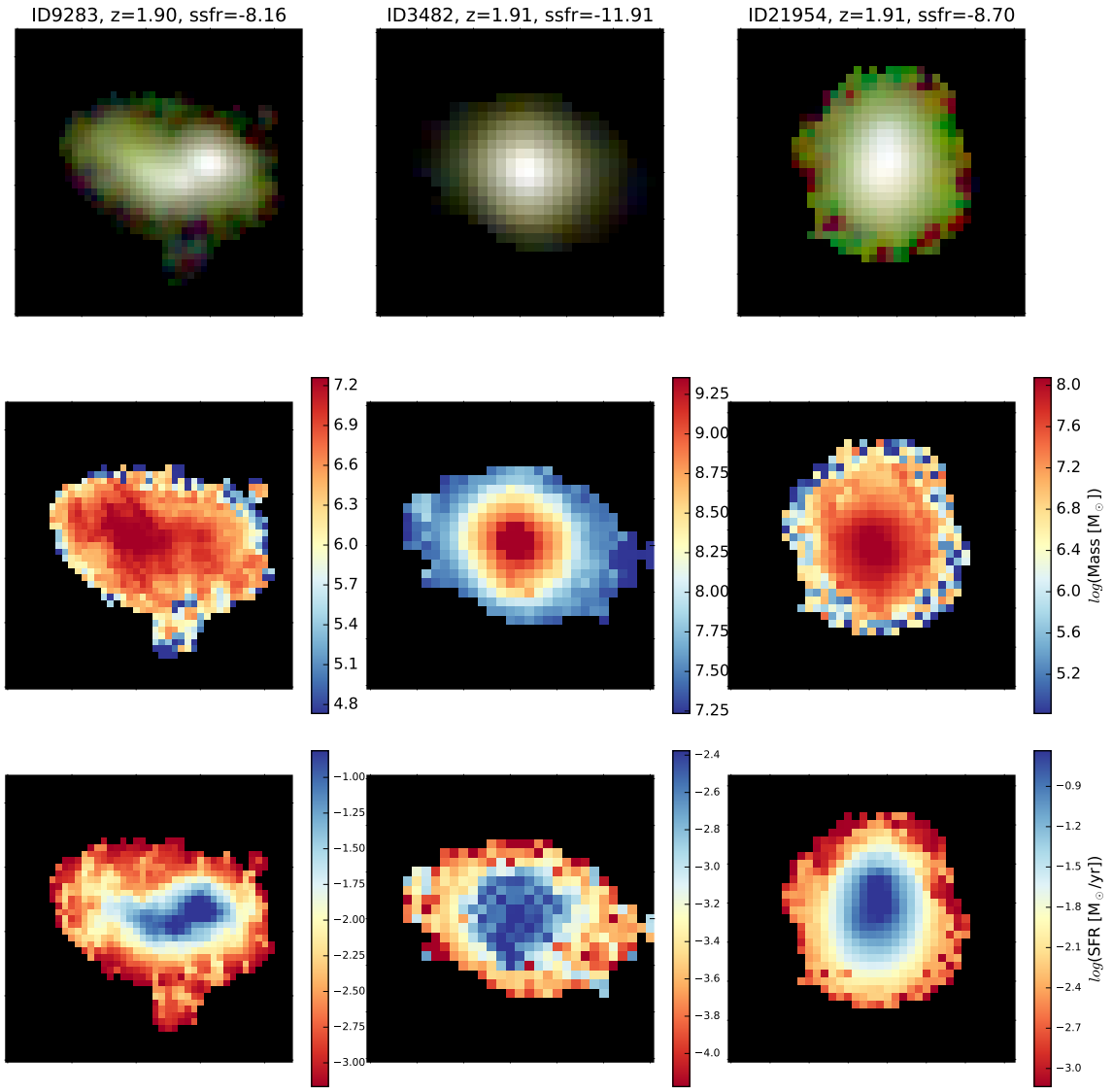
ID9283, z=1.90, ssfr=-8.16
ID3482, z=1.91, ssfr=-11.91
ID21954, z=1.91, ssfr=-8.70
7.2
6.9
6.6
6.3
6.0
5.7
5.4
5.1
4.8
9.25
9.00
8.75
8.50
8.25
8.00
7.75
7.50
7.25
8.0
7.6
7.2
6.8
6.4
6.0
5.6
5.2
log(Mass [M⊙])
−1.00
−1.25
−1.50
−1.75
−2.00
−2.25
−2.50
−2.75
−3.00
−2.4
−2.6
−2.8
−3.0
−3.2
−3.4
−3.6
−3.8
−4.0
−0.9
−1.2
−1.5
−1.8
−2.1
−2.4
−2.7
−3.0
log(SFR [M⊙/yr])

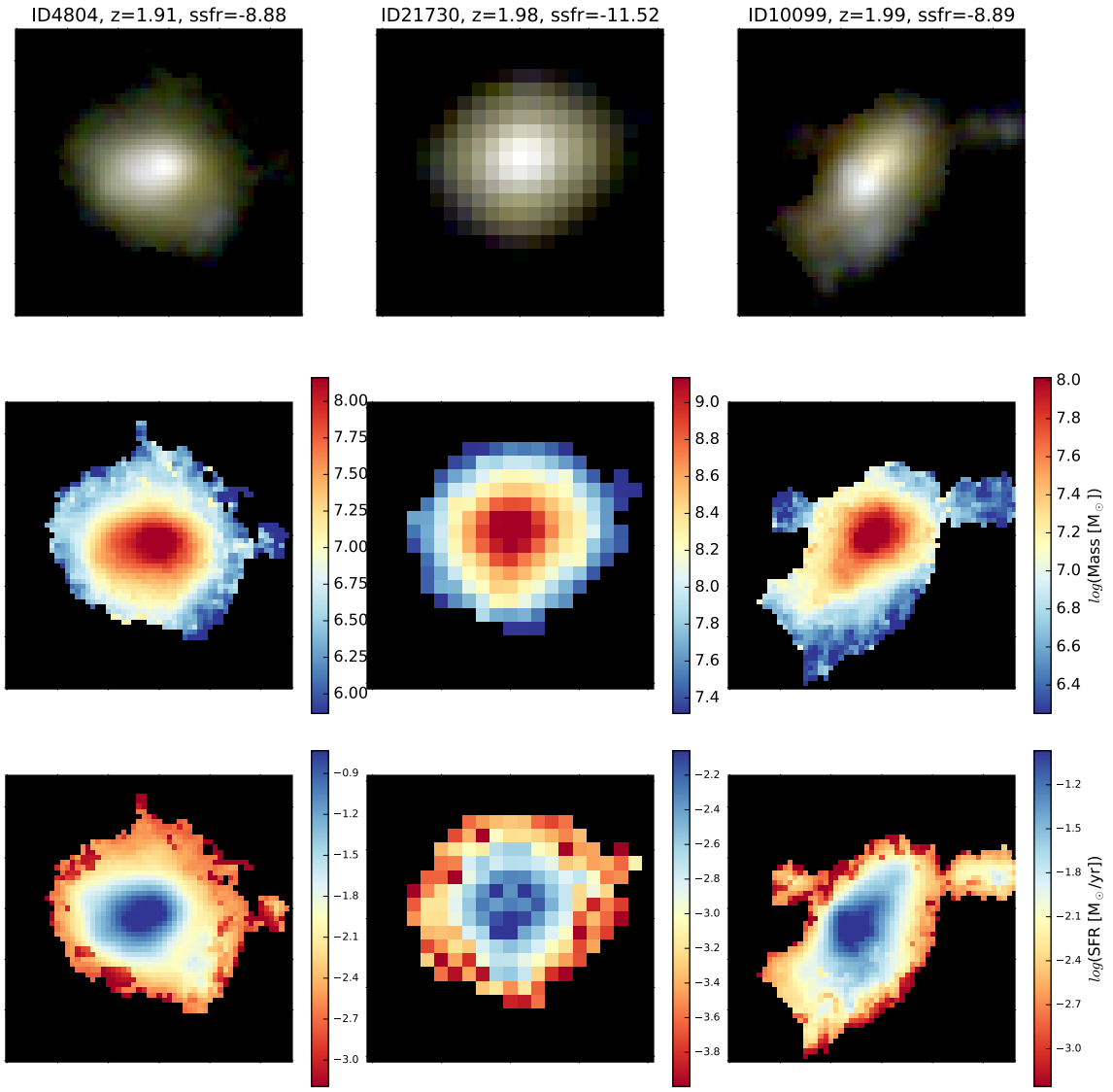
ID4804, z=1.91, ssfr=-8.88
ID21730, z=1.98, ssfr=-11.52
ID10099, z=1.99, ssfr=-8.89
8.00
7.75
7.50
7.25
7.00
6.75
6.50
6.25
6.00
9.0
8.8
8.6
8.4
8.2
8.0
7.8
7.6
7.4
8.0
7.8
7.6
7.4
7.2
7.0
6.8
6.6
6.4
log(Mass [M⊙])
−0.9
−1.2
−1.5
−1.8
−2.1
−2.4
−2.7
−3.0
−2.2
−2.4
−2.6
−2.8
−3.0
−3.2
−3.4
−3.6
−3.8
−1.2
−1.5
−1.8
−2.1
−2.4
−2.7
−3.0
log(SFR [M⊙/yr])